NASA-CR-199696

CSTAR
TECHNICAL SYMPOSIUM

The University of Tennessee - Calspan
Center for Space Transportation
and Applied Research

The Fifth Annual Technical Symposium November 10, 1993

At The University of Tennessee Space Institute
Tullahoma, Tennessee

ATTACHMENT I
NAGW-1195
CSTAR-FINAL REPORT

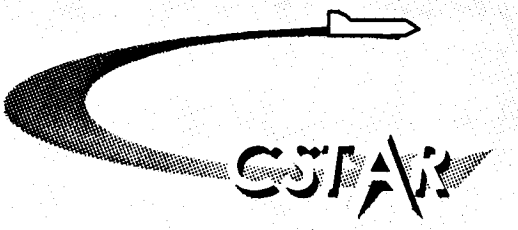

CSTAR
UTSI Research Park
Tullahoma, TN 37388-8897
(615) 454-9294
FAX: (615) 455-6167

Laser Material Processing

Artificial Intelligence/ Expert Systems

Space Transportation

Computational Methods

Chemical Propulsion

Electric Propulsion

TABLE OF CONTENTS

CSTAR
FIFTH ANNUAL SYMPOSIUM PROCEEDINGS
November 10, 1993

The University of Tennessee-Calspan
Center for Space Transportation and Applied Research

UTSI RESEARCH PARK TULLAHOMA, TN 37388-8897 FAX (615) 455-6167

November 10, 1993

Welcome to the Fifth Annual Technical Symposium sponsored by the UT-Calspan Center for Space Transportation and Applied Research (CSTAR).

CSTAR, one of the 17 NASA Centers for the Commercial Development of Space, has just completed its sixth year of operation. In conjunction with 14 industrial and 10 university partners, the Center is engaged in 17 projects, with active participation by more than 50 faculty, staff and graduate students. NASA's Marshall Space Flight Center, Lewis Research Center and AMES Research Center support several projects. The CSTAR investigators deserve significant recognition and all the credit for the Center's accomplishments and continued growth.

This Technical Symposium is organized to provide an overview of the technical accomplishments during the past year in the Center's five Research and Technology focus areas:

Chemical Propulsion
Electric Propulsion
Commercial Space Transportation
Computational Methods
Laser Materials Processing

The Center broadened its scope of responsibility three years ago when it accepted management of the COMmercial Experiment Transporter (COMET) program. COMET is scheduled to be launched from Wallops Island during FY94. Two significant flight experiments continue to be developed: first, the Electric Propulsion Orbital Platform, a consortium consisting of McDonnell Douglas, Boeing, Rocket Research and CSTAR; second, the Space Applications of Industrial Laser Systems, a cooperative effort between CSTAR, Lumonics, Auburn University, and Tennessee Technology University.

Paula Reed and Cherie Olive deserve considerable recognition and credit for assimilating the proceedings and organizing this symposium. Sandy Shankle and her staff in the UTSI Short Course Office have efficiently handled the registration and logistics. To all of you, thank you for your dedication and assistance.

We believe the CSTAR Technical Symposium will be a helpful and rewarding experience. While here, please feel free to talk to the investigators and visit the facilities and laboratories at The University of Tennessee Space Institute, at AEDC and at the CSTAR building.

Sincerely,

George W. Garrison, PhD.
Executive Director

cro

CSTAR TECHNICAL SYMPOSIUM
LASER MATERIAL PROCESSING

A

Space Applications Industrial Laser System (SAILS)
An Update

Laser Industrial Partnership Program (LIPP)
Annual Progress Report

Laser Welding Dissimilar Reflective Alloys

Laser Material Processing

Artificial Intelligence/ Expert Systems

Space Transportation

Computational Methods

Chemical Propulsion

Electric Propulsion

Space Applications Industrial Laser System (SAILS)[1]:An Update

T.D. McCay, J.B. Bible, R.E. Mueller, M.H. McCay, C.M. Sharp, and J.A. Hopkins

The University of Tennessee-Calspan
Center for Space Transportation and Applied Research (CSTAR)
Tullahoma, Tennessee 37388-8897
USA

and

The University of Tennessee Space Institute (UTSI)
Center for Laser Applications
Tullahoma, Tennessee 37388-8897
USA

ABSTRACT

A program is under way to develop a YAG laser based materials processing workstation to fly in the cargo bay of the Space Shuttle. This workstation, called the Space Applications Industrial Laser System (SAILS), will be capable of brazing, cutting, welding, drilling, and surface treating various materials proposed for use on the Space Station Freedom, including steel, aluminum and inconel alloys planned for use in construction. As well as demonstrating the ability of a YAG laser to perform remote (fiberoptic delivered) repair and fabrication operations in space, fundamental data will be collected on these processes for comparison with terrestrial data and models.

The flight system, scheduled to fly in late 1996, will be configured in three modules using standard Get-Away-Special (GAS) canisters. The first module holds the laser head and cooling system, the second contains a high peak power electrical supply, and the third module houses the materials processing workstation and the command and data acquisition subsystems. The laser head and workstation canisters are linked by a fiberoptic cable to transmit the laser light.

The team assembled to carry out this project includes Lumonics Industrial Products Division (laser), Tennessee Technological University (structural analysis and fabrication), Auburn University Center for Space Power (power supply), University of Waterloo (low-g laser processing), and CSTAR/UTSI (data acquisition, control, software, integration and experiment design).

This report describes the SAILS program, highlights recent accomplishments and projects the schedule for upcoming activities.

INTRODUCTION

The mission of CSTAR is to team with industry and academia in the development of new and innovative space technologies. The SAILS program has been developed under this mission because of its broad potential to benefit industry, academia, and government through advanced laser materials processing technology, both in terms of space and ground-based applications. The long term space missions planned by NASA will require some form of machining and repair capability. The SAILS experiment will act as the proof-of-concept to firmly establish the YAG laser as a viable materials processing tool for space applications. Follow-on phases to the program will develop the infrastructure necessary for implementation on long-term space structures.

As the lifetime and complexity of space structures increase, the ability to construct, maintain, and repair these structures in space must also be improved. The industrial laser represents a possible solution to the problem of conducting multiple task manufacturing and

[1]This work is supported by NASA Code C under grant NAGW-1195, The University of Tennessee Space Institute, and Lumonics Industrial Products Division.

repair operations at remote, hostile locations such as an orbiting platform. The purpose of the SAILS project is to demonstrate the capability to employ a YAG laser processing facility in space and to perform practical laser materials processing operations under microgravity conditions. The objectives of this project may be grouped under the following categories:

Science: Determine the effects of reduced gravity on welding, drilling, cutting, brazing, and soldering. Use the experimental results in conjunction with numerical models to improve predictions of process behavior in both one and low g.

Space Engineering: Demonstrate the viability of laser technology to perform repair and fabrication type operations in space. Applications include a laser repair kit for Space Station, manned Mars missions, a Moon base, and a laser-based factory in space.

Laser Engineering: Refine and demonstrate the industrial YAG laser to show that it has become a simple, compact, efficient, and rugged tool capable of operating in any environment. It is of particular importance to show the advantages of fiberoptic beam delivery, including ruggedness and the ability to operate in remote and harsh environments.

The 1996 flight, designated SAILS-01, is the first in a series of experiments designed to validate the YAG laser as a viable multipurpose energy workstation for space. Interest by the microgravity science community as well as other industry, academia, and government organizations has resulted in plans for at least two follow-on flights. Figure 1 indicates the current flight strategy for the SAILS facility. The Auburn flight is devoted to precise materials property measurements whereas the two In-Step experiments are associated with developing laser assisted coating technology for space missions.

SAILS EXPERIMENT SELECTION

As the SAILS experiment is designed to demonstrate the viability and practicality of laser materials processing in space, the processes to be tested and the materials used are based upon possible applications in space systems. After initial trials to show that the materials could be processed with the available laser power anticipated for the flight system, the materials and processes were selected as shown in Table 1.

The processes all have obvious practical applications in space and on earth. Structural joining operations (welding and brazing) will be needed in the assembly and repair of man-rated habitats. Cutting will be required for removing damaged components for repair and in the recycling of space debris. Soldering of electrical and electronic components could be accomplished remotely using a dexterous manipulator and a fiberoptic delivered laser beam, with much less heat input to nearby components than with a conventional solder iron.

GROUND EXPERIMENTATION

Preliminary studies were carried out during 1991-92 using a 400 W Lumonics JK701 YAG laser to ensure that the materials and processes under consideration could be processed with a relatively low power laser. Since that time, the operating characteristics of the flight laser have been made available with the introduction of the LUXSTAR laser by Lumonics Corporation, the industrial sponsor for the program (see Table 2). Detailed experiment studies will be completed in late 1993 at CSTAR using the LUXSTAR laser to establish the precise processing conditions anticipated for each of the flight experiment samples. As well as finding workable combinations of processing parameters, this study will be used to determine scaling relationships (depth and width of weld vs power, metal structure) between the flight power level and projected full-scale space-based laser power levels. This will allow the prediction of the performance of higher power lasers operating under space conditions.

FLIGHT HARDWARE DESIGN

The SAILS flight experiment will be housed in three Get-Away-Special (GAS) canisters mounted on the HitchHiker cross-bay carrier as shown in Figure 2. These canisters will be interconnected via the top plates for experiment control and distribution of power and laser energy. Figure 3 shows this three-canister configuration and the major components in each module.

The first canister, CAN 1, will contain the laser head, output module (capacitor bank), and cooling system for generation of the laser energy necessary to conduct the experiments. The laser head and output module will be acquired and repackaged from the LUXSTAR Nd:YAG 50 W laser system, a new commercial product manufactured by Lumonics. The cooling system, consisting of a pump and heat exchanger, will be fabricated at CSTAR to provide removal of the heat generated in the laser cavity during processing.

The second canister, CAN 2, contains the electrical power supply for providing the high peak power necessary to generate the laser energy in CAN 1. This can will consist of Silver-Zinc battery cells housed in a vented container (power source), a DC-DC

convertor for electrical power conditioning, and the laser control module. The DC-DC convertor will condition the battery energy to the proper voltage for transfer to the capacitors in CAN 1. The Auburn University Center for Space Power will design and fabricate the power conditioning system in this canister and the power source will be provided by CSTAR. Use of orbiter power was considered as an alternative to the batteries for laser power. However, the peak power requirements for the experiment is approximately 5 kW, which is greater than the maximum of 3.5 kW available to a HitchHiker payload.

CAN 1 and CAN 2 will be connected via an electrical cable for transfer of the high voltage battery power from the power supply to the laser head. The connectors, cable support structure, and canister modifications will be provided by Goddard Space Flight Center (GSFC) and are currently under development. CSTAR will provide the electrical cable.

The combination of CAN 1, CAN 2, and the voltage interconnection produce a complete, self-contained, ruggedized Nd:YAG laser system for delivery of laser energy to the experiment workstation, CAN 3. The design is such that the two laser/power supply canisters can serve as a test bed for other materials processing systems which might be envisioned in the future.

The third canister, CAN 3, contains the workstation for conducting the SAILS experiments. This canister consists of the experiment samples, workhandling, and command and data acquisition systems. The sixteen samples (2.5 cm x 5.5 cm each) will be rotated on a platen and positioned under the laser beam for processing. A given sample will be processed for approximately 15 seconds, followed by a monitoring period to allow each criticalsubsystem to return to appropriate operating conditions before moving to the next sample. This will continue until all 16 samples have been processed. The internal laser beam will be delivered as a free-space beam with moving optics. This configuration mimics the current industrial laser practice of using a moving optics end effector to achieve more motion flexibility. The data acquisition will include video recording of the actual process (coaxially and along the sample), sampling of the environmental conditions before and during each process, and monitoring of the laser process parameters (pulse length, energy, and duration) for each sample.

CAN 3 will be linked to CAN 1 via a fiberoptic cable for delivery of the laser energy to the workstation. This cable will consist of a 400 micron fiber surrounded by a copper shield and control/continuity data lines all encompassed in a nylon outer cover. The connectors will be designed for a hermetic seal at the canister with lid modifications to be provided by GSFC and the fiber/connectors to be provided by CSTAR.

Each of the three canisters will be filled with gas pressurized to one atmosphere. CAN 1 and CAN 2 will use dry N_2 while CAN 3 will use Argon to provide enhanced processing conditions for the flight hardware components.

PROGRESS TO DATE

The SAILS program was approved in 1990 and the payload plan received approval from NASA in 1991. As described above, work through FY92 focussed primarily on establishing the operating envelope necessary to accomplish the experiment objectives of the program. FY93 has centered on design and development of the flight hardware required to accomplish these objectives. To date, the following activities either have been completed or are significantly underway:

- Completion of preliminary design of the components in each of the three canisters, including the interconnecting fiberoptic and electrical systems.
- Candidate hardware systems for many of the components in the sample workstation canister, CAN 3, have been identified and several components have been procured. The computer/control, VCR, and camera systems have been purchased and are currently under development and integration at CSTAR. TTU has completed preliminary design of the internal experiment structure and a prototype test frame has been fabricated for vibrational testing.
- The Lumonics LUXSTAR laser, CAN 1, has been installed at CSTAR and is currently undergoing operations testing. A prototype cooling system has been designed and will be tested with the laser in early FY94.
- The electrical and fiberoptic interconnection systems have been discussed with GSFC. Design and fabrication of the external mounting hardware will be provided by GSFC and development of the cables will be done by CSTAR.
- The Carrier Payload Requirements (CPR) document has been submitted to the GSFC Small Payloads Office with final approval by November 1993. The Safety Data Package has been

initiated with the potential hazards identified in the Payload Safety Requirements Matrix. Submittal of the package to NASA Johnson Space Center for the initial safety review is expected shortly after the CPR is approved.

FY94 ACTIVITIES

Activities in FY94 will focus on continued development of the flight hardware with completion of procurement and fabrication of the sample workstation canister (CAN 3) modules and most of the laser (CAN 1) and power (CAN 2) canister components anticipated. Some of the major milestones planned for FY94 include:

- Procurement/fabrication of the experiment motion system, internal optics, sample carrier, and internal frame for CAN 3 will be completed. Integration and testing of the canister will be initiated.
- Development of the power supply, cooling system, batteries, and internal frames for CAN 1 and CAN 2 as well as integration of these modules into the LUXSTAR laser for operational tests will be initiated.
- Design of the fiber, voltage, and control interconnects will be completed and fabrication will be initiated.
- Identification of the payload safety-critical items and safety verification procedures will be completed. The first (Phase 1) safety review will be completed and the Phase 2 review process will be initiated.

The SAILS Program Schedule is shown in Figure 4 and illustrates the overall timetable planned to achieve the FY96 shuttle flight. The numerous major tasks illustrate the technical significance of the overall endeavor.

SUMMARY

A program is well underway to develop the first laser materials processing workstation for use in space. As well as providing fundamental information on several laser-material interactions, this program will demonstrate the ability of laser processing to perform useful repair and fabrication operations in space. The three canister system is designed to operate autonomously on orbit after experiencing the rigorous launch environment and is expected to serve as a basic laser system test bed for other flight experiments in the future.

Table 1. Materials and Processes Selected for Testing in the SAILS Experiment.

Material	Spot/Seam Weld	Drill/Cut	Braze	Solder
316L Stainless	✓	✓	✓	
2219 Aluminum	✓	✓		
6061 Aluminum	✓	✓		
Inconel 718	✓	✓		
Copper				✓
Kapton		✓		
Lead/Tin	✓			

Table 2. Flight Laser Operating Characteristics.

Parameter	Value
Average power	50 W
Peak optical power	3000 W
Pulse length	0.5 - 20 ms
Pulsing rate	to 100 Hz
Pulse energy	to 30 J [10 J]
Fiber core diameter	400 μm
Minimum spot size	200 μm
Dimensions (Industrial unit)	86.5x56.5x77.5 cm
Weight (Industrial unit)	200 kg
Input voltage	200-240 VAC [28 VDC]
Output voltage to Flashlamp	660 V pulses
Power Consumption	5.5 kW

SAILS Facility Flight Plans

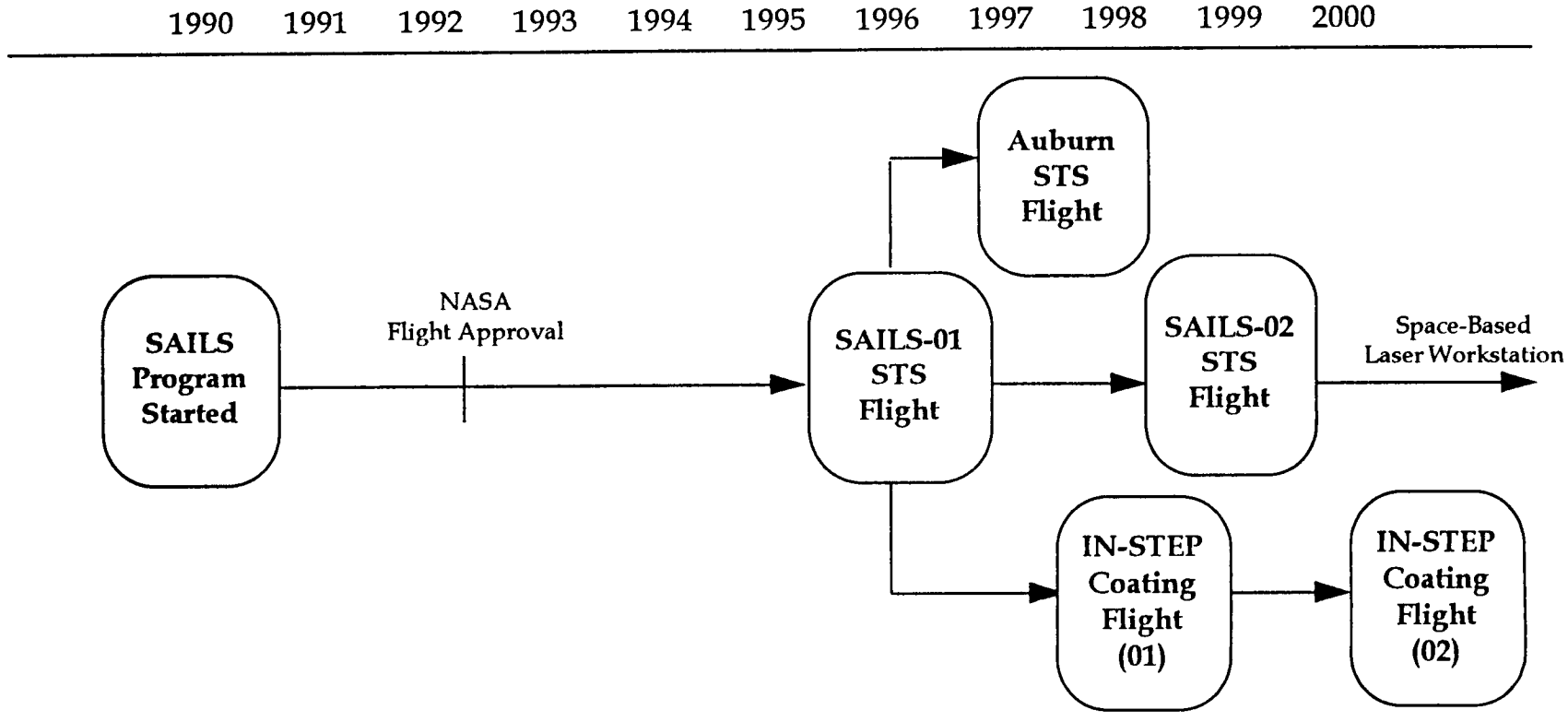

Figure 1 SAILS Facility Flight Plans

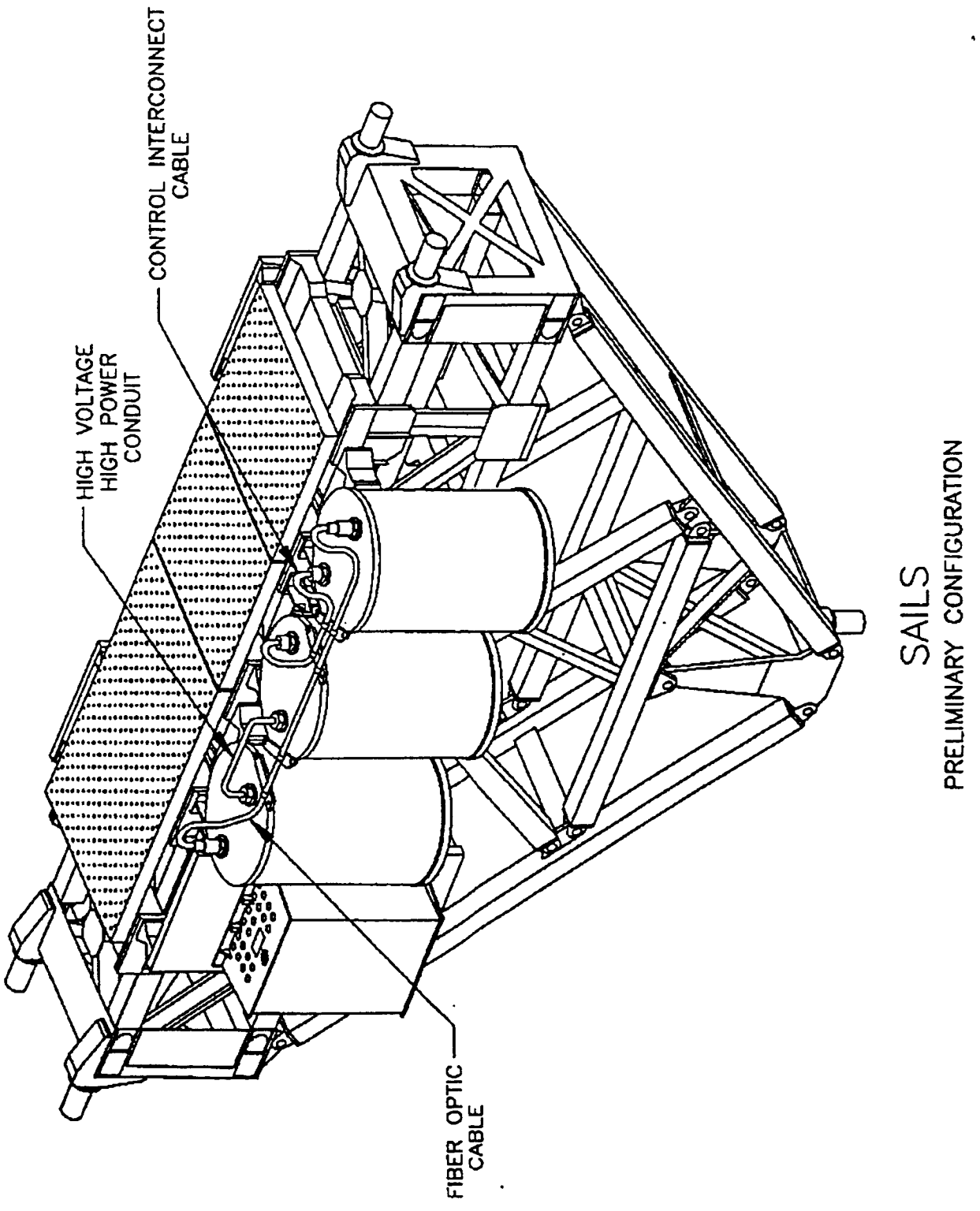

Figure 2 SAILS Preliminary Configuration

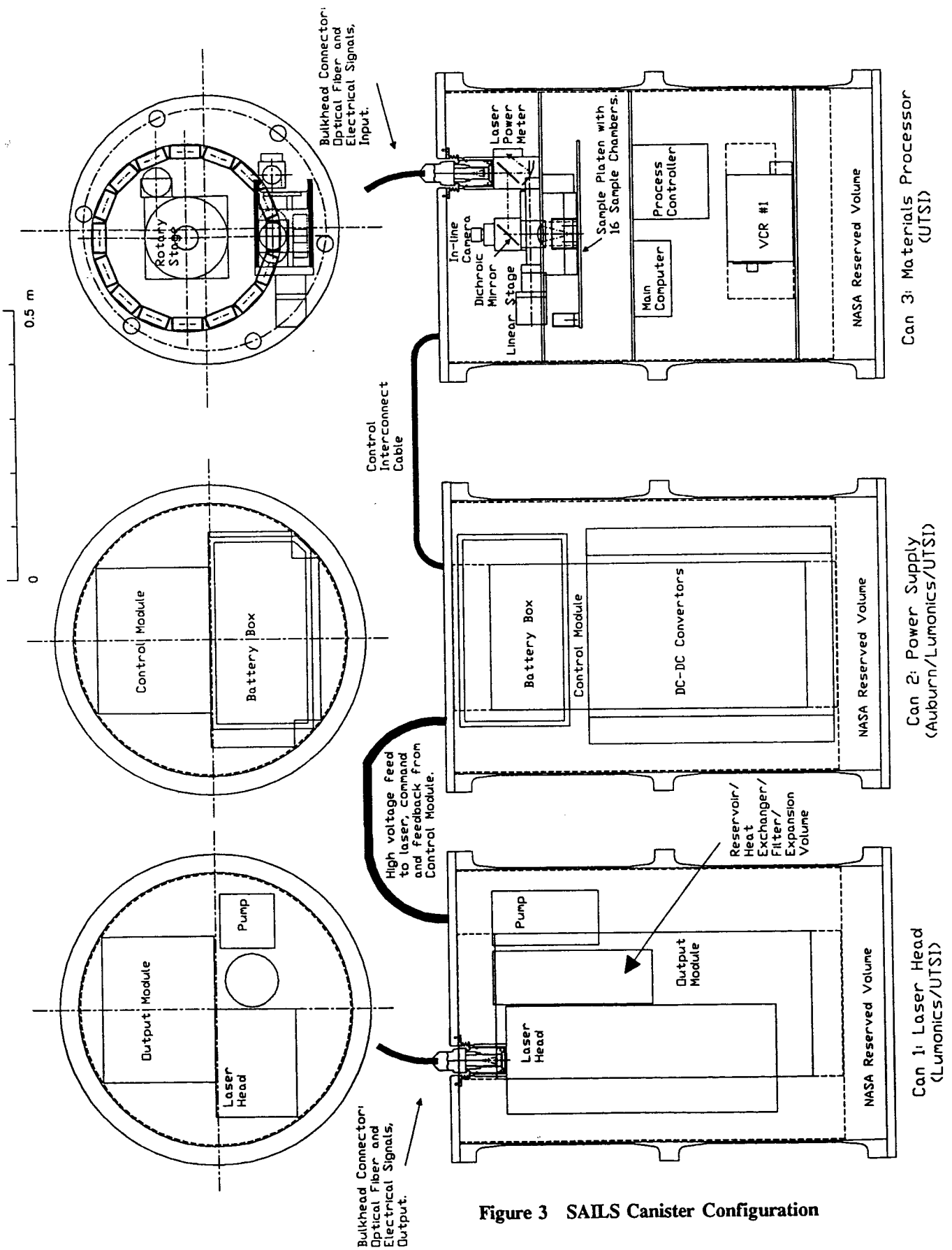

Figure 3 SAILS Canister Configuration

SPACE APPLICATIONS INDUSTRIAL LASER SYSTEM (SAILS)

PROGRAM SCHEDULE

Task Name	Start Date	Due Date
Program Concept	Jul/01/91	Jul/01/91
SAILS Program Management	Jul/09/91	Apr/28/98
LIPP	Jul/02/91	Jan/13/97
Ground Experimentation	Oct/02/91	Jan/04/94
Computer Modelling	Dec/14/93	Jan/02/97
Flight Hardware Development	Aug/19/92	May/08/95
LUXSTAR Preparation	Aug/02/93	Jan/12/94
Laser Canister	May/03/93	Jan/03/95
Laser Head	Jun/01/93	May/19/94
Laser Cooling System	Jul/01/93	Jul/22/94
Laser GAS Can Structure	May/03/93	Jan/03/95
Laser Control Interfaces	Sep/01/93	May/18/94
Laser Beam Delivery	Jun/01/93	Apr/19/94
Power Canister	Mar/01/93	Jan/03/95
Laser Power Supply	Sep/01/93	Sep/01/94
Laser Batteries	Mar/01/93	Jun/21/94
Power Control Interfaces	Sep/01/93	Jul/21/94
Power GAS Can Structure	May/03/93	Jan/03/95
Process Canister	Aug/19/92	Jul/06/94
Computer System	Aug/19/92	Jan/21/94
Sample Materials /Carrier	Oct/01/92	Apr/01/94
Data Logger System	Aug/19/92	Mar/03/94
Sensor System	Aug/19/92	Jun/01/94
Control Interfaces	Nov/20/92	Apr/01/94
Beam Delivery	Dec/31/92	Jul/06/94
Visual Data System	Oct/01/92	Jan/03/94
Motion Drive/Control System	Jan/04/93	Mar/01/94
Process Gas Can Structure	Apr/01/93	May/20/94
Fiberoptic Interconnect	Mar/01/93	Sep/01/94
Voltage Interconnect	Sep/01/93	Sep/21/94
Control Interconnect	Sep/01/93	Jul/21/94
Software Development	Sep/01/93	Oct/03/94
Support Equipment	Apr/01/93	May/08/95
Integration and Testing	Oct/13/94	Sep/10/95
KC-135 Flight Experiments	Mar/06/95	Jun/06/95
Flight Preparation	Aug/08/95	Nov/13/95
Launch	Mar/21/96	Mar/21/96
Post Flight Analysis Complete	Sep/26/96	Sep/26/96

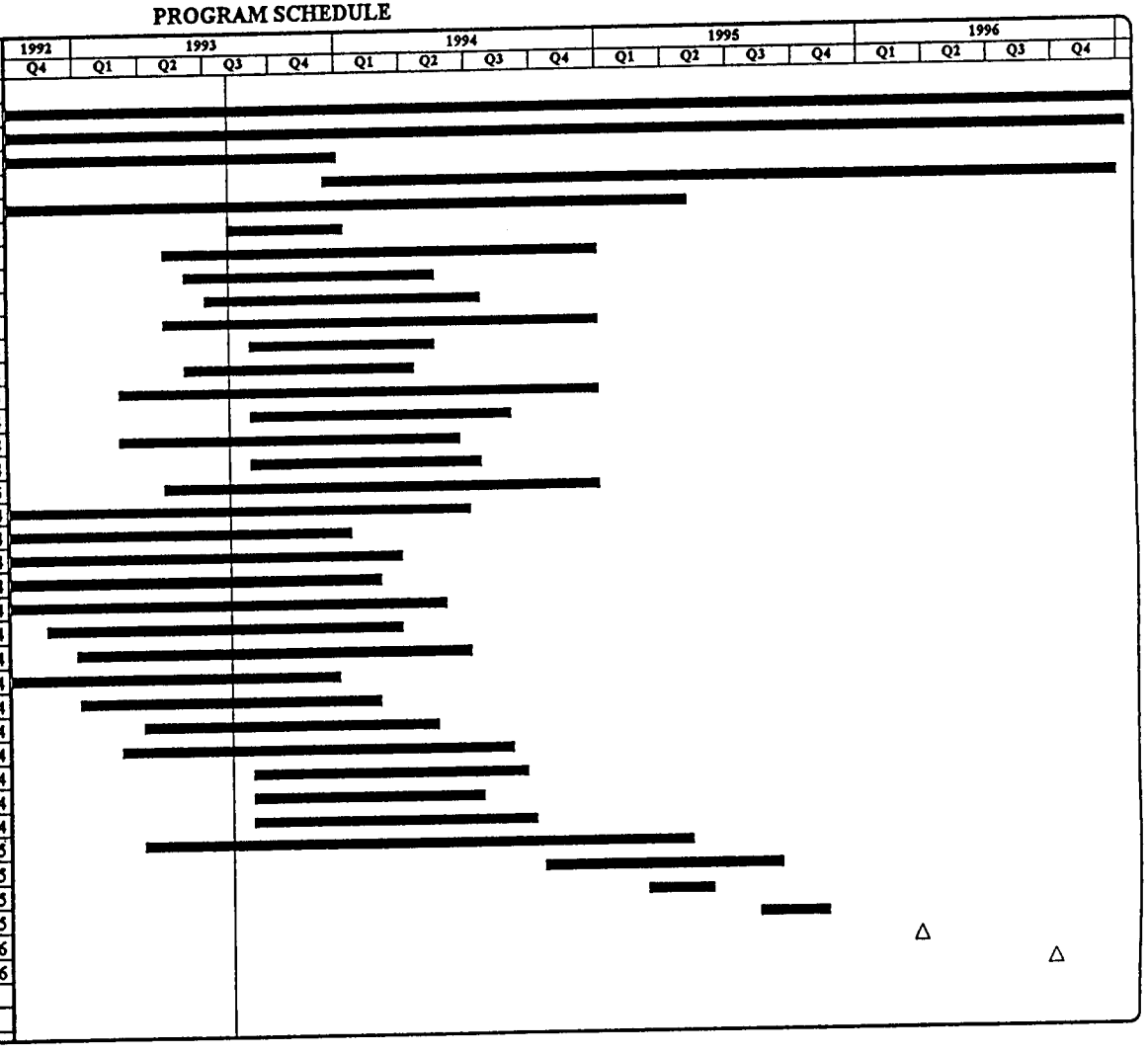

Last Update: 8/2/93

Figure 4. SAILS Program Schedule

Laser Industrial Partnership Program (LIPP)
Annual Progress Report

T.D. McCay, C.M. Sharp, J.B. Bible, and R.E. Mueller
The University of Tennessee-Calspan
Center for Space Transportation and Applied Research (CSTAR)
Tullahoma, TN 37388-8897

The University of Tennessee Space Institute (UTSI)
Center for Laser Applications
Tullahoma, TN 37388-8897

PROGRAM SUMMARY

The Laser Industrial Partnership Program (LIPP) is a technology transfer program for applying laser materials processing (LMP) technology to U.S. industry. This is accomplished by providing a multi-disciplinary group of scientists/engineers with state-of-the-art laser and diagnostic facilities for evaluation and implementation of LMP into manufacturing applications.

Specifically, CSTAR provides the following services to industry:

- *On-site visits and manufacturing floor surveys to identify potential laser applications*
- *Laboratory experimentation to establish feasibility of LMP for specific industry applications*
- *Detailed parametric studies to optimize the laser process for production*
- *Generation of prototype components and pre-production batches for testing and evaluation*
- *Design of new products and/or processes for LMP*
- *Techno-economic appraisal of industrial laser systems for a selected product/process*

The LIPP was formalized in conjunction with the Space Applications Industrial Laser System (SAILS), a program developing a compact laser workstation for a 1996 space shuttle flight. SAILS, along with the UTSI Center for Laser Applications, provide much of the personnel and equipment infrastructure necessary to operate this technology transfer program. Additional information on the SAILS program may be found in another section of this CSTAR Annual Report. Since beginning at UTSI in 1987, the LIPP has proven a successful model for transferring LMP technology to U.S. industry. To date, thirteen (13) industrial lasers have been installed in U.S. industry as a result of this program.

Progress for FY93 will be reported in four areas: 1) Facility Enhancements, 2) Major Industry Projects, 3) Proposals In Progress, and 4) Marketing Efforts.

1) FACILITY ENHANCEMENTS

During FY93, a 12,000 square foot addition to the UTSI Advanced Technology Laboratory was completed. This facility includes a high bay for high energy lasers and diagnostic equipment, laboratories for metallurgical equipment, and support areas for offices and computers. To fully utilize this building and to create one of the most comprehensive academic laser facilities in the U.S., the CLA and CSTAR laser laboratories were combined at this location. CSTAR provided the 450 watt JK701 Nd:YAG laser, a 50 watt Luxstar Nd:YAG laser, a TEA laser, and a drill head with milling machine base. CLA provided a 3.7 kilowatt CO_2 laser, two excimer lasers, and metallurgical and photographic equipment. This combinated laser facility is an asset to both UTSI and CSTAR for acquiring research contracts.

2) MAJOR INDUSTRY PROJECTS

Robert Shaw Industries

CSTAR provided assistance to Robert Shaw last year (July 1992) for proving feasibility of laser welding of an automotive bellows assembly. Based on this work, Robert Shaw has decided to proceed with laser development for replacement of the existing brazing process. CSTAR was contracted to provide prototype components for evaluation (Phase I) with assistance in implementing a production system at the Carthage, TN plant to follow (Phase II).

The bellows assemblies consist of three separate joints for laser welding development:

1) Stainless steel spud to Monel transition material. This is required to transition between the

metallurgically incompatible Berylium copper bellows and stainless steel spud.

2) Monel transition material to Berylium copper bellows for the same reason as 1).

3) Berylium copper bellows to brass and steel base. Both base materials are to be attempted due to potential savings in raw material cost.

An initial set of weld trials was completed for each of the three joints. The first joint appeared to weld successfully but leak testing revealed microcracking. The second joint was successfully laser welded but required joint modification due to poor fit up. The third joint was successfully laser welded and produced a satisfactory joint. Although it was established that the laser could weld several of the materials of interest, it is necessary that Robert Shaw modify the material finish and joint fit up before proceeding with Phase II.

BENDIX Atlantic Inflator Company (BAICO)

CSTAR was requested by BAICO, a division of Bendix Corporation, to survey their manufacturing floor, to evaluate their current laser utilization, and to identify potential new applications. It was discovered that BAICO had purchased two Coherent Arrow CO_2 lasers with LANCO automated workstations for hermetic welding of burst discs for an airbag inflator assembly. Although in the prototype production stage, this setup did not produce consistent welds and generated a rejection rate of approximately 25 percent. At this rate, the system could not achieve the targeted production rate of 2000 units/day.

In addition, CSTAR identified a potential laser application in the joining of a glass/metal vacuum plug to an assembly endcap. The joint was currently being produced by resistance welding and did not generate a satisfactory product.

CSTAR provided a report to BAICO which suggested the following modifications be made:

1. BAICO personnel should receive basic training in laser operation, beam delivery, and welding techniques to help in problem identification and resolution.
2. The beam delivery, workpiece handling, and fixturing systems for the burst disc welding application should be modified for improved alignment, workpiece fitup, and shield gas flow.
3. Procedures for determining focus positioning and laser parameters should be developed through parametric welding trials.

A SOW was provided to BAICO proposing CSTAR to provide modification #3 through laser trials at both CSTAR and BAICO, but it was rejected due to their interest in resolving the problems through "in-house" methods.

Medical Company XYZ (confidential)

In October 1992, CSTAR and Medical Company XYZ jointly conceived the concept of laser texturing medical implants. The surface finish of implants can greatly effect the stability of the prosthesis with the surrounding bone. A finish which could allow the bone to grow effectively into the implant would enhance stabilization and improve the success of the replacement.

CSTAR developed a four (4) phase statement of work for laboratory development of this concept through to assistance in implementation of an industrial laser system in the manufacturing plant. The four (4) phases were as follows:

Phase	Description
I	Preliminary laser laboratory drill trials to establish feasibility.
II	Detailed parametric and metallurgical studies, corrosion and structural testing, and preliminary economic appraisal to determine optimum laser configuration.
III	Prototype component generation and medical studies.
IV	Equipment procurement and installation

CSTAR received a contract for Phase I and presented the feasibility report to Medical Company XYZ in March 1993. The report and sample laser textured materials revealed that the Nd:YAG laser was applicable to this product and the company was convinced to proceed with Phase II of the project. One of the reasons for this positive response was that CSTAR employed a patentable technique for generation of a spatter free surface texture (Figure 1). CSTAR has began the patent application process and anticipate completing the filing by December 1993. Because of royalty and patent rights issues, Phase II has been delayed until negotiations are completed on the Research and Royalty Agreements. It is anticipated that the agreements will be completed and work on Phase II will begin in early November 1993.

Rocketdyne, Huntsville

Rocketdyne contacted CSTAR requesting assistance in transferring to industry the vacuum plasma spray technologies developed at MSFC. A presentation on the LIPP program during a recent progress meeting on the Laser Welding Dissimilar Alloys project prompted the inquiry. A team of UTSI, CLA, ECP, Calspan, and TVAR personnel were assembled for a preliminary meeting to discuss the project scope. A tour and demonstration of the VPS facility at MSFC and the thermal spray facility in

LIPP program during a recent progress meeting on the Laser Welding Dissimilar Alloys project prompted the inquiry. A team of UTSI, CLA, ECP, Calspan, and TVAR personnel were assembled for a preliminary meeting to discuss the project scope. A tour and demonstration of the VPS facility at MSFC and the thermal spray facility in Huntsville were conducted to provide better understanding of the capabilities.

CSTAR provided a project plan to Rocketdyne which outlined a four (4) phase approach to transfer of this technology to industry. A preliminary marketing survey (phase I) is currently underway to identify the potential of this technology for commercial application and to identify funding sources for the follow on phases.

3) PROPOSALS IN-PROGRESS

NSF LMP Research Center

CSTAR and CLA have combined to submit a pre-proposal to NSF for a laser materials processing research center. This $2.5M per annum proposal would provide a comprehensive approach through research in seven (7) broad areas; 1) Advanced Alloys, 2) Emerging Materials, 3) Process Monitoring and Control, 4) Laser Assisted Synthesis, 5) Computational Tools, 6) Process Diagnostics, and 7) Laser Expert Systems. In addition, the LIPP program has been proposed as the technology transfer mechanism for each of these areas. It is expected that acceptable pre-proposals will be invited to submit full proposals for funding to begin in FY94.

Welded Bellows ARPA Proposal

CSTAR has been contacted by Welded Bellows Engineering to provide process development on an ARPA SBIR to develop the laser joining technique for an advanced welded bellows concept. The work could begin as soon as ARPA awards are announced, possibly as early as first quarter 1994.

State of Tennessee ARPA Proposal

The LIPP program was included in both the TVAR and UT-CIS sections of the State of Tennessee ARPA proposal. If awarded, CSTAR/CLA could receive $100,000 per year beginning next year for laser materials processing technology transfer.

Hermetic Laser Welded Probe Assembly

Alabama Laser Technologies visited CSTAR and requested a quotation for development of a hermetic laser welded probe assembly. The CSTAR proposal was submitted and is currently under evaluation at Alabama Laser.

Laser Drilling of Wire Blanks

In 1992, CSTAR consulted with Lukens Medical Corporation to demonstrate the applicability of lasers for drilling of 304 stainless steel blanks for medical applications. Although feasibility was established through this effort, the project was delayed due to the need for a specialized drilling head to generate the small diameter holes (less than 0.050"). Since that time, CSTAR has acquired the drilling head from Lumonics and a milling machine base has been donated by one of the LIPP partners. It is anticipated that the drilling head will be operational by November 1993 and the project will be restarted with Lukens.

4) MARKETING EFFORTS

The first step to technology transfer is to locate and establish contact with industries for transfer of the technology. CSTAR employs an aggressive marketing program that targets and solicits industries in specific manufacturing areas for application of LMP. This is accomplished through seminars, mailings, conference exhibitions, technical presentations, networking through existing affiliations, and establishing alliances with laser manufacturers.

Specifically, the CSTAR display booth was upgraded and exhibited at the following conferences:

- 1992 CSTAR Annual Technical Symposium, Tullahoma, TN (November 1992)
- Technical Association of Business and Engineering Societies (TABES) conference, Huntsville, AL (May 1993)
- Technology 2002 Conference, Baltimore, MD (December 1992)
- AWS Welding Conference, Houston, TX (April 1993)
- International Conference on Application of Lasers and Electro-Optics (ICALEO), Orlando, FL (October 1993)

In addition, more than 50 direct consultations other than those listed above were provided to industry by CSTAR/CLA during the year either by phone or industry site visits.

Figure 1 Titanium 6-4 sample comparing laser texturing with and without the CSTAR spatter free technique.

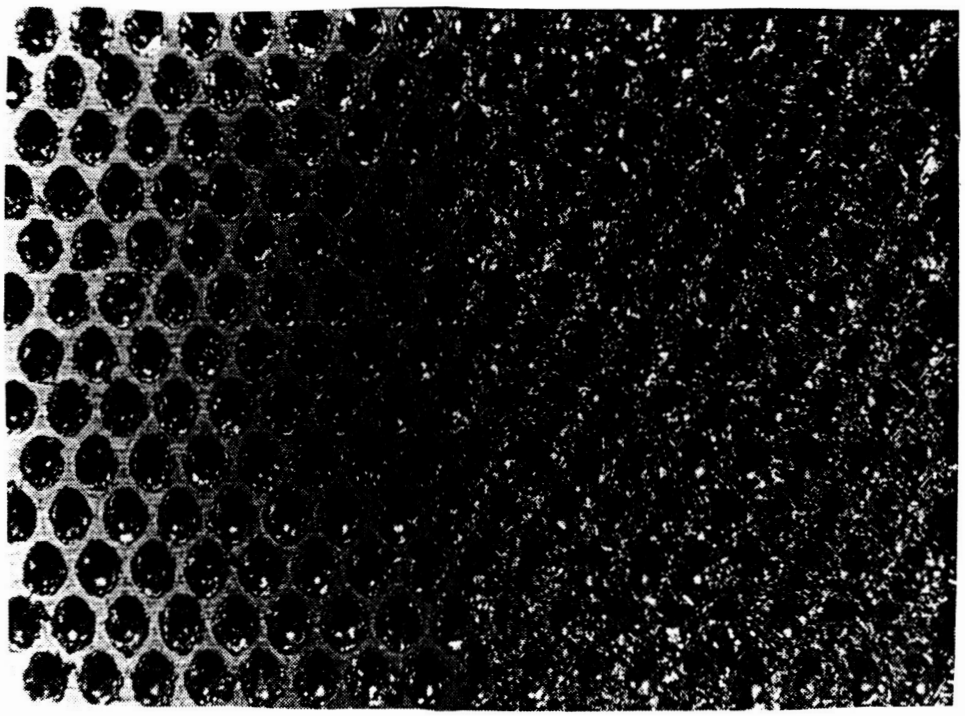

LASER WELDING DISSIMILAR REFLECTIVE ALLOYS

M.H. McCay, S. Gopinathan, F. Kahlen, L. Speigel
The University of Tennessee Space Institute (UTSI)
Center for Laser Applications
Tullahoma, TN 37388-8897

Overview

This project, jointly sponsored by Rocketdyne and CSTAR, involves the development of laser joining of materials which have heretofore been impractical to bond. Of particular interest are joints between stainless steel and copper and also aluminum 6061 to aluminum 2219. CSTAR has a unique opportunity in this area since both the process and development and diagnostics are of interest to industry. Initial results using the pulse tailored laser welding technique developed in CLA for joining crack sensitive materials have proven promising for the aluminum joints based upon metallurgical and electronic microprobe analysis. Declaration of success requires additional mechanical testing. A CW technique has been applied to the stainless-copper joining with some preliminary success. These joints are of significant interest for aeronautics and rocket propulsion applications and the project is expected to continue.

The following describes the work accomplished during 1993 on the Laser Welding of Dissimilar Alloy project for each task defined in the Statement of Work.

TASK 1: LASER PROCESSING DATA BASE:

The aim of this database system is to provide information on (i) The properties of the materials to be joined and (ii) The weldability of the material using different types of lasers as well as other conventional/nonconventional joining methods. The emphasis is on laser welding of materials. This menu-driven, user-friendly database will also provide prominent references for further in-depth information. Programming on this database is essentially completed and data entry has been done on basic material properties for 280 aluminum and copper alloys.

TASK 2: ALTERNATE LASERS AND WELDING TECHNIQUES:

(a) Al2219/Al6061 Joining:

(i) Nd:YAG Laser Welding of Al2219 to Al6061

Low power pulsed Nd:YAG laser welding was performed at CSTAR on a Lumonics, JK701 laser capable of 150 Watts average power. Samples of Al6061 and Al2219 were butt welded using Argon as the cover gas. Al4047 shims were used as filler material. The welds were characterized by insufficient penetration and root porosity.

(ii) Multiwave Laser Welding of Al2219 to Al6061

High power continuous wave Nd:YAG laser butt welding was done at Lumonics in Livonia, MI at 2000 Watts using various cover gases. It was observed that the use of He, Ar and N_2 resulted in inconsistent coupling and incomplete penetration. Samples welded using compressed air however exhibited better coupling.

(iii) Copper Vapor Laser Welding of Al2219 to Al6061

Samples were sent to Rocketdyne to provide to Lawrence Livermore Labs for processing.

(iv) Electron Beam Welding of Al2219 to Al6061

Samples were processed at AEDC.

(v) TIG Welding of Al2219 to Al6061

Typical TIG welds between the two alloys were provided and evaluation showed that there does not appear to be very much mixing.

(b) Copper-Stainless Steel Joining:

(i) Electron Beam Welding

Electron beam butt welding of copper-stainless steel was carried out at AEDC using the following conditions: 100kv, 15MA, 22 1/2"/Min, X amplitude 1%, Y amplitude 1%, 100 hZ frequency and gun to work distance of 10.00. Two samples were processed on-seam, one sample was processed 1 mm on the copper side and one sample was processed 1 mm on the steel side. The samples exhibited complete penetration. Preliminary microstructural evaluation revealed cracking and insufficient mixing of the steel and copper. The

1 M.H. McCay, Professor ESM, UTSI
2 S. Gopinathan, UTSI
3 F. Kahlen, UTSI
4 L. Speigel, Technical Monitor, Rocketdyne

electron beam was also observed to "wander" towards the stainless steel side during welding.

TASK 3: PROCESS PARAMETER DEVELOPMENT AND OPTIMIZATION

(a) CO_2 Laser Welding of Al2219 to Al6061:

Bead-on-plate laser welding was carried out using both continuous-wave as well as pulsed CO_2 laser welding in order to study the effect these techniques have on laser coupling with the aluminum alloys. For the same average delivered laser power, enhanced coupling resulted in weld widths an order of magnitude higher for pulsed laser welding compared to cw welding. A comparison between the top bead widths produced by pulsed and cw welding with the same average power revealed that the weld widths are an order of magnitude higher in the pulsed welds. This is probably attributable to the leading edge spike which occurs on each pulse.

Having established the effectiveness of pulse tailoring, autogenous butt welds were made between Al2219 and Al6061 plates using a matrix of pulsing conditions and cover gases. The pulse-on time was kept constant and the pulse duty cycle and hence the input power were varied by changing the pulse-off time.

In order to characterize the Al2219-Al6061 butt welds, the top and bottom beads of the butt welds were photographed and weld bead width measurements made. The butt welds were later cross-sectioned, mounted, polished, etched and metallographically evaluated.

The effect of cover gas and pulse duty cycle on weld widths was also evaluated. It is observed that in general, the top bead widths increased with increase in pulse duty cycle for all assist gases. The welds made with argon as the assist gas were the widest, while helium resulted in the narrowest welds. Nitrogen and compressed air welds exhibited widths that were in between those of helium and argon. Pulse duty cycle seemed to have a bigger effect on weld penetration depth than cover gas. Full penetration was achieved in all samples for a duty cycle above 44% i.e. (20ms/25ms on/off times).

(b) CO_2 welding of Copper to Stainless Steel:

For the case of copper to stainless steel, continuous wave was determined to be the preferred mode. Autogenous butt laser welding experiments on copper-stainless steel samples were carried out using helium, nitrogen, compressed air and argon as the shield gases. Figure 1 shows a weld cross-section made with compressed air as the cover gas. The cross section accentuates the problem of porosity encountered by the use of compressed air. The same problem is apparent in Figure 2, which shows the cross-section of a weld made with ambient air as the cover gas. The weld made with inert argon as the cover gas showed both porosity as well as fusion zone cracking. The cross-section of the butt weld made using He revealed only slight porosity and no cracking was observed. The welds made with compressed air and ambient air were fully penetrated while those made with helium and argon showed incomplete penetration. The position of the laser beam with respect to the interface between the two materials was very critical to successful welding.

Another experiment was carried out in order to study the importance of beam position on the weld integrity. The position was varied in 0.1mm increments from the copper side to the stainless steel side. When the 3000 Watt continuous wave laser beam was made to impinge on the copper side of the assembly at distances of 0.1 to 0.5mm from the interface, there was no coupling of laser beam energy and no resultant weld. When the beam impinged on the steel side up to 0.3mm from the interface, coupling and penetration resulted. It was noted that in this case, the two pieces were physically joined, but the joint was very fragile and could easily be broken. At further distances there was no effect. A copper-steel joint was also produced by the laser beam impinging the assembly at the interface. A visual inspection of the joint revealed visible mixing between the constituents of the two materials.

TASK 4: PROCESS MONITORING AND BEAM DIAGNOSTICS:

The spectroscopic measurements of the composition of the near-surface plasma induced during laser processing can provide significant information on the welding parameters. To obtain this information, an experimental technique of spectral measurements using an Optical Multichannel Analyzer (OMA) was designed for CO_2 laser welding.

Two types of spectral measurements were carried out:
1. Spatially and temporally unresolved measurements were made of plasma plume composition during the welding of SS304, Al2219, Al6061, Cu, and SS304. The spectral investigations of the plasma plume were also carried out for the dissimilar metals laser welding. The plasma plume image was created on the OMA entrance slot using a lens. The axis of plasma plume image coincided with the OMA slot, and the detected data represent the spectra integrated over the plasma plume length. The spectra near the surface plasma were measured for the cases of welding Al6061 to Al2219 and stainless steel SS304 to copper. The spectra were

detected in spectral regions from 380 nm to 520 nm and from 580 nm to 720nm. These data show that the spectrum for the case of welding of different aluminum alloys is the combination of spectra for the welding of separate alloys. For example, the line of CrI occurs only in spectra of Al6061 and not in the spectra of Al2219 since only Al6061 contains the element Cr. This line can be observed for the welding of Al6061 to Al2219.

Stainless steel 304 contains copper, thus, it was expected that the spectra of welding of SS304 to copper would differ only by the relative intensity of the copper line, unlike the case of welding different alloys containing different elements. The spectral data proves this expectation. The relative intensity of the copper line 579 nm is higher for the case of steel to copper welding. Figure 3 shows the relative intensity of the CuI to the MnI as a function of the beam location with respect to the joint between the copper and 304 stainless steel.

2. Measurements of plasma composition without temporal resolution and with spatial resolution along the laser beam/plasma plume axis were made during the welding of SS304 and Al2219 in the spectral region 570-710nm.

The results from the first set of measurements showed that it is possible to detect the different species in the plasma/vapor plume and consequently it may be possible to monitor the weld parameters by measuring the spectral composition of the plume.

The results from the second set of measurements showed that a detectable boundary exists between the vapor plasma and the surrounding gas plasma. It means that by measuring the temporal dynamics of the boundary location one can detect instabilities in the welding process, since the boundary location depends strongly on the vapor pressure, which in turn depends on the weld temperature and molten metal hydrodynamics (keyhole dynamics). This boundary measurement technique could prove to be a very sensitive on-line diagnostic tool to monitor weld quality.

(ii) High Speed Video Photography:
High speed photography of the welding process was carried out using a Kodak EktaPro high speed camera capable of filming 1000 frames/sec. Since the pulsing rates were on the millisecond scale, the framing speed was ideal to study the welding process. In Figure 4, a digitized image of the recording of the welding process is illustrated.

TASK 5: SAMPLE EVALUATION AND TESTING:
(a) Al2219/Al6061 Joining:
The microstructure of the welded samples was metallographically analyzed. The observations have been summarized in Table I. At low duty cycles (40%) the samples were not fully penetrated and cracking was observed for all samples. At higher duty cycles (20/15,20/20), the welds made with argon as the shield gas exhibited low porosity and no cracking. The welds using helium as the cover gas showed some degree of cracking in all pulsing conditions. The aluminum butt welds using compressed air as the cover gas exhibited extensive porosity. The nitrogen welds exhibited no cracking but did show some porosity. The welds fusion zone is also characterized by the presence of certain inclusions. Similar inclusions have been observed during the laser welding of Al1100 under a nitrogen atmosphere. They were identified as aluminum nitride, AlN. Similar lamellar inclusions were also reported in studies of the feasibility of nitrating of aluminum using TIG welding with argon-nitrogen mixed shield gas.

Electron microprobe analysis and elemental X-ray mapping of the weld zone were performed in order to determine the distribution of the alloying elements. A typical SEM micrograph of the Al2219 weld zone and the corresponding silicon image are illustrated in Figures 5(a) and (b) respectively. The unaffected Al2219 region consists of elongated solid solution grains with second phase particles of $CuAl_2$ and $(Fe,Mn)_3SiAl_{12}$. This region is followed by the Al2219/Al6061 fusion zone which exhibits a columnar dendritic structure bounded by a region consisting of equalized grains. The silicon map on the Al2219 side shows the presence of silicon in the weld zone. Figure 6(a) show the Al6061 weld zone interface. The Al6061 base structure reveals Mg_2Si particles in the aluminum solid solution grains adjacent to the fusion region. Figure 6(b) shows the corresponding X-ray map of copper in the Al6061 side of the fusion zone. The presence of copper on this side of the fusion zone is apparent. From the X-ray maps in Figures 5(b) and 6(b) the good mixing of the major constituents is apparent.

Hardness measurements were made along the weld cross-section. It is observed that there is a modest drop in hardness along the center of the weld, the minimum hardness being 83VPN.

(b) Copper-Stainless Steel Welding:
Initial microstructural evaluation indicated that the best microstructures were obtained by using He and compressed air as the assist gases. Electron Microprobe analysis was carried out on the He welds to study mixing

of the various alloying elements of the steel with copper. As shown in Figure 7(a), the steel/weld interface shows three regions. The base steel structure on the left is followed by the first fusion zone, referred to here as the "steel fusion zone". The steel fusion zone is characterized by a iron-copper matrix with a dispersion of particles. The EDS spectrum of these particles (Figure 7(b)) reveals that they are copper rich. The steel fusion zone is followed by the regular fusion zone which consists of circular regions (later determined to be iron-rich regions) dispersed in a copper-steel mixture. X-Ray maps for copper, iron, nickel and chromium corresponding to Figure 7(a) were also generated. Equilibrium thermodynamics dictates that the solid solubility of Cu in Fe is very small and that of Ni in Cu is very high. The Xray maps however revealed much better than expected mixing between copper and iron. The copper rich regions in the steel fusion zone were found to contain nickel as well. This could be due to a Cu-Ni solid solution formation in this region. The vigorous stirring in the melt combined with the high temperatures encountered during laser processing may be responsible. Figure 8 shows the weld-copper interface. Large elongated copper grains are present in the heat affected zone surrounding the fusion zone. The X-ray maps for iron, copper, nickel and chromium revealed the degree of mixing between the constituents of the two material. It was apparent that the copper and steel constituents have indeed mixed. Figure 9(a) shows the copper steel fusion zone. The fusion zone consists of iron-rich regions in the matrix of the copper-steel fusion zone. Figure 9(b) represents the EDS spectrum of the iron-rich region. The X-ray traces for iron and copper in the weld fusion zone revealed the presence of some sort of copper-iron solid solution matrix with some iron rich regions in between.

AMENDED STATEMENT OF WORK

TASK 1: CO_2 Processing of Narloy Z

A set of trial experiments was performed to identify pertinent CO_2 laser operating conditions which affect the laser melting of 2 mm thick Narloy Z samples. The matrix is given in Table II for three of the samples. Laser power was kept constant (approximately 3 kW delivered to sample), and traverse speed, beam focal position, and surface finish were modified. An argon flood cover gas was used during all experiments.

A total of four 2.5 cm x 5 cm samples have been processed: Six processing runs were performed on the first sample. The surface of the first sample was unmodified for the first five runs except for cleaning with methanol. For the sixth run, powdered graphite was applied to enhance the surface energy absorption.

One half of the second sample was dipped in a graphite/methanol mixture and allowed to dry so that the surface was coated with carbon. This was done to enhance the absorption of the CO_2 laser energy. One calibration run (run number one) was performed on the unmodified (except for methanol cleaning) half and four runs (runs four through five) were made on the coated half.

The surface of sample three was modified by oxidizing the surface. The third sample was placed in a furnace at 500C for approximately 10 minutes to form an oxide layer. Ten runs were performed on sample three.

Sample four was treated the same as sample three so that an oxide film was present on the sample surface. It was instrumented with thermocouples so that high sample rate (100hz) temperature measurements could be made during processing. Five runs were made on sample four. Two thermocouples were placed on the sample using a high conductivity, high temperature cement. The thermocouples were sampled at an acquisition rate of 100hz using a multi-channel, high-speed amplifier system and a pc-based A/D data acquisition board. One of the thermocouples was apparently destroyed by the plasma generated during the first processing run, therefore only one thermocouple was measured during runs 2-5. It also appears that some melting of the thermocouple shield wire occurred during the last two runs (runs 4 and 5) so that the data for these runs is questionable. Thus, it is believed that only run 1,2, and 3 have valid measurements.

Figure 10 shows cross-sections of three of the Narloy Z single glazes made with the CO_2 laser. Particles of zirconium are present in the base alloy but are no longer visible in the glazed material. The glazed region also appears to have solidified with a cellular dendritic structure. SEM and Energy Dispersive Spectroscopy (EDS) analysis however, does indicate the presence of zirconium distributed throughout the glazed region. Figure 11 presents the relationship between the traverse speed and the width of the glaze track for the different surfaces and focal locations.

Spectral investigations of the plasma plume were made during CO_2 glazing with argon and helium as the cover gases. The zirconium spectra were not visible when using argon due to the high background intensity. Spectra taken with helium as the cover gas revealed the presence of zirconium along with copper and silver.

TASK 2: Nd:YAG Processing of Narloy Z

A set of trial experiments were performed on 3 mm thick Narloy samples with two surface finishes unmodified and sanded. Both surfaces were cleaned with methanol before processing. A 5mm x 25mm matrix was done at each condition using an argon cover gas. Four sets of glazing was done on each surface at the conditions given in Table III.

Figure 12 shows surface view of glazed tracks processed the Nd:YAG laser. Additional samples have been sent to Lumonics for processing with the Multiwave Nd:YAG.

FUTURE WORK

1. Narloy Z processing:

Results indicate that it is feasible to glaze Narloy Z using either a CO_2 or a Nd:YAG laser. The glazed regions exhibit cellular/dendritic solidification structure and according to energy dispersive spectroscopy, contain dissolved zirconium. Since it is not known if the dissolved zirconium can impart the desired creep properties to the glazed region, these regions should be further characterized. In addition, since there is zirconium present in the laser sustained plasma which is formed during processing, further analysis should be done to determine the extent to which zirconium is lost as a result of this mechanism.

The Nd:YAG laser offers the greatest flexibility for glazing Narloy Z since the beam can be delivered fiber-optically. Further glazing studies should be conducted using the 2kW multiwave Nd:YAG.

The joining of reflective materials such as copper and Narloy Z to themselves is a great interest to industry. The narrow fusion zone provided by the laser offers great promise for this task. It is suggested that further effort be expended to determine the laser joining parameters and analyze the resultant structure in copper and Narloy Z joints.

2. Dissimilar metal joining:

The copper/stainless steel and Al2219/Al6061 joints produced using the laser appear to be sound and have constituent mixing. Mechanical and chemical tests should be conducted on these and joints of other selected dissimilar materials to substantiate that the joints have desirable properties.

3. Development of spectral weld monitor:

Based on spectral analysis taken during the joining of copper to 304 stainless steel, it is possible to use the relative peak heights of elements in the alloys to determine the beam location with respect to the joint. This knowledge is extremely significant when welding dissimilar materials (whether it be by electron beam or laser) since any variation in beam location will significantly alter the mixing and therefore the soundness of the joint. A simple detector/feedback control device could be built that would be applicable to lasers or electron beams and provide the necessary control to maintain the beam in the correct position during welding.

Table I: Summary of the low magnification evaluation of the Al2219/Al6061 weld cross-sections.

	Duty Cycle %			
Cover Gas	40%	44%	50%	57%
Argon	C,NP	P,C	P	P
Compressed Air	C,NP	C,P,PO	P,PO	P,PO
Nitrogen	C,P,I, NP	P,PO,I	P,PO,I	P,I
Helium	C,PO, NP	P,C	P,C	P,C

Table II
CO_2 Glazing Parameters

Sample	Run	Surface	Focus	Speed
I	1	As received	O	25.0
	2	As received	0	12.5
	3	As received	+2	12.5
	4	As received	+1	12.5
	5	As received	+1	19.0
	6	As received	+1	19.0
II	1	As received	+1	19.0
	2	Graphite Paste	+1	25.0
	3	Graphite Paste	+1	19.0
	4	Graphite Paste	+2	19.0
	5	Graphite Paste	+1	35.0
III	1	Oxidized	+1	35.0
	2	Oxidized	+1	50.0
	3	Oxidized	+2	50.0
	4	Oxidized	+2	35.0
	5	Oxidized	+2	25.0
	6	Oxidized	+2	12.5
	7	Oxidized	-2	6.0
	8	Oxidized	-2	25.0
	9	Oxidized	-4	25.0
	10	Oxidized	-3	25.0

TASK 3: Microstructural Evaluation

Table III
Nd:YAG Glazing Parameters

Sample#	Surface	Power (Watts)	Energy/pulse	Step Distance	Rep Rate
1	Unmodified	18	0.62	100	30
2	Unmodified	27	0.91	100	30
3	Unmodified	42	1.42	100	30
4	Unmodified	56	1.90	100	30
5	Sanded	18	0.61	100	30
6	Sanded	27	0.93	100	30
7	Sanded	42	1.42	100	30
8	Sanded	56	1.89	100	30

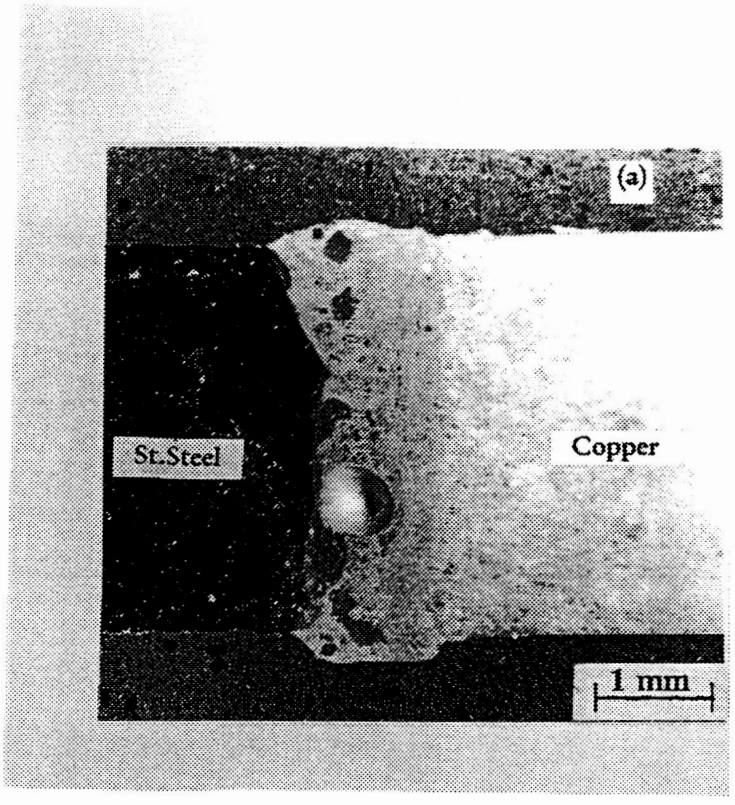

Figure 1 - Cross-section of copper/stainless steel weld. Compressed air cover gas.

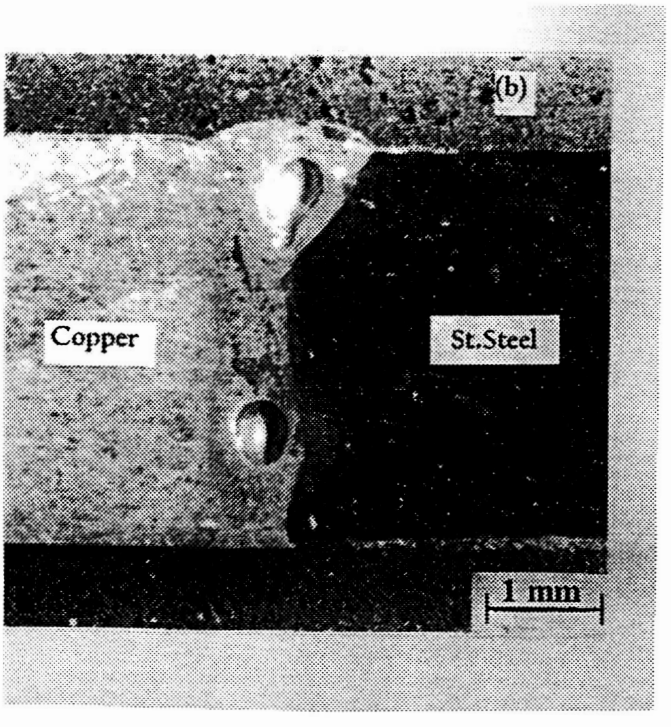

Figure 2 - Cross-section of copper/stainless steel weld. Ambient air cover gas.

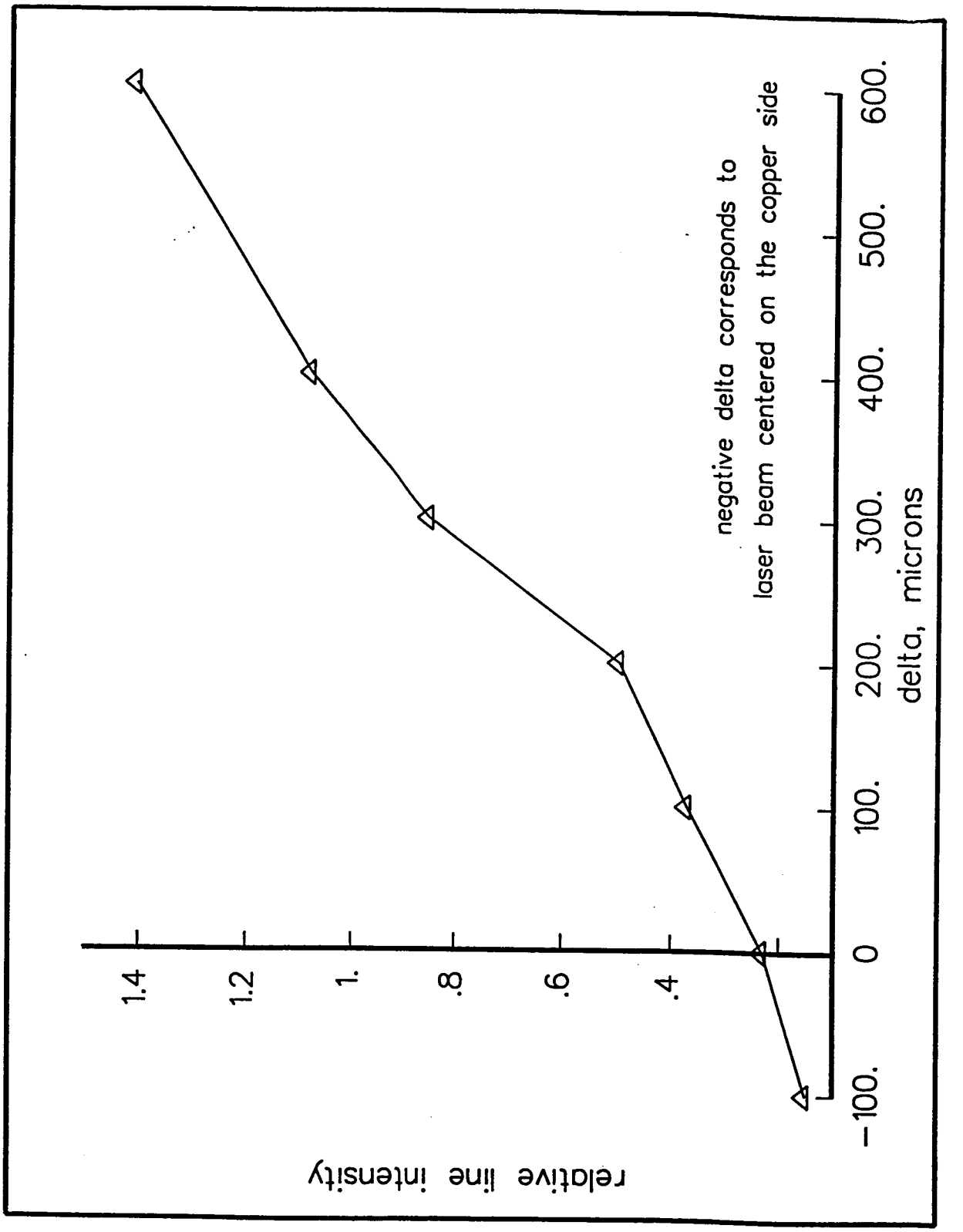

Figure 3 - Relative intensity of CuI line to MnI line as a function of laser beam location with respect to the joint.

Figure 4 - High speed photograph of the laser welding of Al2219 to Al6061.

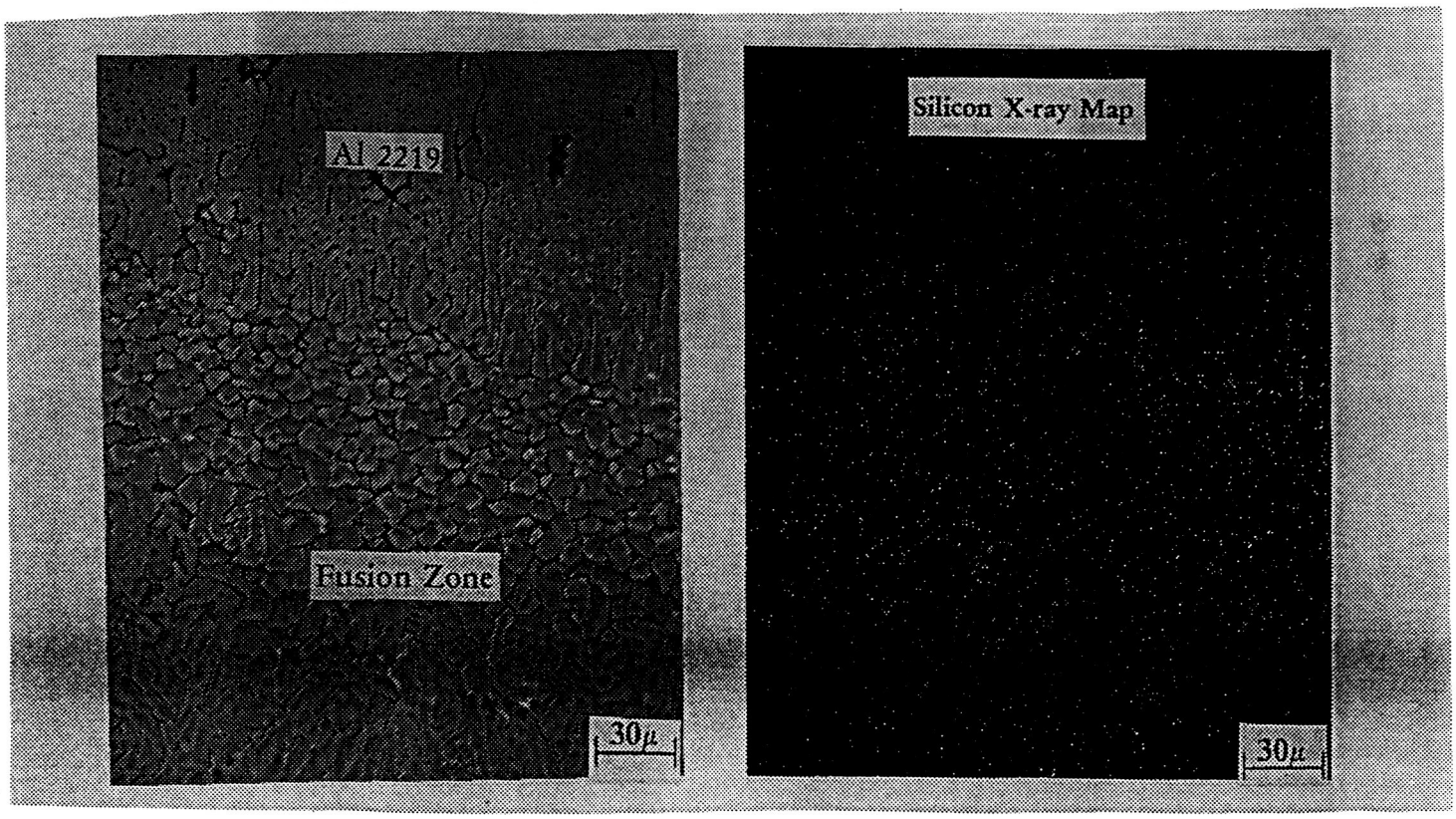

Figure 5 - Micrograph of the Al2219/weld interface (a) SEM micrograph (b) Silicon X-ray map of the interface.

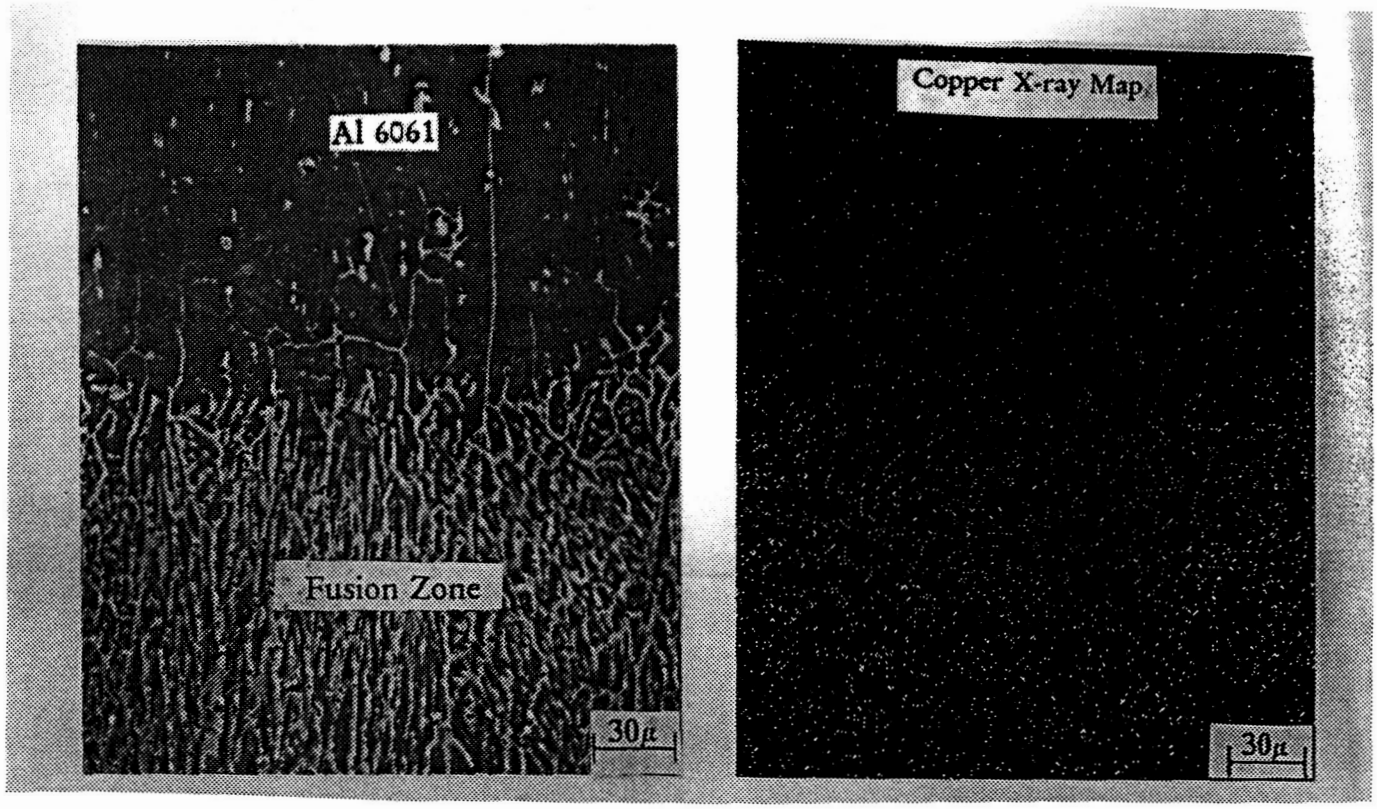

Figure 6 - Micrograph of the Al6061/weld interface (a) SEM micrograph (b) Copper X-Ray map of the interface.

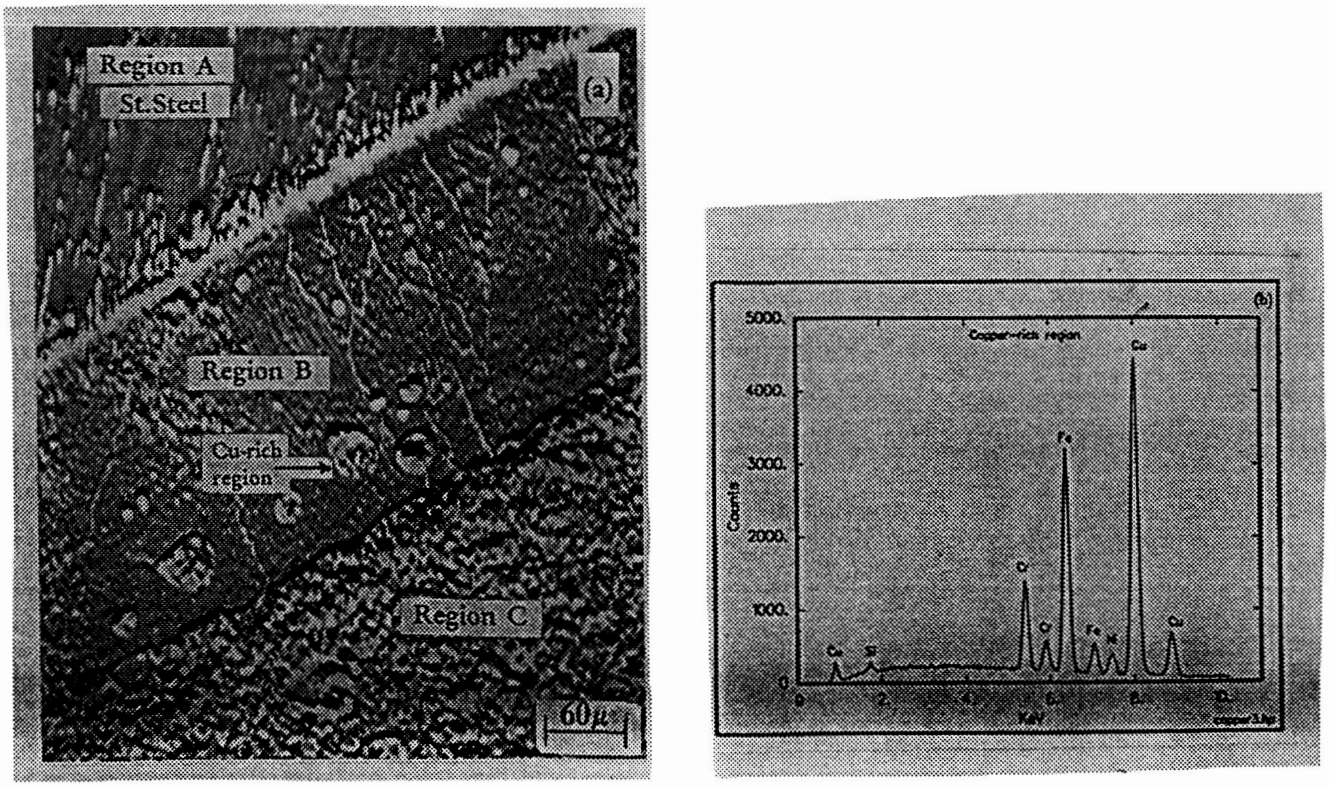

Figure 7 - SEM micrograph showing the three regions in the stainless steel/weld interface. Region A: Base steel structure, Region B: Steel fusion zone, Region C: Copper steel fusion zone. Figure 7(b): EDS spectra of copper rich region.

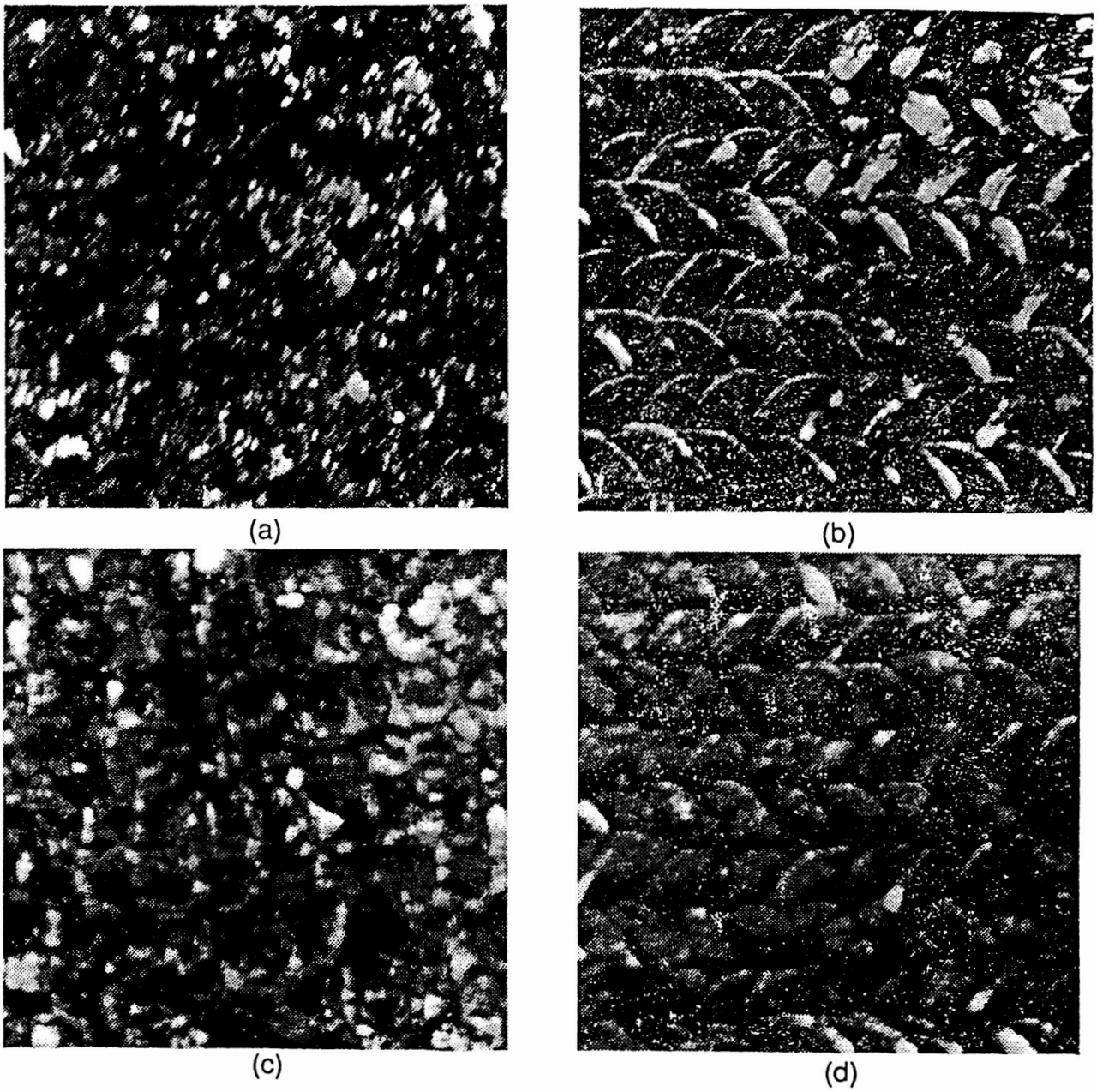

Figure 12 - Narloy Z glazed with Nd:YAG laser (a) as received surface, 0.62 Joules, (b) as-received surface, 1.90 Joules, (c) sanded surface, 0.62 Joules, and (d) sanded surface, 1.90 Joules.

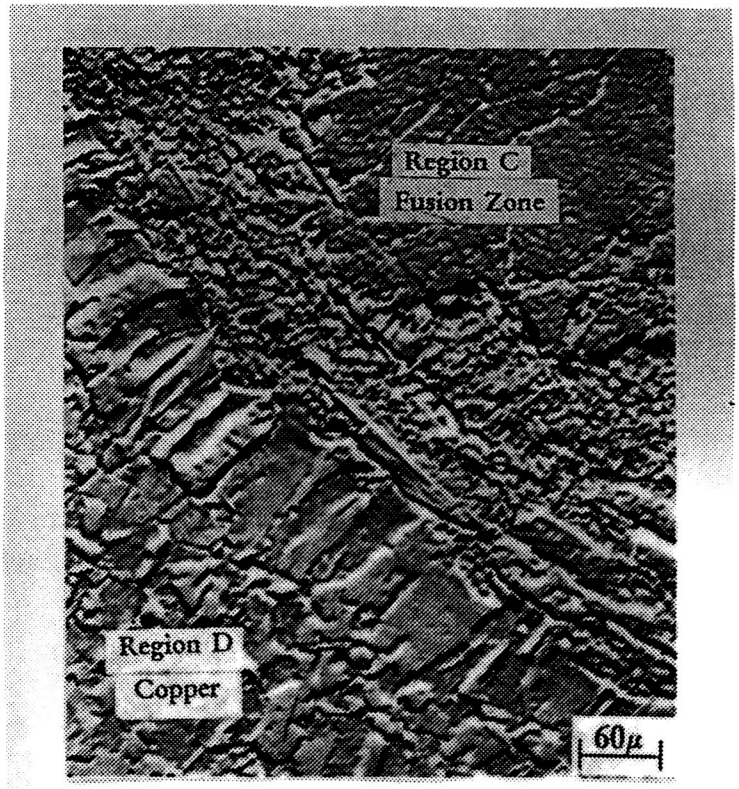

Figure 8 - SEM micrograph showing the copper-weld interface. Region C: Copper steel fusion zone, Region D: Copper heat affected zone.

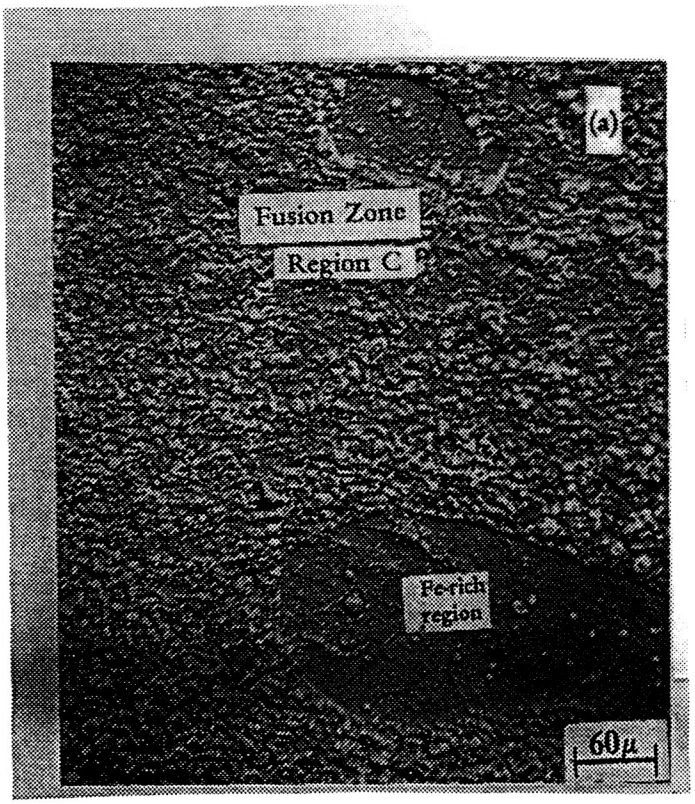

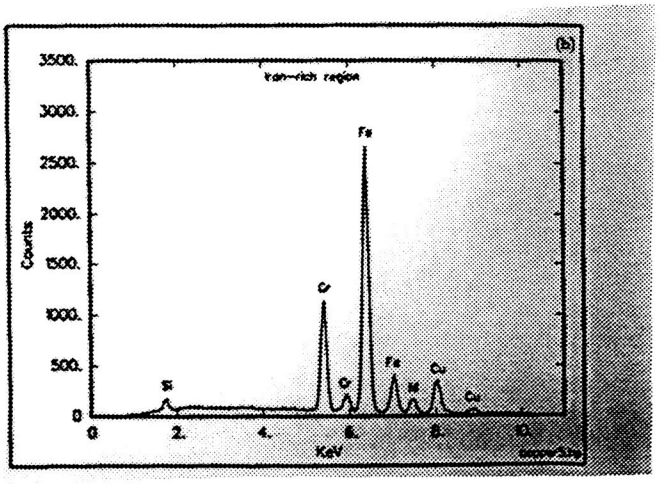

Figure 9(a) SEM micrograph showing the copper-steel fusion zone. Figure 9(b): EDS spectrum of the iron rich regions in Region C.

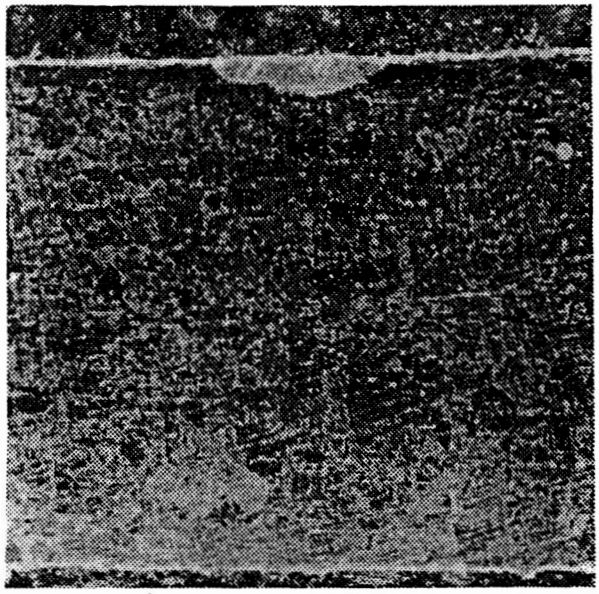

(a)

(b)

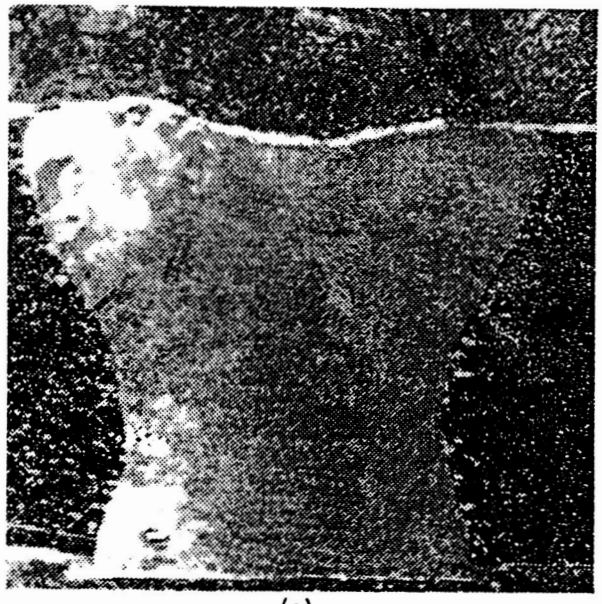

(c)

Figure 10 - Glazed Narloy Z Cross-Sections (a) Oxidized Surface, -4 Focus, 25mm/sec, (b) Graphite Paste on Surface, +1 Focus, 25mm/sec, and (3) As-Received Surface, +1 Focus, 12.5mm/sec.

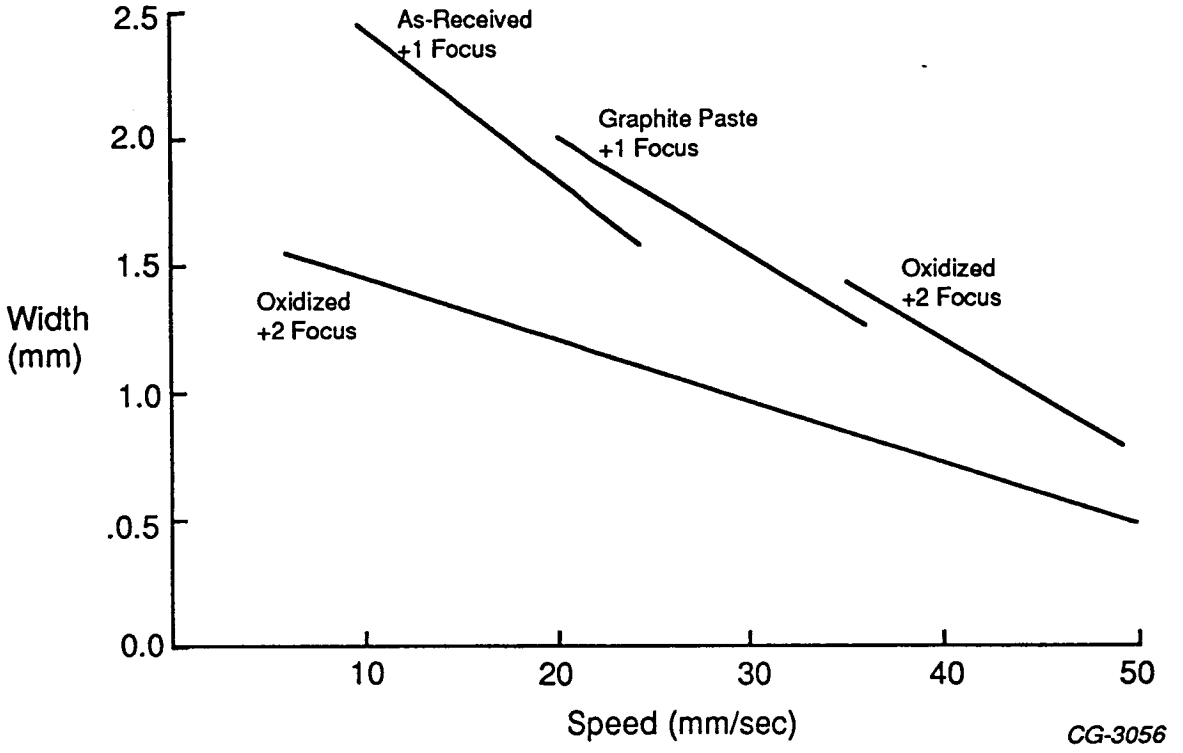

Glaze Track Widths as a Function of Processing Speed
for Different Surfaces and Focal Locations.

Figure 11 - Glaze track widths as a function of processing speed for different surfaces and focal locations.

CSTAR TECHNICAL SYMPOSIUM

ARTIFICIAL INTELLIGENCE/EXPERT SYSTEMS

B

Neural Networks Analysis on
SSME Vibration Simulation Data

A Knowledge-Based System Developer for
Aerospace Applications

SSME Propellant Path Leak Detection

Laser Material Processing

Artificial Intelligence/ Expert Systems

Space Transportation

Computational Methods

Chemical Propulsion

Electric Propulsion

Neural Networks Analysis on SSME Vibration Simulation Data

C. F. Lo† and K. Wu*

University of Tennessee-Calspan
Center for Space Transportation and Applied Research
UTSI Research Park
Tullahoma, TN 37388-8897
(615) 454-9294

Abstract

The neural networks method is applied to investigate the feasibility in detecting anomalies in turbopump vibration of SSME to supplement the statistical method utilized in the prototype system. The investigation of neural networks analysis is conducted using SSME vibration data from a NASA developed numerical simulator. The limited application of neural networks to the HPFTP has also shown the effectiveness in diagnosing the anomalies of turbopump vibrations.

Introduction

A software system has been constructed to detect anomalous Space Shuttle Main Engine (SSME) behavior in the early stages of fault development significantly earlier than the indication provided by either redline detection mechanism or human expert analysis(Ref 1). This prototype expert system was developed on both PC and Symbolics 3670 lisp machine based on the statistical method for detecting anomalies in turbopump vibration data from ground tests of the Space Shuttle Main Engine. As reported previously in Ref. 2, the results of the neural networks approach are given the successful detection to identify either normal or abnormal running condition based on the experimental data only. Since the experiment data are limited in certain conditions, to further the confidence of neural networks capability, the investigation of neural networks analysis is conducted using SSME vibration data from a NASA developed numerical simulator. The investigation procedure and results are presented in this paper.

1. Neural Network Algorithm Description

A three-layer Back-Propagation (BP) Neural Network has been selected for the present study. Multilayer BP networks have been studied extensively and are widely used for pattern classification. Multilayer networks are able to classify non-linearly separable classes. In the present case, a three layer network is utilized including input layer, hidden layer and output layer. A 3-layered (input, hidden,output), fully connected, feed-forward network as shown in Figure 1. The normalized data sets are utilized. Both input and output are continuous-valued (between -0.5 and 0.5) vector. The outputs generated by the network are compared with the desired or target outputs. Errors are computed from the differences, and the weights are changed in response to these error signals as dictated by the Generalized Delta Rule (Ref. 3). Thus, a BP network learns a mapping function by repeatedly presenting patterns from a training set and adjusting the weights. A commercial neural network program named ANSim (Ref. 4) is utilized for the training process as well as the testing process.

The Training Procedure is in the iterative fashion. It loops repeatedly over the set of training patterns until the total root mean square (RMS) error for all patterns is less than the specified value, e.g. 0.1. The Testing Procedure is forward feed processing.

2. Neural Network ANSim Software

A commercial neural network program named SAIC ANSim 2.30 is a graphics oriented, menu-based artificial neural system (ANS) simulation program, which provides a complete complement of neural model development, allocation and analysis capabilities, including a powerful ANS creation, training, execution and monitoring tool. ANSim enables users to quickly implement and utilize ANS models using 13 paradigms such as Back Propagation (BP), Hopfiled Network, etc. ANSim enables the user to configure any number of ANS neural networks. It drives each network with a sequence of training and/or input data. For each model, ANSim will

† UTSI Professor, CSTAR Principal Investigator
* CSTAR Research Engineer

(1) monitor the response, (2) capture the output, and (3) save the configuration for later re-use. ANSim is integrated under Microsoft Windows to provide an effective, easy-to-use interface. A Floating Point Processor for ANSim is available to speed up the training clock time. A PC 386 (VGA or EGA monitor) with the SAIC's Delta Floating Point Processor, which is a 22 MFlop AT bus compatible processor, allows for high speed Neural Network Systems training and processing.

3. Results Obtained from Numerical Simulator

The results have indicated that the application of Neural Network to the available SSME vibration data sets in diagnosing existing faults in the data is a viable method. To reassure the neural network's effectiveness, the investigation of more cases and more fault scenarios are required. Since the limited ground test data is available, the study using the data generated from a NASA/MSFC's numerical simulator is reported as follows.

The current simulated data were provided by Fred Kuo at MSFC from a numerical simulator (Ref. 5) developed at NASA/MSFC. Three data sets are obtained from the Numerical Simulator. These cases received from NASA on Nov. 15, 1992 and Feb. 18, 93 have been studied. Two of these sets are "Rotor.DB" and the other is "Rotor.UB". The displacement response in the Y and Z direction and the side-force in the Y and Z direction vs. dimensionless time as shown in Figures 2, 3 and 4, respectively. These sample numerical data were analyzed by fast Fourier Transform in the spectrum plots with three different sizes of window for sample response-amplitude data plotted in Figures 5, 6 and 7. The side-force sample data are shown in Figures 8, 9 and 10. The sample results are given in Tables 1 and 2 for both Y-response and Y-force of Rotor.UB and Rotor.DB, respectively. Even with the limited data base, the successful rate is very reasonable after 300 training cycles in SAIC ANSim 2.30.

4. Comments on the Approach of Neural Networks

For the training process of the Neural Networks, the clock time of computer computation on a PC-386 with Floating Point Processor is less than 1 minute. The testing time of the feed-forward process is near real time in the present case. This is important to know this computation time for planning on-line or off-line operation in addition to its ability to identify the correct anomalies.

The limited application of neural networks to the HPFTP has also shown the effectiveness and feasibility to diagnose the anomalies of turbopump vibrations. The further investigation on data from experimental data sets and the numerical simulator is recommended before implementing for the on-line ground testing.

REFERENCES

1. C. F. Lo, B.A.Whitehead, and K. Wu, "Automatic Detection of Anomalies in Space Shuttle Main Engine Turbopumps", AIAA Paper No. 92-3329, Joint Propulsion Conference, July 1992

2. C. F. Lo, K. Wu, and B.A.Whitehead, "Anomaly Detection of Turbopump Vibration in Space Shuttle Main Engine Using Statistics and Neural Networks", AIAA Paper No. 93-1777, Joint Propulsion Conference, June 1993

3. D. E. Rumelhart, G. E. Hinton, and R. J. Williams "Learning Internal Representations by Error Propagation", Parallel Distribution Processing, Vol. I, 1986

4. Science Application International Corp. "ANSim Artificial Neural Systems Simulation Program", April, 1989

5. S. G. Ryan "Limit Cycle Vibrations in Turbomachinery", NASA Technical Paper 3181, December 1991

ACKNOWLEDGEMENTS

This research was supported by the Structure and Dynamics Laboratory of NASA-MSFC Grant No. NAG 8-166. The investigators would like to thank Pat Vallely, Technical Monitor, NASA/MSFC, Tom Fox and Fred Kuo of NASA/MSFC for their technical advice.

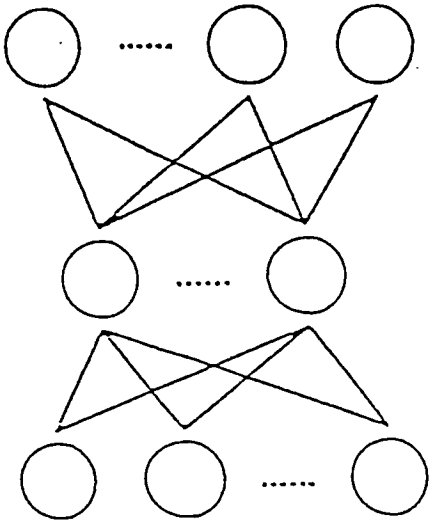

Input Layer

(13 nodes : Shaft fundamental
Shaft fundamental's three harmonics
cage fundamental
Cage fundamental's three harmonics
Inner race,outer race,240HZ,Sub-sync
thrust-level)

Hidden Layer

(6 nodes)

Output Layer

(2 nodes: for FASCOS-HPFP, normal & 240HZ abnormal
for HPFP-RAD, normal & Sub-sync abnormal)

Figure 1. Three-layer Back-propagation Neural Network Architecture.

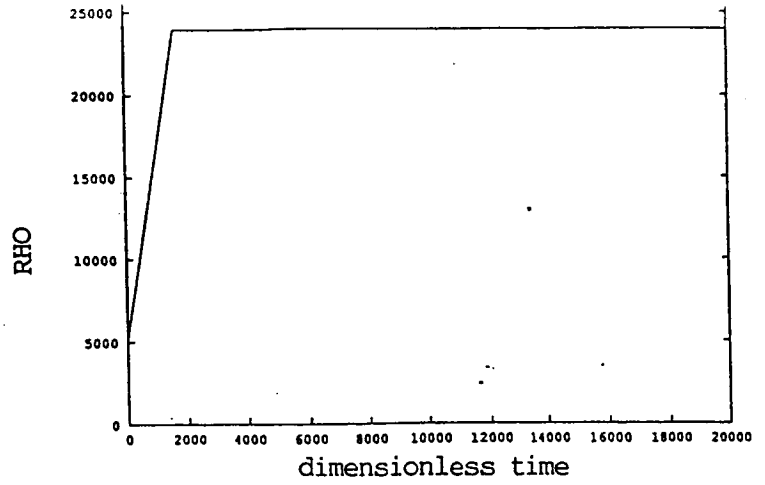

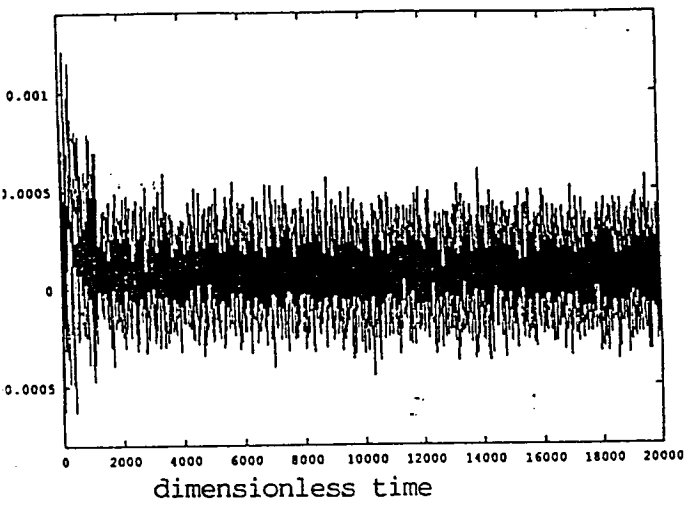

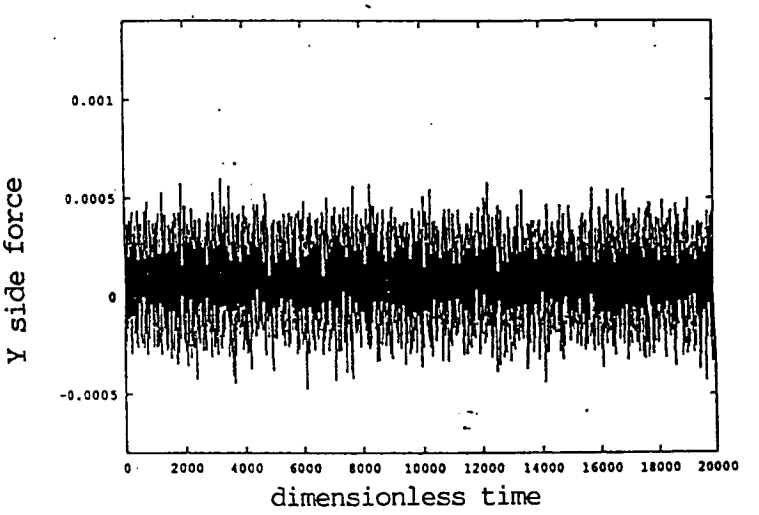

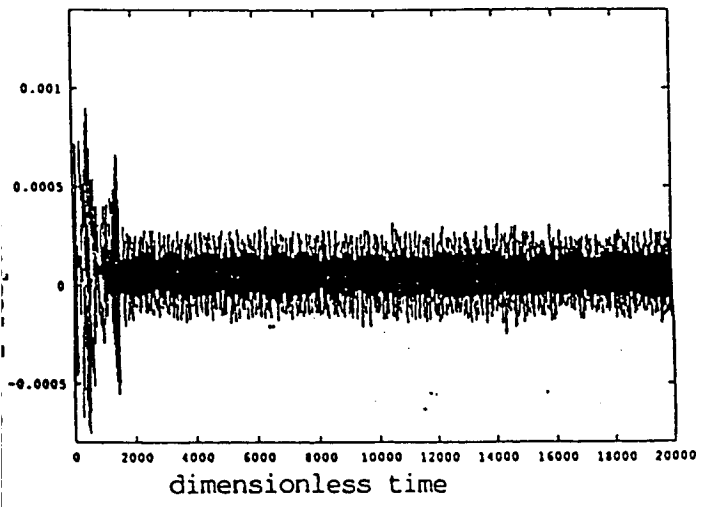

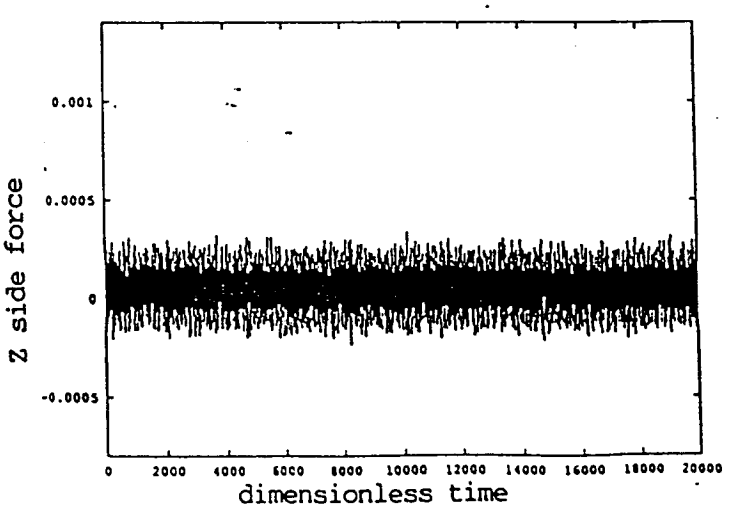

Figure 2. Sample Data Received on Nov. 15, 1992 (ROTOR.DB).

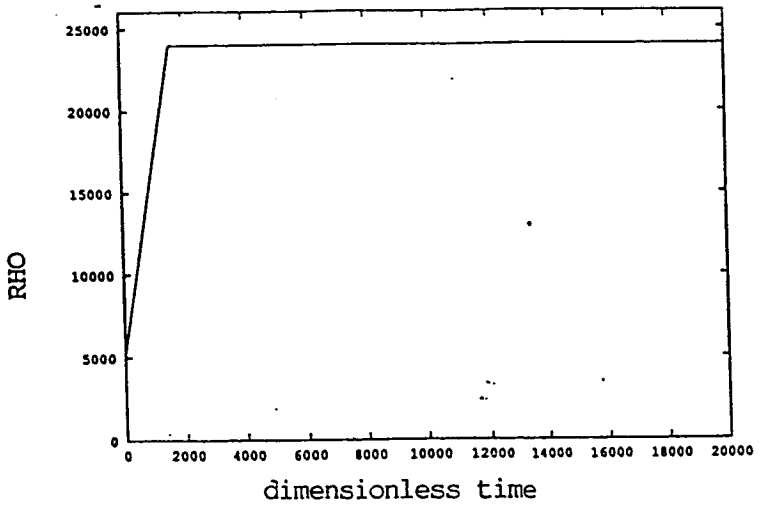

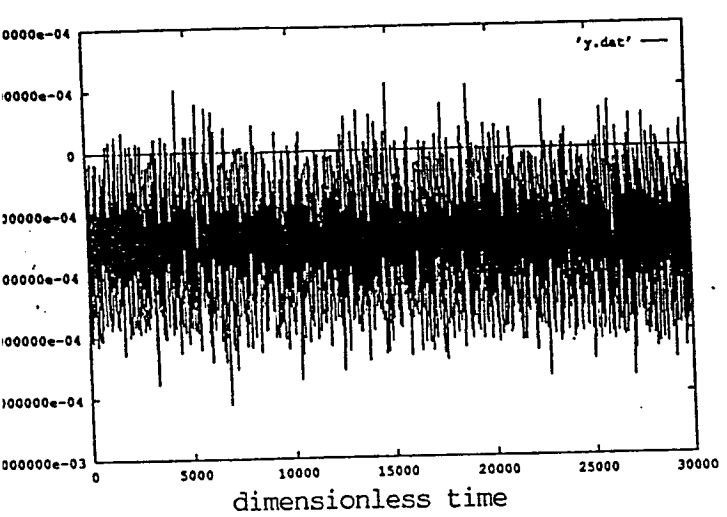

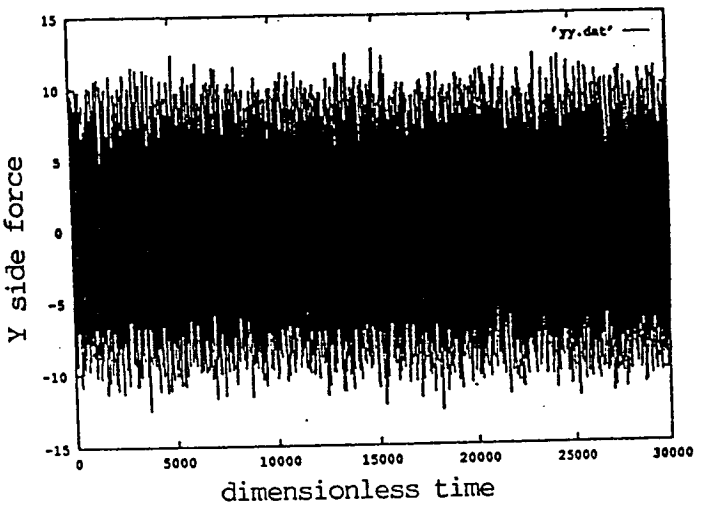

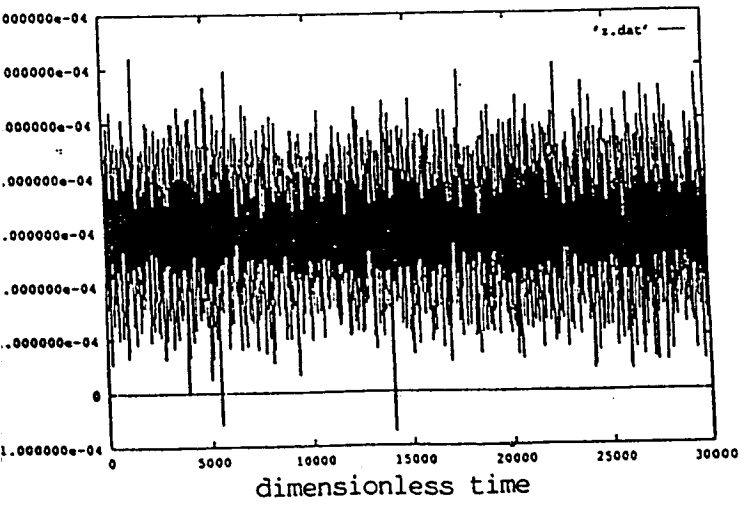

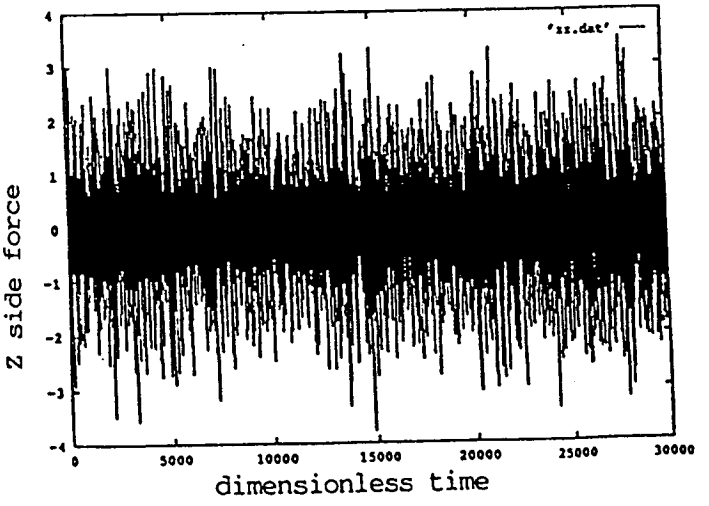

Figure 3. Sample Data Received on Feb. 18, 1993 (ROTOR.DB).

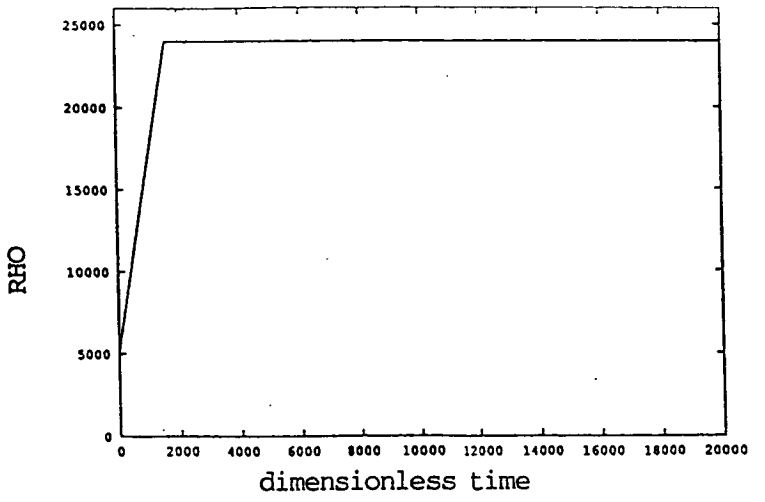

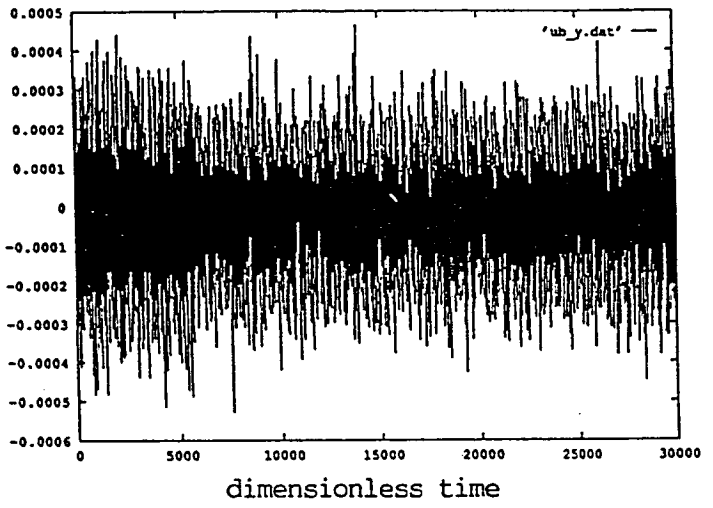

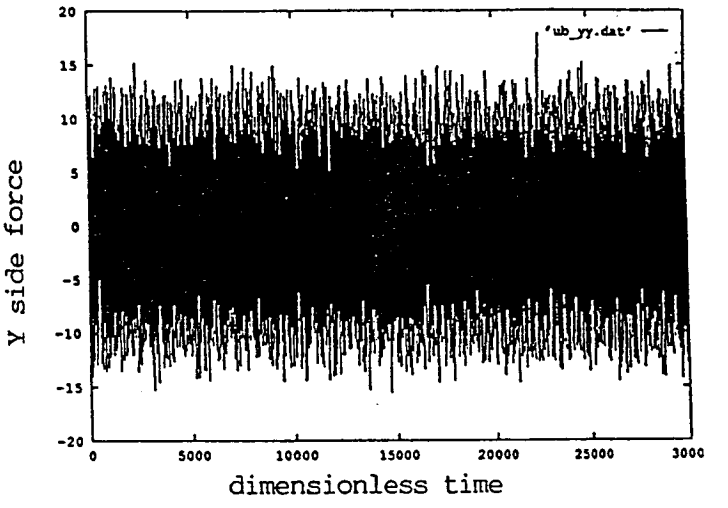

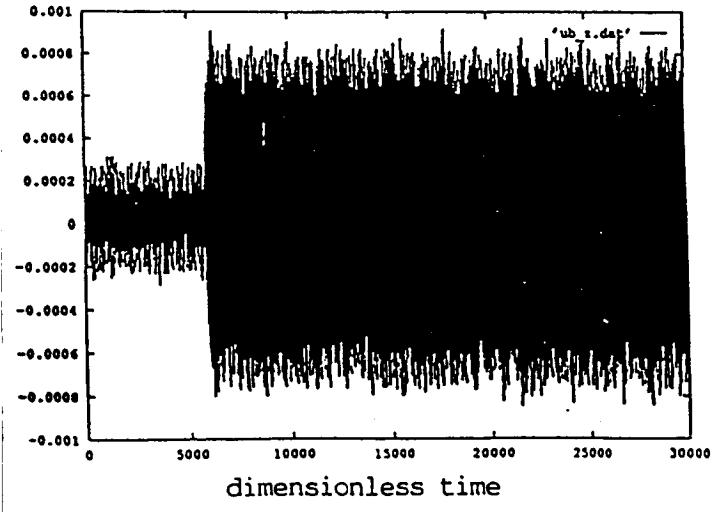

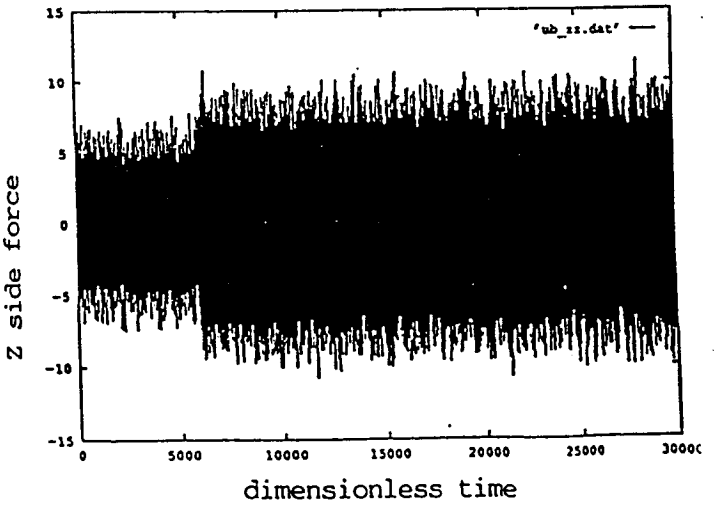

Figure 4. Sample Data Received on Feb. 18, 1993 (ROTOR.UB).

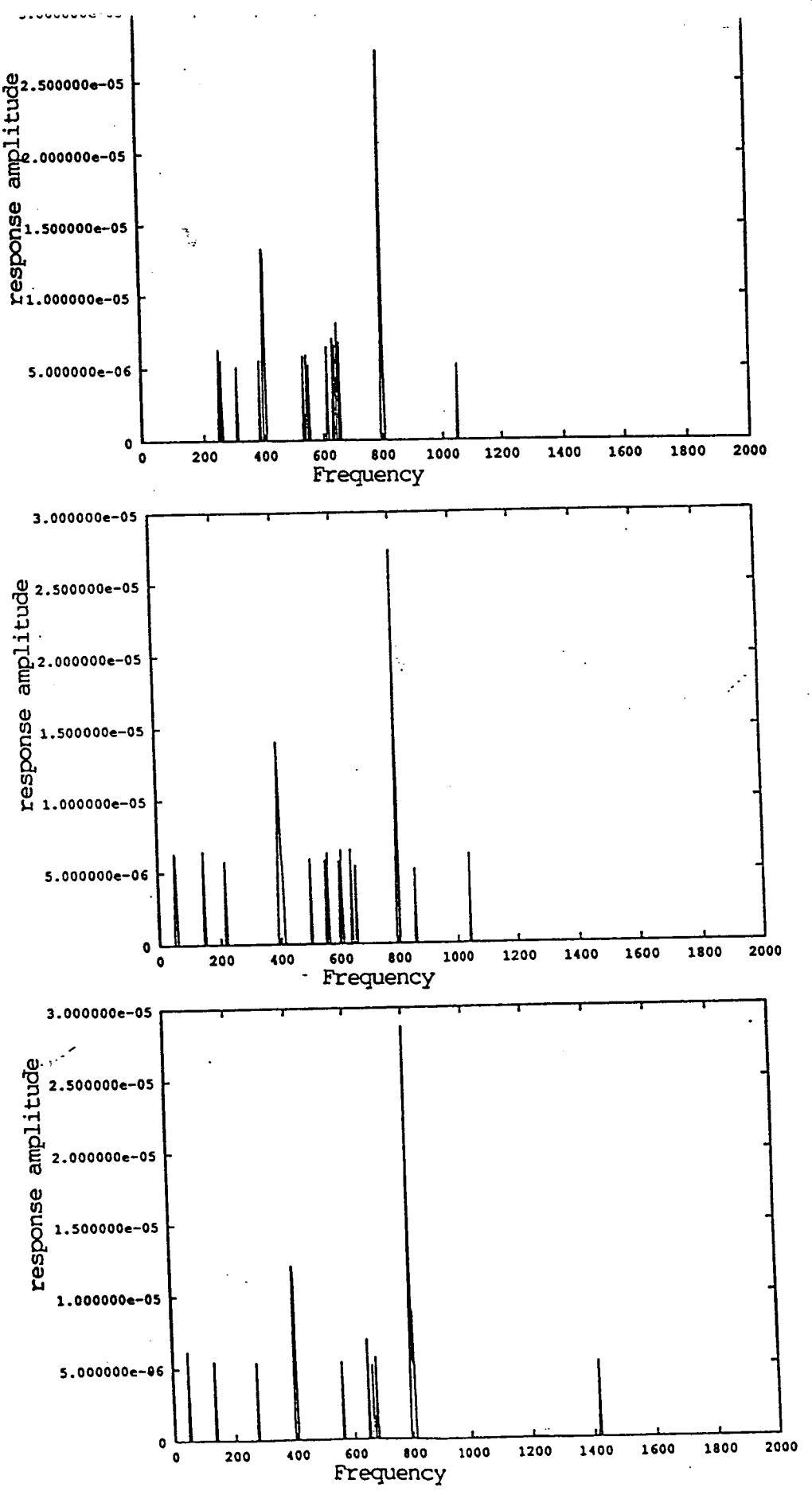

Figure 5. Response Amplitude After Frequency Extraction from Sample Data Received on Nov. 15, 1992 (ROTOR.DB).

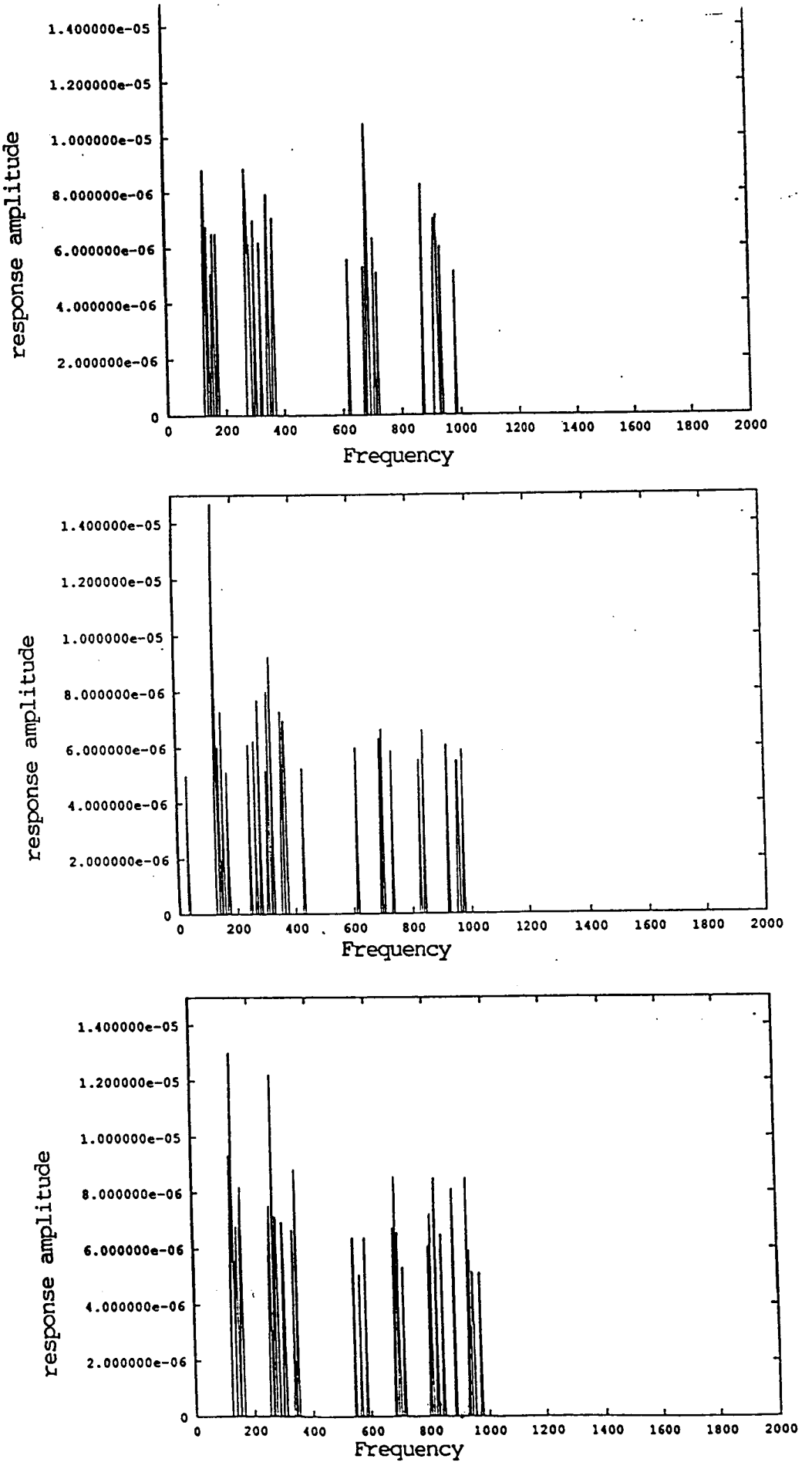

Figure 6. Response Amplitude After Frequency Extraction from Sample Data Received on Feb. 18, 1993 (ROTOR.DB).

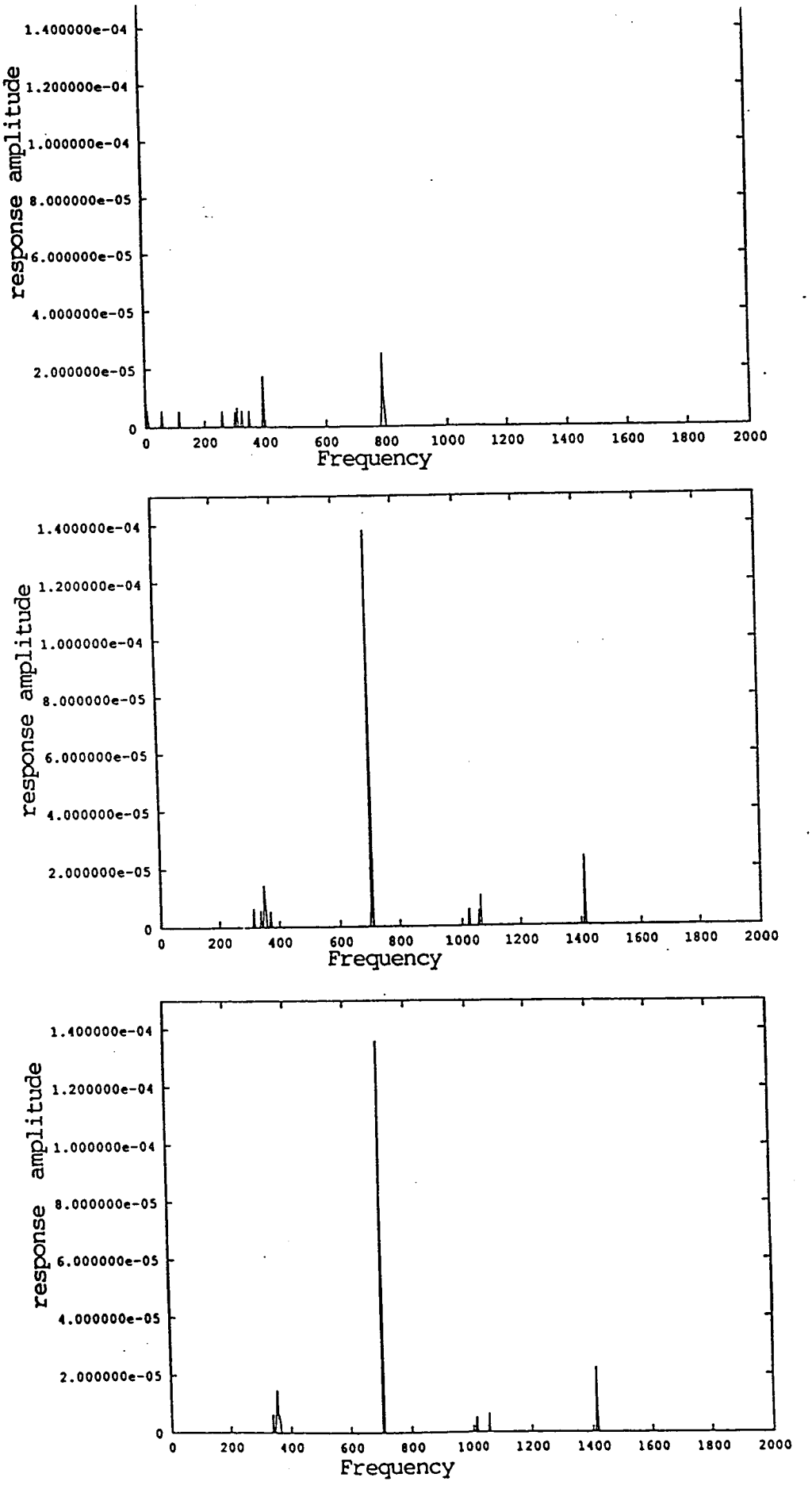

Figure 7. Response Amplitude After Frequency Extraction from Sample Data Received on Feb. 18, 1993 (ROTOR.UB).

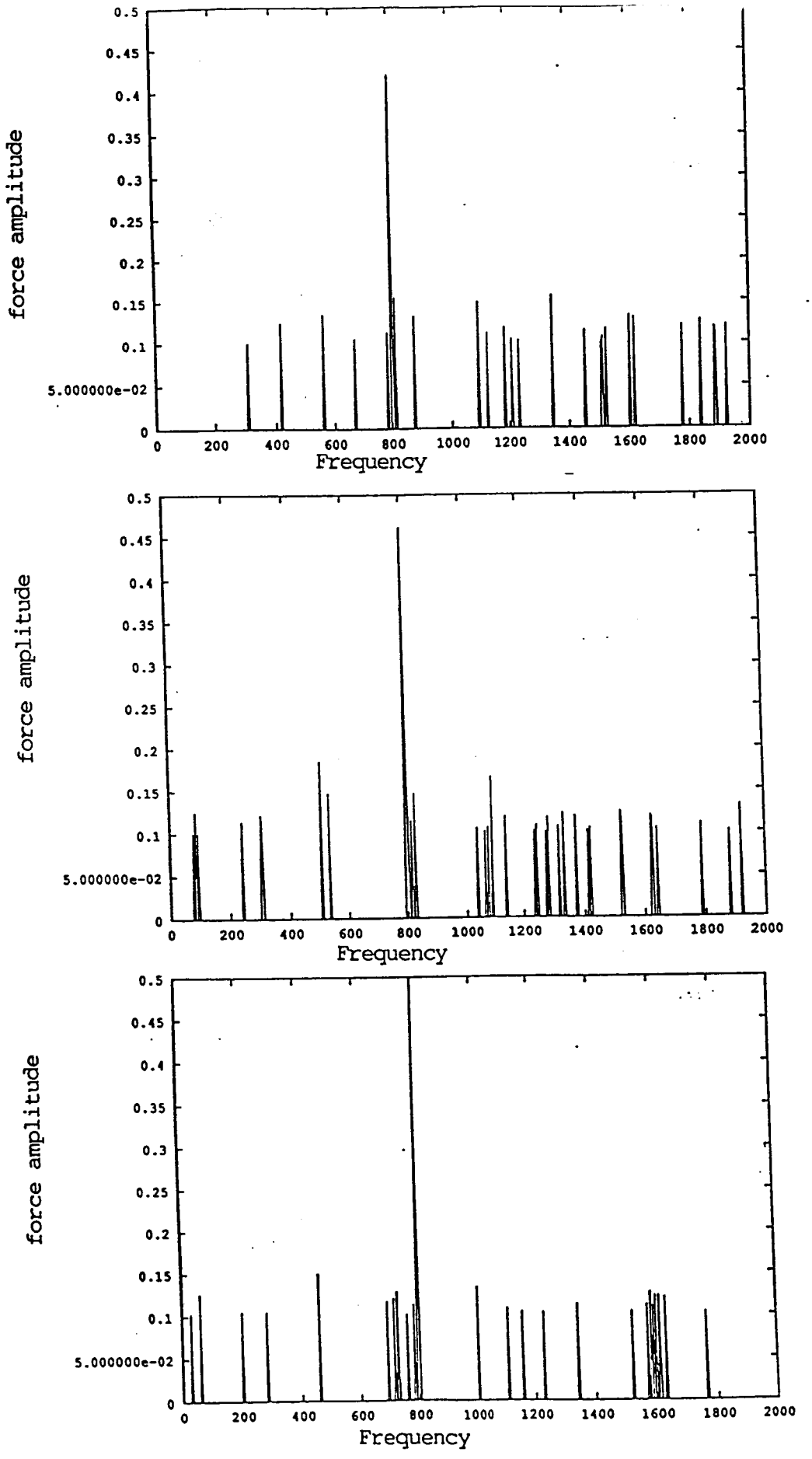

Figure 8. Force Amplitude After Frequency Extraction from Sample Data Received on Nov. 15, 1992 (ROTOR.DB).

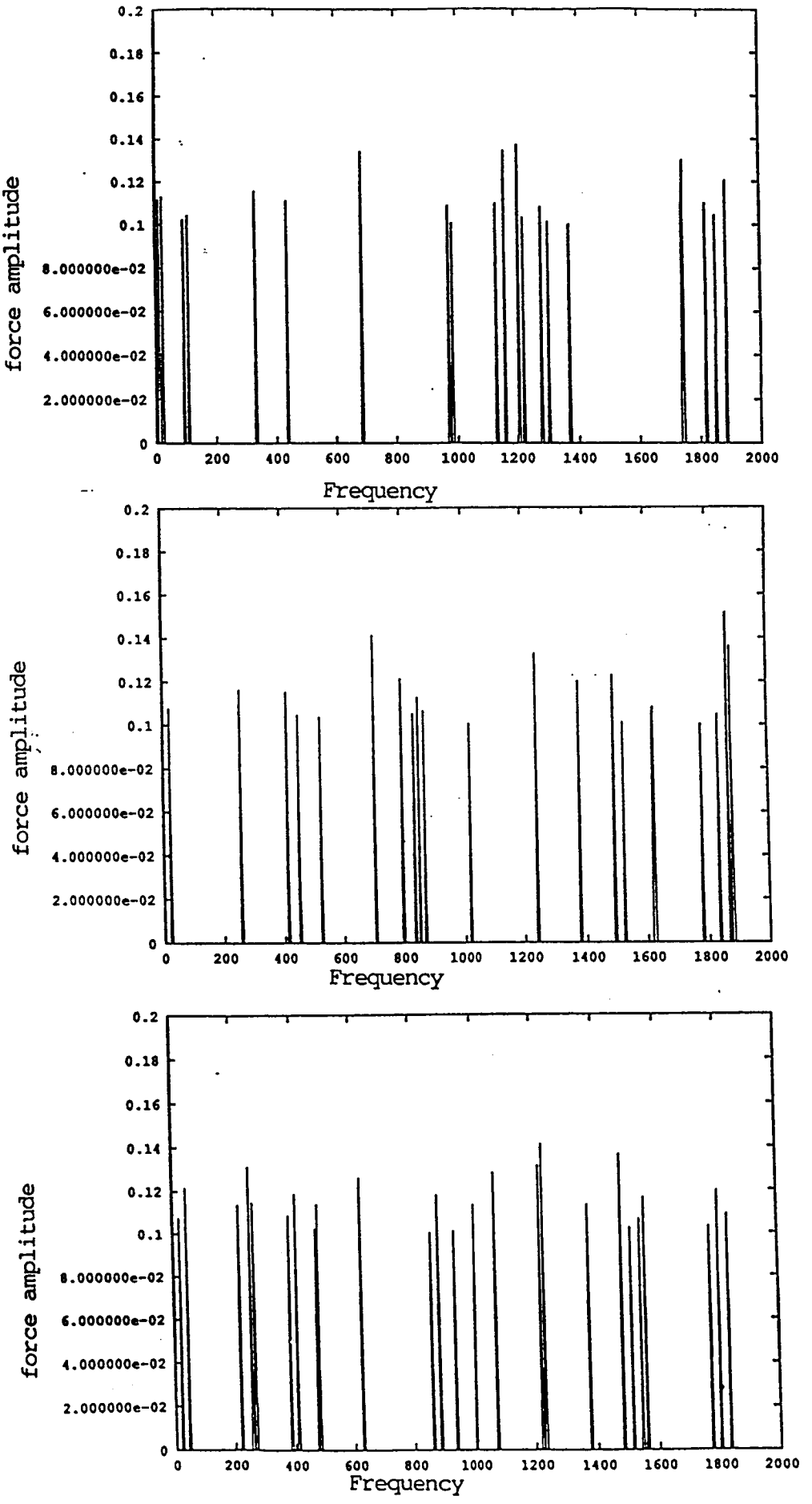

Figure 9. Force Amplitude After Frequency Extraction from Sample Data Received on Feb. 18, 1993 (ROTOR.DB).

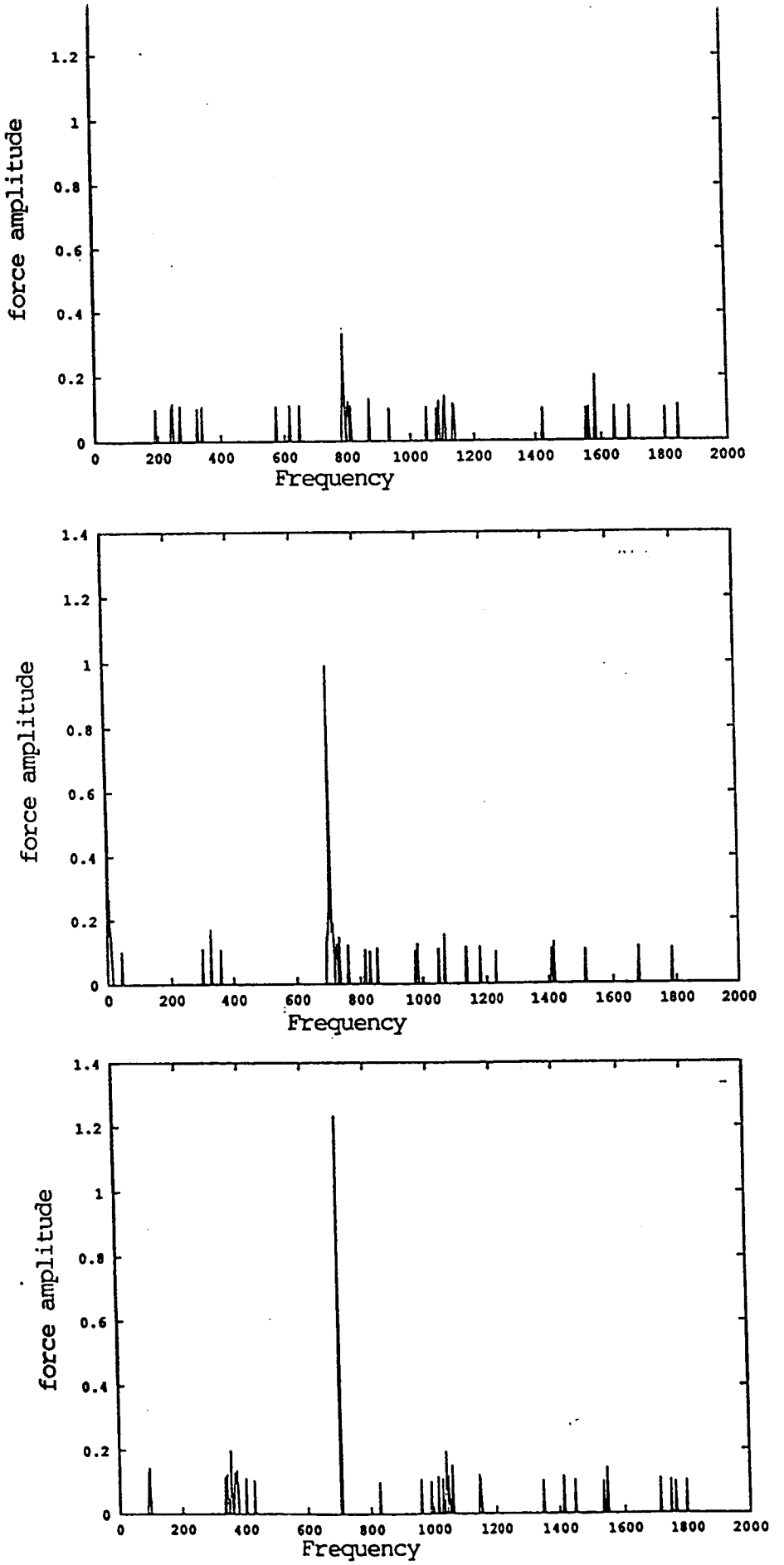

Figure 10. Force Amplitude After Frequency Extraction from Sample Data Received on Feb. 18, 1993 (ROTOR.UB).

Raw Data (Y-Response of ROTOR.UB, Received on Feb 18,1993)
After 300 training cycles
Random Selection of Training Data Sets

Self-Testing After Training

Actual Class of Observation

	Normal	Abnormal	Total	P2%
Normal	3	0	3	100
Abnormal	0	5	5	100
Total	3	5	8	100
P1%	100	100	100	100

New Data Testing After Training

Actual Class of Observation

	Normal	Abnormal	Total	P2%
Normal	1	0	1	100
Abnormal	1	5	6	83
Total	2	5	7	91
P1%	50	100	75	83

NOTE: P1: p(prediction=x, actual=x), P2: p(actual=x, prediction=x)

Table 1. Neural Networks Results of ROTOR.UB
a. for Y-Response

Raw Data (Y-Force of ROTOR.UB, Received on Feb 18,1993)
After 300 training cycles
Random Selection of Training Data Sets

Self-Testing After Training

Actual Class of Observation

	Normal	Abnormal	Total	P2%
Normal	3	0	3	100
Abnormal	0	5	5	100
Total	3	5	8	100
P1%	100	100	100	100

New Data Testing After Training

Actual Class of Observation

	Normal	Abnormal	Total	P2%
Normal	1	0	1	100
Abnormal	2	4	6	67
Total	3	4	7	84
P1%	33	100	67	75

NOTE: P1: p(prediction=x, actual=x), P2: p(actual=x, prediction=x)

Table 1. Neural Networks Results of ROTOR.UB
b. for Y-Force

Raw Data (Y-Response of ROTOR.DB, Received on Feb 18,1993)
After 300 training cycles
Random Selection of Training Data Sets

Self-Testing After Training

Actual Class of Observation

	Normal	Abnormal	Total	P2%
Normal	6	0	6	100
Abnormal	0	1	1	100
Total	6	1	7	100
P1%	100	100	100	100

New Data Testing After Training

Actual Class of Observation

	Normal	Abnormal	Total	P2%
Normal	5	2	7	71
Abnormal	0	1	1	100
Total	5	3	8	85
P1%	100	33	67	76

NOTE: P1: p(prediction=x, actual=x), P2: p(actual=x, prediction=x)

Table 2. Neural Networks Results of ROTOR.DB
a. for Y-Response

Raw Data (Y-Force of ROTOR.DB, Received on Feb 18,1993)
After 300 training cycles
Random Selection of Training Data Sets

Self-Testing After Training

Actual Class of Observation

	Normal	Abnormal	Total	P2%
Normal	6	0	6	100
Abnormal	0	1	1	100
Total	6	1	7	100
P1%	100	100	100	100

New Data Testing After Training

Actual Class of Observation

	Normal	Abnormal	Total	P2%
Normal	6	1	7	86
Abnormal	0	1	1	100
Total	6	2	8	93
P1%	100	50	75	84

NOTE: P1: p(prediction=x, actual=x), P2: p(actual=x, prediction=x)

Table 2. Neural Networks Results of ROTOR.DB
b. for Y-Force

A Knowledge-Based System Developer for Aerospace Applications

53-82

N96-16943

George Z. Shi [1], Kewei Wu[1], Connie S. Fensky[2] and Ching F. Lo[3]

University of Tennessee-Calspan
Center for Space Transportation and Applied Research
Tullahoma, TN 37388-8897

5700

Abstract

A prototype Knowledge-Based System Developer (KBSD) has been developed for aerospace applications by utilizing artificial intelligence technology. The KBSD directly acquires knowledge from domain experts through a graphical interface then builds expert systems from that knowledge. This raises the state of the art of knowledge acquisition/expert system technology to a new level by lessening the need for skilled knowledge engineers. The feasibility, applicability, and efficiency of the proposed concept was established, making a continuation which would develop the prototype to a full-scale general-purpose knowledge-based system developer justifiable. The KBSD has great commercial potential. It will provide a marketable software shell which alleviates the need for knowledge engineers and increase productivity in the workplace. The KBSD will therefore make knowledge-based systems available to a large portion of industry.

1. Introduction

The effective development and implementation of advanced software for knowledge-based systems is limited by the level of knowledge acquisition, representation, and utilization technology. Skilled knowledge engineers are needed to translate experts' knowledge into heuristic rules for the applicable technical domain.

This NASA SBIR research project aimed to design and construct a Knowledge-Based System Developer for aerospace applications by utilizing artificial intelligence technology, including dynamic interfaces, expert systems, and interactive-multimedia. The resulting KBSD software will directly acquire knowledge from domain experts and then build expert systems from that knowledge. The knowledge acquisition is performed through a graphical interface which helps the domain experts organize their knowledge. The KBSD also has the capability of building hypermedia documents and user interfaces which are important parts of any knowledge-based system. This project thus raises the state of the art of knowledge acquisition/expert system technology to a new level by lessening the need for skilled knowledge engineers. The KBSD will help NASA to preserve its domain-experts' knowledge and increase productivity of NASA personnel.

The main effort of Phase I (6 months) was to build a prototype system on the Macintosh platform to establish the feasibility of the concept. To achieve these objectives, the following tasks were carried-out during Phase I to implement the proposed approach of the KBSD:

1. Design of the methodology and system architecture for the KBSD.
2. Construction of the prototype KBSD by implementing the designed methodology and architecture.
3. Building trial knowledge-based systems using the prototype KBSD for testing.
4. Demonstration and evaluation of the prototype KBSD.

2. Approach

The KBSD is designed to be hosted on the Macintosh platform. It was constructed using both custom code written in C/C++ language and HyperCard [Ref. 1]. Several advantages were gained by using HyperCard:

1 All of HyperCard's functions can be directly used for the KBSD, as well as many external commands and external functions. This saved development time.

2 User familiarity is enhanced, while a major time saving tool is still provided.

The C programs were coded for the KBSD where its functions were difficult to achieve in HyperCard, and complex enough to require significantly faster run times.

3. KBSD Overview

The prototype KBSD consists of three major components: the Knowledge Acquisition and Rule Writer (KARW), the Hypertext Documentation Builder (HDB), and the User-Interface Builder (UIB), as shown in Figure 1. The KARW is used for knowledge acquisition, knowledge verification/validation, and heuristic rule creation. The formatted knowledge is exported to knowledge-bases for use by the end-user. The HDB builds knowledge in the form of hypertext

---

[1] Research Engineer, CSTAR
[2] Graduate Research Assistant, UTSI/CSTAR
[3] Professor of AE/ME, UTSI

documentation, an important part of a knowledge-based system. The UIB builds the user-interface for a knowledge-based system.

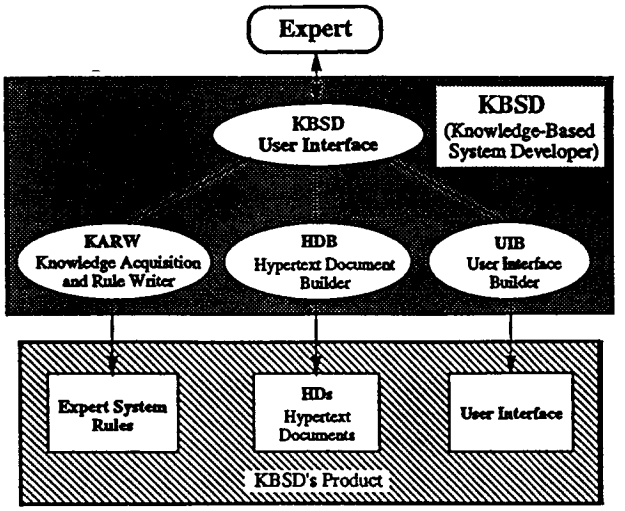

Figure 1. KBSD overview

Each product knowledge-based system created by the prototype KBSD consists of a friendly user-interface, several expert systems with domain experts' knowledge to provide advice, and a set of hypertext documents.

4. Knowledge Acquisition and Rule Writer

The KARW is the core of the prototype KBSD and was programmed entirely in the C language. In Phase I, the heuristic rules produced by the prototype KBSD were exported into the format of a commercial expert system shell, LEVEL5 [Ref. 2], for testing and consultation. Coding of an inference-engine for the KBSD will be carried-out in the future.

4.1 Principles of Knowledge Acquisition

The following basic knowledge-acquisition principles were used to construct the KARW:

1. Decompose a large-scale knowledge topic into several manageable sub-topics.
2. Elicitation: provide the user with hints and reminders, rather than asking the user to recall everything.
3. Provide a graphical working environment to help the user organize the knowledge base.
4. Break the knowledge acquisition process into a series of steps.

4.2 Elements of the KARW

The KARW consists of the following elements [Ref. 3], whose functional relation is shown in Figure 2:

The **Elicitation Element** provides an interactive graphical elicitation environment for experts to input domain knowledge such as domain definition, object definition, and rule definition and creation in production rules format.

The **Comparison Element** (verification and validation) compares new rules to existing rules to determine consensus, conflict, subsumption, and redundancy. If conflicts occur, questions will be asked and corresponding modifications will be made

The **Inductive Element** derives constraints within the conceptual structures through empirical induction analyses. It enables the attributes of an entity, or the evaluations of a decision-making situation, to be derived from other attributes.

The Export Element converts product rules into a form understandable by different expert system shells. For Phase I, this element is limited to export rules to only the LEVEL5 [Ref. 2] expert system shell.

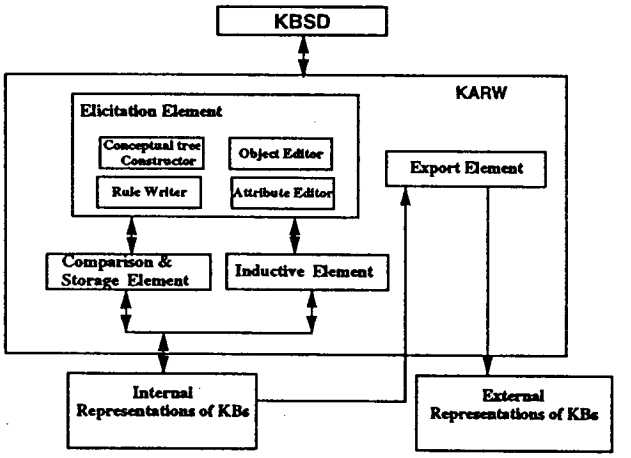

Figure 2. The KARW's elements and their functions

4.3 KARW's Working Environment

Figure 3 illustrates the KARW's working environment, which has three major windows: the object window, the conceptual-tree window, and the rule-writer window. The object window is a scrollable window which lists all objects related to the current topic. Users can add, edit, and delete objects, or copy objects into the conceptual-tree as nodes. The conceptual-tree window is a graphical window with both vertical and horizontal scrollbars. Users can construct a knowledge tree in this window by selecting the node items from the object window, dragging them into position, grouping nodes, and making links between nodes. The rule-writer window is a moveable window. Users can edit text in this window to write rules based on a format provided by the KARW. The KARW alerts the user of any syntax errors, conflicts, subsumption, or redundancy.

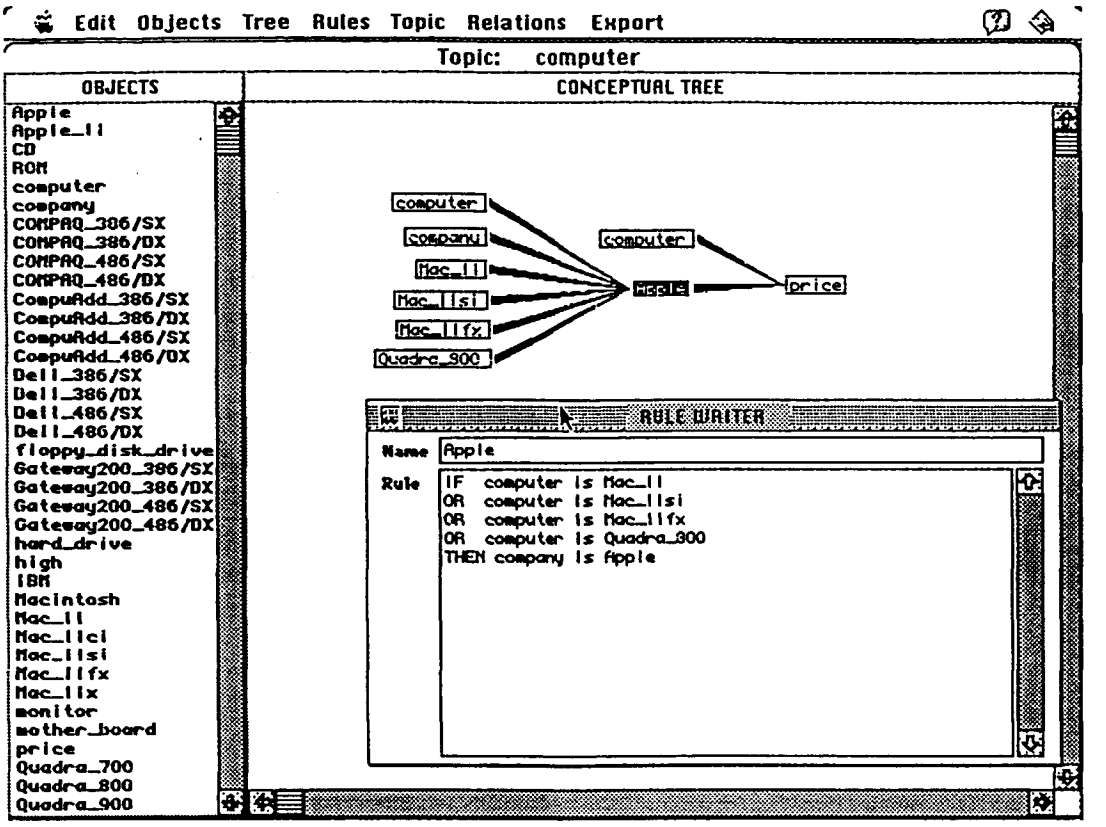

Figure 3. An illustration of the KARW's working environment

Seven pull-down menus are included in the KARW's working environment: **Edit, Objects, Tree, Rules, Topic, Relations**, and **Export**, as shown in Figure 4. The **Edit** Menu has the standard Macintosh functions, and is used during rule writing. The **Objects** Menu adds, deletes and changes objects in the object-window. The **Tree** Menu is used to build and edit the conceptual knowledge tree. The **Rules** Menu is used to manage rules. The **Topic** Menu is used to create new topics and switch between them. (Each topic has its own object list and knowledge tree). The **Topic** Menu also allows the user to quit the KARW. The **Relations** Menu is used in conjunction with the **Rules** Menu in writing rules. Finally, the **Export** Menu is used to export the heuristic rules in the format of an external expert system shell.

4.4 Knowledge Base Construction Procedure

During knowledge acquisition, the user only works in the Elicitation element's graphical environment. The KARW decomposes the knowledge acquisition process into a series of distinct steps which ease the user into the task:

1. After being prompted to select a topic, a user is presented with a list of objects in the object window (variables, conclusions, etc.), if the selected topic exists. If the user chooses to create a new topic, the object window is blank.

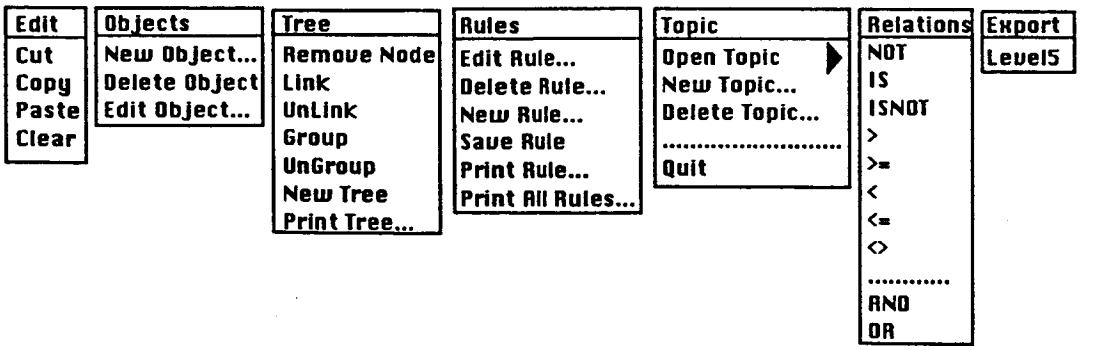

Figure 4. The pull-down menus of the KARW's working environment

2. The user may add relevant new objects, and delete irrelevant objects in the object window.
3. The user selects objects from the object window and drags them into the conceptual-tree window to become nodes in the conceptual-tree. He/she then graphically organizes nodes into a knowledge tree, linking related conditions and conclusions.
4. The user takes groups of nodes (by clicking on the conclusion part of a group) and writes rules for them. After writing a new rule, the KARW calls the Comparison Element to check for consensus, conflict, subsumption, and redundancy. If problems exist, questions will be asked of the user and the corresponding modifications made.
5. The user can go back to any previous step to modify the knowledge-tree or rules at any time during knowledge base construction.
6. After a knowledge base has been completed, the Export element converts the knowledge to the format of the LEVEL5 expert system shell.

4.5 Knowledge Rule Organization

The rules in the knowledge base are structured in two levels: the rule table and the index array. Each item in a rule is stored at its corresponding location in the index array as shown in Figure 5. Each row in the table represents a rule which consists of a condition side and a conclusion side.

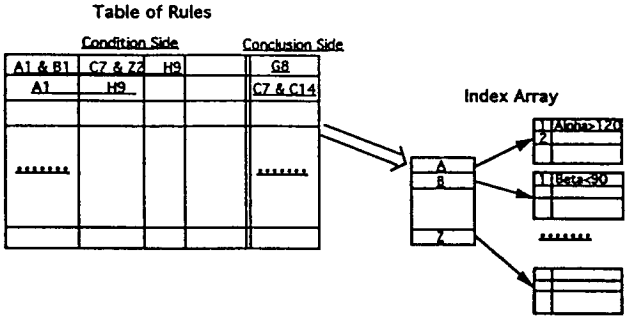

Figure 5. The organization of knowledge base rules

5 Hypertext Documentation Builder

A knowledge-based system is not complete without supporting documentation. Hypertext documentation is the most effective format for presentation in a computerized knowledge-based system. The Hypertext Documentation Builder (HDB) is designed to build hypertext documents in HyperCard format from existing computerized document files. The text can be input from either a text file or the clipboard. Users can also type text in the HDB for their document. Figures can be imported from a MacPaint file or from the clipboard into the HDB for hypertext documents.

The HDB has a set of pull-down menus which are similar to those in word-processor software, as illustrated in Figure 6. This set of menus carries out functions such as open/close file, save, copy, cut/paste, change fonts and size, etc. The HDB also includes a set of document-building buttons: Document Title, Section Title, Body Text, and Figure, also shown in Figure 6. The user highlights desired text and then clicks on one of these buttons. The HDB automatically puts the highlighted text into its corresponding place and assigns a size and style to the text according to its type (text font, size, and style for the different parts of the document, such as title, section title, and body text, are selected by the user). The hypertext links between standard parts of a document are established automatically by the HDB during the building.

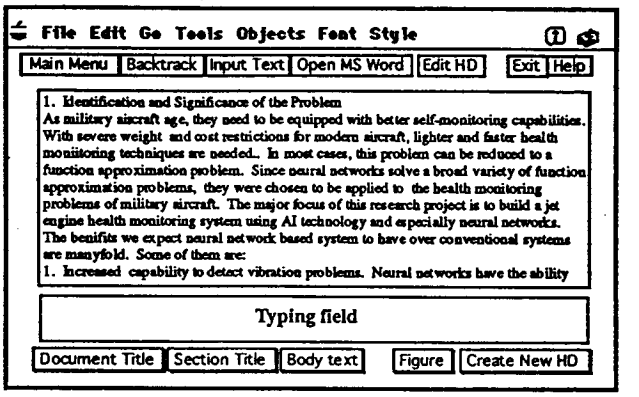

Figure 6. An illustration of the HDB's Interface

All hypertext documents produced by the HDB will have a preamble and a body text. The preamble includes the title page, table of contents, and list of figures. There is a set of standard navigational buttons on every display screen of the document. These buttons are **Table of Contents, BackTrack, Previous, Next,** and **List of Figures** (if necessary) as shown in Figure 7. The **Next** and **Previous** buttons bring the adjacent pages in the document to the screen, and **BackTrack** directly brings the last page viewed back into view, even if it was in a different document.

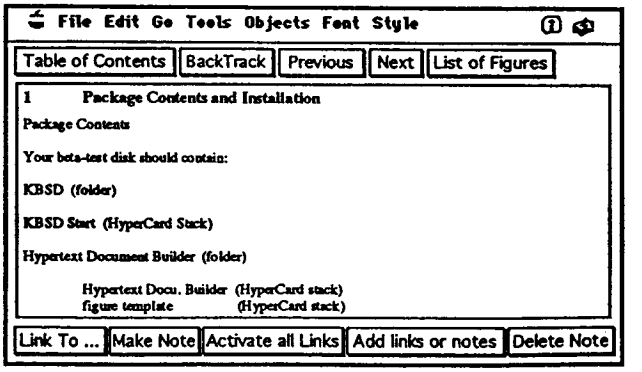

Figure 7. A typical hypertext document body page

The user can also create customized links between a word and a specified page within the product document, as well as to other documents. Note fields can also be automatically created for certain words in the body text, allowing comments related to the text to be stored. The **Link** and **Note** buttons are also shown in Figure 7.

6. User-Interface Builder

Every knowledge-based system needs an interface through which the end user communicates with the computer. The User-Interface Builder (UIB) enables users to build a menu-driven user-interface for their knowledge-based system with a minimum of effort. The UIB is a HyperCard-based shell which works in conjunction with the HDB at this time.

The UIB provides three standard menu formats for the product user-interface, as shown in Figure 8. Buttons and fields are designed as a group for the product menu. Individual buttons and fields can be changed if desired. Some steps in the UIB automatically take the user to the next step when they are completed. Otherwise the **Continue** button can be pressed when all of the functions on a page have been utilized. While building the menus, standard buttons such as **Start Over**, **Help** and **Exit** are always available to the user.

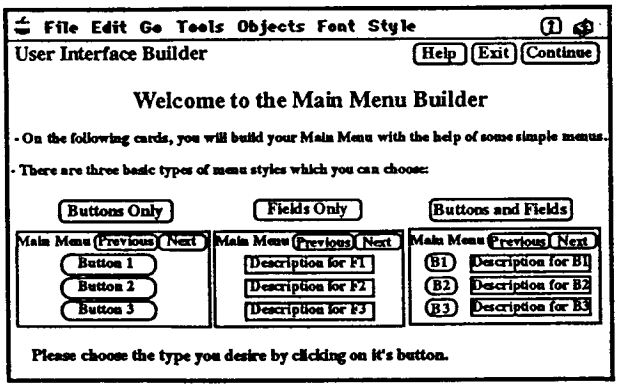

Figure 8. Menu choices in the User-Interface Builder

The basic user-interface contains a set of push-buttons which provides the user with certain standard navigational functions such as **BackTrack**, **Previous**, **Next**, **Exit**, and **Main Menu**, as shown in Figure 9. A set of buttons are also included to provide the user with the ability to build links to the knowledge-based system.

7. Conclusions and Future Plans

7.1 Concluding Remarks

During Phase I, a prototype KBSD was constructed with the following features: knowledge acquisition, knowledge verification and validation, rule writing, user-interface construction, and hypertext document building. The system is reliable, easy to learn, easy to use, and produces heuristic rules which are comparable to those written by an expert. The prototype KBSD establishes the feasibility of the proposed concept.

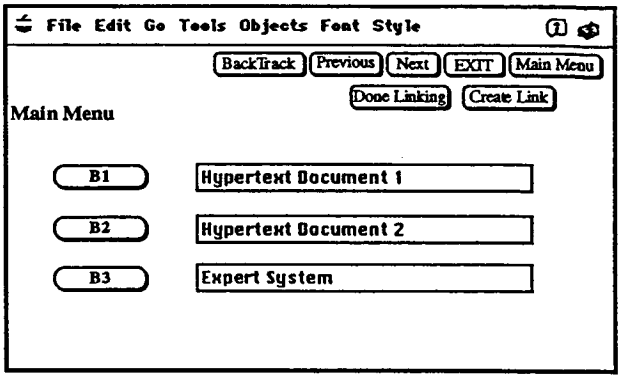

Figure 9. A sample product user-interface

The KBSD has great commercial potential. It can be used for any application for which a knowledge base can be built and utilized. The KBSD shell will provide an effective and cost-efficient tool for the development of advanced knowledge-based systems for aerospace applications. It will provide a marketable software shell which alleviates the need for knowledge engineers and increases productivity in the workplace, therefore make knowledge-based systems available to a large portion of industry.

7.2 Future Plans

A Phase II proposal for continuing to develop the KBSD has been submitted. The objective of Phase II is to develop the prototype KBSD into a full knowledge-based system building software shell. Figure 10 shows an overview of the structure of the final KBSD. The KBSD will have the following main components and features:

1. **A Knowledge Acquisition and Expert System Builder (KA-ESB) with a graphical working environment including three windows:**

   (1). Object window:

   - An editable object window with object addition, deletion and editing.
   - Automatic retrieval of related objects for new topics from a relational database of objects, sorted by topics and key words.

   (2). Conceptual-tree window:

   - Ability to point-and-drag objects from the object window to the conceptual-tree window to create nodes, with automatic prompting for node properties upon creation.
   - Capability to create, cut, copy, and paste nodes and node groups in the conceptual-tree window.

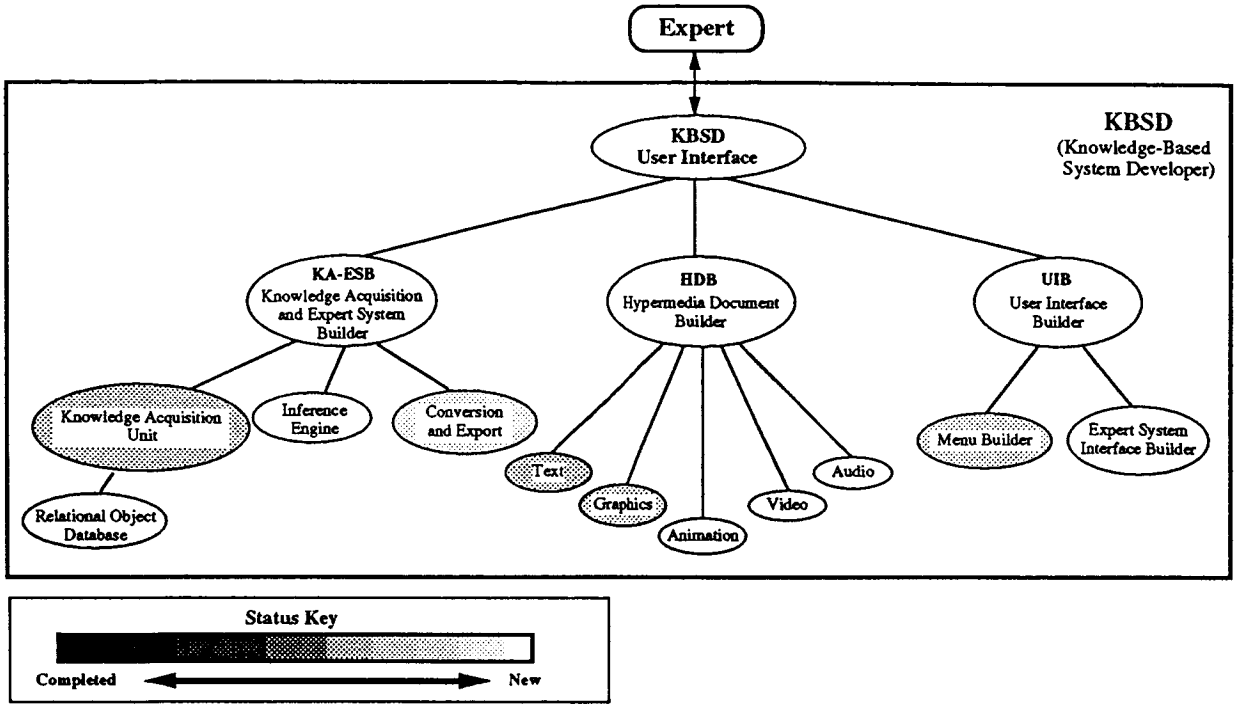

Figure 10. Overview of the KBSD

- Ability to make a link between two nodes in the tree by clicking on each.
- Capability to move a node group in the conceptual-tree while keeping its links intact.
- Capability to save, recall and edit a conceptual-tree for a topic.

(3). Rule-writer window:

- Capability to compose rules for a node group or a single node.
- An induction table for creating multiple rules for a single node structure.
- Range reminders for variables.
- Capability to handle probabilities.

(4). An inference engine for testing and running the product expert systems

(5). Export capabilities:

- Capability to export rules to several commercial expert system shells.
- Capability to convert the expert system to run under other commercial shells.

2. A Hypermedia (interactive multimedia) Document Builder:

- Automatic incorporation of standard document structure and hyper-links into the product document.
- Capability to build custom hyper-links and notes.
- Capability to include video/audio and animation sequences.

3. A User-Interface Builder:

- Capability to build menu-driven system user-interfaces.
- Capability to build custom user-interfaces for expert systems.

8. References

1. HyperCard 2.0, Apple Computer Inc., 1990.
2. LEVEL5 Expert System Software, Information Builders, Inc., 1988.
3. Gaines, B.R. and Marc Linster, "Integrating a Knowledge Acquisition Tool, an Expert System and a Hypermedia System," International Journal of Expert Systems, Vol. 3, No. 2, 1990, pp. 105-130.

SSME PROPELLANT PATH LEAK DETECTION

54-28

N96-16944

L. M. Smith* and W. A. Hunt†

University of Tennessee – Calspan
Center for Space Transportation and Applied Research
University of Tennessee Space Institute
Tullahoma, Tennessee 37388-8897

ABSTRACT

Initial research established that the occurrence of a leak in the powerhead of the Space Shuttle Main Engine (SSME) is accompanied by a sudden, but sustained, change in intensity in a given region of an image. Based upon this, temporal processing of video images on a frame-by-frame basis has been used to detect leaks within a given field of view. The leak detection algorithm developed in this study consists of a digital highpass filter cascaded with a moving average filter applied at each point in the image field. The absolute value of the output is then averaged over the full frame to produce a single time-varying mean value estimate that is indicative of the intensity and extent of a leak. Recent work has included the processing of an extensive amount of data obtained from NASA MSFC to verify the performance of the leak detection system. Further research is being conducted on applying the leak detection algorithm to anomaly detection in the SSME exhaust by means of three channel color processing as opposed to single channel monochrome processing in the case of the leak detection system.

INTRODUCTION

Detection of leaks from the Space Shuttle Main Engine (SSME) during test firing is an important step in preventing possible failures. Ruptures of high-pressure lines and internal components due to thermal shock, mechanical stress, erosion, and material fatigue often result in failure modes with sufficiently long time constants to allow detection and safe shut down. The fields of imaging and image processing technology provide the hardware necessary for visual and infrared observation of these phenomena and the computing capability required for processing the signals and automatically detecting the occurrence of a leak within the field of view.

Thus, a system for detecting leaks from images acquired sequentially during test firing in real time is of value to the development of the program and is realizable with current technology. This study has investigated this approach and established its feasibility and applicability to the program.

In previous work, Shohadaee and Crawford [1-2] concentrated on establishing the feasibility of observing hot or cold leaks using infrared imaging. The theoretical models developed were used to predict radiation transport in absorbing, emitting and scattering media. These models predicted the intensity of both background and plume radiation reaching a sensor location, and were used for designing validation experiments. The feasibility of infrared detection of leak plumes was demonstrated in these experiments, as both hot and cold leaks were readily detected as measurable intensity changes by the sensor.

To detect a leak, the temporal aspects of the process must be considered. The time variation of the image intensity at a point within the area of a leak is a sudden, but sustained, change and, therefore, should be similar to that of a step function, although other smaller intensity variations are also present due to normal operating conditions. The problem becomes that of detecting a step function in the presence of additive noise.

Previously in this study, a step/leak detection processing algorithm was developed that quickly and automatically detects a step-like change in intensity in a sequence of images [3-4]. Temporal processing is carried out at each point in full-frame digitized video data. The system consists of a causal, recursive high-pass filter that removes slowly-varying background intensities cascaded with a moving average filter that accumulates transmitted sustained changes. The absolute value over the full output frame is averaged to produce a time-varying mean value indicative of the level and spatial extent of a leak.

This algorithm has been implemented on a general purpose digital image processor and successfully applied to experimental laboratory and actual test-stand firing data processed off-line at reduced framing rates [5]. A PC-based system capable of real-time processing has been specified with commercially-available add-in cards utilized where possible [6].

* UTSI/CLA/CSTAR, Assistant Professor of ECE

† UTSI/CLA/CSTAR, Graduate Research Assistant

Most recently, work has concentrated on refining and streamlining the processing and on establishing a database of test-stand data to verify system operation under a variety of conditions.

In the past year a considerable amount of video data of SSME tests was obtained from NASA MSFC for processing in the laboratory. The data on these particular tests had no known leak occurrences. This enabled the creation of a database of results from processing by the algorithm in the absence of anomalous events. From this data, a good idea of the performance characteristics of the algorithm for instances where no leaks occur was gained, and showed that the probability of false alarm is sufficiently low for actual applications. Other data that recorded the occurrence of a leak had previously been obtained from NASA. This data was processed several times to examine the useful range of the algorithm parameter for actual implementation to the detection of leaks while reducing the noise effects.

The following section provides a background presentation of the leak detection algorithm and discusses the implementation specifications for real-time digital image processing equipment. The section after that discusses work performed in the previous year in processing test-stand data. Present and future work efforts are next presented. A summary and conclusions are given in the final section.

BACKGROUND – THE LEAK DETECTION ALGORITHM

Video images are an inherently discrete signal with a sampling rate of 30 Hz for standard television format. Therefore, techniques of digital signal processing are directly applicable to the analysis. A detailed derivation of the step detection algorithm used in this study was given in reference 4 along with a numerical analysis of its performance. For completeness, a brief description of it is presented here.

While the overall processing can be integrated into a single system, it is conceptualized by the following component blocks. A highpass filter is applied to remove the constant or slowly-varying background intensity level. Then, a moving average filter accumulates any sustained changes transmitted through the highpass filter. The absolute value of the output from the moving average is taken to allow for detection of positive or negative intensity changes, and the pixel values of the output image are summed or averaged over the field of view to produce a single time-varying quantity indicative of the extent and intensity of a leak.

The highpass filter/moving average cascade system implemented at each point in the field of view can be realized via the following difference equation

$$y(n) = \beta y(n-1) + \frac{\beta+1}{2}\left[x(n) - x(n-N)\right], \tag{1}$$

where $x(n)$ is the input sequence, $y(n)$ is the output sequence, n denotes the sample index, N is the number of terms in the moving average, and the cutoff frequency of the filter is determined by choice of the pole value β. As was shown in reference 4, the optimal choice of N for a given β that maximizes signal-to-noise ratio is given by

$$N = -\frac{1.2564}{\ln \beta}. \tag{2}$$

This condition sets the memory requirements of the system in terms of previous input images that must be stored.

Once this filtering is carried out at each point in the image, the absolute values of the result are summed and averaged over the field of view to produce a single time-varying sequence that is indicative of the general health of the SSME. This time-varying value can then be compared to a pre-set threshold to determine a "red-line" condition for shutdown.

This general algorithm has been implemented on a PC-based image processing system and tested with both laboratory and actual test-stand data. The processing rate of the present system is limited to approximately 1 video frame/second, therefore necessitating that data be acquired and played back off-line with a laser videodisc recorder. For real-time implementation, a system with memory for approximately 16 previous frames and a processing throughput of 37 million operations/sec is required. Thorough hardware/software specifications for a system capable of processing standard RS-170 video signals with this method has been completed [6], thus indicating the realizability of such a system with current technology.

APPLICATION TO TEST STAND DATA

The system for leak detection has been implemented in the laboratory using a PC, a PC-based frame grabber board, and a laser disc recorder. The laser disc player is ideally suited for this application for two reasons. First is the fact that each frame of video data is stored as a separate digital image and can be played back in a jitter-free single-step mode. The second reason is that the laser disc recorder has a built-in standard RS-232 serial communications port for PC interfacing. This allows exact control of the recorder by computer.

The software that implements the algorithm was written in FORTRAN and uses subroutines provided

with the frame grabber card for image processing. As each frame is processed, the program must advance the laser disc recorder to the next frame. This requires the transmitting of commands via the serial communications port. In the past this was accomplished by using a FORTRAN command, but problems were encountered using this method. At times a loss of synchronization between the computer and the laser disc recorder occurred.

To overcome this synchronization problem, an assembly language subroutine was written to provide exact control over the transfer of commands between the laser disc recorder and the computer through the serial port. It was also hoped that the processing speed of the software would be enhanced by eliminating some of the overhead encountered by using a FORTRAN command to access the port. The assembly language subroutine did eliminate the synchronization problem, but offered no significant increase in processing speeds.

In the past year a considerable amount of data was obtained from the NASA Marshall Space Flight Center (MSFC) in the form of VHS video, transcribed onto video laser disc, and processed to establish a database for verification of effectiveness of this system. The video data obtained was from SSME Technology Test Bed (TTB) tests 30, 31, 32, 35, 36, and 37. These TTB tests were conducted over a period of months in 1992. The video data for each test included views of the powerhead and exhaust from various points about the engine totalling about eight or nine different view points. The video footage for tests 35 and 37 was transcribed to laser disc and processed. Each of these TTB tests lasted for a period of eight to nine minutes resulting in the recording of over 16000 frames per camera position. No leaks occurred during any of the tests received from MSFC. Processing times of approximately four hours per view were encountered during processing.

Figure 1 displays a plot of the results of processing video footage of test 37 with a view of the powerhead section of the engine. The recording of the test began before engine ignition and continued until after engine shutdown. Because it is the nature of the algorithm to detect sudden sustained step-like changes, anytime there is a large sustained change in the image, it will show up in the output of the algorithm or more exactly in the mean value output. The large spike in the early frame numbers is a result of the engine startup, which creates a large sudden change in the image. The same is true when the engine shuts down as can be seen by the large spike toward the end of the test. Thus for practical application of the leak detection system described herein, the system would have to have some manual override option during ignition and shutdown to avoid the occurrences of false detections. The smaller variations that can be seen between the startup and shutdown spikes are the result of noise. Figure 1 is representative of the other views of the powerhead and the results obtained from both tests 35 and 37.

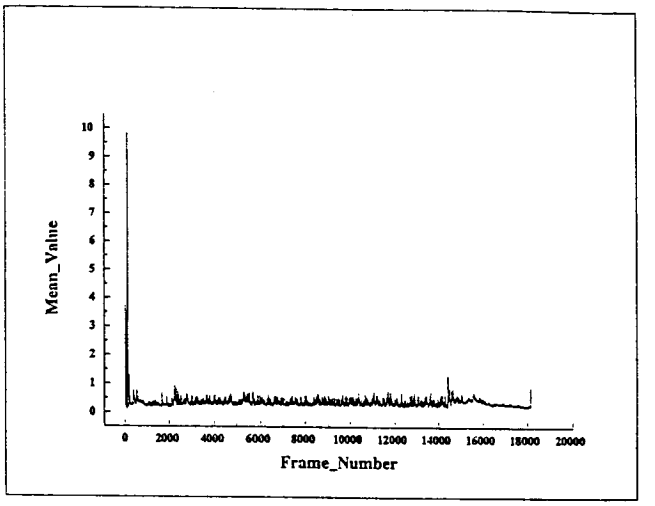

Figure 1. Typical plot of output gray level mean value versus frame number (time) for SSME test 37.

To experimentally determine the effect of varying the pole location β, a portion of a test where a leak had occurred was processed several times with different values for β each time. The resulting mean values were plotted versus the frame number for each case. The plots for β equal to 0.5, 0.759, and 0.91 are shown in Figure 2(a), Figure 2(b), and Figure 2(c), respectively. The intent of this investigation was to determine the value of β that would yield the best system performance for video footage of actual tests.

Video data with a recorded leak occurrence was previously obtained from NASA and is designated test 215. A frame sequence of 200 frames in a region of video data where a large "glitch" in the video signal and a leak was known to have occurred during test 215 was processed by use of the system previously discussed. By analyzing the video visually frame by frame, the glitch was found to occur at frame 100, the leak was established to occur at frame 122, while a fire appears around frame 160. This particular test was filmed using a high speed camera that had a framing rate of about 64 frames per second as compared to the RS-170 standard of 30 frames per second.

As previously stated, the pole location β not only determines the frequency cutoff of the highpass filter, but also determines the number of terms, or in this case, frames in the moving average filter by (2). As it can be seen from Figure 2 as β is increased, the effects of noise are decreased. The amplitude of the

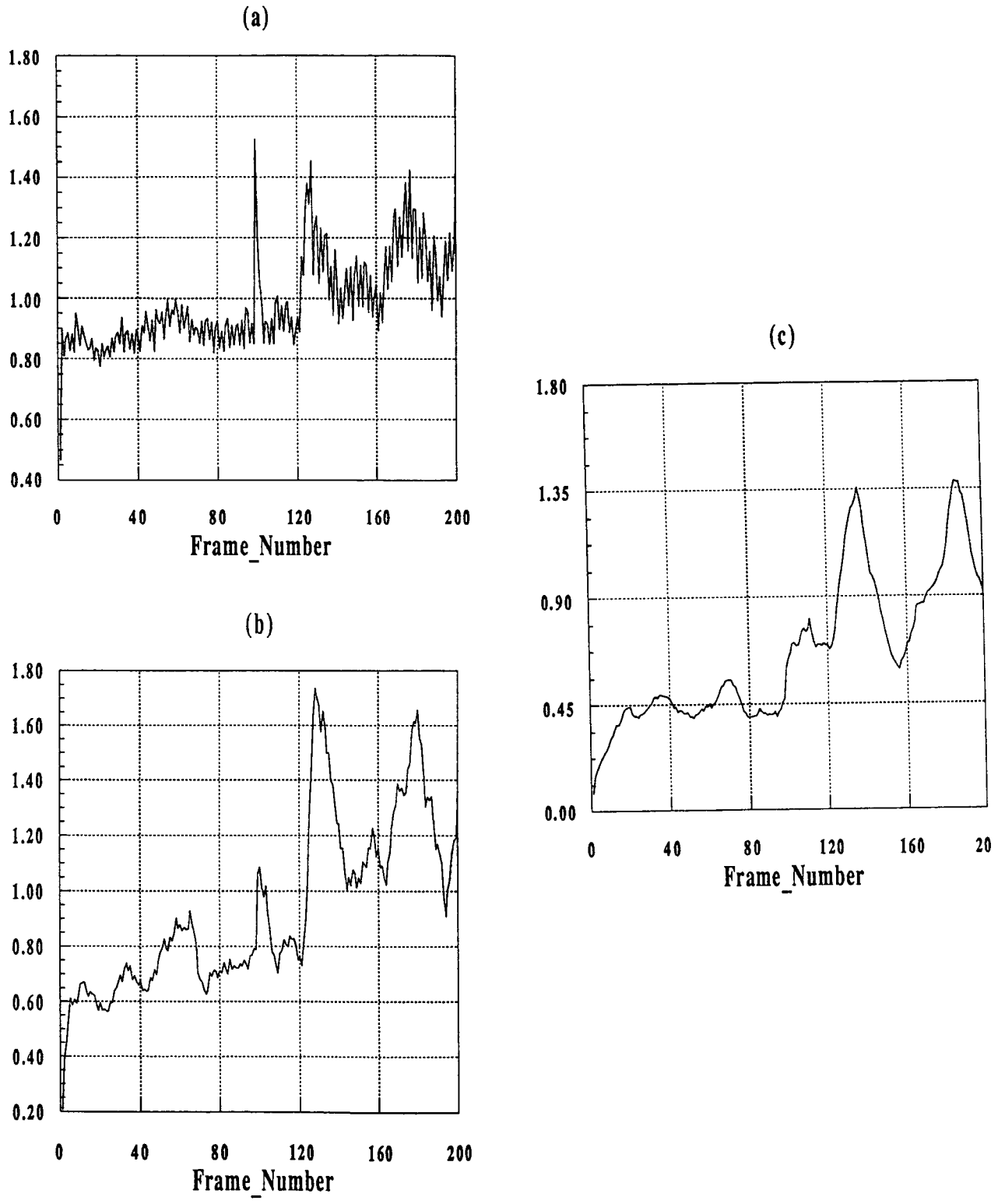

Figure 2. Effect of varying pole value β on sensitivity of the algorithm to anomalous events and noise. (a) $\beta = 0.5$ (b) $\beta = 0.76$ (c) $\beta = 0.91$.

spike caused by the video glitch in Figure 2(a) is larger than that caused by the leak occurrence. The β used to process this data was 0.5 which means that two frames were part of the moving average. As β was increased to 0.759 which corresponds to five frames in the moving average, the effects of noise were decreased. Note that in this case the amplitude of the video glitch spike is below that of the spike caused by the leak occurrence, yet the amplitude is still significant. In Figure 2(c), β has been increased to 0.91 which means that there were thirteen frames as part of the moving average. The noise in this case has been significantly reduced. Notice that as β was increased, the amplitude of the spike corresponding to the leak occurrence had been reduced and the maximum amplitude of the spike occurred later. Though the leak spike had been reduced in each case, the difference between the leak spike and the level due to noise had increased. Thus by using a larger value for β, the possibility of a false detection due to noise would decrease while the amplitude of the leak spike would decrease and occur later.

From this analysis, it was concluded that pole values near 0.9 will be required for actual test-stand processing. This in turn sets the data storage requirement of the system in excess of ten frames, which is still within the capabilities of the specified real-time operating system.

PRESENT AND FUTURE RESEARCH

Another relevant area of application for the basic algorithm being investigated is in the detection of internal component failure in the SSME. As internal components of the SSME begin to deteriorate due to various stresses there is a substantial increase in certain metal concentrations in the engine exhaust. When one particular metal, copper, enters the exhaust due to one of these failures, the exhaust can undergo a distinct visible color change. Because this color change is a step-like change, the algorithm used for leak detection is also applicable here.

In the original procedure for detecting leaks, only a monochrome image was considered. Each frame was an image described by only the pixel location and corresponding intensity. A color image, however, is not described by one intensity value but three. Each pixel will have a separate intensity value for red, green and blue colors. The intensity of each of these colors determines the broadband spectral content of that pixel.

As in the case of the monochrome image, the color pixels that make up the view of the exhaust will tend to remain constant or only slowly vary during the operation of the engine and thus the algorithm can be applied to each of the three color intensities separately. Instead of having three separate threshold levels, the output of each channel will be squared and a weighted sum computed to determine the overall time varying signal to compare with a threshold for the "red-line" condition.

At present, numerical trials are being conducted to establish the viability of this technique and methods for choosing the threshold condition to control sensitivity and probability of error. A Monte-Carlo analysis will be performed on several sets of computer-generated signals with known noise levels to determine the range of detectable changes as a function of noise level. Further work will apply this method to laboratory experiments in which color changes in simulated exhaust plumes will be produced, recorded in three-color video format, and processed.

CONCLUSIONS

The leak detection algorithm has been shown to perform as expected. The algorithm has been shown to be robust, will detect changes in noisy images, and is not prone to false detections during operation. With respect to other means of leak detection, this system is advantageous in terms of implementation. The factors that determine whether or not the system is practical have been met. The system will perform in real-time using existing off-the-shelf components, minimizing false detections due to noise, and most importantly, detecting leak occurrences.

Due to the nature of the breakdown of internal components of the engine, it is hoped that the same algorithm that is used to determine gas leaks in the engine can be modified to detect when certain materials in the exhaust have reached abnormal levels using three-color video processing. The appeal of this method is that its measurement devices, video cameras, are already in place and are more rugged than standard spectrometers. Thus, this method would be relatively inexpensive to implement compared to other spectrographic methods. Present and future efforts will be directed toward numerical and laboratory experimental trials to verify the applicability and effectiveness of this approach.

REFERENCES

[1] A. A. Shohadaee, "Leak detection feasibility investigation using infrared radiation transfer in absorbing, emitting and scattering media," Doctoral dissertation, Dept. of Mech. Engr., Univ. of Tennessee, Knoxville, TN, 1990.

[2] A. A. Shohadaee and R. A. Crawford, "SSME leak detection feasibility investigation by utilization of infrared sensor technology," Center for Advanced Space Propulsion Second Annual Technical Symposium Proceedings, Tullahoma, TN, Nov. 1990.

[3] J. A. Malone, "A system for leak detection using sequential image processing," Master's, Tennessee, Knoxville, TN, 1991.

[4] J. A. Malone and L. M. Smith, "A system for sequential step detection with application to video image processing," *IEEE Trans. on Industrial Electronics*, Vol. IE-39, pp. 277-284, Aug. 1992.

[5] J. A. Malone, L. M. Smith and R. A. Crawford, "Detection of leaks from the space shuttle main engine using sequential image processing," submitted to *IEEE Trans. on Industrial Electronics.*

[6] L. M. Smith and B. W. Bomar, "Digital image processor system specifications for real-time SSME leak detection," unpublished report to sponsor, NASA Grant NAG8-140, July 1992.

CSTAR TECHNICAL SYMPOSIUM
SPACE TRANSPORTATION

C

omit

COMET: First Mission Progress

Separation Dynamics of the Comet Freeflyer and an Upper Stage Star48V Motor

CSTAR Support for the Commercial Launch Voucher Demonstration Program

WCSC Environmental Process Improvement Study and Demonstration Program

The Castor 120™ Motor: Development and Qualification Testing Results

Laser Material Processing

Artificial Intelligence/ Expert Systems

Space Transportation

Computational Methods

Chemical Propulsion

Electric Propulsion

COMET: First Mission Progress[1]

N96-16945

J. F. Pawlick[2], E. G. Allee[3], and C. H. Myers[4]

University of Tennessee - Calspan
Center for Space Transportation and Applied Research (CSTAR)
UTSI Research Park
Tullahoma, TN 37388

Abstract

The COMmercial Experiment Transporter (COMET) is a set of hardware and related infrastructure used to support orbital experiments of the Commercial Centers for the Development of Space (CCDS's) and their industrial partners. During the three years since the program started, contracts have been signed, design reviews conducted on all components, experiments selected for the first mission, all hardware has been manufactured, the first phase of integrated testing of the satellite, the experiments, and the Launch Facility have all been completed.

The program experienced several delays in 1993. A component failure in the Service Module during preparation for environmental testing in January resulted in an eight-week delay for the Service Module part of the FreeFlyer. Discovery of large overruns of the mass budget required a major revision of the mission profile for COMET 1. In spring of 1993, Space Industries Incorporated (SII) and Westinghouse stopped work because of a lack of funds. EER continued to work toward completion of their launch systems. SII and Westinghouse resumed work in September 1993. Since resumption of work, a technical review of all systems to ascertain their state of readiness has been completed. No major problems were discovered. All systems are proceeding toward a launch date in the first quarter of 1994.

COMET Overview

The COMET FreeFlyer (Figure 1) will be launched with CCDS payloads aboard both the Service Module and Recovery System into a 250 nm circular orbit from the Conestoga Launch Vehicle.

The non-recoverable Service Module will contain about 15 cubic feet of payload volume while the Recovery System will have about ten cubic feet. Command and control of the FreeFlyer and experiment data communications will be through the Commercial Payloads Operations Control Center (COMPOCC) in League City, TX.

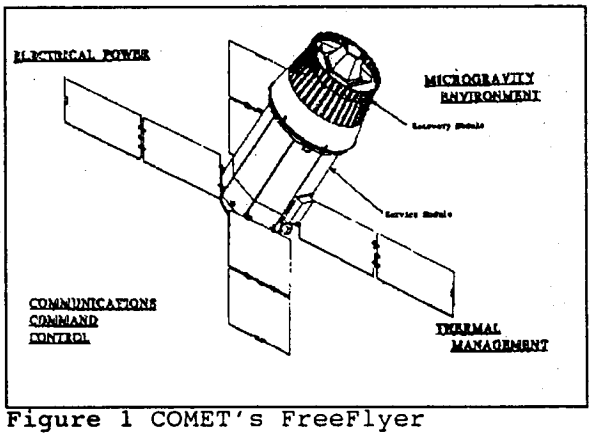

Figure 1 COMET's FreeFlyer

---

[1] This work is supported by the Center for Space Transportation and Applied Research (CSTAR) under NASA Grant NAGW-1195.

[2] CSTAR/UTSI, Associate Director of Space Transportation

[3] CSTAR/Calspan, CSTAR COMET Program Manager

[4] CSTAR/Calspan, Operations Analyst, Systems Engineering Monitor
Other Contributors Include:
Dr. F. Wessling, CMDS, University of Alabama, Huntsville
Dr. M. Robinson, BioServe, University of Colorado
Mr. R. Martinez, CSP, Texas A & M University
Mr. T. Gallimore, CMC, University of Alabama, Birmingham
Mr. N. Combs, SVEC, University of Houston

The Recovery System will separate from the Service Module after about a month in orbit and will be recovered near the Great Salt Lake Desert in the Western Test and Training Range (WTTR).

During the period of April 8, 1991, through October 30, 1993, the COMmercial Experiment Transporter progressed from Authorization to Proceed for the Contractors, through Critical Design Reviews, fabrication, and initial testing.

The Service Module has undergone extensive testing, including an integration and test program at League City, TX. The Recovery System has followed almost the same path, and it has completed an initial series of integration tests with the Service Module in League City, TX. The COMPOCC was used throughout the integrated testing at League City to command and control the Service Module, experiments, and Recovery System. Experiments were installed into the Service Module and Recovery System for the tests.

The Launch Vehicle is essentially complete. The Castor and Star motors have been delivered to Wallops Island, VA, the flight avionics mounted to the Payload Attach Fittings (PAF) are completing testing, and the Interface Module and the FreeFlyer are proceeding toward a joint acoustic test at Goddard Space Flight Center, MD. The Flight and Ground Software has completed testing. The Launch Complex, started in July 1992, is ready for the first launch of COMET.

The next major step will be full integration and testing of the FreeFlyer and experiments at a Westinghouse facility outside Baltimore, MD. In addition to the integrated checkout of the systems, mission simulations will be conducted to exercise all systems, experiments, and personnel in as realistic a situation as possible.

COMET Status Update

Following is an update on the status of the COMET Program.

Launch Vehicle

The Launch Vehicle has progressed from the initial design stage into the Conestoga 1620 depicted in Figure 2. The core motor is a Castor IVB with thrust vector control. Attached to the core motor are two Castor IVA's and four Castor IVB's. On top of the core motor, the fourth stage motor is a Star 48V with thrust vector control.

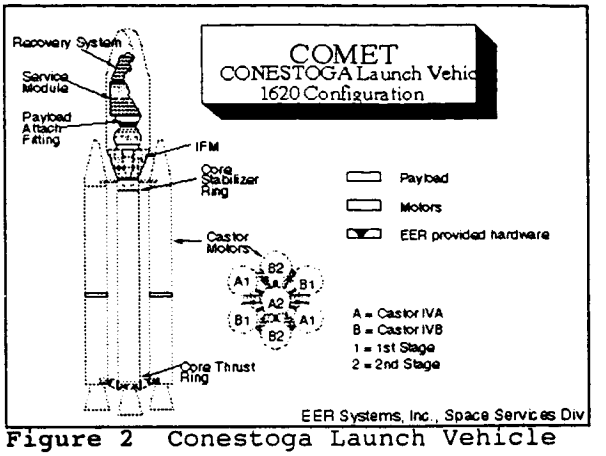

Figure 2 Conestoga Launch Vehicle

The Launch Complex was completed at Wallops Island this summer. It will support the Launch Vehicle on a pedestal approximately 15 feet off the pad. Two clam shells will close around the vehicle to allow easy, air-conditioned access to the experiments and function as work platforms for assembly and checkout of the Launch Vehicle. The facility is designed to support the T-6 hours experiment late access requirement for loading perishable experiments. Flight software has completed simulated trajectory runs using the Marshall SFC rate table and a Kearfott IMU similar to the one used for the flight vehicle. Results show that the Launch Vehicle should easily make its $\pm$ 50 nm tolerance on orbital insertion. The COMET Launch Control System (CLCS) is undergoing final tests and verification. The system scans numerous sensors on the pad and in the vehicle and will rapidly flag any off-nominal condition to the launch control team. The CLCS also identifies conditions where groups of data taken together indicate problems. All mechanical and electrical launch vehicle assemblies are completed and have been integrated with the Launch Vehicle. Avionics assemblies are undergoing integrated testing.

Kitting of ordnance is in progress at Wallops Island, VA. The Launch Vehicle upper stack (the Interface module, and the PAF) has undergone EMI testing at Goddard. Next step is accomplishing acoustical testing with the Service Module.

Information continues to be provided to the Department of Transportation (DOT) in support of mission licensing. Recent changes in the Space Launch Act may again cause changes in mission licensing guidelines.

Service Module

The Service Module (Figure 3) has had more than its share of problems this year. After successfully completing the first integration and test program in League City, TX, it was shipped back to Westinghouse near Baltimore for environmental tests. During assembly for the tests, an internal electrical short damaged numerous circuit boards. The cause of the short was not immediately obvious. Finding the origin of the short and repairing the damage resulted in a delay of approximately eight weeks.

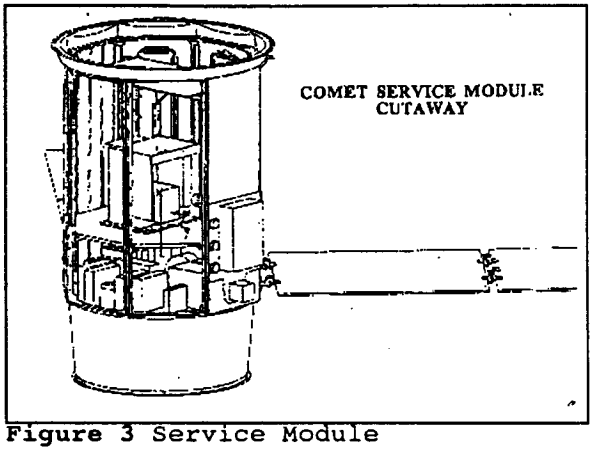

Figure 3 Service Module

After completion of repairs, the Service Module underwent random vibration testing in all axes. Several problems were encountered and fixed. One of the positive results of the test was the low frequency vibration levels (below 10 hz) experienced by the IMU was much less than had been anticipated. This resulted in a decrease in random noise level output by the IMU and a corresponding decrease in orbital insertion uncertainty.

Discovery of an out-of-spec weight condition revealed the Service Module to be approximately 120 lbs over its mass budget. In order to complete a usable mission, a weight reduction program has been instituted and the COMET's first mission orbital altitude has been lowered. With a resumption of work by Westinghouse, the Service Module has completed vibration and thermal cycle testing, integration with launch vehicle avionics, and is being prepared for thermal vacuum testing.

Recovery System

The Recovery System (Figure 4) is essentially complete. Avionics supplied by the SouthWest Research Institute have been integrated into the flight system along with SII supplied software.

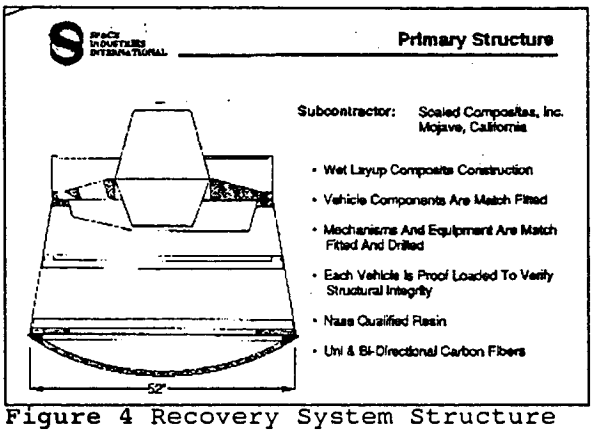

Figure 4 Recovery System Structure

After integration and test, the Recovery System proceeded with software and electronics modifications. These were identified during interface tests with the Service Module, Orbital Operations, and the experiments. Problems encountered ranged from software interface and ground loop problems to avionics lock ups. These problems were reworked and a mini integration and test was held in March 1993 with one of the experiments.

Vibration testing indicated the resonance frequency response of the Recovery System is lower than desired by about 5 hz. This lower resonance point is of concern in terms of dynamic clearance with the shroud during launch; however, it is believed to be related to the test set-up and is being investigated.

Work also continues with the Department of Transportation on the license requirements for the Recovery System. The Recovery System is scheduled to land at the Western Test and Training Range in Utah 30 days after launch. The Recovery System deorbit sequence is shown in Figure 5.

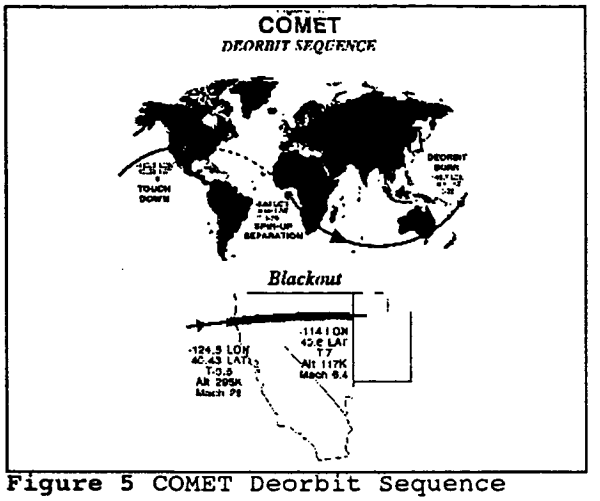

Figure 5 COMET Deorbit Sequence

Overall, the Recovery System will be ready for the next integration and test program in January 1994.

Orbital Operations

The COMPOCC has reconfigured its software based on the results of the integration and test at League City. Some COMPOCC software interfaces were found to be configured to previous versions of Service Module and Recovery System software. This software had to be modified to incorporate new commands and interfaces. All changes have been programmed and tested. As the result of several COMPOCC computer crashes during last year's integration and test program, Orbital Operations procured and installed a front-end data recorder. The recorder will allow full data capture of all telemetry. Thus, if the COMPOCC experiences a failure during a pass, the information will not be lost. Typical ground tracks for COMET are shown in Figure 6. The COMPOCC is ready for final integration and testing.

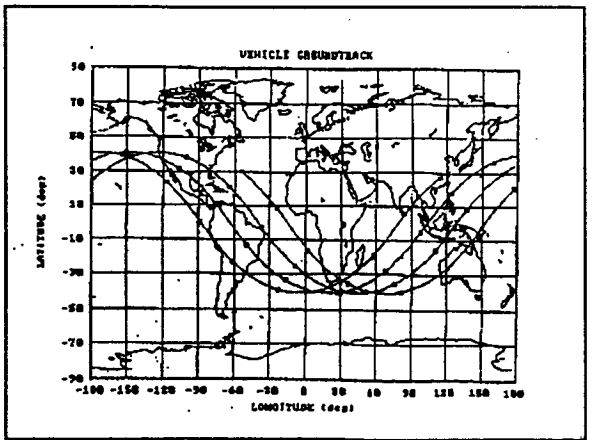

Figure 6 COMET Typical Ground Track

Experiments

All experiments have completed integrated testing in League City, TX, with the Service Module, the Recovery System, and the COMPOCC. Experiment location is shown in Figure 7.

Following are the experiments manifested for COMET Mission #1:

Recovery System

[1] Biomodule (Penn State).
[2] Non Linear Organic Thin Films and Crystals (University of Alabama at Huntsville).
[3] MDA Minilab (University of Alabama at Huntsville).
[4] Animal Autonomous Space Support Module (BioServe Space Technologies).
[5] Plant Autonomous Space Support Module (BioServe Space Technologies).
[6] Protein Crystal Growth-Batch (PCG-M) (University of Alabama at Birmingham).
Utility - Acceleration Measurement System (AMS) (Universtiy of Alabama at Huntsville).

Service Module

[7] Oxygen Atom Flux Monitors for Spacecraft (SURSAT) (CMDS).
[8] Frozepipe (Frozen Heat Pipe Experiment) (Texas A&M - Center for Space Power).
[9] LEOEX (Low Earth Orbit Communications) (Florida Atlantic).

- Biomodule is a cellular growth experiment.
- MDA, NLO, and PCG-M are all experiments dealing with the growth of crystals in a microgravity environment.
- SURSAT is an atomic oxygen flux monitoring experiment desiring proximity to the atomic oxygen present in Low Earth Orbit. It will be placed on the outside surface of the Service Module, in the ram direction, and will remain in operation for the duration of the spacecraft's orbital lifetime.
- Frozepipe is an experiment measuring the performance of heat pipes during extreme temperature variations. It is manifested to be installed on one of the outside experiment panels.
- LEOEX is a communications experiment testing various communication configurations in anticipation of future communications satellites.
- AMASS and PMASS deal with plant and small animal tissue changes that occur in a microgravity environment.

The weight growth of the Service Module has made COMET 1 unable to reach the desired 300 NM orbit. Because the resulting 250 NM orbit could leave the Autonomous Rendezvous and Docking Experiment (ARD) in too low of an orbit by the launch of the second COMET in two years (required for docking), ARD decided to withdraw from the COMET 1 mission.

One other component on the Recovery System is being provided by a CCDS, but is being flown as a utility on COMET. The University of Alabama at Huntsville is providing microgravity measurement equipment, similar to that flown on the Consort missions, to quantify microgravity disturbances during the mission. This is of particular importance to the crystal growth experimenters who need to know the microgravity conditions very accurately.

Communication with the FreeFlyer and the experiments was successfully performed through the Service Module command control and telemetry system via the COMPOCC.

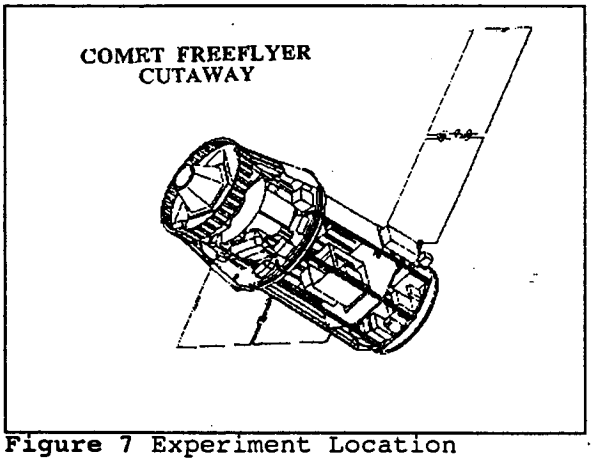

Figure 7 Experiment Location

Programmatic Issues

In Spring of 1993, Westinghouse and SII notified CSTAR that they would stop working on COMET because of a lack of additional funds in FY93. After extended negotiations, an agreement was reached allowing a short term re-allocation of funds within the contracts. SII and Westinghouse resumed work in September 1993.

During negotiations, the COMET team took the opportunity to address some programmatic issues that had become evident during the progression of the program. The major problem was there was no one point of authority among the contractors to resolve interface problems between the various companies. To address that issue, the COMET contractors established a COMET Contractors Program Manager's office. The contractors signed a Memorandum of Understanding giving this manager the authority to work across company lines to resolve any interface issues and accomplish the mission.

Summary

COMET has had an eventful year. The program has weathered several setbacks; however, it is moving forward again. Testing of individual systems is essentially completed. Problems have been identified and corrected. In addition, the first integration and test program involving both the FreeFlyer and the experiments has been successfully completed. The next major milestones before heading for the launch pad are joint environmental testing of the Launch Vehicle components, Service Module, and Recovery System. The system and experiments will then undergo final integration and testing. This last integration and test sequence will include mission simulations to exercise all systems, including experiments, in the same configuration as they will be operated on orbit.

After these tests are successfully completed, COMET will be launched from Pad 0 at Wallops Island, VA, in the first quarter of 1994. About 30 days later, the first land recovery of an unmanned, commercial spacecraft will occur at the Western Test and Training Range in Utah.

With the completion of this first mission, the United States will have an important new commercial capability for accessing the unique environment of space.

List of Major COMET Contractors and Supplies

Service Module

Westinghouse - Prime Contractor
- Defense Systems Inc. - Service Module Manufacturer
- OAO Inc. - Thermal Control System Supplier
- Space Sciences Corp. - Attitude Control Systems
- Kearfott-Siegler - IMU

Recovery System

Space Industries, Inc. - Prime Contractor
- Pioneer - Parachute Systems.
- Scaled Composites - Recovery System structure.
- SouthWest Research Institute - Avionics.

Launch Vehicle
EER Systems, Inc. - Prime Contractor
Morton Thiokol - Motors.
Logicon Control Dynamics - Flight Software.
Altair Aerospace Corporation - Ground Control Software.
Tracor - Fairing.

Orbital Operations
Space Industries, Inc. - Prime Contractor
Space Applications Corporation - Software Development.

Payload Integration
Space Industries, Inc. - Prime Contractor
SouthWest Research Institute - Environmental Testing.

COMET Contractors Program Manager's Office
EER Systems Corp. - Huntsville Division

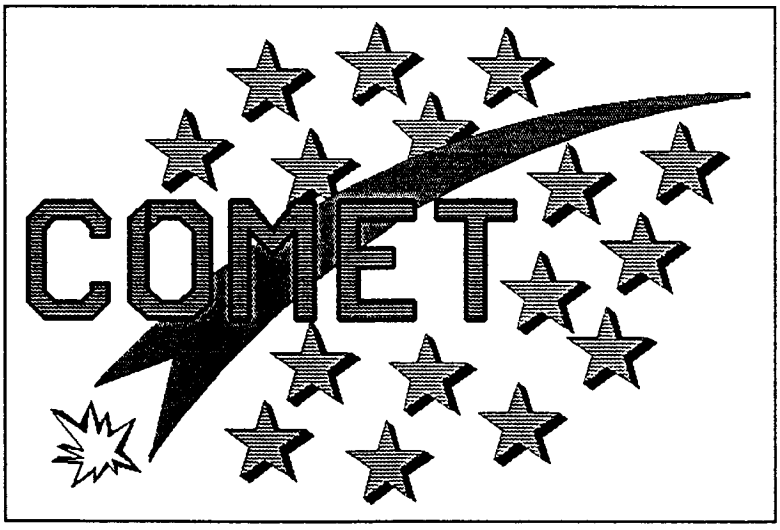

SEPARATION DYNAMICS OF THE COMET FREEFLYER AND AN UPPER STAGE STAR-48V MOTOR[1]

by

Kevin M. Fuller[2] and Carter H. Myers[3]
Center for Space Transportation and Applied Research (CSTAR)
UTSI Research Park
Tullahoma, TN 37388

ABSTRACT

In this report, the orbital separation between a STAR-48V upperstage motor and the COMET FreeFlyer is investigated. The time from nominal STAR-48 engine burnout is to be determined such that the STAR-48 will not collide with the FreeFlyer once the separation process has been initiated. To analyze this separation, the forces acting upon both the FreeFlyer and the STAR-48 are described in a body fixed coordinate system. These coordinates are then transformed into an Euler coordinate system and then further transformed into a relative inertial coordinate system.

From this analysis and some basic assumptions about the STAR-48/FreeFlyer vehicle, it can be concluded that the STAR-48 will not collide with the FreeFlyer if the separation occurs at 120 seconds after nominal burnout of the STAR-48. In fact, the separation delay could be a shorter period of time, but it is recommended that this separation delay be as long as possible for risk mitigation. This delay is currently designed to be 120 seconds and the analysis presented in this report shows that this time is acceptable.

INTRODUCTION

The COMercial Experiment Transporter (COMET) is a commercial space transportation and recovery system developed by a team of contractors and managers from both the private sector and NASA's CCDS program. COMET is intended to carry experiments to the microgravity of a 300 N.Mi. orbit and return a portion of these experiments back to earth in the Recovery Module. This capability makes COMET a unique space vehicle since it can both return experiments back to earth after a 30 day microgravity exposure period as well as expose additional experiments to 130 days of microgravity all within the same mission. With its first planned launch in the Spring of 1994, COMET will become a significant asset to the United States space community.

The upperstage rocket motor that is used to assist COMET into its designated orbit is a STAR-48V solid rocket motor designed by Thiokol. This is a specially designed motor that has a gimballed nozzle in order to control the vehicle during the burn without the requirement of spin stabilization. Thus the COMET vehicle does not have to endure the rigors of spin stabilization as it is boosted into its designated orbit.

The STAR-48 is attached to a Payload Attach Fitting(PAF) so that it can be easily integrated with the COMET vehicle. The PAF is then fastened to COMET by the use of explosive bolts. The connection area between the PAF and COMET contains eight compressed separation springs that are designed to provide the necessary force to separate the two vehicles. When the explosive bolts are fired by the flight computer at the designated time, the compressed springs uncoil and force the STAR-48 to separate from the COMET spacecraft.

There are two conditions, though, that make this simple separation more complex. The first condition is that there is still some thrust being

[1] This work is supported by the Center for Space Transportation and Applied Research (CSTAR) under NASA Grant NAGW-1195.

[2] UTSI, Graduate Research Assistant, COMET Program

[3] CSTAR/Calspan, Principal Investigator

produced by the STAR-48 after nominal burnout. This unwanted thrust acts to offset the separation force provided by the springs and causes the situation where the STAR-48 now has a chance to collide with the COMET FreeFlyer. The easiest solution to this problem is to wait for all of the residual fuel in the STAR-48 to burn up before initiating separation. But this cannot be done because of a time constraint created by a second condition. This condition requires that the separation must occur no later than 120 seconds after the nominal burnout of the STAR-48. This is due to the limited battery life on board the vehicle. With a larger redesigned battery (and therefore a reduction in payload) the separation delay time could be increased long enough for all of the propellant within the STAR-48 to be consumed. But this solution is unacceptable and others should be sought.

There is one more variable that plays a significant role in the separation of the STAR-48 and the COMET FreeFlyer. That variable is the thrust vectoring capability of the nozzle on the STAR-48V. This thrust vectoring might be large enough to start the STAR-48 into a pin wheeling motion that could reduce the probability of a collision. But if the STAR-48 acquires a large enough residual roll, the vehicle will be spin stabilized and the effects of the gimballed nozzle could be offset. It is apparent from these circumstances that further investigation into the dynamics of the system must be undertaken in order to determine if the STAR-48 will collide with the COMET FreeFlyer. It is this deduction that motivates the following analysis.

This analysis begins by determining the forces that act upon both the STAR-48 and the FreeFlyer in a general sense. Once these forces have been determined, it will be seen that they can be easily described in a body-fixed coordinate system, rather than the usual inertial coordinate system. It is this difficulty in describing the forces in an inertial system that adds to the complexity of this problem. Once the equations of motion are determined in the body fixed coordinate system, they can then be transformed into an inertial system so that the separation distances between the STAR-48 and the FreeFlyer can be determined. This is accomplished by transforming the body-fixed coordinate system into a 3-1-3 Euler coordinate system and then transforming this new system into a relative inertial coordinate system. The following analysis is presented in order to clarify this procedure.

EQUATIONS OF MOTION

The general external forces and moments acting upon the STAR-48 and the FreeFlyer are shown in the free body diagram in Figure 1.

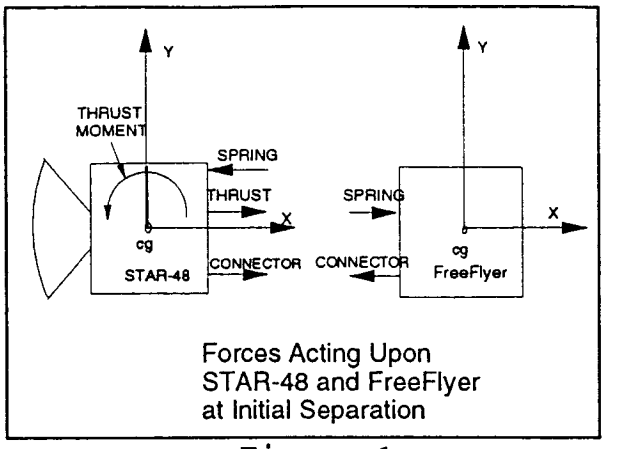

Figure 1

The forces and moments that act upon the STAR-48 and the FreeFlyer during separation are described in a body fixed coordinate system. There are three forces and one moment that act upon the STAR-48, but there are only two forces that act upon the FreeFlyer. The forces on the STAR-48 are due to the separation spring force, an electrical connector force, and the thrust force. When the nozzle on the STAR-48 is gimballed, the thrust force acts both in the +X direction and the -Y direction initially. There also is an additional moment caused by the off-axis thrust force once the nozzle has been gimballed. It can be seen that neither the thrust force nor the thrust moment can be easily described in an inertial reference frame as one steps forward in time. But it can be seen that it is fairly simple to describe both the thrust force and moment in a coordinate system that is attached to the Body. It is because of this that the body-fixed coordinate system is used as a starting point for this problem.

The two forces on the FreeFlyer are due to the separation spring force and the connector force. There is no problem describing these forces in an inertial coordinate system or a body-fixed coordinate system. But it is the thrust force that determines the best coordinate system in which to describe the applied forces and moments. The equations used to determine the values for these forces were determined by Dr. Keith Reiss(Reference 1) and are repeated here for completeness.

Thrust force $= 44.275 * e^{(0.02093204) * t}$

Spring force $= n*Ks*(ds - dsep)$ for $dsep < ds$
$= 0$ for $dsep > ds$

Connector force = Fc for desp > dc
= 0 for dsep < dc

In these equations, t is the time delay since STAR-48 nominal burnout, n is the number of separation springs, Ks is the spring constant, ds is the spring stroke length, dsep is the separation distance of the STAR-48 and the FreeFlyer, Fc is the electrical connector force, and dc is the electrical connector length. From Reference 1, Fc was found to be 20 lbs and dc was found to be 0.2 inches. Once the separation distance between the STAR-48 and the FreeFlyer is greater than the electrical connector action distance, there is no longer a connector force acting upon either the STAR-48 or the FreeFlyer. A similar situation arises in the spring force where there is no longer a spring force acting upon either body once the STAR-48 has separated a distance greater than the spring stroke length. It is assumed that these are the only forces acting upon the STAR-48 and the FreeFlyer throughout the following analysis.

A moment is also applied to the STAR-48 due to the gimballing of the motor nozzle and the thrust force. This causes a pin wheeling effect upon the STAR-48 about the Z-axis in the body fixed coordinate system. This nozzle should be gimballed after the STAR-48 is a safe distance away from the FreeFlyer so that the simple rotation of the STAR-48 does not have a chance to collide with the FreeFlyer. This problem is addressed later in the Assumptions section of this report. The equation to determine the moment on the STAR-48 is:

Thrust moment = d * Thrust force * SIN(γ)

γ is the gimbal angle of the STAR-48 and d is the moment arm measured from the pivot point of the nozzle of the STAR-48 to the center of mass of the STAR-48. The value for d was given as 26.5 inches in Reference 1 and this can be seen in the general configuration of the STAR-48/FreeFlyer in Figure 2. Also, the nozzle is assumed to have a maximum gimbal angle of at least 4 degrees. It will be seen later that this gimballing ability of the STAR-48V nozzle is critical in order to obtain a separation between the STAR-48 and the FreeFlyer without resulting in a collision.

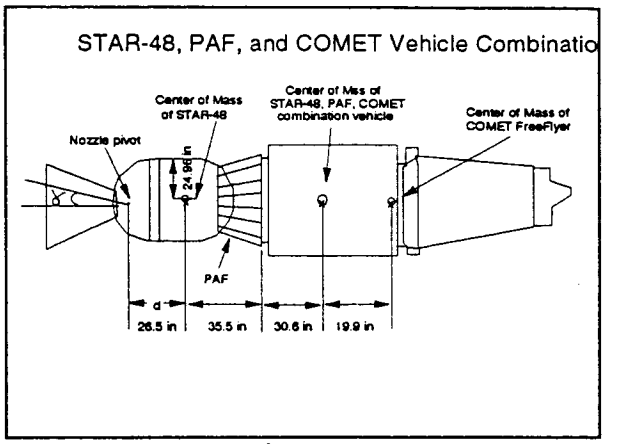

Figure 2

BODY FIXED COORDINATES

In the body fixed coordinate system, the axes are fixed to the vehicles; one to the STAR-48 and the other to the FreeFlyer as shown in Figure 3:

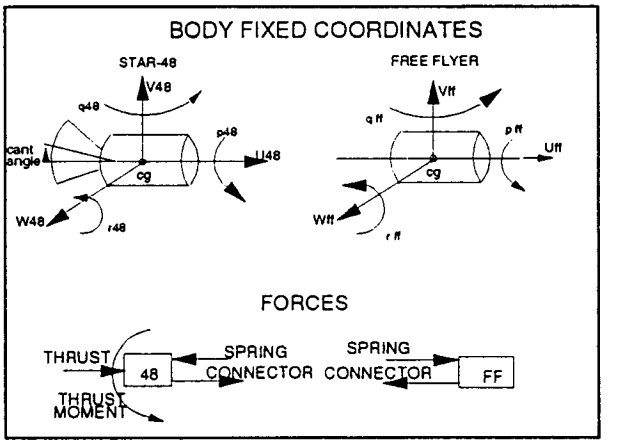

Figure 3

The forces as described previously are easily defined in this system and are given in Cartesian coordinates. There are three force equations each for the STAR-48 and the FreeFlyer and there are also three moment equations each for the STAR-48 and the FreeFlyer. The forces in this coordinate system are defined as follows:

F_{u48} = Thrust force * COS(γ) + Connector force - Spring force

F_{v48} = - Thrust force * SIN(γ)

F_{w48} = 0.0

F_{uff} = Spring force - Connector force

$F_{vff} = F_{wff} = 0.0$

and the moments are:

$M_{u48} = M_{v48} = 0.0$

$M_{w48} = d * \text{Thrust force} * SIN(\gamma)$

$M_{uff} = M_{vff} = M_{wff} = 0.0$

From Newton's equation of motion, F = ma, a second order differential equation can be obtained for the equations of motion in the body fixed coordinate system. One must be very careful when describing the acceleration in these coordinates due to the rotation of the coordinate system. The acceleration in the body fixed coordinates is the derivative of the velocity as measured in a reference coordinate system plus a term to account for the rotation of the body fixed coordinates. The derivative of a vector in a body fixed coordinate system is given by the following equation from Reference 3:

$$V'_{fixed} = V'_{rotating} + \omega \times V_{rotating}$$

$\omega \times V_{rotating}$ is the cross product between the angular velocity of the rotating coordinates and the velocity of the body as measured in the rotating frame. $V'_{rotating}$ is the total acceleration in the rotating frame and V'_{fixed} is the acceleration as measured in a fixed reference frame. ω, as described in the body fixed system in Figure 3, is given in vector form as:

$$\omega = (p)\,i + (q)\,j + (r)\,k$$

i, j ,and k are the usual Cartesian unit vectors in the X, Y, and Z directions respectively and p, q, and r are the angular velocities about these respective axes. Since the body-fixed coordinates are rotating, $V'_{rotating}$ is the acceleration as described in the body-fixed coordinates. By performing the cross product multiplication and solving for $V'_{rotating}$ in Newton's equation, it can be seen that this gives the general body fixed accelerations as given in Reference 4. These equations are:

$$u'' = F_x/M - qw' + rv'$$

$$v'' = F_y/M - ru' + pw'$$

$$w'' = F_z/M - pv' + qu'$$

F_x, F_y , and F_z are the forces in the i, j, and k respective directions as described in the body fixed coordinate system and M is the mass of the object. Applying this to the STAR-48 and the FreeFlyer body fixed coordinate system results in:

u''_{48} = ((Thrust force * COS(γ) + Connector force - Spring force) /M_{48}) - (q_{48} * w'_{48}) + (r_{48} * v'_{48})

v''_{48} = - ((Thrust *SIN(γ)) /M_{48}) - (r_{48}*u'_{48}) +(p_{48}*w'_{48})

w''_{48} = 0.0 - (p_{48} * v'_{48}) + (q_{48} * u'_{48})

u''_{ff} = (Spring - Connector) /M_{ff} - (q_{ff}*w'_{ff})+ (r_{ff}*v'_{ff})

v''_{ff} = 0.0 - (r_{ff}* u'_{ff}) + (p_{ff}* w'_{ff})

w''_{ff} = 0.0 - (p_{ff} * v'_{ff}) + (q_{ff} * u'_{ff})

u, v, and w are the designated axes that correspond to the body fixed coordinate system above, M_{48} is the mass of the STAR-48 at nominal burnout, and M_{ff} is the mass of the COMET Free Flyer. The 48 subscript designates the STAR-48 and the ff subscript designates the COMET FreeFlyer. Also, " indicates a second order derivative(acceleration). This notation will be carried throughout this report.

Euler's equations of motion as given in Reference 3 are needed in order to keep track of the rotating body and are listed below:

$$M_x = I_x * W'_x - ((I_y - I_z) * W_y * W_z)$$

$$M_y = I_y * W'_y - ((I_z - I_x) * W_z * W_x)$$

$$M_z = I_z * W'_z - ((I_x - I_y) * W_x * W_y)$$

M here is the moment acting about the subscripted axis, I is the moment of inertia about the subscripted axis, W is the angular velocity about the subscripted axis, and W' is the angular acceleration about the subscripted axis. It follows that for the body fixed coordinate system:

p'_{48} = ((Iv_{48} - Iw_{48}) / Iu_{48})* q_{48} * r_{48}

q'_{48} = ((Iw_{48} - Iu_{48}) / Iv48)* r_{48} * p_{48}

r'_{48} = ((Iu_{48} - Iv_{48}) / Iw_{48})* p_{48} * q_{48} + (d * Thrust * SIN(γ) / Iw_{48}

p'_{ff} = ((Iv_{ff} - Iw_{ff}) / Iu_{ff})* q_{ff} * r_{ff}

q'_{ff} = ((Iw_{ff} - Iu_{ff}) / Ivff)* r_{ff} * p_{ff}

$r'_{ff} = ((Iu_{ff} - Iv_{ff}) / Iw_{ff})^* p_{ff} * q_{ff}$

EULER TRANSFORMATION COORDINATES

Now both Newton's equations of motion and Euler's equations of rotation are transformed into a 3-1-3 Euler rotation coordinate system. This transformation is necessary in order to determine Θ, ϕ, and Ψ at any time, t, in the relative inertial coordinate system that will be developed later. The relative inertial coordinate system is the coordinate system of choice when describing the separation of the STAR-48 and the FreeFlyer.

The first Euler rotation of the body fixed coordinates is a pitch through angle ϕ about the w axis as seen in Figure 4a. p, q, and r are the angular velocities of the STAR-48 and the FreeFlyer as described in the body-fixed coordinate system before. The second Euler rotation is a roll about the new u' axis through angle Θ. This can be seen in Figure 4b. The third Euler rotation is a pitch about the new z" axis through an angle Ψ. This can be seen in Figure 4c. The transformation from the body fixed coordinate system to the 3-1-3 Euler coordinate system is given by Reference 3 as:

$$\Theta' = (p * COS(\Psi)) - (q * SIN(\Psi))$$

$$\phi' = (p * SIN(\Psi)) + (q * COS(\Psi) / SIN(\Theta))$$

$$\Psi' = r - ((p * SIN(\Psi)) + (q * COS(\Psi))) * (COS(\Theta) / SIN(\Theta))$$

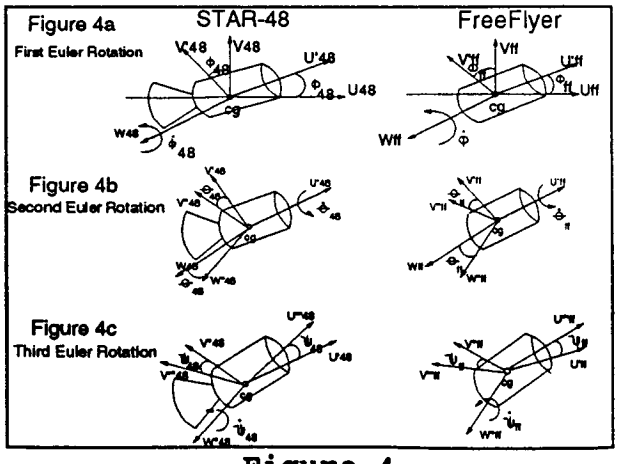

Figure 4

Applying this transformation to both body fixed coordinate systems results in the equations of motion and rotation for the STAR-48 and the FreeFlyer as described in the 3-1-3 Euler rotation coordinate system. Values determined within this system are needed later to evaluate the relative inertial coordinate system.

RELATIVE INERTIAL COORDINATE

The STAR-48/FreeFlyer separation distances will be determined in a relative inertial coordinate system. This system travels with the same initial speed and direction as the orbit of the STAR-48/FreeFlyer combination at nominal burnout. Relative to the STAR-48 and the FreeFlyer, this system is inertial and therefore can be used to measure the separation distances and velocities of the STAR-48 and the FreeFlyer after the separation springs are released. The transformation matrix from the 3-1-3 Euler coordinate system to the relative inertial coordinate system is given in Reference 3 as:

$$Wu = (\Theta' * COS(\phi)) + (\Psi' * SIN(\Theta) * SIN(\phi))$$

$$Wv = (\Theta' * SIN(\phi)) - (\Psi' * SIN(\Theta) * COS(\phi))$$

$$Ww = (\Psi' * COS(\Theta)) + \phi'$$

Applying this transformation to both 3-1-3 Euler coordinate systems results in the equations of motion and rotation for the STAR-48 and the FreeFlyer in a relative inertial coordinate system. All three of these systems can then be evaluated using a Runge-Kutta numerical analysis scheme to obtain the position of both the STAR-48 and the FreeFlyer at any time, t.

To obtain the overall separation distance between the STAR-48 and the FreeFlyer, the relative inertial coordinates for the STAR-48 were then subtracted from the relative inertial coordinates of the FreeFlyer vectorially. This gives a 3-axis separation coordinate frame and from this it can be determined if the STAR-48 will re-contact the FreeFlyer after the separation has been initiated. The total separation distance is then obtained by summing vectorially.

ASSUMPTIONS

One of the assumptions used in this analysis is that the nozzle on the STAR-48 can be gimballed in an upwards direction aligned with the relative inertial

Y-axis. This is needed in order to give the nozzle angle an initial orientation. Also, the gimballing of the nozzle is assumed to occur instantaneously after the STAR-48 and the FreeFlyer are no longer in contact and are a safe distance away from each other in order to avoid re-contact due to the pin-wheeling STAR-48. This safe distance can be determined from the geometry of the separating vehicles. From Figure 5, it can be seen that this distance is r - 35.5 inches = 7.9 inches. If the gimballing of the STAR-48 nozzle is delayed 1 second after separation, the safe separation distance is easily achieved for all cases that were analyzed in this report. Only for very large gimbal angles or for very short separation delays would this safety margin need further investigation. This conservative 1 second gimballing delay after the separation springs have fired was used throughout the following analysis.

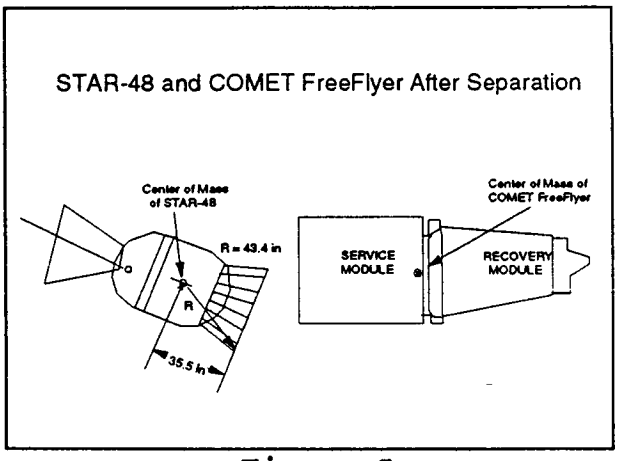

Figure 5

The spring multiplier of 0.9 is also used throughout this analysis. This was determined by Dr. Keith Reiss (Reference 1) and the analysis used to arrive at this number was deemed logical and correct. Further more, a thrust multiplier of 1.0, 1.5, and 0.5 was used as noted by Dr. Reiss due to the somewhat suspect thrust characteristics of the experimentally measured tail-off thrust of the STAR-48V motor. A multiplier of 1.0 represents a normal motor burn, a thrust multiplier of 1.5 represents a thrust amplitude that is one and a half times the nominal thrust of the STAR-48, and a thrust multiplier of 0.5 represents only half of the amplitude of the experimentally determined thrust curve.

The mass properties of the two vehicles were also taken from Reference 1 and are reproduced in Table I. These properties are assumed to be constant throughout the entire time frame under analysis. Also, the position of the center of mass of the two vehicles is assumed to be constant throughout the analysis.

For the concluding analysis, it has been assumed that there are 8 separation springs, n=8, with an effective stroke length of 1.3 inches. The energy imparted to the STAR-48 due to the separation springs will be half of the total potential energy stored in the spring system. Likewise, the energy imparted to the FreeFlyer due to the separation springs will also be half of the total potential energy stored in the spring system. The spring constant for each of the 8 springs is assumed to be 180 lb/in as given in Table I. Any other design changes in the spring system can be easily analyzed if needed.

TABLE 1

FreeFlyer

Mass	= 55.946 slugs
Roll Inertia	= 117.16 slug-ft^2
Pitch Inertia	= 466.03 slug-ft^2
Yaw Inertia	= 467.99 slug-ft^2

STAR-48

Mass	= 16.774 slugs
Roll Inertia	= 40.17 slug-ft^2
Pitch Inertia	= 50.26 slug-ft^2
Yaw Inertia	= 50.49 Slug-ft^2

Separation Springs

Quantity(n)	= 8
Spring Constant	= 180 lb_f/in
Stroke Length	= 0.65 in

Electrical Connectors

Pull Force	= 20 lb_f
Action Distance	= 0.20 in

The emphasis of this report is to determine how the initial roll rate of the STAR-48/FreeFlyer Combination effects the separation of the two bodies. It has been determined by Mr. Mark Daniels (Reference 5) that the maximum expected initial roll rate should not exceed 0.5°/s. Larger roll rates were analyzed in order to see their effects on the separation, but they are not expected for the

actual separation. Smaller roll rates are also analyzed since they are likely to occur.

It is also assumed that the initial pitch and yaw rates are 0°/s. This may not be the case due to the unsymmetrical forces that are inevitably applied to both the STAR-48 and the FreeFlyer by the separation spring system. Accurate maximum expected values for these two rates are not available. Thus arbitrarily large rates will be analyzed in order to see their effect on the separation of the STAR-48 and the FreeFlyer.

FURTHER ANALYSIS

It is apparent from the previous discussion that the separation of the STAR-48 and the COMET FreeFlyer requires analysis. It is logical that it would be best to wait until the STAR-48 is no longer producing any thrust before initiating separation. But this is not possible due to the limited life of the on-board batteries. The launch vehicle power system as designed allows for only a 120 second delay after the STAR-48 has reached its nominal burnout point. Thus the analysis presented here will target this separation time, knowing that if the separation is successful for this delay, that a longer delay would also be successful due to the reduction in residual thrust.

The equations of motion and rotation, along with the transformation equations listed earlier, were all numerically analyzed using the fourth order Runge-Kutta integration method. These results were then plotted and compared to the results obtained by Dr. Reiss in Reference 1. Overall, the analysis presented here coincides favorably with the analysis developed by Dr. Reiss only for conditions where the nozzle gimbal angle is 0° or when there is a very substantial initial roll rate. Due to two inconsistencies in Dr. Reiss' analysis that will not be discussed here, it is believed that the analysis presented in this paper is more applicable to the actual separation conditions that are to be anticipated in the STAR-48/FreeFlyer separation.

Figure 6 shows the separation distance and the effect of the initial roll rate for a gimbal angle of 4.0°. Initial roll rates of 0.1°/s and 0.01°/s were also investigated and were found to lie exactly upon the curve for 0.5°/s. They are not presented due to the cluttering effect upon the plot. Thus it can be seen that there is no collision for initial roll rates of about 10°/s and less. But if the roll rate is any higher than this, the STAR-48 is going to collide with the FreeFlyer after separation due to the spin stabilization characteristics of the STAR-48.

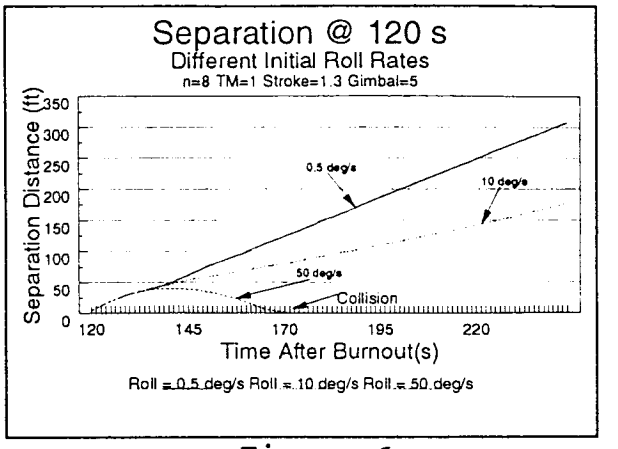

Figure 6

Figure 7 shows a longer time interval for the separation to insure that there is no re-contact after separation. The maximum predicted roll rate is believed to be less than 0.5°/s, therefore it is believed that the separation could be initiated at 120 seconds after STAR-48 nominal burnout.

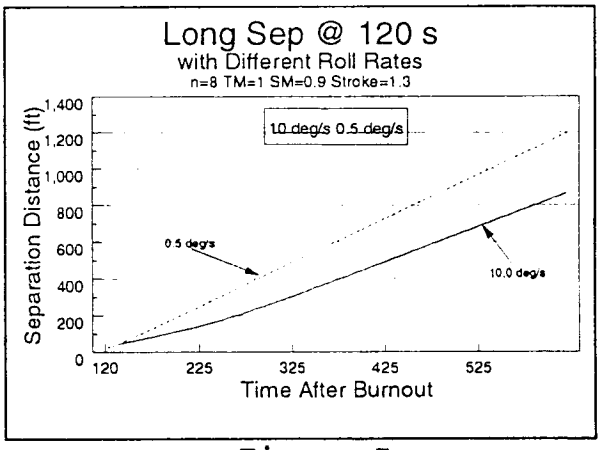

Figure 7

Figure 8 shows a similar plot with the same baseline parameters but with the separation delay reduced to 80 seconds. It can be seen that for a roll rate of 0.5° that there is a successful separation and collision should not result. But it can also be seen from the 50°/s curve that the time until collision is shortened from about 50 seconds for a delay of 120 seconds to about 20 seconds for a delay of 80 seconds. This shows that the energy resisting the separation (due to the thrust of the STAR-48) is much higher for shorter delay times. Thus, shorter delay times increase the potential for re-contact as

expected. The separation can be initiated successfully for a delay of only 80 seconds with the known highest roll rate of 0.5°/s, but this gives the system much more potential for re-contact than if a delay of 120 seconds is used.

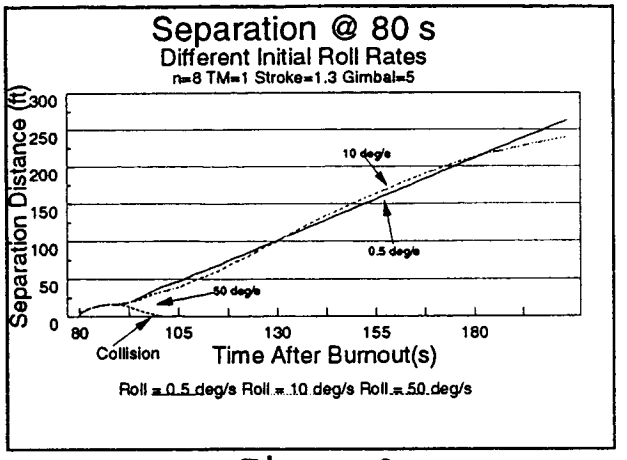

Figure 8

Since the thrust characteristics of the STAR-48 are somewhat suspect as noted by Dr. Reiss, Figure 9 investigates what occurs to the separation if the measured thrust is either reduced by 50% or increased by 50%. It can be seen that for a separation delay of 120 seconds, that the success of the separation of the STAR-48 and the Free Flyer is not greatly effected by the known accuracy of the thrust of the STAR-48 as long as the Star-48 nozzle is gimballed.

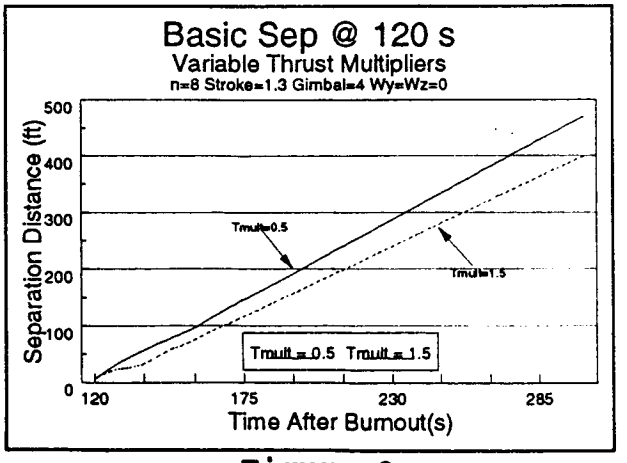

Figure 9

In figure 10, the effects of the gimbal angle are investigated for the basic initial conditions of the STAR-48 for gimbal angles of 5°, 1°, and 0°. It can be seen that the gimballing of the STAR-48 nozzle is crucial to the success of the separation. Without the gimballing of the nozzle, the STAR-48 will collide with the FreeFlyer if the separation delay is at 120 seconds. Even a small gimbal angle of only 1° is enough to obtain a successful separation assuming that the initial roll rate does not exceed 0.5°/s. As this angle is increased, it can be seen that the separation distances also increase. To reiterate, the gimballing of the STAR-48 very shortly after separation has been initiated is critical in order to ensure a safe separation between the STAR-48 and the COMET FreeFlyer.

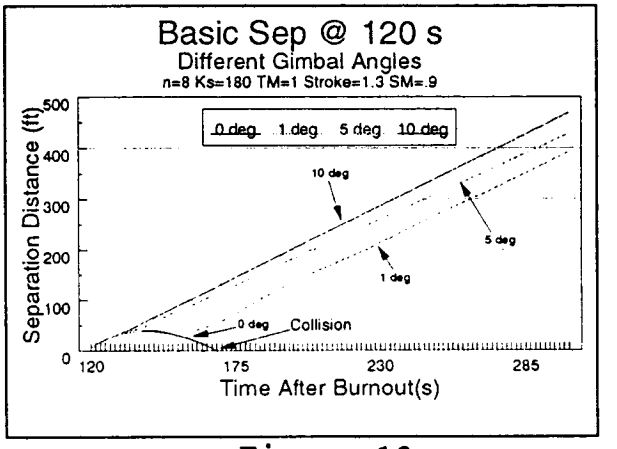

Figure 10

Another problem that could arise during the separation is that an initial wobble rate could be placed upon both the STAR-48 and the FreeFlyer due to the asymmetrical firing of the separation springs. It is believed that this wobble will be minimal, but an accurate maximum expected initial wobble rate has not been determined. Figure 11 shows the baseline STAR-48 with an initial wobble rate of 0.5°/s about the pitch axis and 0.5°/s about the yaw axis.

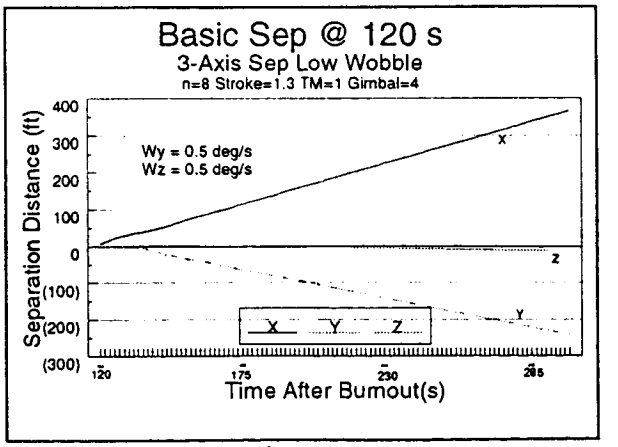

Figure 11

Figure 12 shows the separation for an initial wobble rate of 50°/s about the pitch axis and 40°/s about the yaw axis. From these plots it can be seen that an initial undetermined wobble could be tolerated without greatly effecting the separation. The point of this is that if the separation springs misfire and cause an initial large wobble rate, the separation will not be greatly effected even though the FreeFlyer would possesses a large unacceptable wobble. Since all values evaluated for the initial wobble rates did not cause re-contact with the FreeFlyer for the basic separation conditions, it was determined that further analysis is not needed in this area unless the delay time is significantly reduced below 120 seconds.

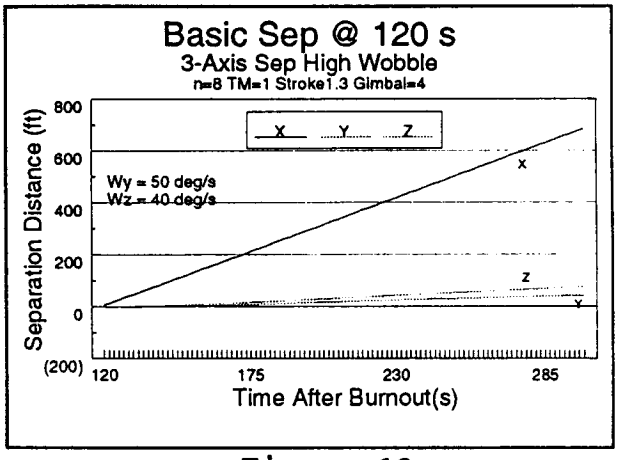

Figure 12

Also included for detail is the separation distances between the STAR-48 and the FreeFlyer for each axis and the rotation of the STAR-48 about each of these axes under normal separation conditions. These are provided so that the reader can obtain a better "feel" of what is occurring physically during separation. The 3-axis separation can be seen in Figure 13 and the roll, yaw, and pitch angles of the STAR-48 in the relative inertial coordinate system can be seen in Figure 14.

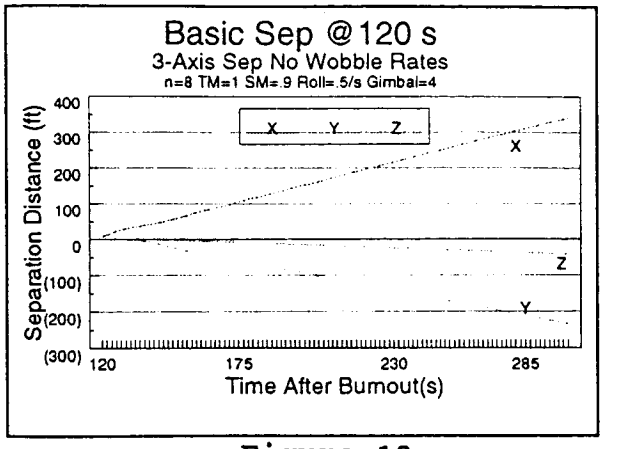

Figure 13

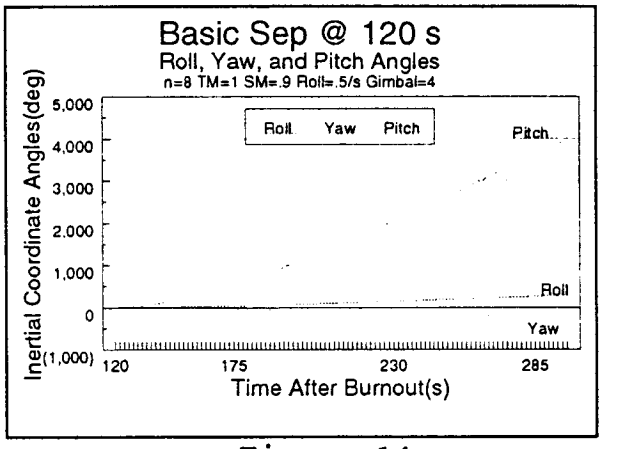

Figure 14

CONCLUSIONS

From the above discussion, it can be concluded that the separation between the STAR-48 and the COMET FreeFlyer will be successful under normal, expected conditions if the delay time between the STAR-48 nominal burnout and the start of the separation is 120 seconds. In fact, the delay time could be reduced even further if necessary. This, however, is not a favorable condition if a 120 second separation delay can be used with the available battery life.

At a delay time of 120 seconds, the separation will even be successful if some unforeseen forces cause some unfavorable conditions, such as a slightly higher roll rate, a smaller than predicted nozzle gimbal angle, or a separation spring induced wobble. But if these conditions are too unfavorable, the STAR-48 could reconnect with the FreeFlyer.

Considering all of the analysis on the separation

between the STAR-48 and the FreeFlyer to date, it is believed that the separation delay time of 120 seconds is sufficient to avoid re-contact with the FreeFlyer.

References

1. *"COMET Study and Options for STAR-48/FreeFlyer Separation"*,Diss., Dr. Keith W. Reiss, October 19, 1992.

2. *"LV/SM Separation Dynamics Analysis"*,EER Systems .

3. *Spacecraft Attitude Determination and Control,* James R. Wertz, Kluwer Academic Publishers, 1978, pp. 509-516.

4. *Store Separation Testing Technics at the Arnold Engineering Development Center*, J.B. Carmen, Jr., D.W. Hill, Jr., and J.P. Christopher, Volume II, ARO,Inc., AEDC Division, June 1980, p. 88.

5. Telephone Conversation, Mr. Mark Daniels, EER Systems Project Manager, Seabrook, MD, Approx. March 15, 1993.

CSTAR SUPPORT FOR THE COMMERCIAL LAUNCH VOUCHER DEMONSTRATION PROGRAM

by

Carter H. Myers
Chief Engineer, COMET Program
Center for Space Transportation and Applied Research
UTSI Research Park
Tullahoma, TN 37388

ABSTRACT

Congress mandated a Launch Voucher Demonstration Program (LVDP) in the NASA FY 1993 Authorization Bill. This program was to have been put into place by October 1, 1993 and would end on September 30, 1995, with a report to Congress on January 31, 1996.

CSTAR was asked to provide a participatory relationship to NASA concerning the Launch Voucher Demonstration Program, specifically due to CSTAR's COMET experience and knowledge of the CCDS payload & transportation planning, budgeting, and contract management process.

This paper describes CSTAR's involvement in the development of the Launch Voucher Demonstration Program.

Background

The original concept for the voucher program was to off-load the backlog of Shuttle GAS Can type of payloads to Expendable Launch Vehicles. In various pieces of legislation, Congressman Robert Walker (R-Penn) initiated this concept to facilitate low-cost access to space for researchers, to remove NASA as the middleman for launch services, and to facilitate the expansion of commercial launch services.

In addition, this concept was supported and given strong justification by research done by a non-profit "think tank," *Resources For The Future.* Ms. Molly McCauley authored several papers describing a launch voucher program, identifying the economic growth factors associated with such a program, and providing comparison with existing government voucher programs.

Congress mandated a Launch Voucher Demonstration Program (LVDP) in the NASA FY 1993 Authorization Bill. This program was to have been put into place by October 1, 1993 and would end on September 30, 1995, with a report to Congress on January 31, 1996.

The Program as defined by Congress would be part of the NASA Grants Program, and Vouchers would be used to pay for launch services and payload integration services. Only payloads funded by NASA's Office of Commercial Programs, both suborbital and orbital, would be covered under the program.

CSTAR Involvement

In May 1993, CSTAR was asked to provide a participatory relationship to NASA concerning the Launch Voucher Demonstration Program, specifically due to CSTAR's COMET experience and knowledge of the CCDS payload & transportation planning, budgeting, and contract management process.

However, the Federal Advisory Committee Act governs relationships such as this and limits involvement of non-government individuals, such as CCDS members. If non-government employees participate in Agency deliberations, then the team must have balanced membership, keep strict records, and appoint members as Special Government Employees, etc. With these restrictions in mind, CSTAR appointed Carter Myers to represent CSTAR, and his charter was to provide information, insight, and ideas pertinent to this Program.

Program Development

In order to bring together specialized knowledge, information, and experiences, the NASA Office of Advanced Concepts and Technology (OACT - formerly Office of Commercial Programs) formed a Process Action Team to determine the best approach to the development of the Demonstration Program. CSTAR

participated in the LVDP Process Action Team as a major player and provided specific insight into orbital and suborbital program development, the launch and launch service industry, and necessary contractual issues. The members of the Process Action Team are listed in Table A.

The team used the following assumptions in the development of the program:

- The LVDP is to facilitate low cost access to space for researchers
- The LVDP is to decrease NASA's role as middleman
- The LVDP is to focus is on domestic commercial services
- NASA would accept reasonable risk
- Adequate funding would be available

The team diagrammed the current CCDS method for supplying payloads and transportation services, analyzed the lessons learned from the Consort, Joust, and COMET programs, and looked at the experience of the NASA-CODE S personnel in acquiring launch services. The team conducted interviews with knowledgeable individuals from other government organizations and interest groups to gain information on how the process might work.

In July 1993 the team conducted a symposium where representatives from the launch service, spacecraft, and payload integration industries were invited to participate and provide their views on how the voucher program might be structured. Some companies came in very knowledgeable on the voucher system, and some came in not knowing what a voucher should be. The major opinion coming out of the symposium was that if the program could not be properly funded, then NASA should not attempt to start the program. Their view was that the program results would be very unfavorable, since the launch industry could not provide competitive prices for such a low launch rate.

In addition, the team provided a survey and follow-up with the CCDS community, as this is the group that would be financially and programmatically responsible for the conduct of the program (after the vouchers are issued). The last piece of information pertinent to the program structure came from reports by two economists that looked at the economic aspects of the program.

What is a Voucher?

Current vouchers used by the government include
-HUD vouchers: used for low income housing
-Education vouchers: used for private education services (being tested)
-EPA vouchers: used by power plants for emission control

A voucher is a guarantee for specified services and is equivalent to a letter of credit. The voucher is only redeemable by the grantee, it has a limited lifetime, and has a fixed maximum face value. It is normally used in a market where the service/product is a commodity type item and is widely available with very little differentiation in characteristics, features, or qualities.

In the context that the voucher is defined for the LVDP, the voucher is to be issued for the payment of Payload Integration, Launch Services, Spacecraft Bus, Orbital Operations, and/or Payload Recovery. What makes the voucher different from the current CCDS system is that the grantee will be responsible for the Request for Proposal, the bidding and negotiation process, and the management of the launch and launch service contract. One other item that is important to the grantees is that the voucher is for a turn-key system. The team investigated multiple vouchers for each type of system and discarded the idea because of the high contract liability even though it probably would have opened up the market to some smaller market entrants.

Since the LVDP is a test of market principles, all Shuttle based payloads were eliminated from consideration in the program. To allow vouchers for shuttle based payloads would have created a system where the government would be competing against private enterprise which means that the intent to increase the competitiveness of the launch service industries would not be met. In addition, the government has certain cost advantages that could be used (accounting methods) which would unfairly skew the market.

Since one intent of this program was to enhance the U.S. Launch Service Industry's competitiveness, the program eliminated foreign launch service entities from bidding on a voucher.

Program Attributes

It was determined that potential providers will be qualified before they are allowed to bid on a payload. Due to NASA acquisition regulations, NASA could not provide this qualification, and would have to come from the CCDS community.

Various methods for determining the value of the voucher was explored and a method very similar to the current system was settled on. This system would allocate the budget for vouchers across the CCDS program, and it would be up to each CCDS to determine the value of each voucher. But a voucher would only be issued for NASA approved payloads.

The program is set up so that each CCDS can Request Proposals, evaluate bids, negotiate contracts, and manage those contracts for their payloads, or they can use a CCDS "broker." The CCDS broker is a CCDS currently experienced in the acquisition of transportation services; ex. CSTAR for orbital launch and operation services, and CMDS(UAH) for suborbital launch services. The CCDS's that recieve a voucher will assign their voucher to the broker. The broker will aggregate payloads and send them out for bid, negotiate and manage the contracts. Financial and program responsibility for payload delivery will still rest with the CCDS that was issued the voucher.

All contracts resulting from the LVDP will fall under the category of "commercial contract" and will be governed by the Uniform Commercial Code, and will not be governed by Federal Acquisition Regulations, other than having to abide by the Grant regulations governing the Grantees. Also, the commercial contract must specify

- The date of launch (a window)
- The payload acommodations
- A firm fixed price
- Milestones and Progress Payments
- Liquidated Damages and Penalties
- Interface and Testing Requirements
- Reflight Insurance and Performance Bonds

And all changes to the contract would be the responsibility of the voucher holder.

Concerns

Some of inputs from the symposium showed that there was concern from the launch and launch services industry that the scope of the program was too limited, that limited funding would be a major impediment, and that the demonstration program was too short. The industry said that NASA and Congress must have a commitment to see it through or don't do it!

The program was not received by the CCDS community very will since this program places significantly more fiscal and program responsibility on the CCDS's than exists today. The CCDS's believe that the current system is adequate and cost effective, that for NASA to ask the CCDS's to partially fund the transportation would put a significant burden on them, and that this program would duplicate efforts and increase administrative costs. Most specifically, they prefer not to work directly with the launch providers and feel that they should concentrate on their center's competitive area.

Results

Due to small existing budget and the two year timeframe for the program, it was determined that OACT could only support one suborbital launch in the demonstration program. NASA went back to determine how to best support the intent of the program and still retain a viable program. It was determined that a single sub-orbital launch would not provide much information and could in fact show results contrary to what the expected results should be. The increased administrative costs of the vouchers would not be off-set by lower launch costs, since the current suborbital launches are already commercial launches and show a price reduction since they are contracted in multiples of three launches.

With the overhead of the voucher recipients, and the fact that this would be for only one launch, the costs would very probably come out much higher than today's system. Due to this fact, OACT in recent congressional testimony identified that they wished to increase the scope of the program to include five Office of Space Science (OSS) suborbital payloads, with a report to Congress in January 1994.

Where do we go from here?

The majority of input that CSTAR can provide to NASA OACT has already been conducted and NASA is determining how to include the OSS payloads in the program.

Future work by CSTAR can include work in voucher valuation and launch and launch service provider qualification.

Summary

The Launch Voucher Demonstration Program seeks to enhance the competitiveness of the U.S. Launch and Launch Services industry. To do this the program must show how this methodology will improve the quality of services and lower costs to the customer. A very limited program cannot by its nature show any of these results. Conversely, a program taking in the total of NASA funded suborbital and small orbital payloads would not be cost effective in that any mistakes that are made would be on a grand scale and all the changes made to the NASA infrastructure would be irreparable should the program not show results.

With sufficient commitment on the part of NASA and the Congress, it is the belief of the author that this program can produce the results that NASA, the Congress, and the taxpayer hope for.

References

1. Macauley, Molly K. and Anex, Robert P., Resources for the Future. *Space Transportation Voucher Research.* Summer 1993.

2. Macauley, Molly K., Resources for the Future.

Launch Vouchers for Space Science Research. Space Policy. November 1989.

3. Reck, Gregory M. *Statement to the Subcommittee on Space, Committee on Science, Space and Technology, United States House of Representatives, 103rd Congress.* October 20, 1993.

Table A. - LVDP Process Action Team

Team Members		
Names	Organization	Expertise
Candace Livingston	NASA - CU	Process Committee Chairman
Lisa MacCauley	Battelle - CCDS	CCDS Payloads (COMET Payload Selection Committee Chairperson)
Tom Gallimore	CMC(UAB) - CCDS	CCDS Payloads (COMET Payload Integration Contract Monitor
Carter Myers	CSTAR - CCDS	Orbital Launch & Operation Systems (COMET Chief Engineer)
Bob Naumann	CMS(UAH) - CCDS	Sub-Orbital Launch & Operation Systems (CONSORT Program Manager)
Mark Nall	NASA - CF	NASA Commercial Transportation
John Emond	NASA - CG	NASA Commercial Programs & Payload Approval
Karen Poniatowski	NASA - SV	NASA Launch System & Launch System Procurement
Vita Cevenini	NASA - CU	NASA Budgeting & Planning
Jack Yadvish	NASA - CU	NASA Commercial Program Planning
Anila Strahan	NASA - HWG	NASA Budgeting & Grants
Bob Bristow	NASA - DD	NASA Advanced Systems Development
Karl Stehmer	NASA - LC	NASA Legal
Bill Bierbower	NASA - GS	NASA Legal
June Edwards	NASA - GS	NASA Legal

Transition from Launch Vehicles to Launch Services

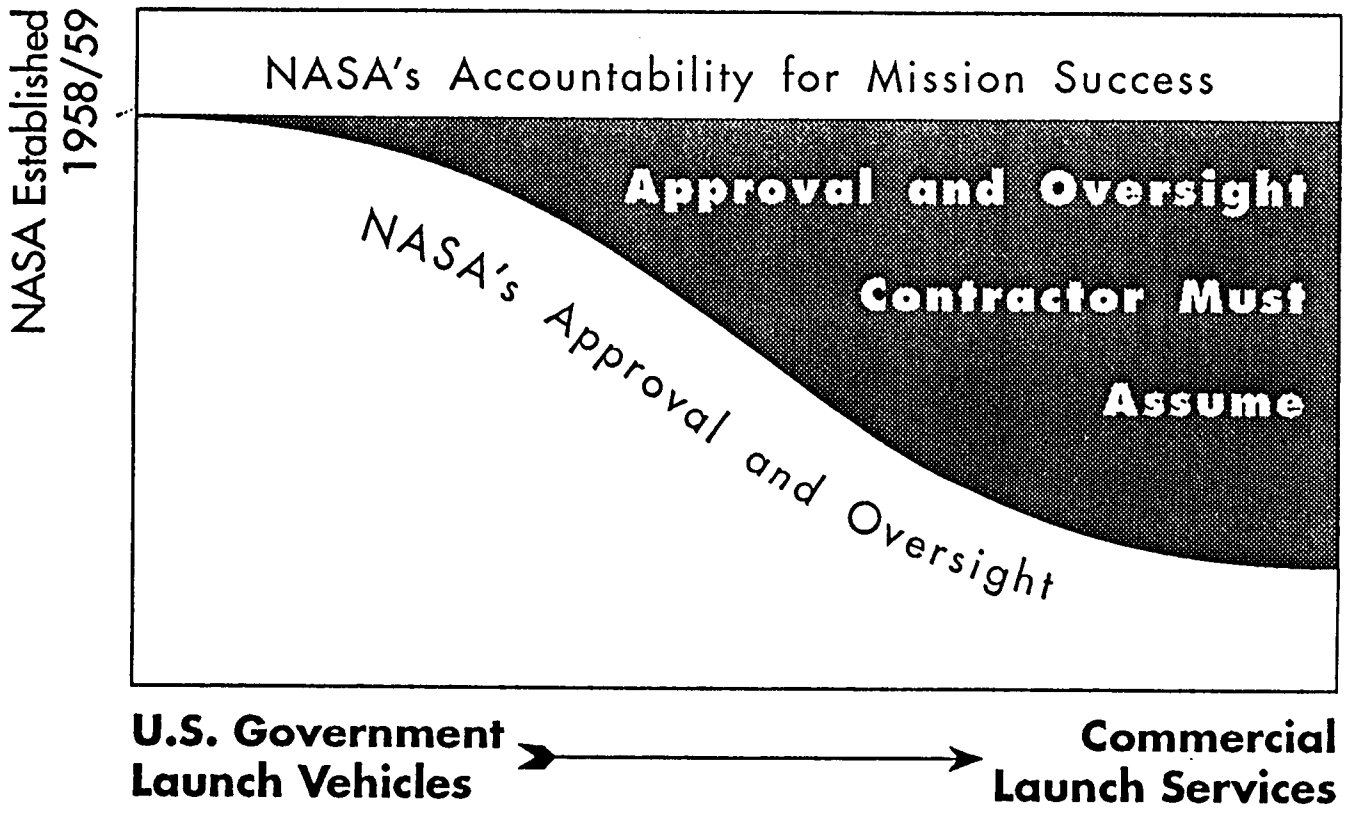

1988 CONSORT RFP
1989 MELV RFP
1990 SELV RFP
1990 COMET RFP

Figure 1

Voucher Payload Evaluation Process

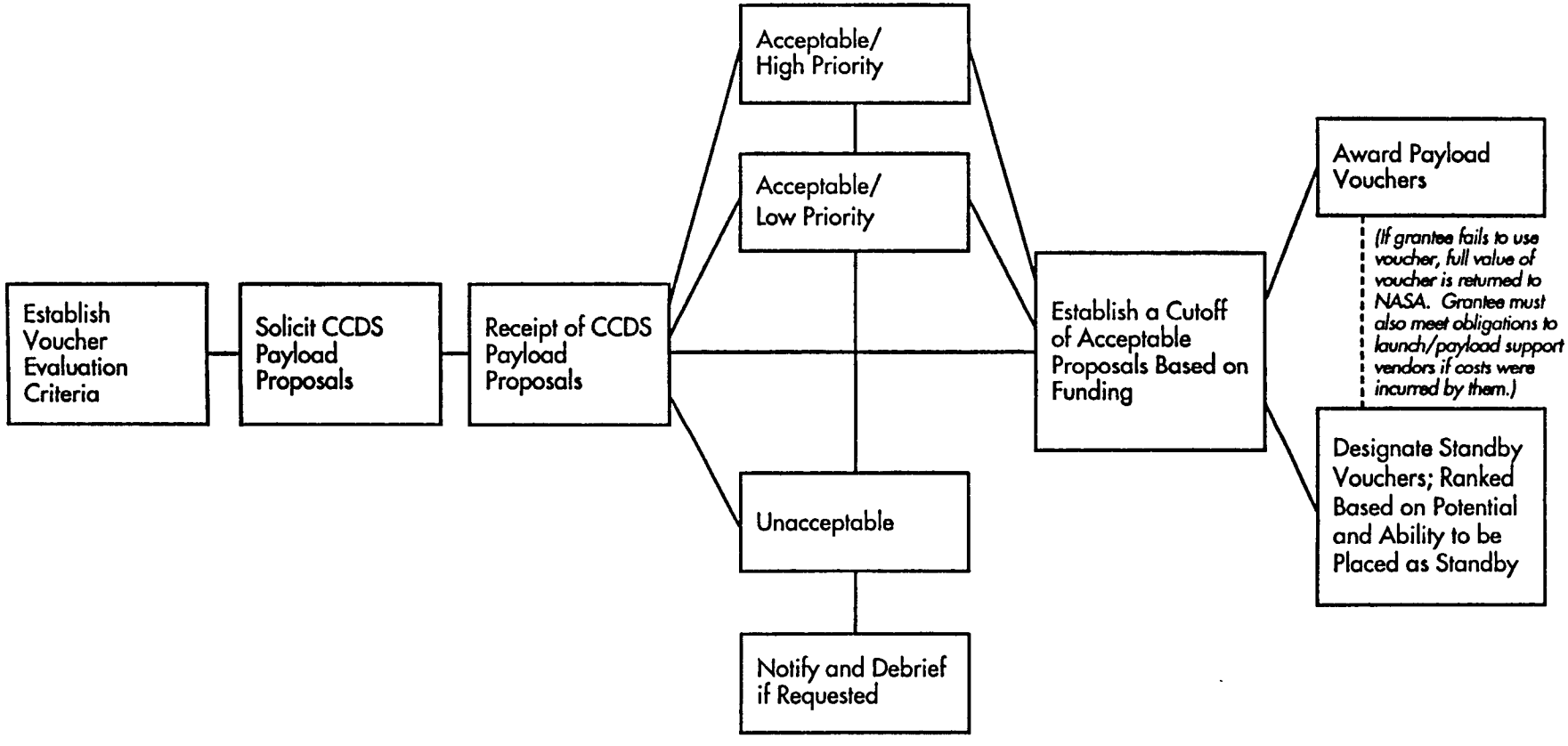

Office of Advanced Concepts and Technology • National Aeronautics and Space Administration

CG-29018 8/31/93

Figure 2

Proposed Launch Voucher Payment Process

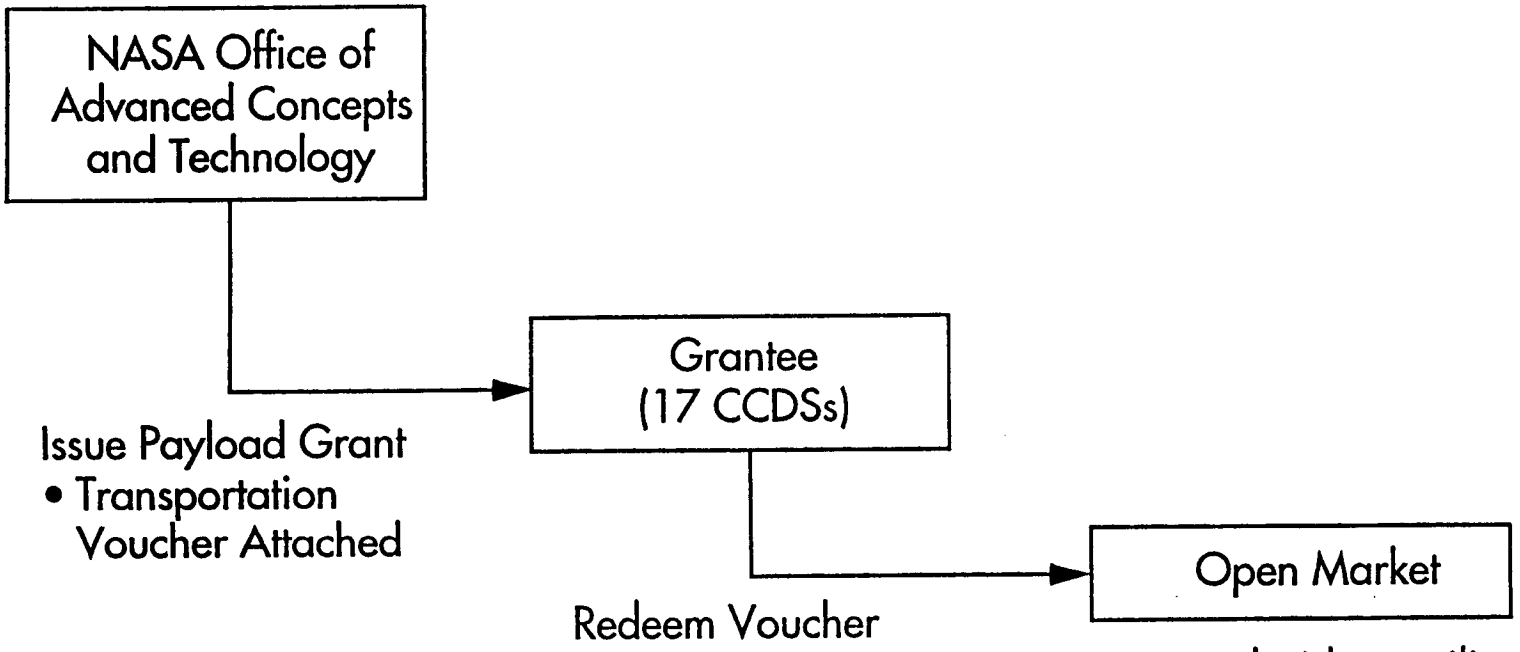

- Grantees can decide to utilize existing CCDS transportation mechanism
- Grantees can identify a different CCDS to serve as "Broker"
- Grantees can complete and select "Broker" from the private sector
- Individual Grantee/CCDS can compete and sign contracts

Figure 3

Transportation Voucher Process

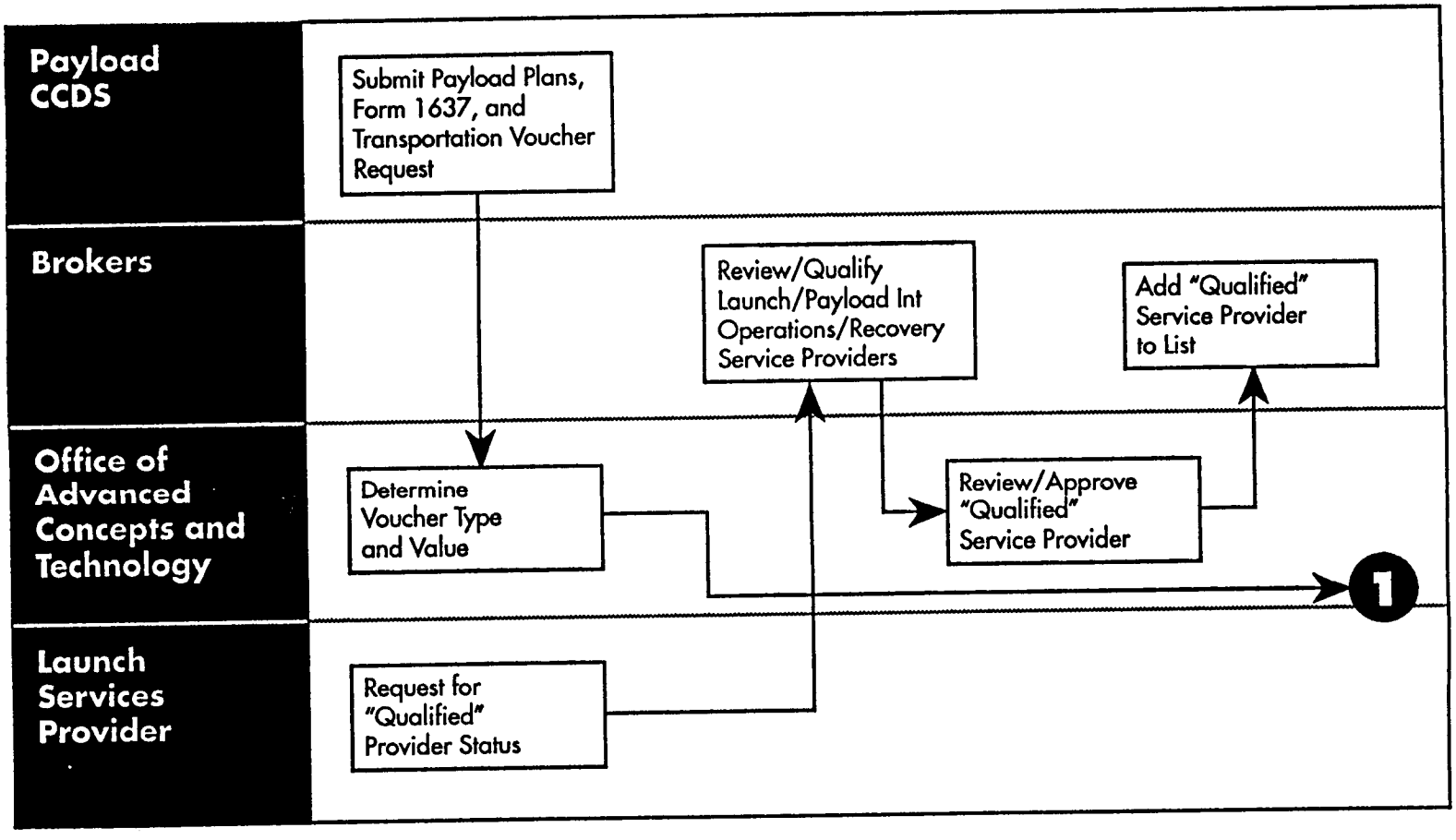

Figure 4A

Transportation Voucher Process (continued)

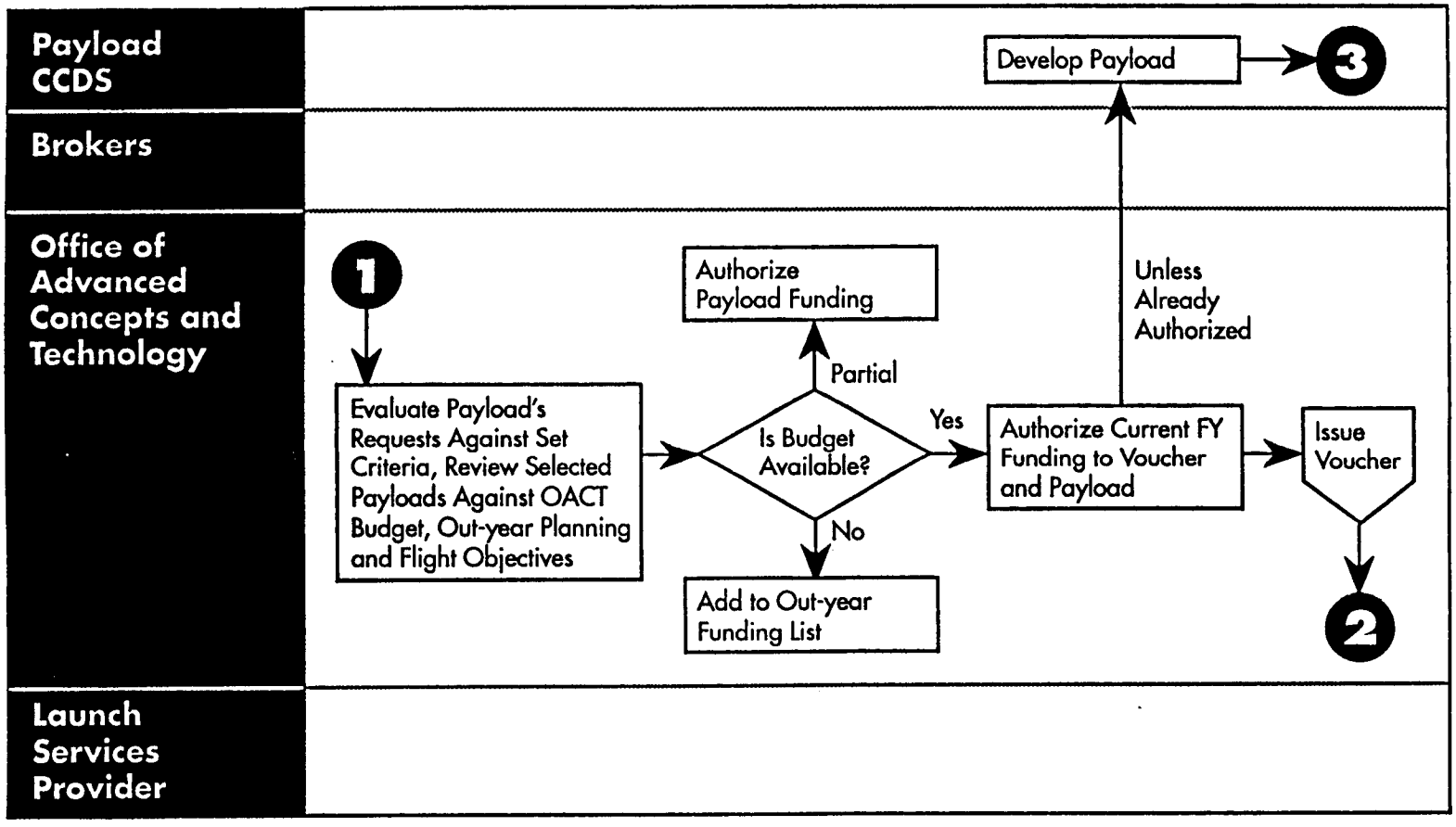

Figure 4B

Transportation Voucher Process (continued)

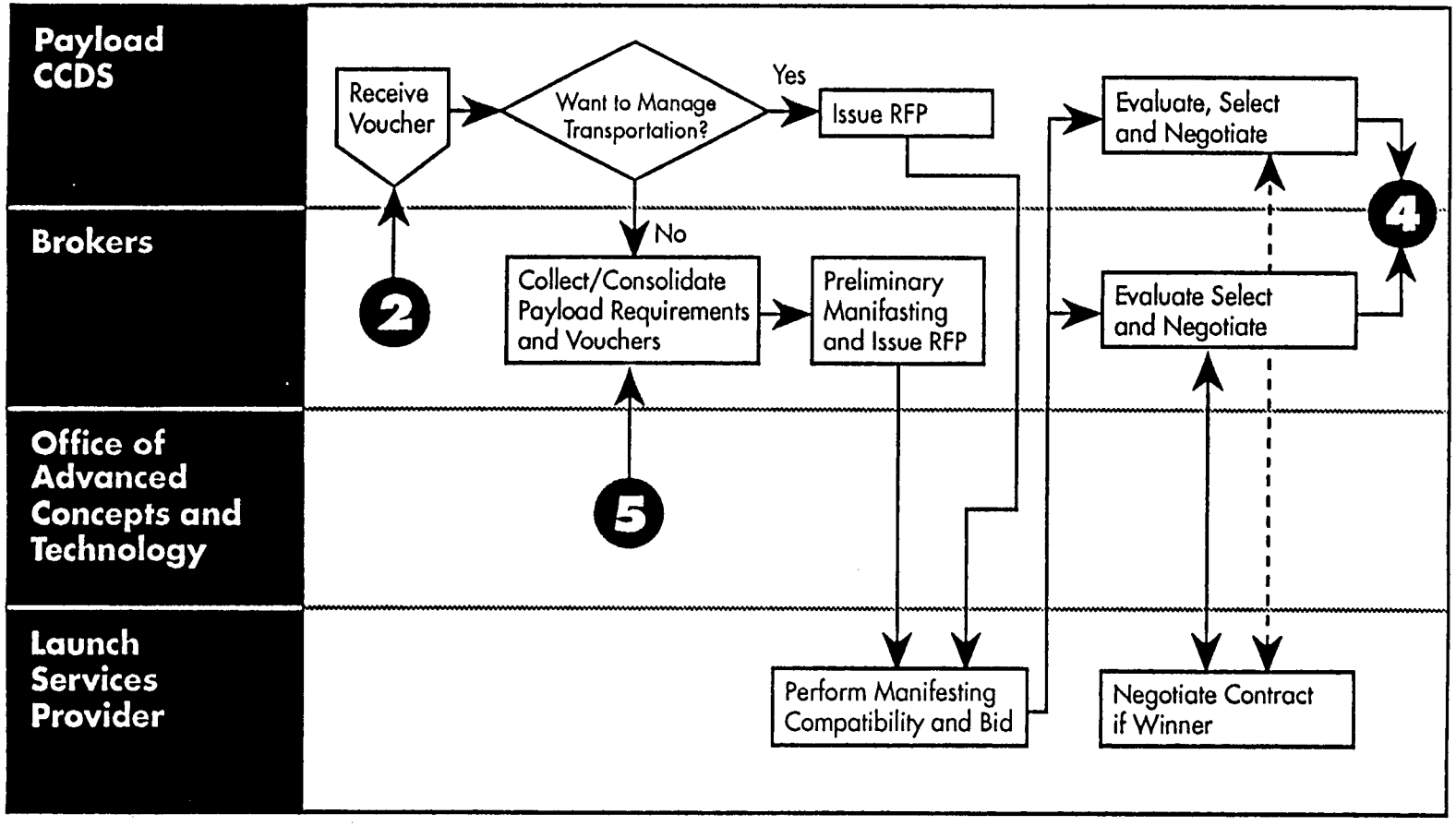

Figure 4C

Transportation Voucher Process (continued)

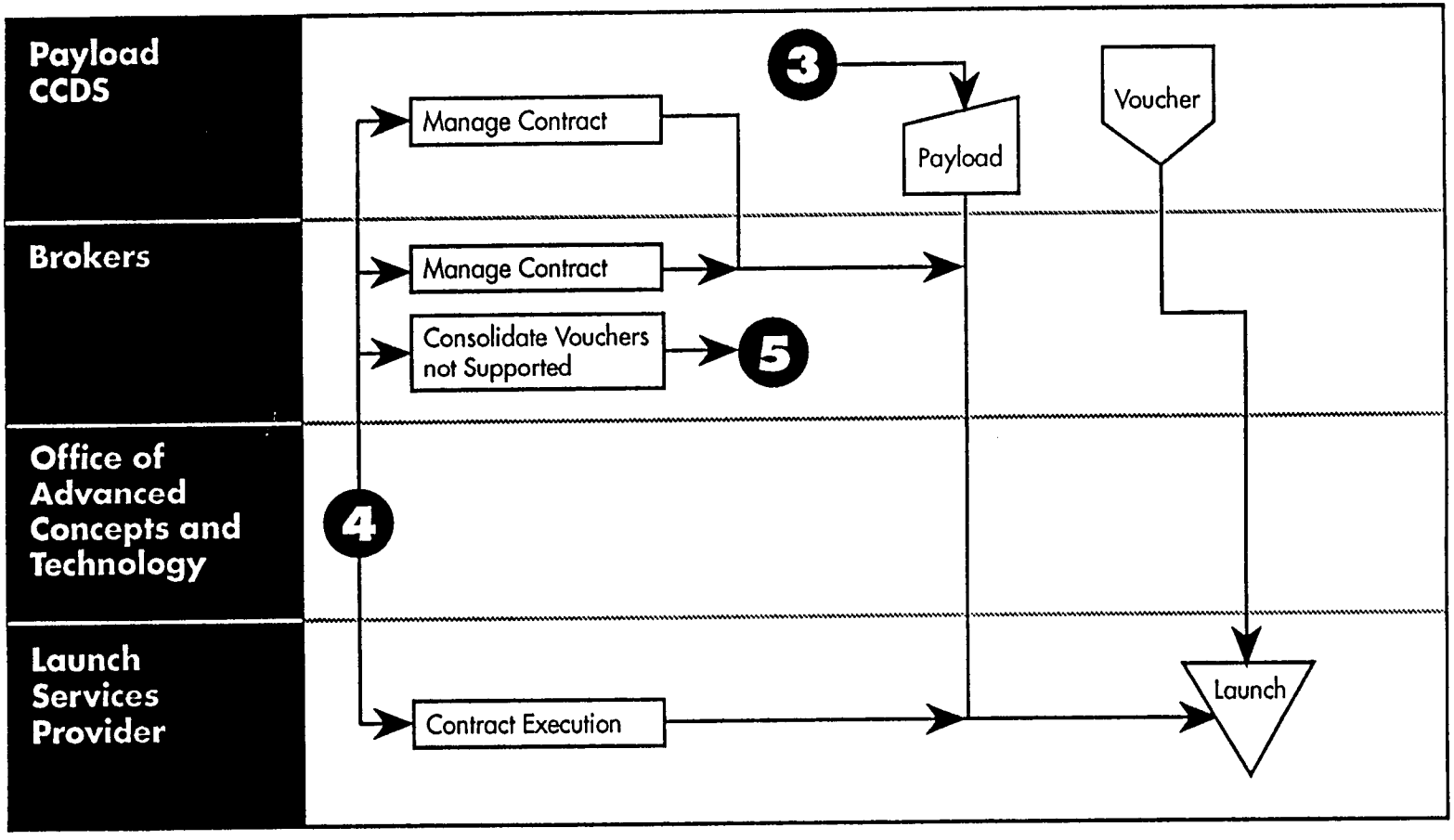

Figure 4D

Launch Voucher Demonstration Program

Schedule

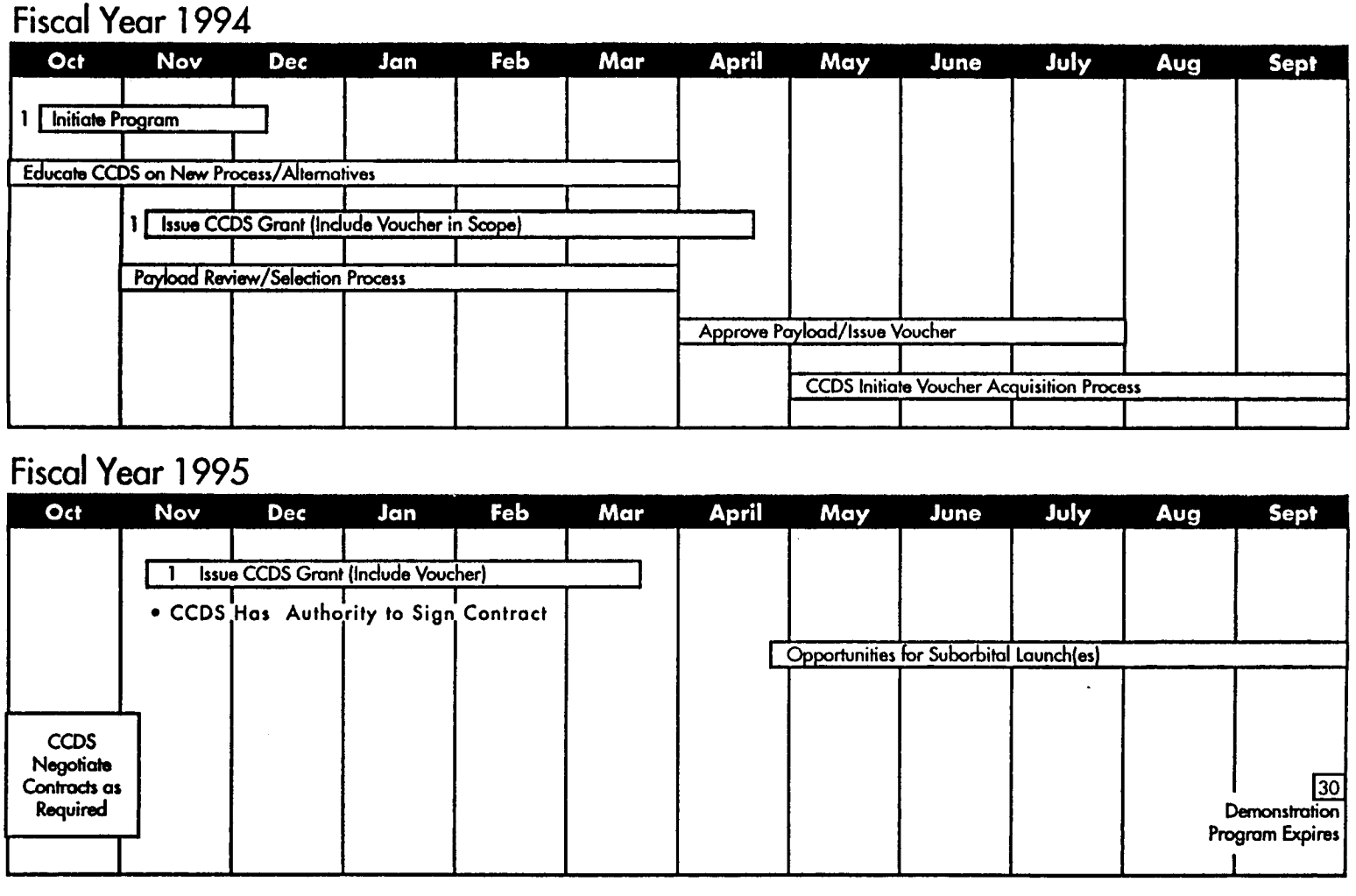

Number of Launches Dependent on Available Funding

Office of Advanced Concepts and Technology • National Aeronautics and Space Administration

CU-28082-27 08/18/93

Figure 5

WCSC ENVIRONMENTAL PROCESS IMPROVEMENT STUDY AND DEMONSTRATION PROGRAM [1]

NPB

N96-16948

5935
P.7

Joseph F. Pawlick, Jr. [2]
University of Tennessee-Calspan
Center for Space Transportation and Applied Research
Tullahoma, TN 37388-8897
(615) 455-9026

Orlando C. Severo, Jr. [3]
245-A Burton Mesa Blvd.
Lompoc, CA 93436
(805) 733-7370

Abstract:

CSTAR's objective to develop commercial infrastructure is multi-faceted and includes diverse elements of the orbital and suborbital missions. Goals of this eight-month project with the WCSC are aimed at simplifying the environmental assessment, approval, and licensing process for commercial users. Included in this overarching set of goals are two specific processes: one, air pollution control, and the second, the environmental assessment mechanism. Resolution of the potentially user unfriendly aspects of these environmentally sensitive criteria are readily transferable to other ranges where commercial space activity will be supported.

Funding for the project has been provided by NASA under CSTAR grant NAGW-1195.

Project Description:

This report documents the progress of the initiative undertaken by CSTAR to streamline processes for commercial users at our nation's test ranges. WCSC's efforts at Vandenberg AFB spotlight one segment of the regulatory process which can severely impact potential users at VAFB due to the diversity and scope of the approval and coordination authorities.

The goal of the WCSC Environmental Process Improvement Program is to define and streamline the end-to-end environmental processes at the federal, state, and county level required to support commercial space at Vandenberg AFB. In order to accomplish that goal this project will identify the parties involved, forms and documentation which must be provided by the commercial user, and the path which approval travels. Based on analysis of this information, agreements will be consummated among the authorizing parties regarding streamlined environmental licensing processes.

Air pollution and control efforts will concentrate on defining those processes, interfaces, documents, (including forms) and participants involved in the air pollution control approval system. These will be used to demonstrate a paperless approach to satisfying the local, county, and state agencies involved in the approval cycle. Generic Environmental Assessment activity will work toward identification of those steps and interfaces necessary to complete the environmental approval cycle at Vandenberg. Again demonstrating, through use of a distributed computer data base, that information concerning construction approvals, generic environmental assessments, forms, schedules, and related policies can be accessed and completed by those involved in approvals. The system will use hypertext architecture and is aimed at establishing and maintaining closer ties between the range users, Air Force environmental offices on Vandenberg, Santa Barbara Air Pollution and Control District and within Santa Barbara County, California, and local offices in Santa Maria and Lompoc, California--all of which are involved in the licensing process.

Outcome of the effort is twofold: (1) a suggested approach to streamlining the approval process by eliminating specifically identified areas of duplication and overlapping requirements and; (2) an understanding and demonstrations of a user-friendly paperless air pollution permitting process and a user-friendly generic environmental impact analysis.

---

[1] This work is supported by the Center for Space Transportation and Applied Research (CSTAR) under NASA Grant NAGW-1195.

[2] CSTAR/UTSI, Manager of Space Transportation

[3] WCSC Chairman

In order to segment the WCSC Environmental Process Improvement Program into manageable components, six tasks have been identified:

Develop System Concepts
Determine Payload/Launch Operation Processes
Identify Environmental Licensing Regulations
Define the Environmental Processes
Consummate Agreements
Demonstration Project

Each of the first three tasks are concerned with in-depth examinations of existing plans, policies, and procedures which effect the environmental approval process. These are binding on any commercial user that attempts to fly a vehicle on the Western Test Range and/or use the launch infrastructure (facilities & capabilities) resident on Vandenberg AFB. Many of these are impressed by parties located clearly beyond the boundaries of VAFB: County Air Pollution Control Board (APCB) in Santa Barbara, Environmental Offices in Santa Maria and Lompoc, and Air Force Environmental Offices at Colorado Springs, and Los Angeles. Additionally, a plethora of offices at VAFB concern themselves with pollution and environmental control: Plans organizations at Headquarters, environmental offices within Safety and Civil Engineering on VAFB, and archeological permitting within the Civil Engineering organization. The hoops which must be negotiated by a commercial range user can be formidable and a source of intimidation.

Also during the first three tasks, images of those forms used in the approval process and related environmental and licensing documents will be placed in a relational data base at WCSC's offices. Later to be moved to VAFB's Environmental Office, this strategically located data base will be the central processor for data retrieval and update. The required environmental information is highly dependent on launch vehicle and experiments. Therefore, a well-characterized two stage vehicle with four strap-on motors and a circularization motor will be examined. The hypothetical payload will be a meteorological satellite (Figure 1).

After the appropriate environmental licensing regulations are identified, the flow of the environmental approval process will be charted and all permits, products and approval authorization will be time-lined. At that time, the steps which can be streamlined or improved will be identified. Some may be duplications; others may cause multiple interactions between the same organizations (do-loops) due to inconsistencies. An overview of the process is depicted in Figure 2.

Using the information made available by the streamlining analysis, actual agreements will be consummated among the authorizing parties, if possible, regarding streamlined environmental licensing processes for commercial space operations.

In the final stage of the WCSC Environmental Process Improvement Program, a pilot run of a user-friendly, paperless air pollution permitting process is planned. The process will demonstrate the use of automated data bases and systems to allow ease of issuance of county air permits. Figure 3 identifies the major participants in this demonstration, type of input generated, and their locations.

Also during the last task a generic environmental impact analysis will be conducted for the test vehicle. This may be a ground support equipment cart which will be used for propellant loading during launch operations of the hypothetical vehicle. Use of the automated data bases and systems will be shown to facilitate decisions at the federal, state, and county level for environmental approval.

Status and Results:

Preliminary work with WCSC resulted in a white paper which was presented to NASA's Office of Expendable Launch Vehicles, Code SV. After modifications, the white paper was accepted by NASA. Shortly afterward, a contract was consummated between WCSC and CSTAR. After review and approval of the contract, funding for the project was received as an augmentation of CSTAR's Commercialization Grant (NAGW 1195). Grant augmentation was received during early July 1992 and work started shortly thereafter.

Skeletal outlines of the environmental approval process and the APCB's activity have been gathered. Flow charting the various approval cycles has started. Many tasks are obviously very labor intensive; others are characterized by "do-loops" which indicates interactive decisions. Accomplishing these tasks are often lengthy since no single party is responsible.

A program, "Automated Data-Driven Environmental-Approval Process Tool (ADEPT)" has been initiated by a WCSC contractor, Design Research Corporation. This is the precursor to the central data base to be used for accumulation of forms, past environmental assessments, scheduling and tracking.

Permits, approvals, and processes have been identified and show the magnitude of the undertaking. There are nine distinct processes which must be overcome by the commercial user. These are governed by three separate laws and directives from five different federal organizations. Even at a point only two months into the program, the inefficiency within the approval system

becomes evident and the need for a streamlined process is mandatory if space commercialization is to be facilitated.

Three months into the project the architecture of both elements of the effort have been defined. Programs developed by subcontractors will be used to facilitate the paperless aspects of the concept. Working associations have been cultivated with the numerous and varied agencies, organizations, and people involved in the assessment process. Progress measured by planned vs. actual status shows this effort to be on schedule and slightly under cost. A Gantt chart (Figure 4) portrays project schedule and progress as of October 1, 1993.

Environmental Process Improvement

WESTERN COMMERCIAL SPACE CENTER

Vehicle Description

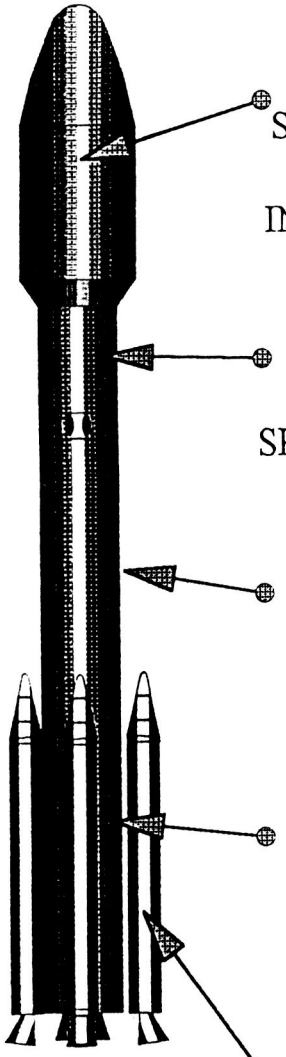

Fairing/METSAT

STAR 37S APOGEE KICK MOTOR, HYDRAZINE ATTITUDE ADJUST

INDIUM, MERCURY, CADMIUM, TELLURIUM, ANTIMONY SENSORS

TOS Upper Stage

SRM, HYDRAZINE RCS, BATTERIES, SEPARATION SYSTEM

2nd Stage - Castor 120

108,005 LBS SOLID PROPELLANT

1st Stage - Castor 120

108,005 LBS SOLID PROPELLANT

Castor IVA Strap-Ons

89,080 LBS SOLID PROPELLANT

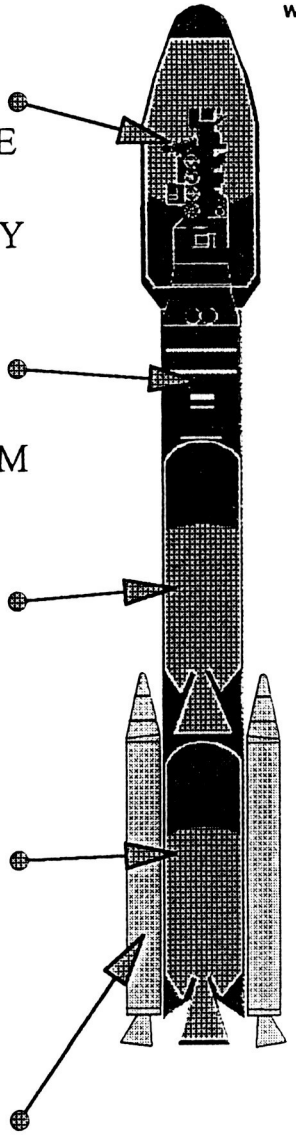

FIGURE 1

Environmental Process Improvement

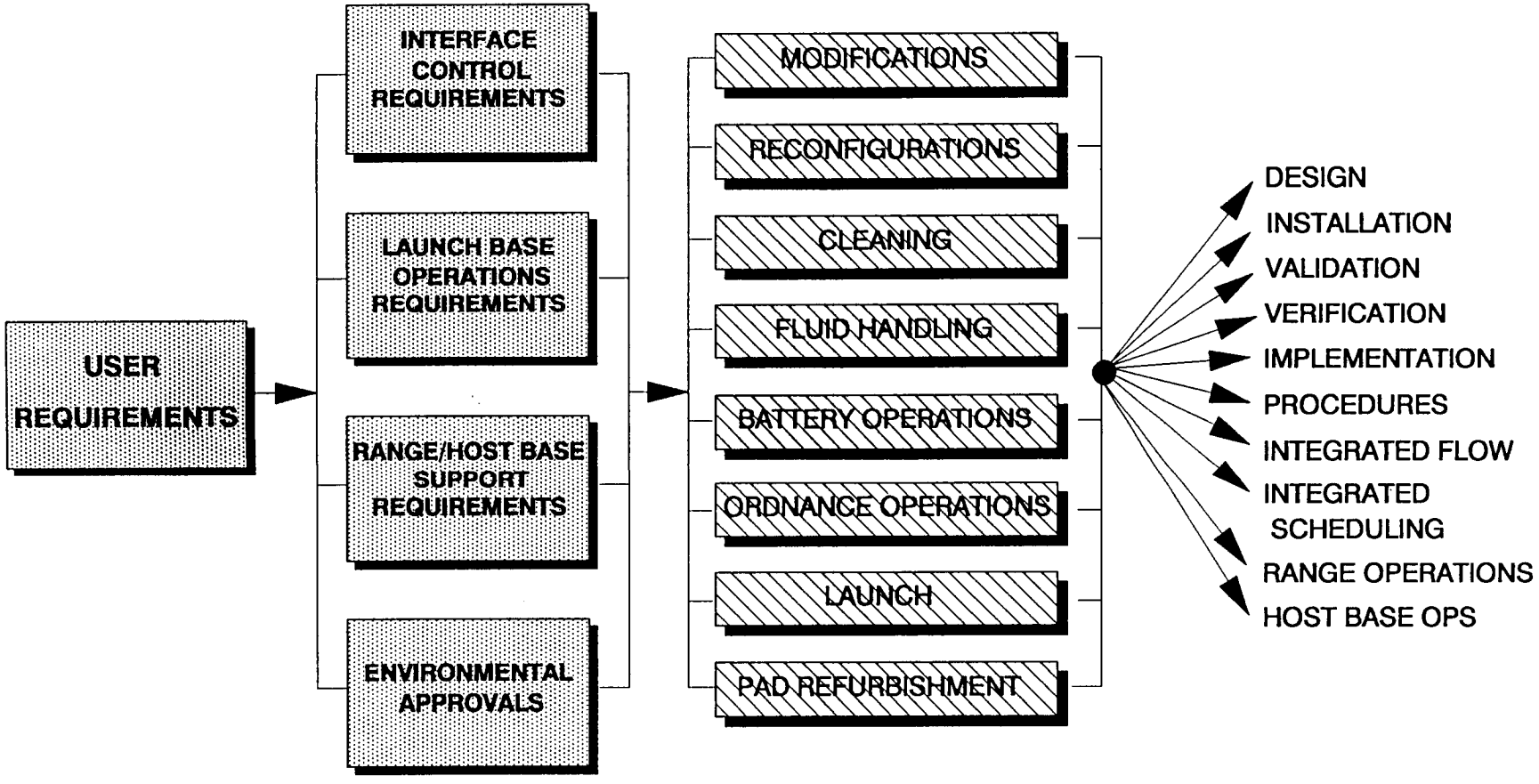

Figure 2

ADEPT PAPERLESS SYSTEM

WESTERN COMMERCIAL SPACE CENTER
(WCSC)
BASIC ADEPT COMPUTER SYSTEM
- COMPUTER PROGRAM DEVELOPMENT AND MAINTENANCE
- SYSTEM INTERFACE SUPPORT TO USER

NEW USER
- ENTERS DATA INTO ADEPT SYSTEM FORMS
  - VEHICLE CHARACTERISTICS
  - SUPPORT EQUIPMENT CHARACTERISTICS
  - OPERATIONS PROCESSES
- SENDS DATA BY MODEM TO 30SPW/ET AT VAFB

ADEPT SYSTEM
- **AUTOMATED, PAPERLESS, MODEM ACCESSED PERMIT APPLICATION SYSTEM FOR APCD**
- **ELECTRONIC FORMS, APPROVAL SIGNATURES, PROCESS AND TIME MANAGEMENT CAPABILITIES FOR USERS, 30SP/ET AND APCD**

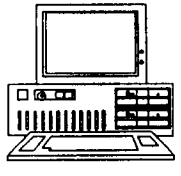

30SPW/ET
(VAFB ENVIRONMENTAL)
- RECEIVES DATA BY MODEM FROM USER AND ENTERS DATA INTO ADEPT SYSTEM
  - VERIFY COMPLETENESS BEFORE TRANSFER TO APCD
  - APPROVAL SIGNATURES
- SENDS DATA BY MODEM TO APCD

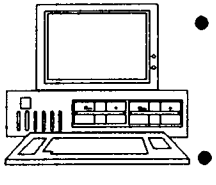

SANTA BARBARA APCD
- RECEIVES DATA BY MODEM FROM 30SPW/ET AND
  - REVIEWS FORMS
  - PROVIDES SIGNATURE APPROVALS
- SENDS APPROVED FORMS BY MODEM BACK TO USER

Figure 3

Pilot Program Study Schedule

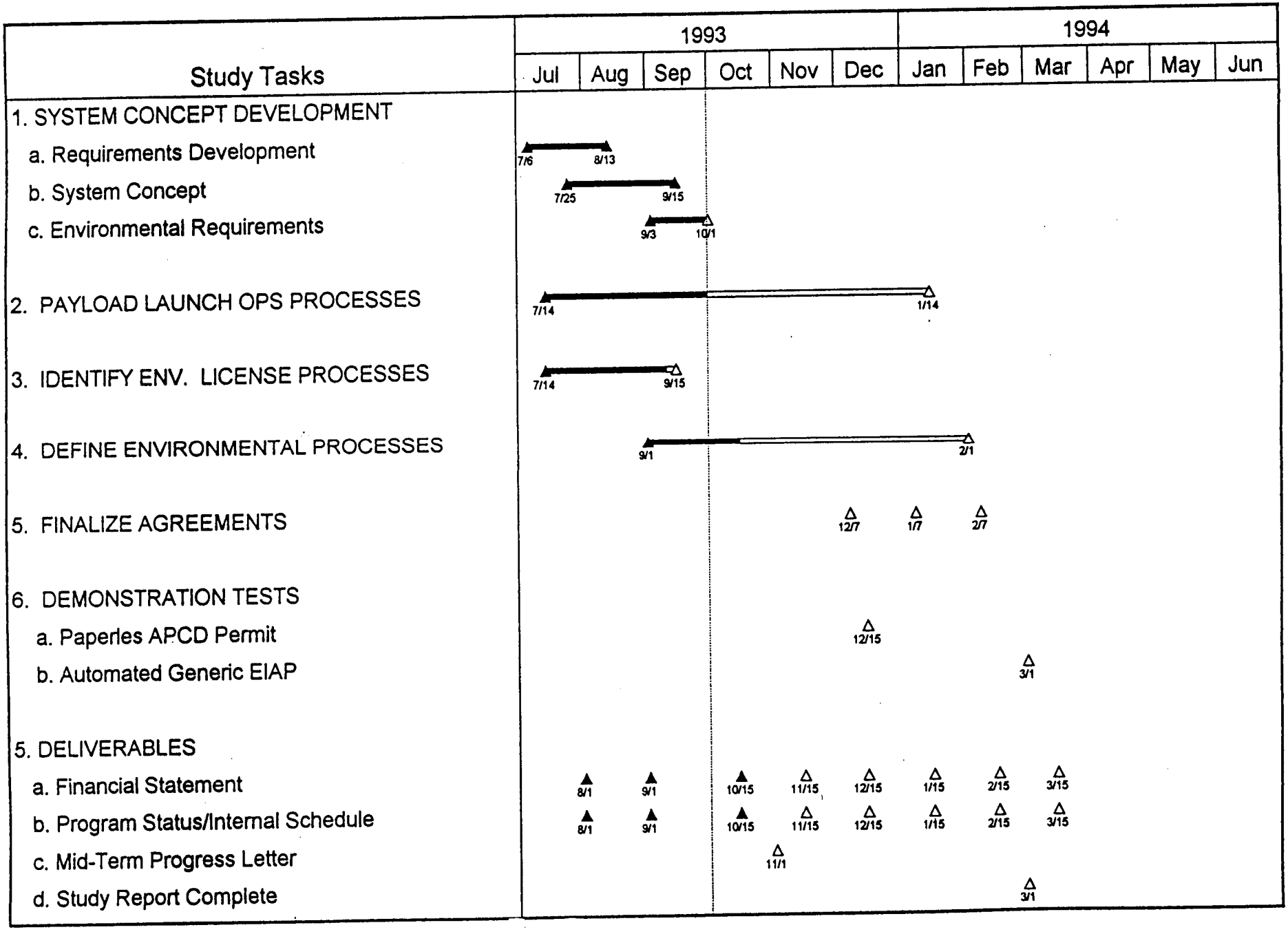

FIGURE 4

THE CASTOR 120™ MOTOR: DEVELOPMENT AND QUALIFICATION TESTING RESULTS

Jack G. Hilden† and Beverly M. Poirier, Ph.D.††
Thiokol Corporation
Brigham City, Utah

Abstract

This paper discusses Thiokol Corporation's static test results for the development and qualification program of the Castor 120™ motor. The demonstration program began with a 25,000-pound motor to demonstrate the new technologies and processes that would be used on the larger Castor 120™ motor. The Castor 120™ motor was designed to be applicable as a first stage, second stage, or strap-on motor. Static test results from the Castor 25 and two Castor 120™ motors indicated the objectives for each motor were met or exceeded. Data from the two Castor 120™ motors are discussed in this paper. The results verified the feasibility of tailoring the propellant grain configuration and nozzle throat diameter to meet various customer requirements. The first and second motors were conditioned successfully at ambient temperature and 28° F, respectively, to demonstrate the design could handle a wide range of environmental launch conditions. Furthermore, the second Castor 120™ motor demonstrated a systems tunnel and forward skirt extension to verify flight-ready stage hardware. It is anticipated the first flight motor will be ready by the fall of 1994.

Program Overview

Five years ago, Thiokol Corporation's Strategic Operations began a company-funded program to develop and demonstrate a new line of solid propulsion motors for the expendable launch vehicle (ELV) market: the Castor 120™ motor. The goal was to combine Thiokol's experience on high performance ballistic missile systems with robust, high safety-factor designs typified by our existing Castor and STAR series of motors. These motors have a distinguished history of successful performance on United States missile and ELV fleets.

The Castor 120™ motors are similar in size to Peacekeeper Stage I production motors. Both motors are about 92 inches in diameter, but the Castor 120™ motor is approximately 20 inches longer (length = 350.9 inches) and weighs about 10,000 pounds more (i.e., 116,000 pounds) than the Peacekeeper motor. This size similarity allows use of existing facilities, tooling, and handling and transportation equipment, thereby keeping development costs to a minimum.

The inherent advantages of the Castor 120™ motor are that it: 1) is relatively easy to handle, 2) is commercially transportable, 3) provides tailorable performance, 4) avoids segmentation which larger motors require, and 5) offers first stage, second stage, and strap-on applications. The motor is designed for ease of manufacture, takes advantage of state-of-the-art technology and processes available today, and maintains high factors of safety. Furthermore, the Castor 120™ motor is designed to achieve a flight reliability of at least 0.999 based on conservative safety factors and flight experience from the Peacekeeper; Castor I, II, and IV; and STAR series of motors.

We began this company-funded demonstration program by designing, manufacturing, and testing a 25,000-pound motor, the Castor 25, to verify selected materials, components, and manufacturing processes. The Castor 25 was static tested successfully in March 1990 and demonstrated those features and processes that would be used on the Castor 120™ motor. The program continued with the fabrication and static test of the first full-scale article of the Castor 120™ motor (DM120-1), in April 1992. Static test of this motor was extremely successful; it met all of the test objectives and verified our pre-test predictions. In addition, the manufacturing cycle-time reductions, planned through concurrent engineering, were verified.

The second Castor 120™ motor, DM120-2, was constructed using the same materials and processes as those verified on DM120-1 and static tested on 4 March 1993 (Figure 1). One of the objectives of static testing this second motor was to confirm tailorability by incorporating a different grain design and a 14.5-inch nozzle throat diameter (vs. 14.0 inches on

†Vice President, Advanced Programs, Strategic Operations; Member AIAA
††Proposal Manager, Advanced Programs, Strategic Operations

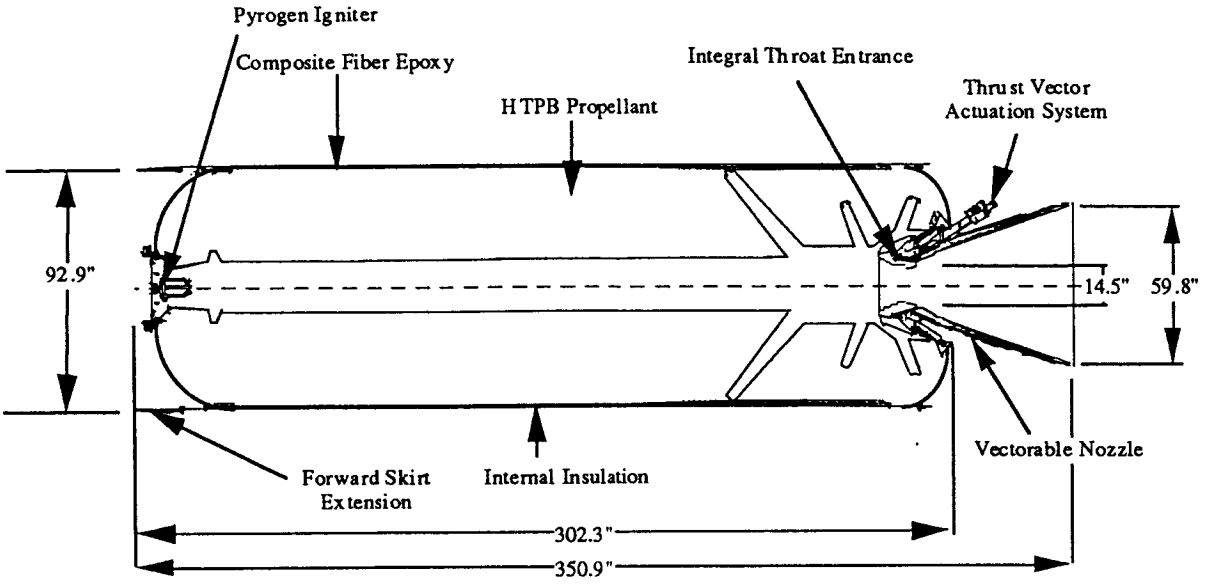

Figure 1. Castor 120™ Motor (DM120-2)

DM120-1). The DM120-2 was conditioned to a propellant mean bulk temperature (PMBT) of less than 30° Fahrenheit (F) to further verify the design capability for various environmental conditions. To the best of our knowledge, no other motor of this size has been tested at this low temperature. A forward skirt extension (FSE) and systems tunnel (i.e., raceway) were added to verify configuration, cost, and processes of these stage hardware items for flight readiness.

Propellant and Grain Design

The Castor 120™ motor's propellant is a modified low-cost, Class 1.3 hydroxyl-terminated polybutadiene (HTPB) propellant. The propellant was formulated to achieve the required burn rate and to lower the burn rate variability. Burn rate variability is 2.7 percent, significantly less than equivalent variability of the Peacekeeper propellant, as demonstrated on two full-scale motor static tests and supported through extensive subscale testing.

The propellant grain is machined allowing for: 1) simple modification of the ballistics in the event that future flight vehicle requirements indicate changes are needed, 2) simplified casting tooling and processes as compared to the more common longitudinal fin designs, and 3) improved safety. The propellant grain for the DM120-2 motor was analyzed over a range of environmental conditions and showed a safety factor of 1.58.

Motor Case and Internal Insulation

The composite pressure vessel component of the motor case is carbon fiber preimpregnated with resin. The fiber and resin were demonstrated successfully during the static tests for the Castor 25, DM120-1, and DM120-2 motors. The resin was demonstrated successfully with carbon fiber in 2 flight tests, 5 burst tests, and 30 first stage ballistic missile motor cases fabricated over a six-year period.

Forward and aft composite skirts also are fabricated with carbon fiber preimpregnated with resin. Polar bosses and end rings feature high-strength aluminum forgings.

The Castor motor case is designed very conservatively using a safety factor of 1.4 times maximum expected operating pressure (MEOP) for the lowest expected burst strength. Motor case skirts are designed to 1.5 times the expected limit of the flight-attachment loads.

The chamber insulation consists of forward and aft insulators. Rubber insulation materials are used to maximize performance. The insulation design is based on extensive performance data and experience on ballistic missile programs. The safety factors (1.25 to 1.5) for these motors compare favorably to the 1.15 factor typically used for ballistic-missile, first-stage motors.

Nozzle

The nozzle uses: 1) common production-proven design features, materials, and processes; 2) standard engineering design practices and analyses; 3) robust factors of safety; and 4) an integral throat entrance (ITE) from materials, processes, and procedures qualified on strategic motors.

Thrust vector control (TVC) is facilitated by a composite flex bearing similar to ballistic motors. Thermal protection for the flex bearing core is provided by thermal extensions used on production flex bearings from prior ballistic missile programs. The exit-cone liner and overwrap structures were demonstrated successfully on the Castor 25, DM120-1, and DM120-2 static tests.

Thrust Vector Actuation System

The cold-gas blowdown thrust vector actuation (TVA) system on the DM120-2 motor was basically the same as the DM120-1 with the addition of an electronic loop closure unit (ELCU) mounted to the stationary shell of the nozzle assembly. Allied-Signal, Garrett Fluid Systems Division, is the TVA supplier. The design requirements and approach were developed concurrently with Allied-Signal which contributed to the low cost of the system.

Igniter and Ordnance

The Castor DM120-2 motor used an igniter developed and flight proven on the Small ICBM program and an HTPB propellant. Static pressure transducers for monitoring the igniter and main motor pressures were installed in the igniter closure along with two through-bulkhead initiators (TBIs).

The ordnance harness assembly (OHA) contained a test harness assembly (THA) and a TBI for both static tests. The THA is an electrically initiated test cable that provides TBI activation from a constant current source for reliable initiation. Since the ordnance system on the DM120-2 was redundant, the igniter assembly used two OHAs.

Systems Tunnel

The systems tunnel was demonstrated on DM120-2 utilizing a low-cost prototype of the intended flight hardware. Enclosed in the environmentally isolated systems tunnel was the guidance, instrumentation, ignition and termination cables, and a flight termination linear-shaped charge (LSC) assembly. To simulate typical motor dynamic loading conditions, the systems tunnel included a mass-simulated cable and an inert LSC assembly. Concurrent product development teams designed, developed, and manufactured the systems tunnel in a record six months.

The next sections will review, more specifically, the data and test results obtained to date. The final section will briefly describe future plans for the program.

Test Results And Conclusions

Ballistic Performance

All pre- and post-fire mass properties and ballistic data were within limits and/or close to expected values. Measured ballistic performance results are provided in Table 1. The data from the two static tests demonstrated the ballistic feasibility of the machined propellant grain. Analysis of the predicted vs. measured data indicated performance can be predicted accurately when alternate grain configurations are used to meet customer requirements.

Table 1. Motor Performance Summary Data for the Castor 120™ Motors

Parameter	DM120-2 (Measured at 28° F)	DM120-1 (Measured at 78° F)
Action time (t_a) sec (15 psia to 150 psia)	87.6	79.0
Average vacuum thrust over t_a, lb_f	341,900	379,400
Maximum vacuum thrust, lb_f	430,000	423,000
Average pressure over t_a, psia	1,055	1,245
Maximum pressure, psia	1,381	1,449
Propellant specific impulse (I_{sp}), lb_f-sec/lb_m	279.9	280.2
Vacuum total impulse over t_a, lb_f-sec	29,872,400	29,974,400

Figure 2 reveals the predicted thrust-time traces for first stage, second stage, and strap-on configurations. Actual thrust traces for DM120-1 and DM120-2 are contained in Figure 3. The DM120-1 thrust trace was tailored to demonstrate a first stage motor configuration while the DM120-2 motor was tailored to a strap-on motor configuration or a first stage motor configuration where maximum dynamic pressure (max Q) was an issue.

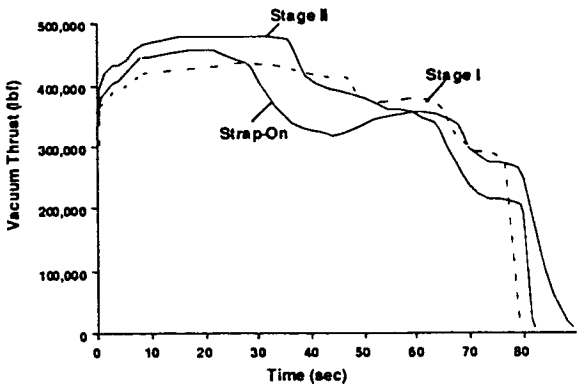

Figure 2. Thrust Time Tailorability

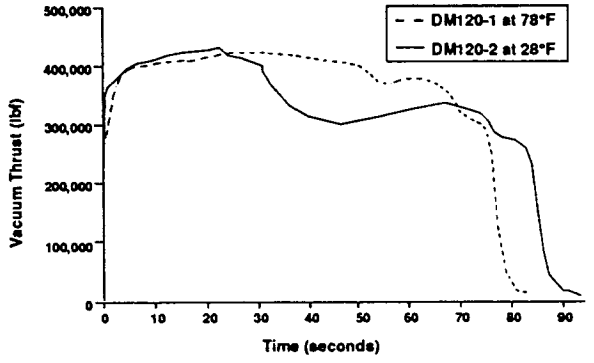

Figure 3. Thrust-Time Trace Profiles for DM120-1 and DM120-2

Propellant mean bulk temperatures for the first and second static tests were at ambient temperature (78° F) and 28° F, respectively. The DM120-2 motor is the largest motor tested at this temperature, demonstrating high margins over predicted temperatures. These demonstration tests confirmed that the Castor motor designs can handle varying environmental launch temperatures successfully.

Motor Case and Internal Insulation

The motor case strains and displacements measured during the static test for the DM120-1 were slightly higher than expected. Additional wafer material was added on the forward and aft domes to decrease these strains. On the DM120-2 motor dome strains were expected to be 80 percent or less of maximum cylinder strain. The maximum forward and aft dome strains were 65 and 73 percent, respectively, of the cylinder strain, and met the test objective. Maximum strain was measured on the mid-cylinder of the case and found to be similar to the strain measured during hydrotest.

Strains measured on the forward skirt and systems tunnel port hole were low in magnitude and within acceptable limits. The port hole was determined to be structurally adequate. Measured strains on the main body of the FSE were fairly low and near those measured on the forward skirt of the DM120-1 and DM120-2 motors.

Evaluation of the post-fired insulation revealed greater internal insulation material loss rates than expected. The cause of the higher loss rates was attributed to: 1) variability in the forward dome environment, 2) changes in localized gas dynamics due to the modified aft-end grain geometry, and 3) variation in the insulation material performance. Because of the excessive margin demonstrated at the majority of the insulator stations in both DM120-1 and DM120-2, a future redesign is being considered to reduce insulator weight by 410 pounds.

Nozzle

The nozzle design from the first to second motor did not modify any of the materials or processes. However, a few variations existed between the nozzles (Table 2). The DM120-2 nozzle was designed to demonstrate design tailorability and thermal and structural robustness of the nozzle components to operate under new environments. Furthermore, the duty cycle for the DM120-2 static test was developed to assess vector angle-over-time capabilities for potential customer requirements.

Table 2. Nozzle Design Characteristics

Parameter	DM120-1	DM120-2
Throat diameter	14.0 in	14.5 in
Exit-cone expansion ratio	17:1	17:1
Exit-cone contour angle	13 deg	13.8 deg

Overall, the nozzle performance on both static tests was excellent. Measured erosion and char data as well as thermocouple instrumentation results showed the nozzle design exceeded desired thermal safety factors. The flex bearing performed as expected. The thermal protection system for the flex bearing successfully verified the capability for use under the extended burn-time conditions (87.6 seconds for DM120-2 vs. 79.0 seconds for DM120-1). Nozzle strain levels were within acceptable levels and verified the nozzle design exceeded desired safety factors. Cause and effect relationships between

nozzle vectoring and material degradation were identified with the tailored duty cycle and will be used to evaluate future duty cycles.

Thrust Vector Actuation System

The TVA for the DM120-2 used refurbished hardware from the DM120-1 motor. During refurbishment, several hardware modifications were incorporated to upgrade the TVA from a demonstration system to a flight-ready system. The intent of this upgrade was to incorporate all TVA features requiring qualification by static test.

Primarily, the static test for the second motor focused on the enable time, step response, and ELCU functionality. Enable time was defined as the time beginning with the TVA initiation signal until the pressure reached 2,800 psi. For the DM120-2 test, enable time was 5.3 seconds which was longer than the DM120-1 test (4.22 seconds) and 0.3 seconds longer than the original design estimates. Analysis showed this increase was due to the additional dead volume which developed in the reservoir piston as the fluid chilled and contracted.

The TVA met both the 20-degree/second slew rate and the 0.060-second step response goals. Slew rate was calculated from the actuator position between 0.5 and 4.5 degrees during a 5-degree step event. Overshoot of the actuator was essentially nonexistent.

Signal conditioning of the ELCU telemetry channels functioned as expected. Actuator feedback voltage recorded for pitch and yaw is shown in Figures 4 and 5, respectively. The effect of bias (to correct geometric position errors due to motor chamber pressure) was evident as the actuator null feedback position varied with time. The ELCU controlled the actuators as expected and conditioned all flight telemetry properly.

Igniter

Igniter performance was adequate to ignite the motor. Ignition transient was within the predicted limits and the igniter closure was found to be structurally adequate. Insulation and bond on the closure protected the metal closure under static test conditions and the central portion of the igniter and closure for the extended motor burn time during the DM120-2 static test.

The Small ICBM igniter provided ignition characteristics more conducive to ELV requirements than the DM120-1 igniter and demonstrated one igniter configuration could be used for first stage, second stage, and strap-on applications.

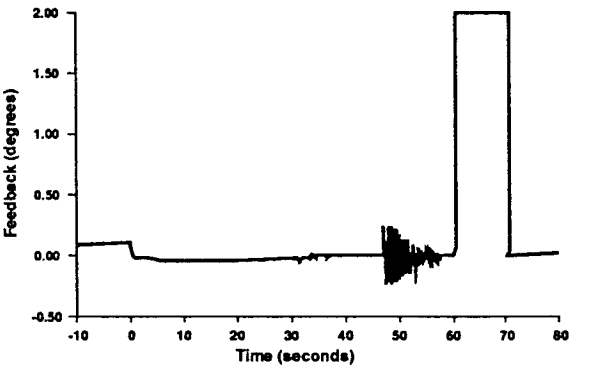

Figure 4. Pitch Actuator Feedback

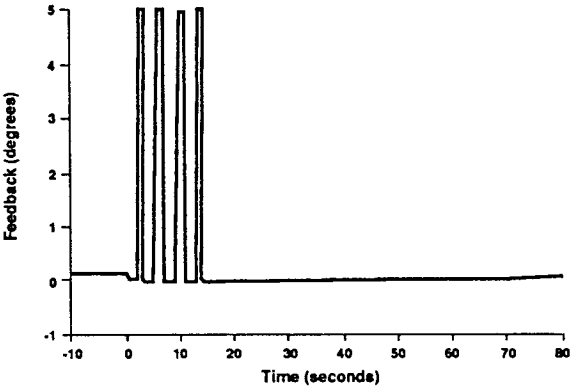

Figure 5. Yaw Actuator Feedback

Systems Tunnel

The bonds (bracket-to-case external protection material (EPM)) were unchanged following the DM120-2 static test. Scuff marks on the rail assemblies (0.0 to 1.4 inches) showed that the rails slid under the brackets, as designed. The aft rail brackets showed no signs of binding indicating smooth sliding as the case both expanded under pressure and contracted as pressure went down. All fasteners used to hold the systems tunnel appeared to be in perfect condition following the test. All seals were in place.

The systems tunnel covers showed no sign of contact with bracket center supports indicating radial movement of less than 0.050 inches. The forward port extension and local interfaces (i.e., end ring and FSE) were unchanged.

The systems tunnel performed as predicted. Bracket bonds and fastening configurations were verified by

the static test. The forward port extension provided adequate strength for the port opening.

Summary

The Castor 120™ motor development and qualification program successfully demonstrated two full-scale motors for flight-ready and production configurations. The Castor program's unique design tailorability feature showed the motor can be modified easily to accommodate specific customer requirements for first stage, second stage, and strap-on applications.

Future Plans

The results of the two static tests, in conjunction with supporting development efforts, demonstrated the Castor 120™ motor is qualified for first-stage flight and strap-on applications. All critical engineering and manufacturing requirements for first-stage operation also were demonstrated. Two launch service suppliers have initiated programs to use the Castor motor in flight applications. First flight is expected in a Lockheed LLV-1 demonstration launch in November 1994. Additional development and another static test will be conducted by Thiokol to complete validation of second stage requirements when those capabilities are needed by an appropriate launch service.

OMIT

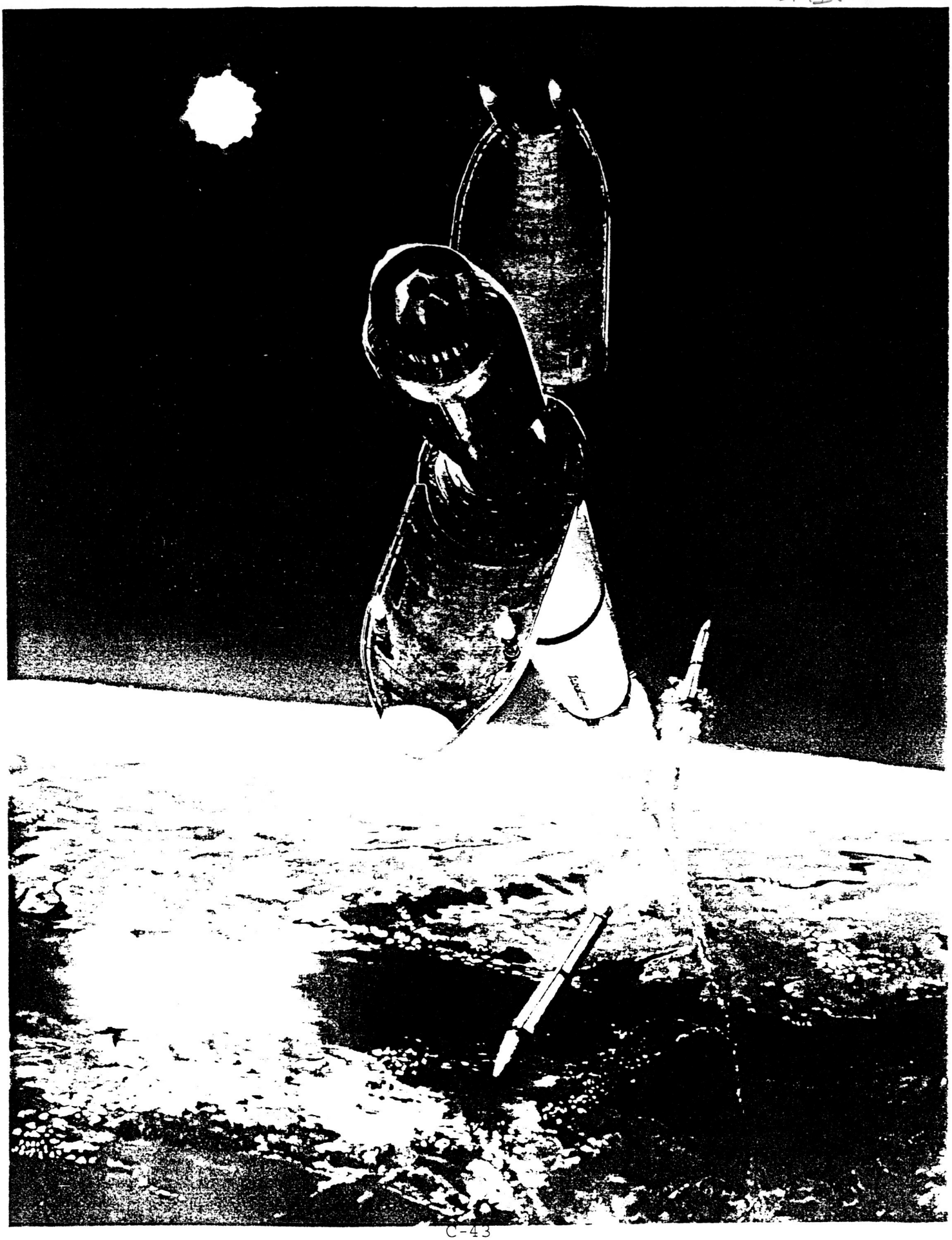

The COMmercial Experiment Transporter

United States' First Complete Commercial Space Service

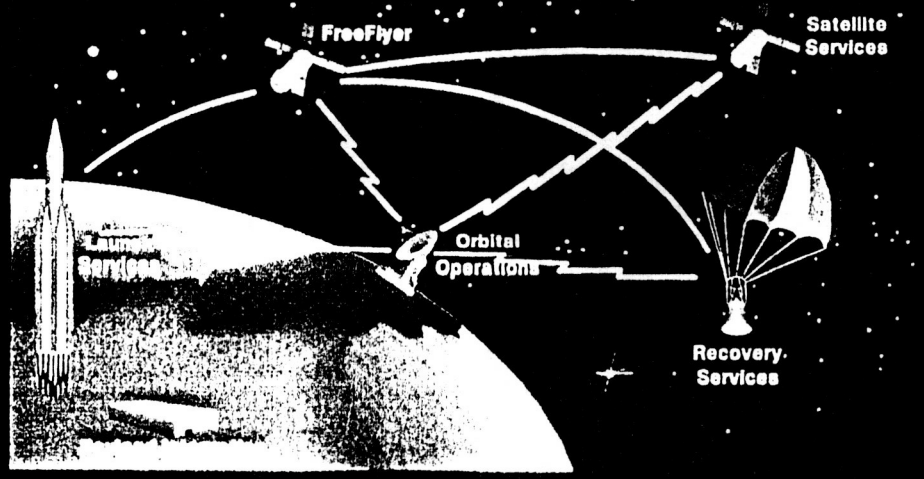

Directed by: Center for Space Transportation and Applied Research (CSTAR)
A NASA Sponsored Center for the Commercial Development of Space

Provided and Operated by the Team of:

SPACE INDUSTRIES

Westinghouse

SPACE SERVICES DIVISION

Payload Accommodations

Parameter	Service Module	Recovery Module
Total Payload Weight	68 kg (150 lb) typical	136 kg (300 lb) typical
Total Payload Volume	0.42 m^3 (15 cu ft)	0.25 m^3 (9 cu ft)
Power Available to Payloads		
- Continuous	350 W	350 W
- Peak	400 W for 200 hr	400 W for 200 hr
- Voltage	28 V ± 4 V dc	28 V ± 4 V dc
Heat Rejection	400 W	400 W
Internal Environment		
- Pressure	Vacuum	1 ATM
- Atmosphere	0 ATM	Dry air
- Temperature	22 ± 3° C (72 ± 5° F) at baseplate	22 ± 3° C (72 ± 5° F) at baseplate
Telemetry		
- Command uplink	9.6 kbps (S-band)	9.6 kbps (S-band)
- Data downlink	250 kbps	250 kbps
- Video downlink	Compressed NTSC - 250 kbps	Compressed NTSC - 250 kbps
- Frequency of transmissions	5 passes/day, 10 min per pass	5 passes/day, 10 min per pass
Loads on Payloads		
- Powered flight loads	< 12 g	< 12 g
- Re-entry loads	NA	< 10 g
Launch Access	NA	Up to (t_L -6) hr
Recovery Access	NA	After (t_R+4) hr

Westinghouse Is Now Using the Systems Developed for COMET To Offer the WESTAR Service

- WESTAR is fully integrated service to launch, operate and recover payloads
- Applications
  - Microgravity experiments
  - Life science experiments
  - Remote sensing
  - Equipment and materials testing
  - Communications

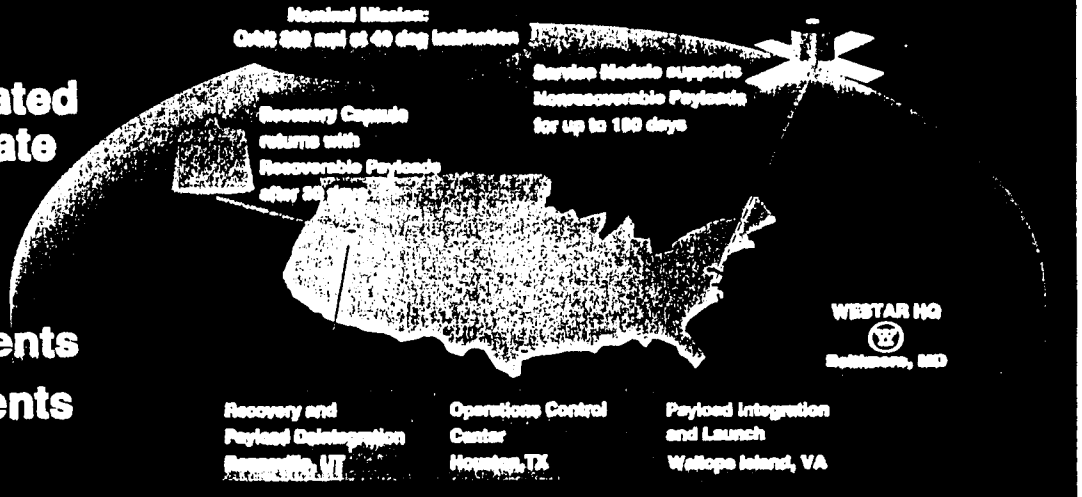

WESTAR Provides One-Stop Service

The Standard WESTAR Mission Is Offered as a Fully Integrated Service Including:

- Payload integration
- Launch services
- Orbital operation
- Recovery
- Program management

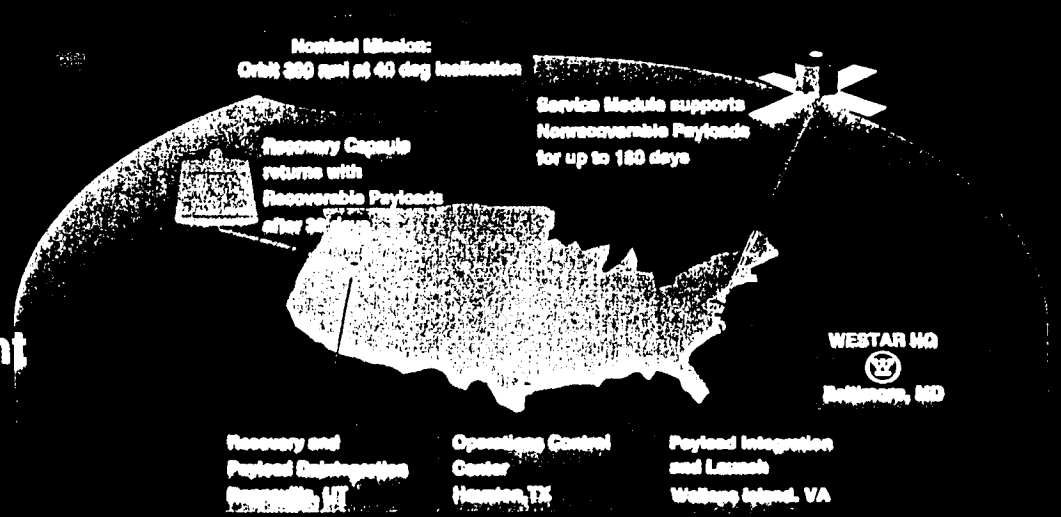

Mission Parameters

Mission Duration	30 days or longer
Nominal Orbit	550 km (300 nmi) 40° inclination
Microgravity Level	$<10^{-5}$g; disturbances minimized
Attitude Pointing	Solar Inertial
Attitude Control	3-axis active control using reaction wheels and mag torquers
Power	
- Housekeeping	115 W
- Payload	400 W

The WESTAR Freeflyer Is a Dual Mission Concept

The WESTAR Recovery Vehicle Has an Orbit Duration of 30 Days or Longer

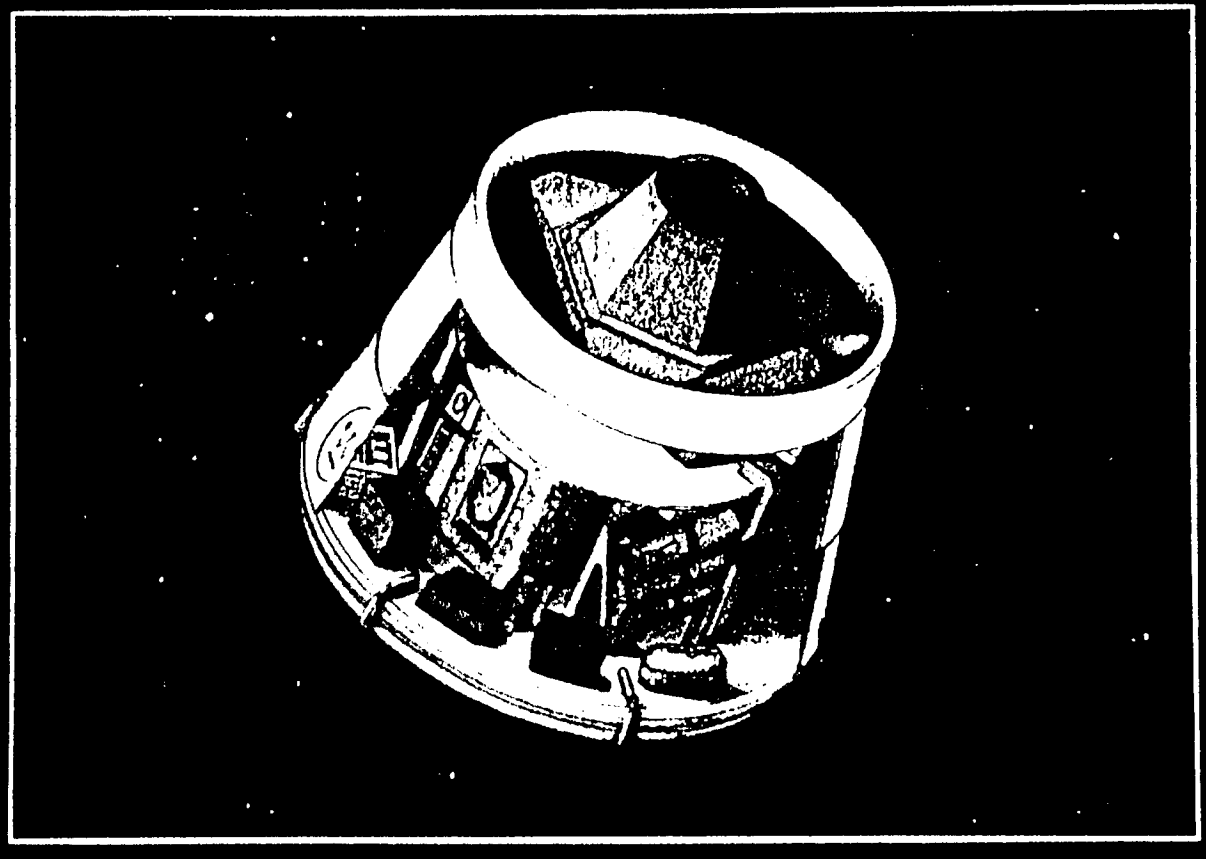

The WESTAR Service Module Has an Orbit Duration in Excess of 2 Years

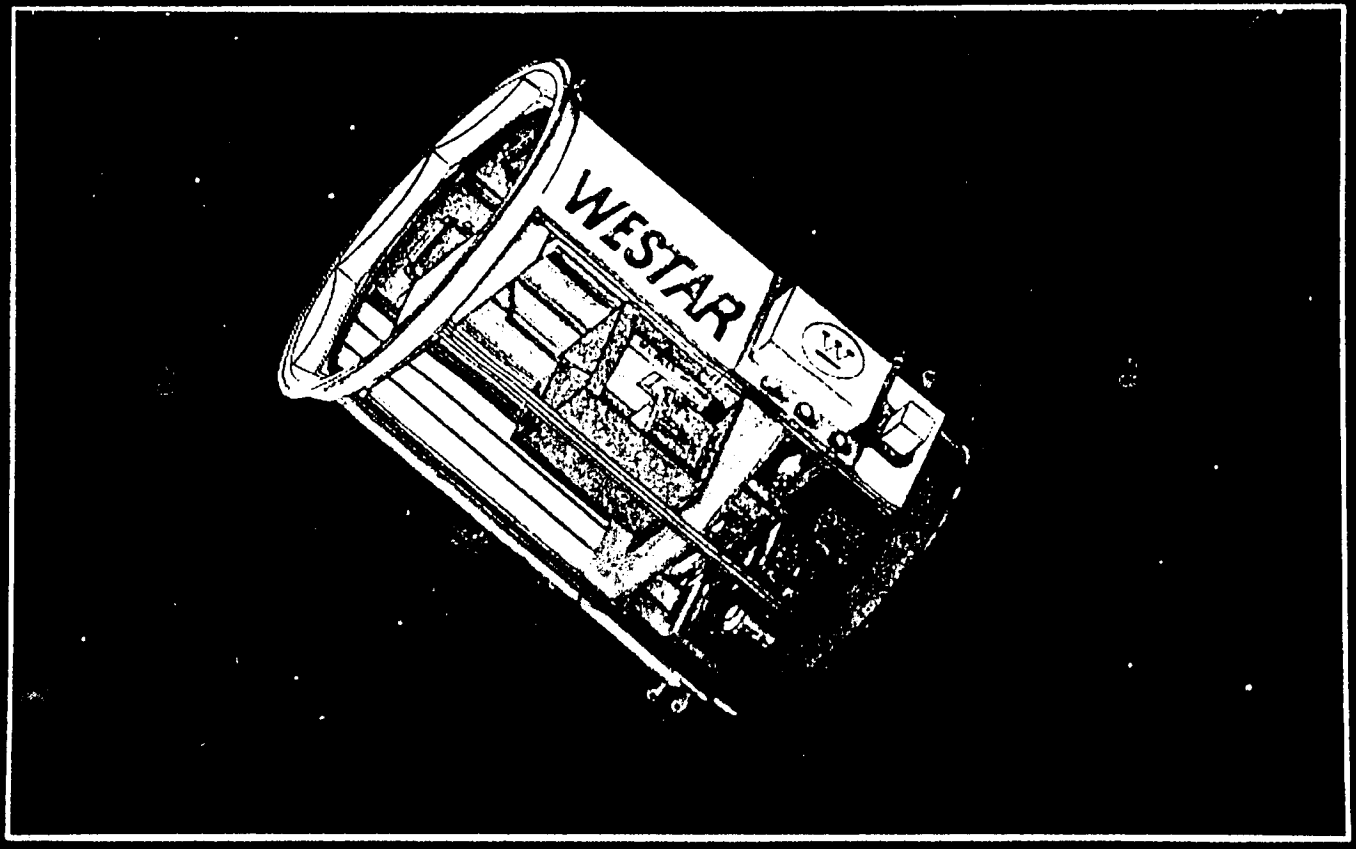

One Way or Round Trip Flights ... on Each Mission

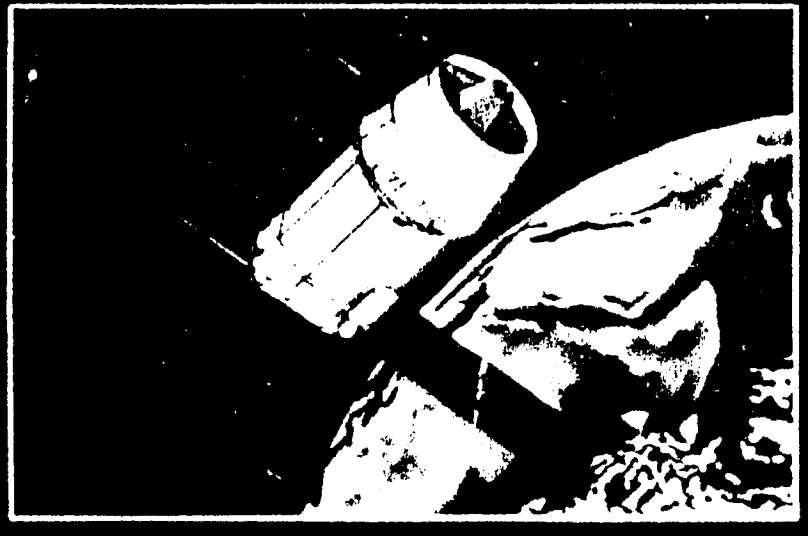

WESTAR Freeflyer Spacecraft

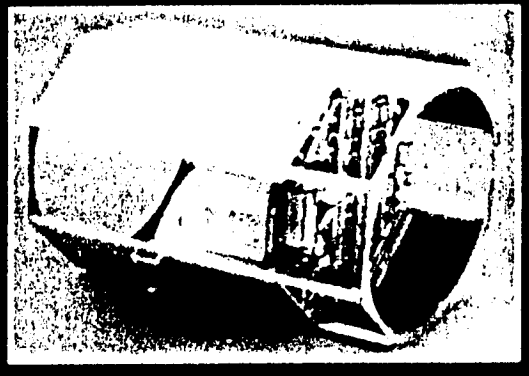

Service Module Shell

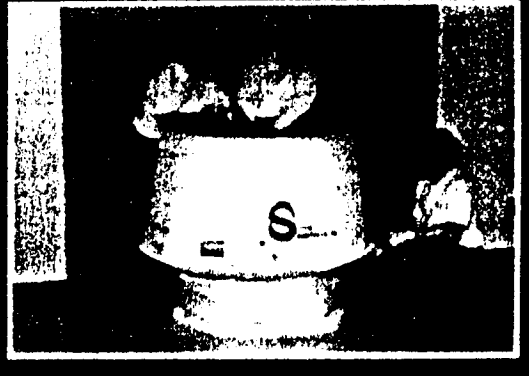

Recovery System

WESTAR User Benefits

- Reliable scheduling
- Fixed price
- Fully integrated service
- Unique recovery capability
- Flexible payload accommodations
- No development required

WESTAR Is Booking Additional Missions ... Now

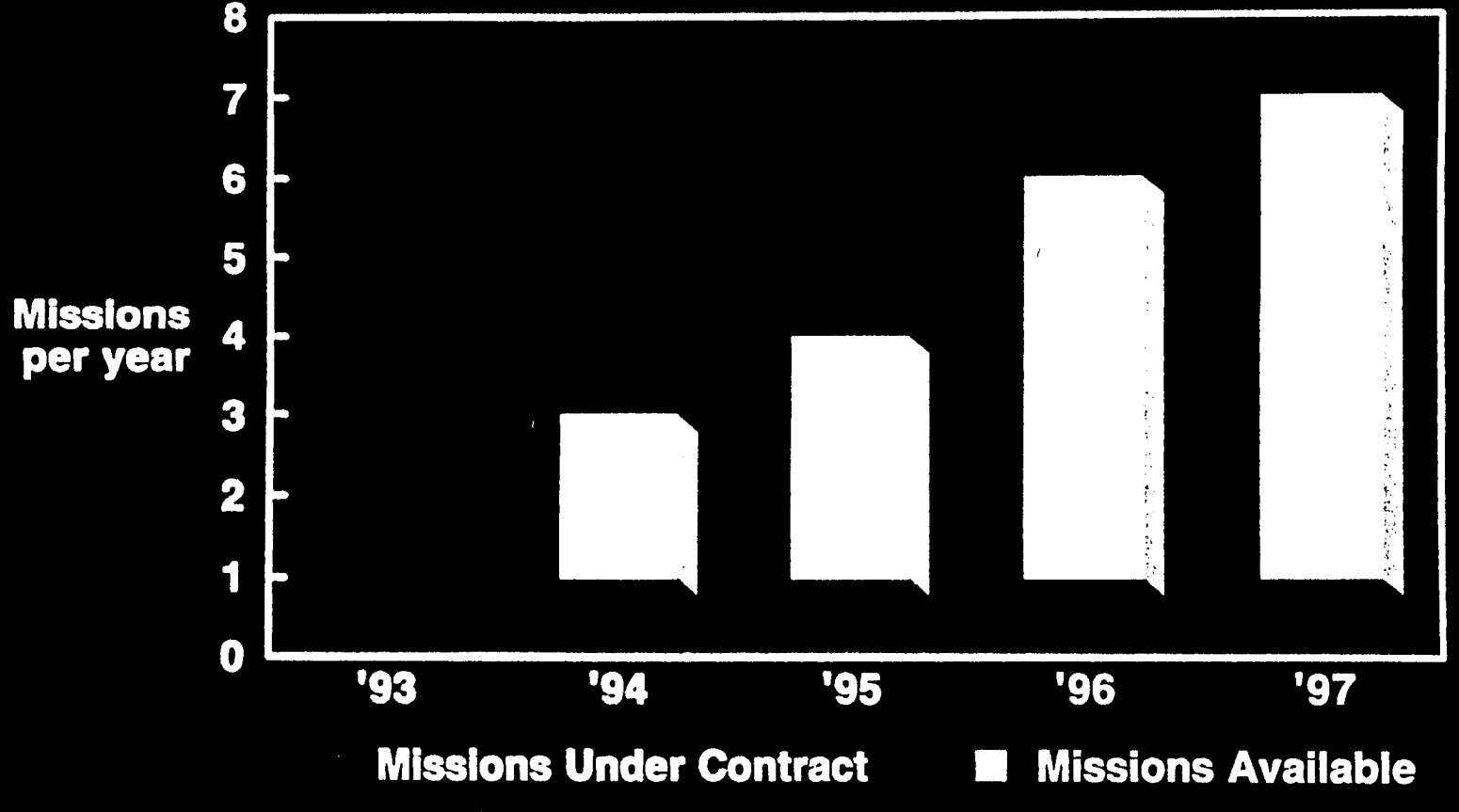

CSTAR TECHNICAL SYMPOSIUM
COMPUTATIONAL METHODS

D

Laser Material Processing

Artificial Intelligence/ Expert Systems

Space Transportation

Computational Methods

Chemical Propulsion

Electric Propulsion

Overview 1993: Computational Applications

COMPUTATIONAL APPLICATIONS

John A. Benek
The University of Tennessee-Calspan
Center for Space Transportation and Applied Research
UTSI Research Park
Tullahoma, TN 37388-8897

Introduction

Computational applications include projects that apply or develop computationally intensive computer programs. Such programs typically require supercomputers to obtain solutions in a timely fashion. This report describes two CSTAR projects involving Computational Fluid Dynamics (CFD) technology. The first, the Parallel Processing Initiative, is a joint development effort and the second, the Chimera Technology Development, is a transfer of government developed technology to American industry.

Parallel Processing Initiative

Background

Over the past 15 years much effort has been devoted to the development of parallel processing hardware and software. Early efforts in Computational Fluid Dynamics (CFD) were based upon vector supercomputers and initial parallelization studies focused on mapping existing algorithms onto the various parallel computer architectures considered for development. These studies focused on "fine grain" parallelism. That is, they were concerned with making various components of the algorithm operate in parallel on several processors. The fine grain approach has not lived up to expectations; the performance of vector-based computers has not even been matched, much less exceeded for CFD applications. Therefore, efforts toward parallel computing are considered to be of academic interest only by many production oriented, analysis groups. To perform analysis on a production basis requires stability based on standards for both hardware and software. Much of the required stability has now been achieved in both hardware and software. Viable parallel computing architectures follow either the shared or distributed memory models.

The shared memory model allows all processors to access all memory. This model has the advantage that no new programming methods are required; it has the disadvantage that realizable performance is limited by memory access. Memory access limitations arise whenever two or more processors attempt to address memory simultaneously and the communication channels between memory and processors do not have the capacity to transfer all the data simultaneously. The practical limit for this architecture is about six processors with the bus-type memory access.

The distributed model closely couples processors with memory; each processor can directly access local memory. This model has the advantage that it is scalable, i.e., the same procedures that work on two processors have the potential to work on systems with hundreds of processors. It has the disadvantage of requiring new programming strategies to map data to processors and assure that non-local data can be accessed in a timely fashion. Thus, the distributed memory model requires extensive recoding of existing programs to achieve significant parallelization. The performance of this model is limited by network (i.e., communication) latency, i.e., the time required to exchange data among memory blocks.

The distributed memory model includes networked computers, especially networked workstations. Parallel computing on a network can be a cost effective means to gain first hand knowledge of parallel computing issues. It is an attractive because it can potentially provide a significant increase in available computing power with existing equipment. Although networked based parallelism is frequently touted as the best means to obtain supercomputer performance at workstation prices, actual performance is severely limited by network latency. Network latency is inherent in the relatively large distance that messages must traverse across the network and the limited bandwidth (transmission volume) of networks. Latency can be minimized by keeping the processors closely connected. Locating processors and memory in the same unit (i.e., a mainframe) significantly

reduces communication distance and makes the use of ultra-high-bandwidth buses for inter-processor communications feasible. This approach is taken by most massively parallel processing computers.

Parallel computing hardware has also been stabilized by using low cost, mass produced, high performance computer chips (both memory and CPU). These chips are typically used in high end workstations and frequently exceed the performance of supercomputers on scalar computations. A significant benefit of using mass produced chips is a factor of 10 decrease in the cost of supercomputer performance ($\$20\text{-}30\text{x}10^6$ to $\$2\text{-}3\text{x}10^6$). An additional stablizing factor is the development of the Mach kernel for the UNIX operating system. It provides the basis for a truly distributed operating system and is currently a standard for most distributed memory architectures.

Several programming languages have evolved to include parallel features. The most widely used include ADA, High Performance FORTRAN (HPF), C++, and Parallel Virtual Machine (PVM). Of these, HPF and PVM offer the easiest transition path for scientific computing. HPF is a subset of the FORTRAN 90 specification with parallel extensions, but production compilers are generally unavailable. PVM is a message passing protocol; it can be used with several languages including FORTRAN 77 and is currently the de facto standard parallel language. Because PVM can be used with FORTRAN 77, many existing codes can be made parallel with a minimum of recoding.

As noted previously, the fine grain approach to parallelism is not yet mature. However, the "coarse grain" approach seems to hold promise for immediate results. While the fine grain approach focuses on details of an algorithm such as DO loops, the coarse grain approach focuses on high level structures of the algorithm. The Chimera scheme, developed by AEDC and NASA, is ideally suited for the coarse grain approach. The scheme is a domain decomposition methodology that partitions the computational domain into subdomains whose intersections are not necessarily empty. The subdomains communicate by exchange of boundary data. The computational data associated with each subdomain may be assigned to a separate processor.

The Project

AEDC and CSTAR have signed a Cooperative Research and Development Agreement (CRDA) and a joint project with Digital has been established to investigate technical issues associated with parallel computing. The goal is to develop a portable, scalable, parallel version of the Chimera scheme based upon the existing FORTRAN 77 computer codes and PVM. The initial implementation will use a coarse grain model. For applications in which the number of processors exceeds the number of domains, a combined coarse grain/fine grain approach will be taken.

CSTAR has developed working relationships with Convex and Digital computer companies and is an active member of the Convex, Scalable Computing Working Group. Convex has agreed to provide CSTAR access to their massively parallel computer, the SPP. In addition, Convex has provided suggestions and recommendations for development of practical parallel algorithms. Digital and CSTAR have forged a close working relationship. Digital is providing state-of-the art, high performance workstations and associated high-speed networking. Digital is interested in production issues associated with using a workstation farm for parallel computing. Work began in October on the conversion of the Chimera scheme to parallel computing using PVM. To date, a prototype version has been completed and tested on a two workstation network. Timings are shown in Table 1. While these results are too preliminary to draw conclusions, the linear scaling is encouraging. Future efforts include refining the prototype code to provide higher performance, and testing the scalability by executing the code on 4, 16, and 64 processor networks. In addition, a large computationally intensive calculation on a complex geometry will be made to determine performance on a true production problem. Finally, AEDC and CSTAR are developing an alliance with Oak Ridge National Laboratories (ORNL), the developers of PVM. The purpose of the alliance is to share parallel processing technology.

Chimera Technology Development

CSTAR and Rocketdyne are cooperating to transfer the Chimera methodology to Rocketdyne. A five-year project has been established to train Rocketdyne personnel in the use of the Chimera scheme and to convert various production codes to use the methodology. The current effort is to convert the REACT code. It is an incompressible, Navier-Stokes flow solver based on the SIMPLE algorithm. To date, CSTAR has conducted a two-day seminar on the use of the Chimera scheme and has completed the conversion of REACT. Validation testing is underway (on the Digital workstations). The converted code will then be applied to several production problems of interest to Rocketdyne.

TABLE 1
INITIAL PARALLELIZATION RESULTS

CONFIGURATION	TIMING (SEC)
Original Chimera Code	28 Min 48 sec
Chimera with C I/O	18 Min 22 sec
Parallel Chimera (Local File, 1 CPU)	17 Min 45 sec
Parallel Chimera (NFS transfer, 2 CPU)	10 Min 41 sec

CSTAR TECHNICAL SYMPOSIUM
CHEMICAL PROPULSION

E

Overview 1993: Chemical Propulsion at CSTAR

Thermally-Choked Combustor Technology

Overview of Initial Research into
the Effects of Strong Vortex Flow on
Hybrid Rocket Combustion and Performance

Laser Material Processing

Artificial Intelligence/ Expert Systems

Space Transportation

Computational Methods

Chemical Propulsion

Electric Propulsion

OVERVIEW
1993

NDB 511-28

N96-16951

CHEMICAL PROPULSION AT CSTAR

William H. Knuth

The University of Tennessee-Calspan
Center for Space Transportation and Applied Research
UTSI Research Park
Tullahoma, TN 37388-8897

1.0 SUMMARY:

Chemical Propulsion at CSTAR continues to expand its activities and areas of interest. Several new initiatives are being developed which are extensions of, or replacements for, earlier projects. One current focus is on reassessing promising engine cycles and the enabling technologies for implementing them. These engine cycles which include advanced hybrids, and staged combustion cycles have the use of oxygen as a working fluid and coolant in common. Oxygen is used as a turbine drive gas, tank pressurant and as a cooling medium for combustion devices.

CSTAR has interest in the propellant feed systems for advanced rocket engines, including propellant conditioning and tank pressurization, gas generators, and turbomachinery. CSTAR's interests also include propellant injection into the main chamber. These aspects of rocket propulsion embody a diverse range of technical disciplines and technologies, critical to the pursuit of low cost space access.

The chemical propulsion program at CSTAR includes active projects investigating hybrid rocket engine oxygen feed systems, hybrid rocket injectors, gas fed hybrid rocket combustion, elements of main injectors for staged combustion engines, and the development of oxygen-rich combustion devices. CSTAR is actively seeking industrial partners interested in joint participation in one or more phases of the analyses, design, development and application of propulsion technologies and related technical disciplines.

2.0 PROJECTS:

This section presents individual Chemical Propulsion project summaries.

2.1 OXYGEN RICH COMBUSTION STUDIES:

This is the foundation project for several of the projects discussed below. Oxygen rich combustion is an element of several advanced rocket engine cycles. It is a significant feature of large Russian liquid rocket engines. The use of oxygen as a working fluid for turbine drive power, coolant and tank pressurant, leads to simplification and cost reduction in rocket engines. For these uses, the low pressure liquid oxygen in the tank needs to be converted to gaseous oxygen at high pressures. A pump-fed combustion process can be used for this purpose. Such a combustion process is, by definition, oxygen rich, since the major species in the combustion products is oxygen. Several rocket engine staged combustion cycles incorporate such combustion devices.

CSTAR, under an initial agreement with AMAR Research, began investigating these cycles in 1990. Conceptual designs from AMAR were evolved and improved. Knowledge of component features was developed, and combined staged combustion and expander cycles were defined and evolved to conceptual designs.

In 1993, more accurate engine balance calculations were made. The results led to refinement of the flow distribution available for turbine drive power. This parametric study allowed the variation of turbine operating temperature with engine chamber pressure to be shown, along with several turbine design variables. Figures 2.0-1 and 2.0-2 illustrate the parametric results.

Figures 2.0-3 and 2.0-4 illustrate LOX and Hydrogen turbopumps respectively. The turbopumps have integral preburners. These designs are sized for direct application to an SSME sized engine.
Extensions of these studies to other applications and sizes are discussed in the sections to follow.

2.1.1 Variable Mixture Ratio Propulsion Systems

CSTAR is conducting in-house studies of variable mixture ratio liquid rocket propulsion systems, (VMRE). We are studying VMRE systems because they are a logical avenue of improvement for the FFSC cycle propulsion systems, offering an avenue to reduced size of the Hydrogen tank, and providing very high thrust to

weight ratio booster propulsion. High initial thrust to weight means that a more constant acceleration profile can be maintained, (within practical Max Q limits), which reduces gravity losses substantially. This means that for payloads capable of tolerating higher launch accelerations, payload improvements of on the order of 20% are possible for the same GLOW.

In our studies we are looking at the VMRE as an alternate to tri-propellant systems. Tri-propellant concepts seek to take advantage of the density impulse gain of using a dense second fuel such as RP-1 during the boost phase of the flight. We recognize that nearly the same benefit can be gained by merely operating the propulsion system oxygen rich during the early phase of the flight. The drawback of the oxygen rich operation is that we do not have a proven material (or coating) for the main chamber when the combustion products have excess oxygen present. We are seeking an industry partner with which to pursue development of the technology.

2.1.2 COMBINED CYCLE ENGINE:

The combined cycle engine is an inhouse CSTAR study that is extending work begun at AMAR Research Corporation during 1990, on combining expander and staged combustion cycles. In the AMAR concept the Hydrogen turbopump is driven by a fuel-rich preburner, using essentially all the hydrogen flow of the engine. The LOX turbopump is driven by oxygen which has been used as the regenerative coolant for the thrust chamber and heated sufficiently to provide the drive power for the LOX side turbine. The advantage of this approach is that the single preburner required operates fuel rich. An oxidizer-rich preburner is avoided, and most of the benefits of a full flow topping cycle are gained.

The disadvantage of the combined rocket cycle engine is that the chamber is LOX regeneratively cooled.

CSTAR's interest in the combined cycle design is from the standpoint of technology requirements definition. By choosing this option, it would be possible to avoid the requirement for developing an oxygen rich preburner, while still obtaining the advantages of the FFSC cycle.

2.1.3 ANNULAR PORT HYBRIDS

Conventional hybrids flow liquid oxidizer (LOX) into the head end of the fuel grain case, where the oxygen partially vaporizes and burns with head end fuel. The local combustion helps to condition the oxygen before it enters the fuel grain ports. Once in the ports, the oxygen flows axially along the port length supporting combustion of the fuel. The fuel sublimes off the grain surface, and migrates among the turbulent combustion products, reacting with the excess oxygen present. This process produces a grain regression rate that has been found to be related to the mass flux through the port area.

CSTAR and our industrial partner, Martin Marietta Manned Space Systems, are investigating annular port hybrids in which the oxygen is injected tangentially into an annular region between inner and outer fuelgrain elements. The injection ports are distributed along nearly the full length of the grain. This is a distinctly different oxygen injection method from the conventional approach described above.

We expect faster regression rate to be exhibited by the annular port design. The strong scrubbing action of the tangential flow of oxygen as well as the migration of hot combustion products to the center of the swirl are expected to enhance the surface combustion process. Success should lead to more compact hybrid fuel grain cases and a more direct control of fuel regression rate. This approach is well suited for use as a turbine drive gas generator for a pump-fed hybrid rocket propulsion system.

2.1.4 PREMIX INJECTORS:

Conventional rocket engine injectors use various means to induce mixing of the propellants once they are injected into the chamber. The mixing process occurs in the same region as, and to a large degree in parallel, with the combustion process. In many designs the combustion products from initial mixing, separate and shield the unmixed propellants from further mixing. This delays the combustion process and gives rise to the potential for several modes of combustion instability. Other designs use elaborate and expensive schemes to achieve mixing. Precisely drilled orifices, complex coaxial designs and many swirl designs have been tried.

CSTAR is investigating approaches in which propellants are premixed in specially designed and controlled regions just prior to injection into the combustion zone. The advantage of this approach, once it has been developed, is that combustion phenomena associated with non-uniform mixing and mixing delays will be eliminated. We anticipate that chamber wall streaking will be prevented, chamber blanching will be reduced, some chug mode instabilities will be eliminated or reduced, and Isp losses from non-uniform mixture ratio operation will be reduced. We expect that chamber L^* may be reduced because of the more concentrated combustion reaction zone. This means that overall chamber length can be shortened, saving cost, weight and installation envelope.

The CSTAR investigations are a precursor to possible SBIR contracts which have been bid with two industrial partners. By conducting early exploratory work we seek to assure effective and productive phase I projects. We are currently conducting small scale combustion tests with oxygen and hydrogen.

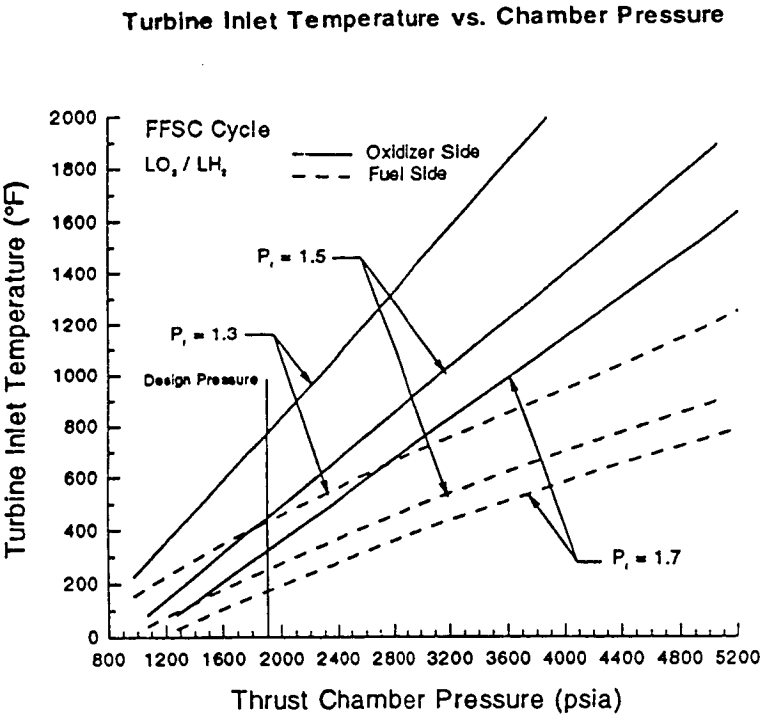

Figure 2.0-1. Full Flow Staged Combustion Rocket Engine Cycle. NOTE: Low turbine temperature allows the use of low-cost turbine materials and simple geometry.

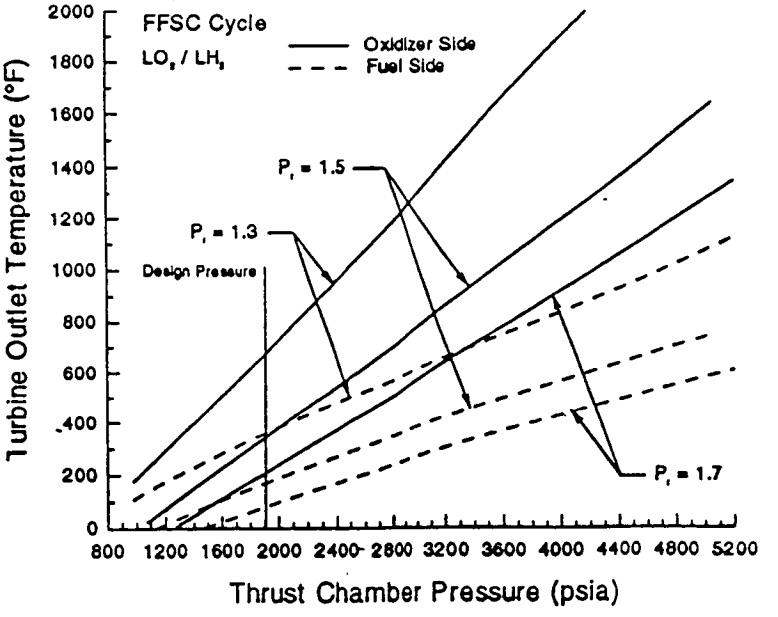

Figure 2.0-2. Full Flow Staged Combustion Rocket Engine Cycle. NOTE: Low outlet temperature delivers cool gaseous propellants to the main injector.

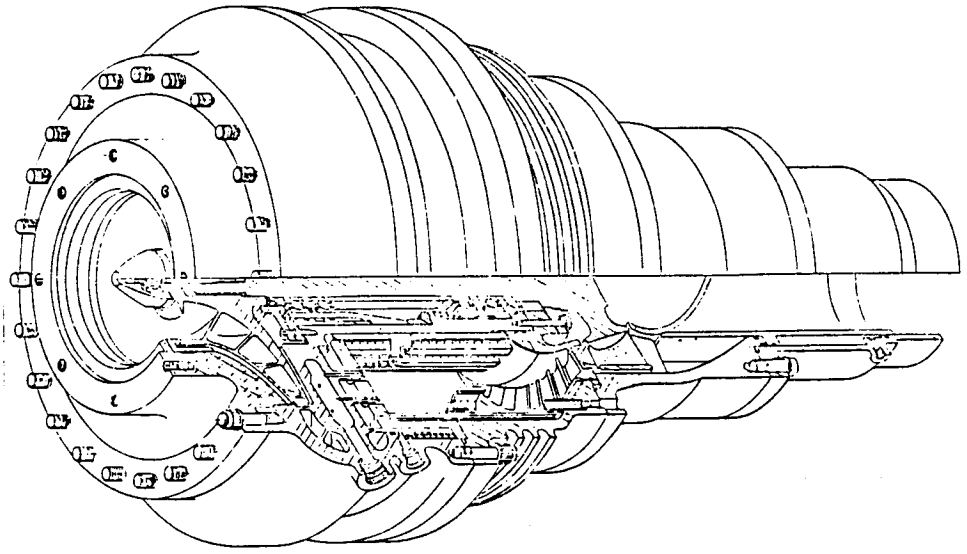

Figure 2.0-3. High Pressure LOX Turbopump with Preburner.

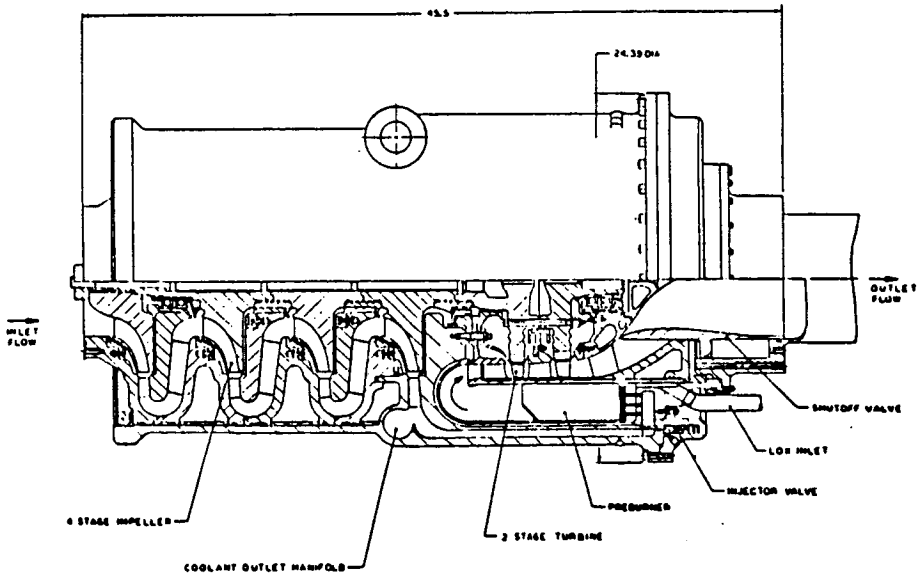

Figure 2.0-4. Four-Stage Liquid Hydrogen Turbopump with Preburner.

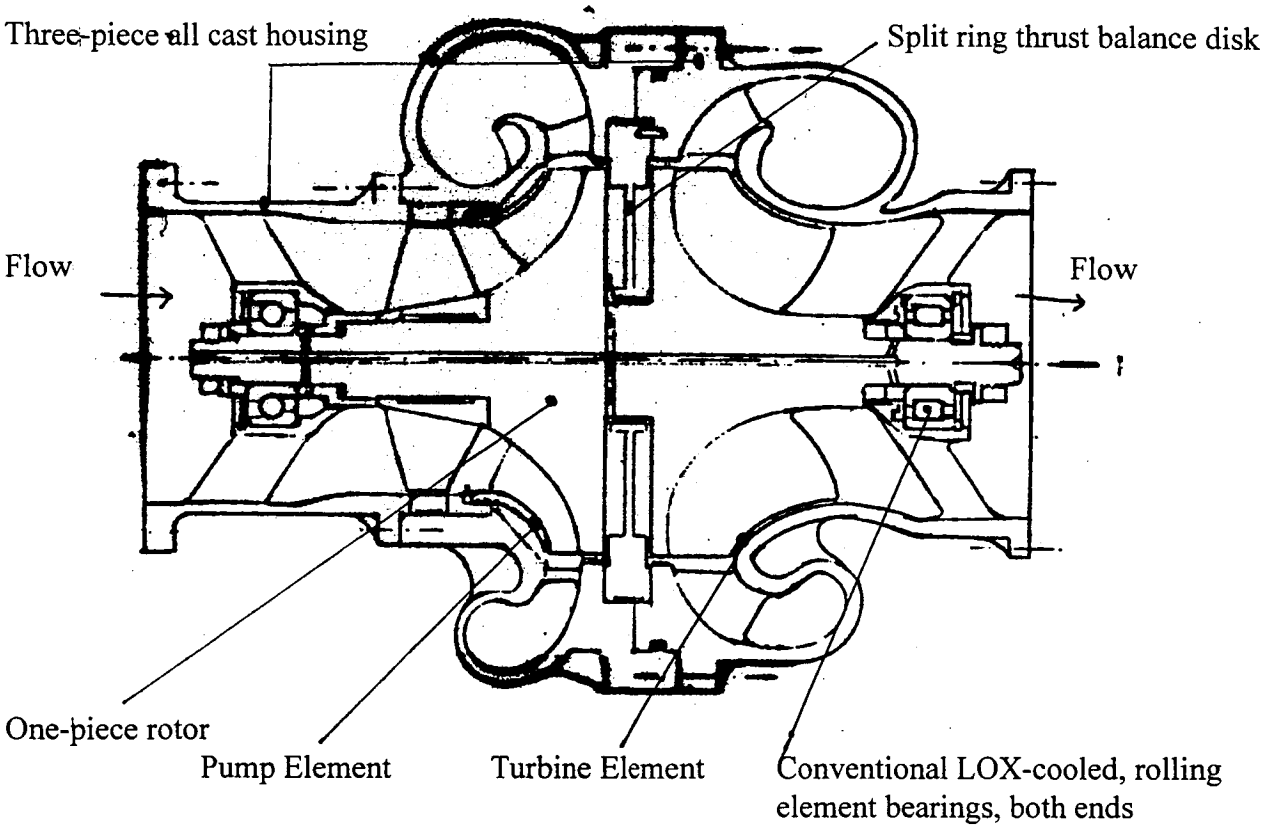

Figure 2.1-1. Ultra Low Cost Oxygen Driven LOX Turbopump for Hybrid Rocket.

Thermally-Choked Combustor Technology

W. Knuth*, P. Gloyer†, J. Goodman‡, and R. Litchford§

University of Tennessee – Calspan
Center for Space Transportation and Applied Research
UTSI Research Park, Tullahoma, TN 37388-8897

A program is underway to demonstrate the practical feasibility of thermally-choked combustor technology with particular emphasis on rocket propulsion applications. Rather than induce subsonic to supersonic flow transition in a geometric throat, the goal is to create a thermal throat by adding combustion heat in a diverging nozzle. Such a device would have certain advantages over conventional flow accelerators assuming that the pressure loss due to heat addition does not severely curtail propulsive efficiency. As an aide to evaluation, a generalized one-dimensional compressible flow analysis tool was constructed. Simplified calculations indicate that the process is fluid dynamically and thermodynamically feasible. Experimental work is also being carried out in an attempt to develop, assuming an array of practical issues are surmountable, a practical bench-scale demonstrator using high flame speed H_2/O_2 combustibles.

Introduction

In chemical rocket propulsion, thrust is generated by converting high-pressure gases at low subsonic velocities to low-pressure gases at supersonic velocities. Traditionally, hot high-pressure gases are formed in an enclosed combustion chamber in which raw propellants are injected at the head and the exit flow is choked through a converging-diverging nozzle. Options for subsonic-to-supersonic flow transitioning other than a geometrical throat are conceivable, however.

For instance, one could utilize Rayleigh flow for heat addition in a constant area duct such that thermal choking back-pressures the system inducing a sonic point. Then, the flow could be transitioned to supersonic conditions in a diverging nozzle. This idea can be pushed even further by requiring that heat addition and thermal choking occur only within the diverging nozzle section. Indeed, this feature forms a central element of the Dual-Mode Ramjet cycle contemplated for hypersonic flight [1-2]; Fig. 1 shows an idealized sketch of the flow field in the ramjet mode. Clearly, the analogy to rocket combustion is direct in that an injector would become the source for gaseous subsonic propellant flow. Although heat addition (Rayleigh) losses are higher for a thermally-choked combustor, the simplicity inherent in the design may offset minor performance concerns.

* Assistant Director for Chemical Propulsion, Principal Investigator
† Graduate Research Assistant
‡ Senior Engineer
§ Research Engineer, Principal Author

This work was supported by the UT-Calspan Center for Space Transportation and Applied Research.

The thermally-choked combustor concept is ideally suited for the Full Flow Staged Combustion (FFSC) rocket engine cycle, shown in Fig. 2, because the main chamber is fed with fully gaseous propellants. By eliminating the main chamber and converging nozzle section and developing an injector for the diverging nozzle section, one could arrive at a simpler, smaller, lighter, and less expensive thrust chamber design as conceptualized in Fig. 3. Such a gas-fed thruster would have an effectively low L* chamber, yet it could still achieve rapid combustion and good c* efficiency.

The basic concept of a thermally-choked combustor is, from a theoretical standpoint, completely valid; however, there are numerous practical issues which make actual construction and operation problematic. Issues such as starting, heat release profile, flame stablization, detonability, and flashback may have an inimical influence on idealized behavior. Ultimately, the practical feasibility of thermally-choked combustors must be determined in the laboratory.

This paper presents our current thinking with respect to this technology and outlines an active program for developing a bench-scale demonstrator. We discuss operational issues using simplified but relevant analysis techniques and summarize progress in developing the demonstrator combustor.

Theoretical

Physical Concept

Fundamentally, there are two alternative injection schemes, premixed or non-premixed, on which to base a thermally-choked combustor design. The dual-mode ramjet cycle is non-premixed by necessity, but rocket engine applications permit a choice. One's instinctive inclination is toward a relatively safe non-premixed design; however, premixed injection offers

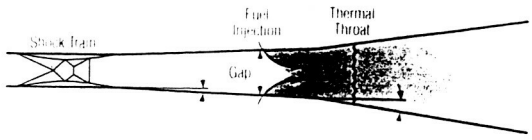

Figure 1: Idealized flow field for the Dual-Mode Ramjet cycle when operating in the ramjet mode (adapted from Edelman et al. [1]).

the best opportunity for collapsing the combustion zone into the smallest region possible. This feature would allow the thermal throat to be very near the injector so that an exaggerated nozzle length would not be necessary. Unfortunately, premixed injection poses significant safety threats which cannot be carelessly dismissed. The practical construction and operation of a thermally-choked combustor will probably hinge on such enabling combustion technology issues.

For illustrative purposes, it is instructive to examine the thermally-choked combustor concept on the basis of premixed injection. Fig. 4 depicts the basic idealized concept. The combustibles enter the nozzle at a subsonic velocity greater than the flame speed and diffuse to higher pressures and lower velocities as the flow area increases. At some point, the flow velocity reaches the burning velocity where a stablized flame front is formed. In the practical case, flame stablization will depend on boundary layer processes and may even reqire the insertion of a coarse mesh bluff body to hold the flame. As combustion proceeds, heat addition dominates over the area change effect, and the flow is forced to accelerate. If the quantity of heat is sufficient, the flow velocity will reach a sonic condition somewhere in the combustion region and a thermal throat will form. Because the area continues to increase, transition to supersonic flow will occur and expansion to lower pressures and higher Mach numbers is possible. In this concept, inertial pressure confinement is provided by a collapsed combustion region rather than a geometrical throat.

To minimize heat addition losses and nozzle size, it is desirable to minimize the size of the combustion region. This implies that one should utilize fuels possessing the fastest chemical reaction rates possible. Furthermore, the classical thermal burning velocity relationship

$$\text{flame speed} \propto \sqrt{(\text{diffusivity})\,(\text{reaction rate})} \quad (1)$$

implies that seeking fast reaction rates corresponds to seeking high flame speeds. There is a bit of good luck in this result since hydrogen gas, a common high-performance rocket propellant, has the highest flame

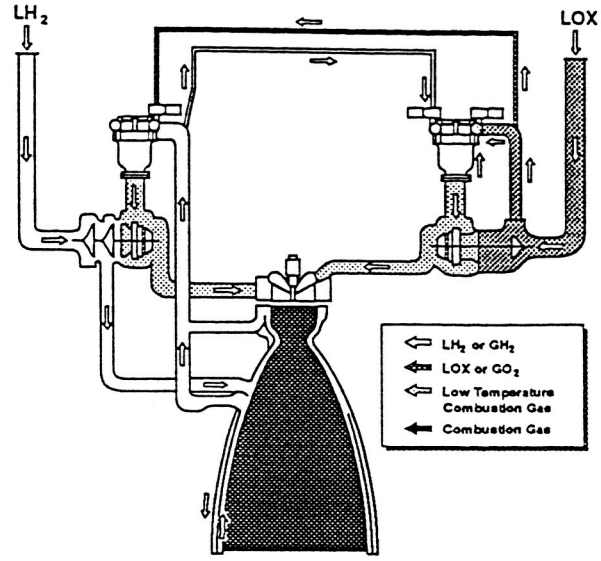

Figure 2: Full Flow Staged Combustion (FFSC) cycle rocket engine schematic (courtesy of Aerotherm Corporation).

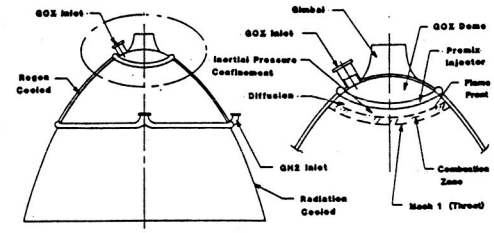

Figure 3: Gas-fed thermally-choked combustor concept for a FFSC cycle rocket engine.

speed of any fuel. High flame temperature acetylene can achieve burning velocities roughly one-half of that attained with hydrogen, but all other hydrocarbons produce burning velocities less than one-half that attained by acetylene.

Measured laminar flame speeds for hydrogen gas burning in air are shown in Fig. 5 as a function of mixture ratio [3]. The maximum flame speed occurs well into the fuel-rich regime (O/F $\approx$ 0.45) because the increased thermal diffusivity associated with excess hydrogen tends to increase the flame speed more strongly than the drop in flame temperature tends to decrease it. Fig. 6 shows the additional effect of oxygenation mole fraction on the laminar flame speed of hydrogen [4]. Increased burning speed with increased oxygen concentration may be attributed, in general, to the influence of flame temperature on reaction rates and diffusivities. For hydrogen burning in pure oxygen, the laminar flame speed is 3.4 times that for combustion with air.

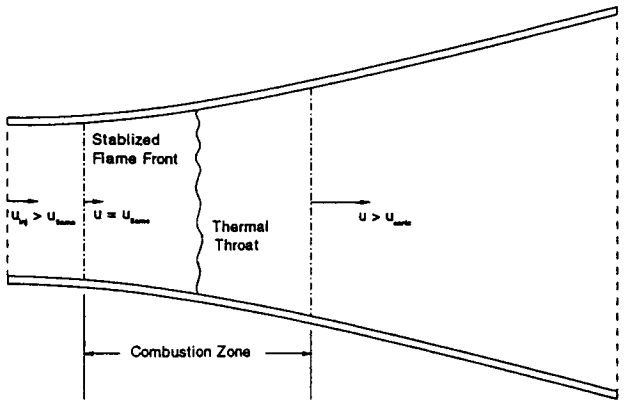

Figure 4: Idealized flow field in a premixed thermally-choked combustor with a stablized flame.

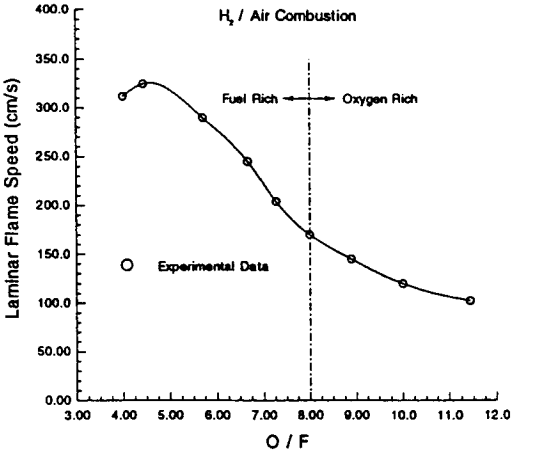

Figure 5: Measured laminar flame speeds as a function of mixture ratio for hydrogen/air combustion (after Gibbs and Calcote [3]).

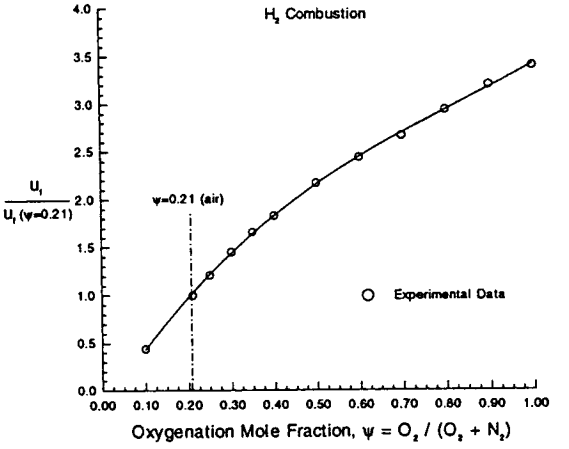

Figure 6: Effect of oxygen concentration, with nitrogen dilution, on the measured laminar flame speed of hydrogen fuel (after Zebatakis [4]).

The effect of turbulence on flame speed is an additional consideration of importance. Turbulent velocity fluctuations produce an apparent flame speed greater than the laminar burning velocity. Indeed, it is not unusual to find apparent turbulent flame speeds 5 to 10 times larger than the laminar value. Unfortunately, turbulence induced amplification effects are configuration dependent, and predictive capabilities for turbulent combustion lack precision. The effectively higher flame speeds for turbulent flow can be used to advantage in the thermally-choked combustor concept, but utilization requires hardware specific development work.

Generalized 1-D Compressible Flow Formulation

In pursuing the development of a demonstrator combustor, it seemed sensible to acquire an analytical support tool. Our immediate needs centered on a simple physical verification of the basic idealized concept and an ability to approximate the expected variation in flow parameters. Clearly, results from simplified one-dimensional gas dynamics theory were not adequate since they do not allow for simultaneous variation in flow area and heat transfer. In contrast, CFD analyses appeared too elaborate and complex for our immediate needs. As a compromise, we settled for a generalized one-dimensional compressible flow analysis of a thermally and calorically perfect gas in conjunction with a very simple combustion model for the heat release profile.

In generalized one-dimensional compressible flows, multiple effects such as area change, heat or mass addition/rejection, and friction can be imposed simultaneously. This generality negates the development of closed-form solutions so that numerical evaluation becomes necessary. The governing system of ordinary differential equations under the above imposed driving potentials are generally presented in terms of influence coefficients for the dependent variable differentials [5]. However, a direct construction by matrix inversion was recently accomplished by Hodge using the symbolic manipulation language MACSYMA [6].

In any case, for a thermally and calorically perfect gas with constant mass flow rate in a duct, the solution of the entire flow field is characterized by a single differential equation for the Mach number squared

$$\frac{dM^2}{dx} = \frac{G(x)}{1-M^2} \tag{2}$$

where

$$G = M^2\Psi\left[-\frac{4}{D_h}\frac{dD_h}{dx} + \gamma M^2 \frac{f}{D_h} + \frac{1+\gamma M^2}{T_0}\frac{dT_0}{dx}\right] \tag{3}$$

with

$$\Psi = 1 + \frac{\gamma - 1}{2} M^2 \tag{4}$$

In the above equations, M is the Mach number, γ is the specific heat ratio, D_h is the duct hydraulic diameter, f is the Moody friction factor, T_0 is the total temperature, and x is the streamwise coordinate.

When $M = 1$ in Eq. (2), the denominator vanishes. Therefore, to insure that the gradient in Mach number remains bounded, $G^* = 0$ at the sonic point where the $*$ superscript indicates that the Mach number has been set to unity. Because dM^2/dx becomes 0/0 indeterminate there, it is further necessary to apply L'Hospital's Rule such that

$$\left(\frac{dM^2}{dx}\right)^* = \frac{[G'(x)]^*}{-(dM^2/dx)^*} \tag{5}$$

implying

$$\left(\frac{dM^2}{dx}\right)^* = \pm\sqrt{-[G'(x)]^*} \tag{6}$$

where $[G'(x)]^*$ has been evaluated by Shapiro [5].

The computational procedure follows that delineated by Beans [7]. First, the total temperature is specified at the inlet. Then, based on an imposed variation in area, total temperature, and friction, the sonic point, if one exists, is located where $G^* = 0$. From the sonic point, Eq. (2) is solved back to the inlet and forward to the exit using a fourth-order Runge-Kutta solver. Once the Mach number distribution is known, the remaining flow properties are obtained by specifying reference conditions and applying the following integral relations.

Integral Relations:

$$\frac{T}{T_i} = \frac{T_0}{T_{0i}} \frac{\Psi_i}{\Psi} \tag{7}$$

$$\frac{P}{P_i} = \frac{A_i}{A} \frac{M_i}{M} \sqrt{\frac{T}{T_i}} \tag{8}$$

$$\frac{u}{u_i} = \frac{M}{M_i} \sqrt{\frac{T}{T_i}} \tag{9}$$

$$\frac{P_0}{P_{0i}} = \frac{P}{P_i} \left(\frac{\Psi}{\Psi_i}\right)^{\frac{\gamma}{\gamma-1}} \tag{10}$$

$$\frac{F}{F_i} = \frac{P}{P_i} \frac{A}{A_i} \left(\frac{1 + \gamma M^2}{1 + \gamma M_i^2}\right) \tag{11}$$

$$\frac{\Delta s}{C_p} = \ln \frac{T}{T_i} - \frac{\gamma - 1}{\gamma} \ln \frac{P}{P_i} \tag{12}$$

where T is the static temperature, P is the static pressure, P_0 is the total pressure, A is the duct cross-sectional area, u is the streamwise velocity, F is the impulse function, s is the entropy, and C_p is the constant pressure specific heat of the gas. The subscript i has been introduced to denote the inlet conditions.

The reference for these integral relations are the inlet conditions which become fully defined when the total temperature, pressure, and Mach number (obtained by marching back from the sonic point) are simultaneously specified. Here, the additional symbols ρ and $\dot{m}$ have been introduced for the density and mass flow rate, respectively.

Inlet Condition Relations:

$$T_i = \frac{T_{0i}}{\Psi_i} \tag{13}$$

$$u_i = M_i \sqrt{\gamma R T_i} \tag{14}$$

$$\rho_i = \frac{\dot{m}}{u_i A_i} \tag{15}$$

$$P_i = \frac{\rho_i}{R T_i} \tag{16}$$

$$P_{0i} = P_i \Psi_i^{\frac{\gamma}{\gamma-1}} \tag{17}$$

$$F_i = P_i A_i + \rho_i A_i u_i^2 \tag{18}$$

Combustion Model

A simple combustion model has been constructed to define the heat release profile. In this model, the flame front is located where the flow velocity just equals the specified flame holding speed. The heat release profile is then represented by a one-parameter shape function over a designated burning length. The streamwise variation in total temperature can then be deduced for the combustor.

The fundamental differential relation which must be satisfied relates the differential heat release dQ to the differential change in total temperature dT_0,

$$dQ = C_P dT_0 \tag{19}$$

where C_P is defined as the constant pressure specific heat. Therefore,

$$\frac{dT_0}{dx} = \frac{1}{C_P} \frac{dQ}{dx} = \frac{Q'(x)}{C_P} \tag{20}$$

Furthermore, we require that

$$\tilde{Q} = \int_{l_p}^{l_p+l_b} dQ = \int_{l_p}^{l_p+l_b} dx\, Q'(x) = \frac{\Delta H_{COMB}}{O/F+1} \quad (21)$$

where $\tilde{Q}$ is the absolute heat release per kg of total flow, l_p is the preburn length, l_b is the burning length, and ΔH_{COMB} is the fuel heat of combustion.

A suitable one-parameter shape function for $Q'(x)$ which satisfies Eq. (21) is

$$Q'(x) = \frac{\tilde{Q}}{l_b}(\alpha+1)\left(\frac{x-l_p}{l_b}\right)^{\alpha} \quad ; \; l_p < x \leq l_b \quad (22)$$

where α defines the heat release profile shape. The rate of reaction is represented in the value specified for α. Increasingly large negative values simulate increasingly large reaction rates. The uniform heat release profile is recovered when α=0. The general behavior of $Q'(x)$ is shown in Fig. 7 assuming l_p=0 and α = 0, -0.25, -0.5, -0.8.

Analysis

To check the validity of the analysis procedure and the coding, calculated solutions were successfully confirmed against known closed-form solutions for isentropic flow in a converging–diverging nozzle and for Rayleigh flow. The geometry and operating parameters for an idealized combustor similar in size to the proposed demonstrator were then selected for analysis.

The selected geometry consists of a diverging circular duct with an injection diameter of 0.5 cm and an exit diameter of 1.25 cm. The total nozzle length was 8 cm. The shape of the diverging section was defined such that the cross-sectional area varies according to the relationship

$$A = A_i + (A_e - A_i)(x/L)^{\beta} \quad (23)$$

where β is a nozzle shape parameter. A quadratic variation in flow area was chosen by setting β = 2. The resulting streamwise variation in nozzle radius is shown in Fig. 8.

Analysis was based on H_2/O_2 combustion at a mixture ratio of O/F=4.5 at which the maximum flame speed is attained. The heat of combustion for hydrogen was taken as ΔH_{COMB} = 120 MJ/kg. The specific heat ratio was estimated as γ=1.3 while the constant pressure specific heat was taken to be C_P=2000 m^2/s^2 K. An apparent turbulent flame speed 10 times the laminar value was assumed. Combustion was estimated to occur over a burning length of no more than 3 cm, and fast chemical reaction was simulated by specifying α=-0.75. Friction effects were neglected. Inlet reference conditions were T_{0_i}=300 K and P_i=14 atm.

Based on the above conditions, iterative calculations revealed that the flame front should be located approximately 1 cm downstream from the inlet. For the assumed heat release profile, computations further indicated that a thermal throat should form roughly 1 cm downstream from the stablized flame

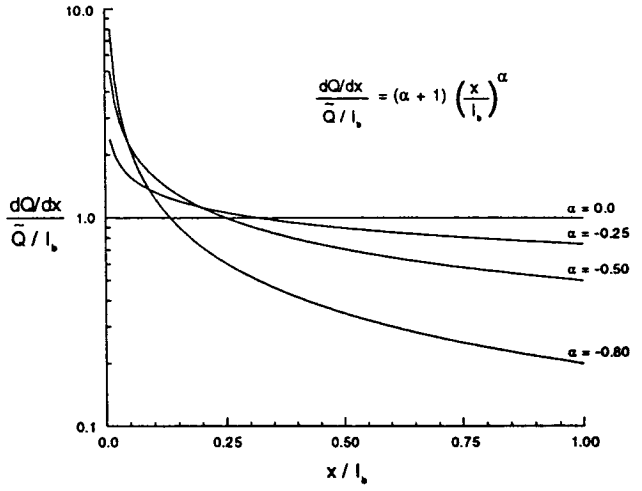

Figure 7: One-parameter reaction rate shape function for various assumed rate profiles. Uniform heat release is achieved when α=0.

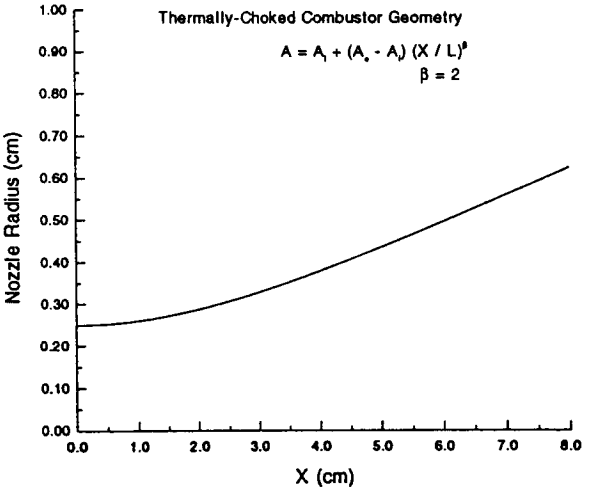

Figure 8: Radial variation in flow area for the analyzed diverging nozzle geometry.

front supporting a mass flow rate of 0.0235 kg/s. The flow was also predicted to accelerate smoothly through the transonic regime with subsequent expansion to high Mach numbers as shown in Fig. 9. There was no violation of the second law of thermodynamics. These results support the contention that thermally-choked combustors are both fluid dynamically and thermodynamically feasible, and they provide useful design estimates for the proposed bench-scale demonstrator.

Experimental

Demonstrator Combustor

Despite favorable theoretical results, practical feasibility must be proven in the laboratory. Thus, the emphasis of our research has been aimed at successfully constructing and operating a bench-scale thermally-choked combustor design. The evolution of our design was driven by a desire for simplicity, flexibility, and limited purpose – that being fundamental demonstration of the technology. Neither heavy diagnostics outfitting nor performance optimization were deemed desirable.

With these goals in mind, a design based on premixed injection appeared to offer the greatest potential for success. Furthermore, we were very interested in adapting high-pressure oxygen/hydrogen torch technology which was readily available for operating pressures up to 200 psi. As a result, our design turned on the idea of mating a commercial oxygen/hydrogen torch with a diverging nozzle combustor section. The configuration which emerged from this exercise is shown in Fig. 10.

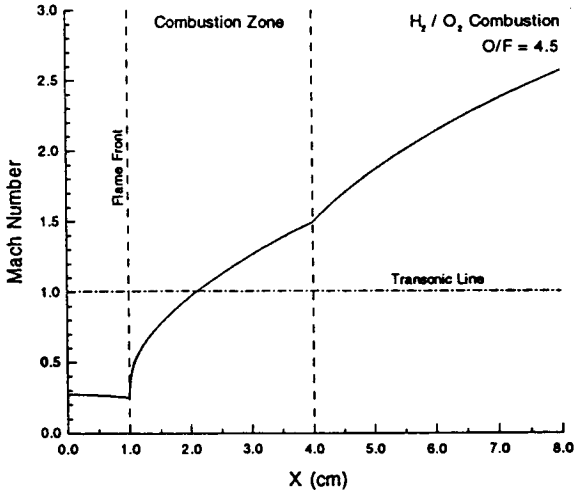

Figure 9: Computed streamwise variation in Mach number demonstrating continuous acceleration through the sonic point in the diverging nozzle combustor.

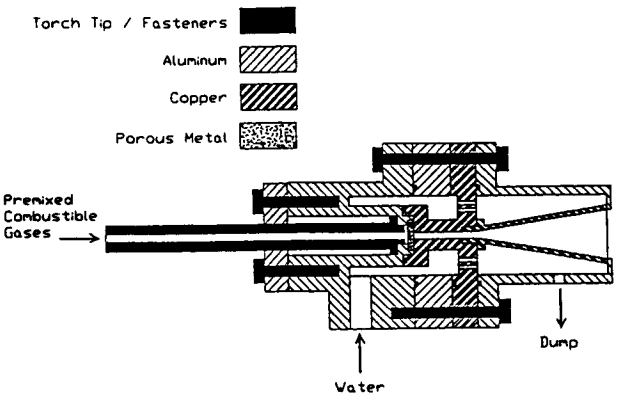

Figure 10: Thermally-choked demonstrator combustor design.

In this design, a large torch tip was cut back and fitted with a mating ring for attachment to the combustor. Premixed combustible gases leaving the torch mixing section and entering through the modified torch tip are forced to pass through a 1/8 inch thick porous metal filter having a 100 μm pore size. This filter is intended to prevent flashback through the delivery system. The gases then pass through a straight section roughly 1 inch long having the same diameter as the torch delivery tube. Then the combustible gases enter a diverging nozzle section where combustion is intended to stablize. The design accomodates interchangable nozzle sections so that different divergence rates and area ratios may be investigated. The entire combustor design is constructed from appropriate materials with adequate sealing between sections, and it is water cooled.

Gases are supplied to the system by two-stage regulators capable of providing 200 psi output. The combustor and gas delivery system are located in an isolated test bay at the UTSI Propulsion Laboratory. Flow control is maintained by control rods which connect to the torch handle valves and pass through the test bay blast wall to a safe control area. The combustor is started by igniting pure hydrogen flow in a diffusion flame. Oxygen and hydrogen flow are then increased to draw the flame into the nozzle section.

Diagnostics

Diagnostics have been intentionally kept to a minimum in keeping with our limited purpose of feasibility demonstration. Currently, we monitor the static pressure and temperature at the wall of the nozzle entrance. The temperature is measured as an indication of the forward location of the flame. The pressure is measured because we expect it to rise when and if thermal choking occurs. In addition, we are

using a schlieren imaging system to actively examine the nozzle exit plume. Because a schlieren optical system directly visualizes the density gradient (unlike a shadowgraph method which visualizes the second derivative of density), it offers high sensitivity to weak shock structures. The sensitivity of this technique can be appreciated when one observes the system easily detect natural room convection currents. If thermal choking occurs with subsequent expansion to supersonic Mach numbers, the schlieren technique should permit us to resolve shock structure in the exit plume. The schlieren images are recorded on tape with a video camera so that they can be digitized and processed later as required.

Test Experience

As of this writing, our test experience has primarily involved practical development issues. Initial attempts at operation revealed flaws in our original design requiring some component modifications and alterations. For instance, the original design did not include a porous metal filter. The filter was added after we experienced a burn through in the torch tip immediately downstream from the mixing chamber exit. It was not clear whether the flame flashed back through the system or ignition occured because of contamination. We therefore decided to add the porous metal filter as a flame arrestor. Fortunately, we have not experienced a recurrence since executing this alteration. Another difficulty encountered was inadequate sealing in the original design. We experienced leakage of combustible gases into the coolant flow and were forced to re-design. Subsequent modifications have eliminated this problem.

In all tests to date, we have had no indication of thermal choking. Actually achieving the desired operating conditions depends on a wide range of practical issues which make the entire matter problematic. We continue to pursue the technology by investigating various nozzle divergence rates and area ratios. We have not yet exhausted all conceivable possibilities with regard to the design.

Discussion

This section is dedicated to a discussion of the numerous practical issues encountered in developing a thermally-choked combustor. It is these practical concerns and the developers' ingenuity in addressing them which will determine the success or failure of this technology.

Starting

The issue of starting is immensely important and immensely uncertain. In a conventional flow accelerator, the rise in chamber pressure forces the flow through a fixed geometric throat. The enforced area change variation requires choking at the throat and continuous flow acceleration through the sonic point. In a thermally-choked combustor, however, the thermal throat must be developed by the combusting flow itself.

Before the thermal throat forms, there is no mechanism for sustaining a large injection pressure. Somehow, the flame must choke the flow while the inlet is at a relatively low static pressure. Then the injection system must rapidly respond by increasing the pressure against the throats resistance. Ideally, the flow would stablize with a thermal throat confining a significant injection pressure.

One technique for attempting a start begins by igniting at fuel-rich conditions which creates an external diffusion flame. By increasing both the oxygen and hydrogen flow rates, we approach a mixture ratio having a flame speed sufficiently high to bring the flame into the nozzle. One then relys on a self-induced start of the system in a thermally-choked mode. The feasibility of this approach has yet to be demonstrated. An alternative may be to pre-choke the cold flow upstream of the nozzle prior to ignition. If a thermal throat can then be formed in the nozzle section such that it chokes with a smaller permissible flow rate, the upstream choke point can dissipate allowing the thermal throat to confine the high supply pressure.

Heat Release Profile

For premixed combustible gases, the rate at which heat is released to the flow depends on the reaction kinetics of the fuel/oxidant system. Furthermore, the ability to achieve high combustion efficiencies at the thermal throat (so that performance losses remain low) requires a very compact combustion zone. Fast chemical reaction rates are therefore necessary, and H_2/O_2 combustibles are optimal in this respect. For a non-premixed injection design, a mixing delay time would also enter consideration.

We have not performed comprehensive calculations based on detailed reaction kinetics to know the probable heat release profile with any degree of certainty. If the combustion zone becomes too enlarged, the entire concept becomes less viable. Prompt combustion and choking near the injector is a critical element for successful and efficient operation.

Flame Stablization

The formation of a stablized flame front near the entrance of the diverging nozzle section is of particular importance. Neither flashback through the delivery system, nor blowout, nor persistent and large flame front oscillations are permissible. By keeping the flow velocity at the nozzle entrance greater than

the burning speed, the flame cannot propagate as a deflagration wave into the delivery system. To prevent blowout, velocities equal to the burning speed must occur just downstream of the nozzle entrance. Our current idea is to try and stablize the flame using the boundary layer velocity profile as occurs for Bunsen burners. As the flow diffuses to lower velocities, a speed will be reached near the wall (but far enough away to prevent quenching) which is equal to the flame speed. The flame can then anchor at that location.

This method may not yield a quality combustion front, however, since the flame could be severely stretched downstream. The combustion zone may become too enlarged for practical operation. Introduction of a bluff body flame holder such as a coarse wire mesh may perform better since it would rely on recirculation of hot combustion products to produce a more uniform flame front.

Detonability

With premixed combustibles, the formation of a supersonic combustion wave (detonation) from a subsonic combustion wave (deflagration) is known as a slow-mode deflagration-to-detonation transition (DDT). This occurs when a pre-flame shock front develops having sufficient strength to cause the mixture to explode. The result is a detonation moving into the unburned mixture at high Mach number (typically 5-10). Obviously, such behavior could have disasterous consequences if unquenched.

Experimental detonation limits for H_2/O_2 mixtures have been acquired demonstrating that limits on detonation are only slightly narrower than limits on deflagration. The deflagration lean limit occurs at 4.6 % fuel by volume as compared to a detonation lean limit of 15 %. The deflagration rich limit occurs at 93.9 % fuel by volume as compared to a detonation rich limit of 90 %. Thus, the detonation limits for H_2/O_2 mixtures are too wide to be ignored.

Since the transition length for slow-mode DDT of hydrogen fuel is on the order of one meter, the problem may not be severe for short length premix sections. However, fast-mode self-ignition detonations have also been observed which do not depend on transition from deflagration to detonation. Prudence dictates that any design should include a mechanism for flame quenching near the nozzle entrance.

Flashback / Flame Quenching

Flashback through the premixed delivery system as either a deflagration or detonation wave raises serious safety concerns. A method for quenching any flashback involves forcing the flame through a flow passage having a diameter less than the quenching diameter. With hydrogen, this is not a trivial task since the quenching distance can be extremely small. For example, the deflagration quenching diameter for hydrogen burning with air at 1 atm is 0.6 mm. Combustion with pure oxygen combined with the known inverse relation between quenching diameter and pressure ($d_q \propto P^{-1}$) implies the need for even smaller quenching distances in our application. To address this concern, we have employed a 1/8 inch thick porous metal filter having a 100 μm pore size. We clearly sacrifice pressure loss – and therefore propulsive efficiency – across this flame arrestor to achieve a measure of safety in operation. An opportunity does remain, however, for optimizing the flame arrestor design in later development work.

Concluding Remarks

The CSTAR organization is actively investigating thermally-choked combustor technology for rocket engine applications. Theoretical analyses indicate that the concept is fluid dynamically and thermodynamically feasible. Our immediate aim is to demonstrate the concept in a bench-scale design based on fast reacting premixed H_2/O_2 combustible gases. Current development effort is directed at addressing the numerous practical issues which affect a functionable design.

Acknowledgments

This work was supported by the University of Tennessee–Calspan Center for Space Transportation and Applied Research, UT Space Institute, Tullahoma, TN 37388 under NASA Grant NAGW–1195.

References

1. Edelman, R., Goldman, A., Halloran, S., and Lynch, E., "Performance Analysis in the Hypersonic Regime," *Threshold*, No. 9, Fall 1992, pp. 28-37.
2. Edelman, R. B., "Scramjet Technology Assessment," AFWAL-TR-88-2015, Technical Review, Vol. 1, May 1989.
3. Gibbs, G. J. and Calcote, H. F., *J. Chem. Eng. Data*, Vol. 5, 1959, p 226.
4. Zebatakis, K. S., *U. S. Bur. Mines Bull.*, No. 627, 1965.
5. Shapiro, A. H., *The Dynamics and Thermodynamics of Compressible Fluid Flow*, Vol. 1, Ronald Press, New York, 1992, Chapter 8.
6. Hodge, B. K., "Generalized One-Dimensional Compressible Flow Matrix Inverse," *J. Spacecraft*, Vol. 27, No. 4, 1990, pp. 446-447.
7. Beans, E. W., "Computer Solution to Generalized One-Dimensional Flow," *J. Spacecraft*, Vol. 7, No. 12, 1970, pp. 1460-1464.

OVERVIEW OF INITIAL RESEARCH INTO THE EFFECTS OF STRONG VORTEX FLOW ON HYBRID ROCKET COMBUSTION AND PERFORMANCE

P. Gloyer, W. Knuth, and J. Goodman

University of Tennessee - Calspan
Center for Space Transportation and Applied Research
UTSI Research Park, Tullahoma, TN 37388-8897

Martin Marietta Manned Space Systems
New Orleans, LA 70189

ABSTRACT

An examination of the effect of vortex flow on hybrid rocket combustion and performance is underway. Emphasis is on response of the fuel regression rate when subjected to vortex flow. Initial results show that there is a definite effect of the vortex on fuel regression rate. Future work will focus on quantitatively measuring this regression rate. This work is part of an overall program to develop an ultra low cost fuel system for hybrid rocket engines.

INTRODUCTION

Hybrid rocket motors are generally characterized as having a solid fuel grain and a fluid oxidizer. Various combinations of fuel and oxidizer have been tested and several observations have become widely accepted:

- Combustion occurs in a narrow mixing zone off the grain surface.
- The solid fuel vaporizes (pyrolizes) prior to combustion.
- Heat transfer from the hot combustion products causes fuel vaporization.
- Convection is the dominant heat transfer mode in non-metalized fuels.
- Fuel regression rates are dependent primarily on mass flux through the grain port.

Aside from varying fuel and oxidizer chemistry or flow, pressure and temperature, still other parameters are available for examination. These include varying the residence time, altering boundary layer characteristics and changing the convective heat transfer.

Several experimental methods are available for examining these parameters. One method, which is directly applicable to actual hybrid rocket motors, is the introduction of strong vortex flow into the combustion port. By injecting oxidizer tangentially into the combustion port to form a vortex, the combustion parameters can be changed. The vortex causes the oxidizer flow to follow a helical path thereby increasing the flow velocity. This gives the effect of higher mass flux. Varying the tangential injection velocity direction and magnitude will alter the boundary layer and convective heat transfer characteristics by changing the combustion port flow profile. An annular grain port geometry is well suited for this approach.

APPARATUS

A test chamber was developed to test the effect of vortex flow on hybrid rocket combustion. The test chamber consists of two concentric plexiglass cylinders and two aluminum end plates, see Figure 1. An oxygen source is attached to the upper plate allowing oxygen to flow into the annular region between the two cylinders. The inner cylinder is perforated to allow oxygen to enter the inner cylinder tangentially, see Figure 2. The combustion occurs on the inner surface of the inner cylinder. The flow exits through a throat and nozzle in the center of the lower plate.

APPROACH

The use of a clear plexiglass fuel and containment wall allows for flow and combustion visualization. A video camera is used to record the combustion and flow images.

The combustion needs to be restricted to the inner surface of the inner cylinder. Therefore a

method to prevent flame propagation back through the perforations must be found. It has been observed in hybrid motors that combustion does not occur in small cracks in the fuel. However, little is known about hybrid combustion back propagation upstream when oxidizer flows through small holes.

We need to find a hole size and/or pressure drop that will prevent the flame propagation. This would be very useful, since other techniques to arrest the flame require complex manufacturing techniques and may interfere with the optical clarity. The initial tests are focused on confining the combustion to the inner cylinder. Later tests will focus on examining the regression rates and performance of the hybrid rocket.

PRELIMINARY RESULTS

The first firing, with a source pressure of 25 psig, was made on a plexiglass cylinder with a range of hole sizes from 0.04 to 0.10 inches diameter. Fire almost immediately propagated upstream to the annular space between the cylinders. It is conjectured that this may have been the result of a chamber pressure spike at ignition. The post firing examination of the fuel cylinder suggested that the 0.04 inch hole diameter should be used for the next test.

The second test cylinder consisted of 40 tangentially located 0.04 inch diameter holes. The video record of the second firing, revealed that most of the holes arrested the flame. However, the downstream holes showed flashback and outflow, beginning shortly after ignition.

Initial observations suggest that the flashback may be due to an increase in wall static pressure along the axis. The static pressure increase is an effect of the vortex flow. To counter this effect, subsequent tests will have a higher source pressure and a larger throat area to reduce the chamber pressure.

Examination of the second test cylinder revealed distinct striations on the wall of the cylinder. This suggests that there may be an effect of vortex flow on the regression rate of hybrid fuels.

These initial tests are promising. Future tests will further explore swirl-driven combustion in annular port hybrids, and focus on quantitatively measuring the regression rate.

RESEARCH OBJECTIVES

The goal of this research program is to develop a better understanding of the parameters that control hybrid rocket motor combustion and performance. The results may lead to new hybrid motor design tools and fuel regression rate equations. These tools may reveal new ways to enhance hybrid rocket motor performance leading to hybrid rocket engines having more compact fuel grains, giving better overall mass fractions.

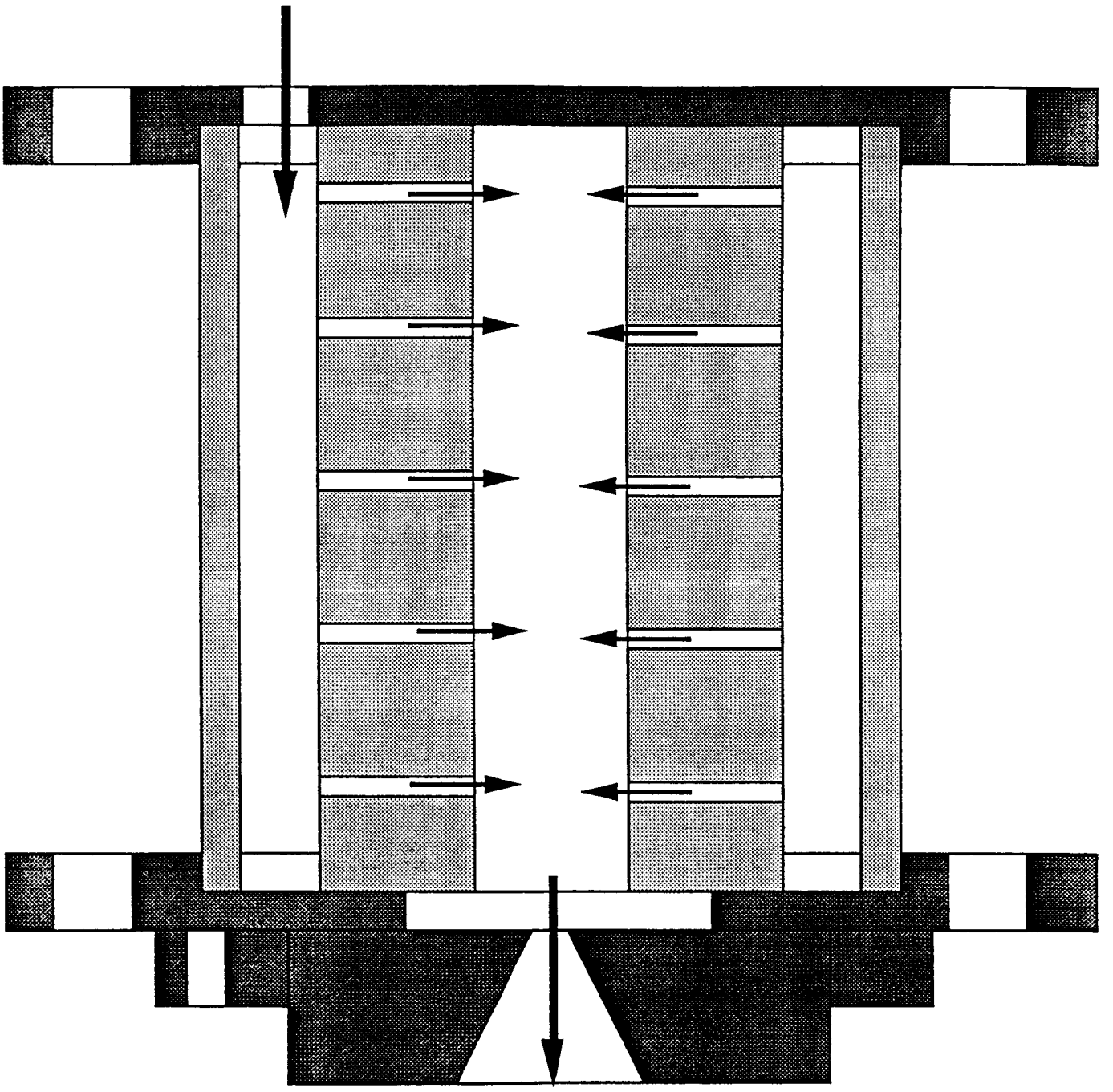

Figure 1 - Cut Away Schematic

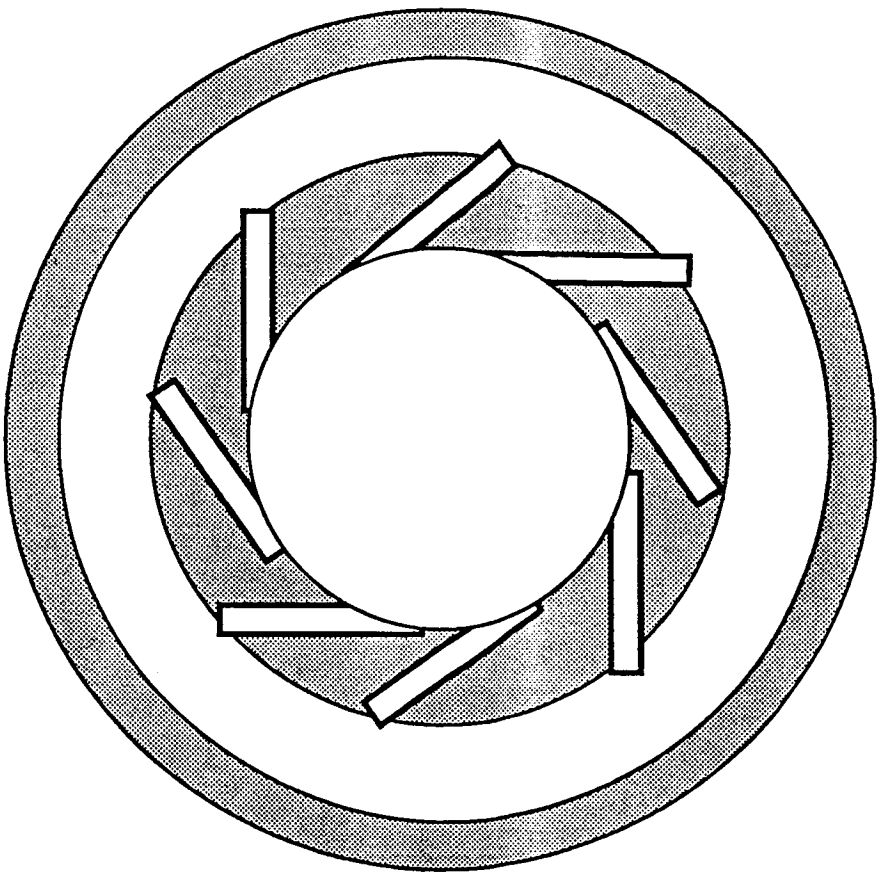

Figure 2 - Combustion Region Cross Section

CSTAR TECHNICAL SYMPOSIUM
ELECTRIC PROPULSION

F

Omit

Electric Propulsion Orbital Platform

Diagnostics Development for the Electric Propulsion Orbital Platform

Experimental and Analytical Ion Thruster Research

Emission Spectroscopy and Laser-Induced Fluorescence Measurements on the Plume from a 1-kW Arcjet Operated on Simulated Ammonia

Charge-Exchange Erosion Studies of Accelerator Grids in Ion Thrusters

Electric Propulsion Technology Applications

Laser Material Processing

Artificial Intelligence/ Expert Systems

Space Transportation

Computational Methods

Chemical Propulsion

Electric Propulsion

Electric Propulsion Orbital Platform

V. J. Friedly*, W. M. Ruyten,† R. J. Litchford§, and G. W. Garrison‡

University of Tennessee—Calspan
Center for Space Transportation and Applied Research
UTSI Research Park, Tullahoma, Tennessee 37388-8897

ABSTRACT

This paper describes the Electric Propulsion Orbital Platform (EPOP), of which the primary objective is to provide an instrumented platform for testing electric propulsion devices in space. It is anticipated that the first flight, EPOP-1, will take place on the Shuttle-deployed Wake Shield Facility in 1996, and will be designed around a commercial 1.8 kW arcjet system which will be operated on gaseous hydrogen propellant. Specific subsystems are described, including the arcjet system, the propellant and power systems, and the diagnostics systems.

INTRODUCTION

Electric space propulsion devices have undergone extensive ground tests. Such tests have clearly demonstrated the superior performance of electric propulsion devices over conventional chemical systems for selected space missions. However, commercial acceptance of this new technology has been hampered by a lack of flight data, both at the system- and component-levels.

To remedy this situation, flight testing of electric propulsion technology is urgently needed. This is particularly true at a time when efforts abroad are outpacing those in the U.S., creating a real threat to the U.S.'s ability to maintain its leadership which has been established in this area over the last two decades.

General objectives of EPOP are: (a) to provide a realistic electric propulsion demonstration in space; (b) to develop an in-space electric propulsion testing capability; (c) to facilitate commercial applications of electric propulsion; and (d) to capitalize on the unique partnership between NASA, industry and a university-based CCDS to transition electric propulsion technology to the marketplace.

The EPOP program will make maximum use of existing or planned NASA flight programs, such as Shuttle experiments, the Wake Shield Facility (WSF) [1;p.161], COMET [1;p.213], and Space Station Freedom (SSF). The program flight plan defined by the consortium strives for an initial gaseous hydrogen arcjet flight on WSF-03, to be followed by an ion thruster flight on WSF-04, a prototype orbit transfer vehicle mission based on a liquid hydrogen arcjet experiment on COMET, and, finally, a high-power, long-duration test of an arcjet or ion-thruster system on SSF. In addition to the demonstration of the electric propulsion systems themselves, EPOP also enables the development and demonstration of specific subsystems, such as solar arrays, batteries, power conditioners, and diagnostics instrumentation.

The EPOP-1 project is a key element in an effort to strengthen this U.S. leadership role in electric propulsion, particularly in the area of orbit transfer of communication and military satellites. The project centers around the flight of a 1.8 kW gaseous hydrogen arcjet system on the WSF, to be performed in 1996.

Specific system level objectives are the characterization of a 1.8 kW hydrogen arcjet in space (includes measurement of thrust level, measurement of thermal and electrical operating parameters and measurement of plume plasma properties) and identification of the electromagnetic noise induced upon spacecraft communications links. The EPOP-1 component level objective is to demonstrate, in space, a unique hydrogen feed system. Comparisons between space-based and ground-based data will be performed to validate the arcjet and its components.

EPOP-1 will provide an initial assessment of the use of an arcjet propulsion system to provide reboost capability to spacecraft by evaluating arcjet propulsion for use on future WSF flights requiring longer orbital stays. A potential benefit to the NASA-OACT sponsored WSF program is the demonstration and use of EPOP-1 technology to provide improved maneuvering capability for these future WSF missions.

The EPOP-1 project will be carried out by a consortium led by The University of Tennessee—Calspan Center for Space Transportation and Applied Research (CSTAR). Industry members of the consortium are McDonnell Douglas

* Research Engineer
† Senior Engineer
§ Research Engineer
‡ CSTAR Executive Director

Aerospace, Olin Rocket Research Company, and Boeing Defense & Space Group. The Space Vacuum Epitaxy Center at the University of Houston is responsible for the WSF program.

All consortium members have substantial ongoing efforts devoted to electric propulsion. In particular, McDonnell Douglas is prime contractor for the Operational Solar Electric Orbital Transfer Vehicle (SEOTV) Concept Study for the U.S. Air Force and considers EPOP-1 a significant step toward upgrading the payload capability of the Delta launch vehicle by the turn of the century. Rocket Research Company is recognized as the world leader in designing and manufacturing arcjet systems. Boeing has a long history as a systems integrator.

Because EPOP-1 will be an attached payload on WSF, it will be launched and retrieved by the Space Shuttle. The experiment will provide 150 minutes of arcjet operation (limited by battery power) within a 24-hour period to verify space-ground correlations for ultimate use in orbit transfer and circularization. The diagnostic system includes RF-signal monitoring, plume imaging, plasma property measurements, and acceleration measurements to correlate space and ground tests.

The EPOP-1 project is of relatively low cost to NASA due to significant contributions to the program by the industrial partners. A potential WSF program benefit of improved maneuvering will also be provided.

JUSTIFICATION for EPOP-1

A. Commercial

The commercial justification for EPOP-1 falls into two categories:

(1) Orbit transfer:

A market analysis of future orbit transfer missions conducted by McDonnell Douglas shows promising payoff for a hydrogen arcjet SEOTV. For medium-lift launch vehicles alone, such as Atlas and Delta, there are an estimated 192 commercial, 89 NASA, and 110 Department of Defense (DoD) payloads projected for the 12-year time period between 1999 and 2010. If half of these payloads were to take advantage of a hydrogen SEOTV upper stage, the resulting launch cost savings would be on the order of a billion dollars. Even larger cost savings would result for heavy-lift launch vehicles.

Another important application of electric propulsion is station keeping for communication satellites at geostationary altitude. High performance satellite propulsion systems yield longer life in orbit for the same amount of fuel or could reduce the total payload mass to such an extent, that a less expensive launch vehicle might be sufficient for a given mission. In a pertinent study by the firm of KPMG Peat Marwick it was concluded that based on the launch activity, electric propulsion for communications satellites would lead to total savings in the order of $260 million per year.

Arcjet technology is already in the process of transitioning to this application area. From a user-risk perspective, there is an important difference between these two application areas: Whereas a failed electric propulsion system which is intended for station keeping will merely cut short the intended mission life of the satellite, a failed electric upper stage would result in a total loss of the intended mission. Because of this, the fact that arcjet technology is transitioning to commercial use for station keeping does not automatically imply that such a transition will follow in the area of orbit transfer. Hence the need for flight demonstration of arcjet technology to open up the market of orbit transfer using electric upper stages.

(2) Wake Shield Reboost:

The duration of future flights of WSF will be significantly longer (on the order of six months and longer) than those of the first few flights (on the order of a week). Thus a reboost capability is required to maintain orbital altitude. An electric propulsion system would be ideally suited to provide this reboost capability, because of the high performance capability (and the associated low mass) of such a propulsion system. In addition, a hydrogen-fueled, electric propulsion system is expected to be more compatible with the requirement that an ultraclean vacuum be maintained around the spacecraft at all times, compared with a chemical system.

EPOP-1 will provide a cost-effective means of assessing the impact of adding an electrical propulsion system on WSF for such future reboost capability.

B. Technical

EPOP-1 bridges the technology gap between current ammonia arcjets and the 10 - 30 kW hydrogen arcjets that are required for orbit transfer vehicles. The validation of ground versus space tests will identify any potential impacts on spacecraft integration. Plume and electromagnetic interference (EMI) interactions with the spacecraft and its mission are of concern to the designer. Ground tests give only limited answers due to wall effects and achievable vacuum levels. Operational characteristics such as voltages, currents, and temperatures may be different in open space. And it is important to validate the ultimate thruster performance in space by determining the specific impulse.

Regarding the technologies required for the development of SEOTV, EPOP-1 provides an important bridge by reducing the development risk for the propellant feed system, the

hydrogen arcjet, and the power control unit. Overall performance, arcjet operation at reduced power and flow, and spacecraft interactions derived from EPOP-1 will be important design inputs for the SEOTV.

The fact that EPOP-1 will be recovered as part of WSF makes it possible to carefully inspect the entire system and determine nozzle erosion and other deterioration due to the space environment. This may provide significant insight regarding long life operations.

ARCJET SYSTEM

Based on maturity of the technology, specific interests on the part of the industrial consortium members, anticipated cost and funding, and consideration of other electric propulsion flight programs, the decision was made to fly a 1.8 kW gaseous hydrogen arcjet experiment on EPOP-1. Missions that will ultimately utilize hydrogen arcjets, for instance orbit transfer missions, will use arcjets that will require input powers of up to 30 kW. These higher power arcjets have been demonstrated in ground-testing to perform at specific impulses of up to 1500 s, at efficiencies of up to 40 percent [2]. However, a number of optimization and technical issues remain. These include performance optimization, establishment of the optimum voltage-current characteristic and mass flowrate for operation in a low-vacuum environment, heat dissipation, and electrode lifetime. We believe that operation of a lower power arcjet will allow some of these technical issues to be addressed along with a demonstration of a complete gaseous hydrogen arcjet.

It is intended to fly, on EPOP-1, a modified version of the 1.8 kW hydrazine arcjet system that has been developed at Rocket Research Company under a NASA Lewis Research Center grant [3]. A flight qualified version of this system [4] has been built by Rocket Research Company (see Fig. 1) for AT&T's Telstar 4 satellite, to be launched in 1993. This RRC 1.8 kW hydrazine arcjet (model MR 508) has a demonstrated Isp in excess of 500 s, and achieves a propellant savings of 200 kg over traditional chemical thrusters for a typical geosynchronous communication satellite, exclusive of mass savings in other areas, such as propellant tanks, support structure and launch vehicle. This mass savings is after the mass for the power source, power conditioning unit, and arcjet are added to the mass of the propulsion system.

The three components of the envisioned arcjet system include the arcjet thruster, the power cable, and the power conditioning unit (PCU). The latter may need to reconfigured for the higher operating voltage for hydrogen. The hydrazine arcjet, shown in Fig. 1, would be stripped of the catalyst bed, gas generator, valve heater, propellant valve, and fluid resistor. This hardware is used when

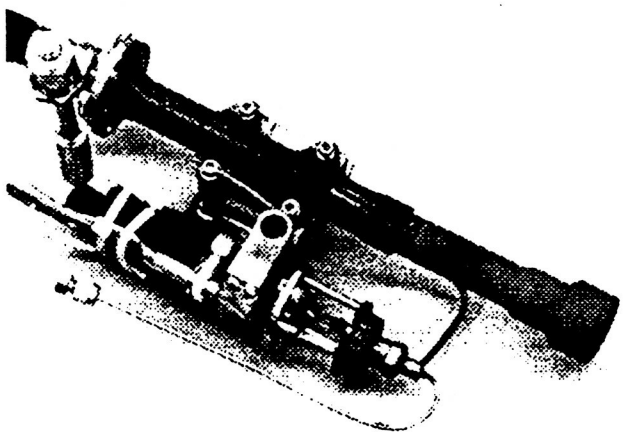

Fig. 1 RRC 1.8 kW arcjet flight model to be flown on EPOP-1.

hydrazine is the propellant to decompose and control the flow of the liquid propellant. Otherwise, it is not anticipated that significant modifications will be required to the design. Total mass of the system should be less than 6 kg.

Thermal considerations regarding integration of the arcjet system with the Wake Shield would center primarily around the PCU, which rejects less than 10 percent of the input power, or typically 160 to 165 W, to the spacecraft mounting interface. By contrast, typical heat rejection to the spacecraft from the arcjet body itself is less than 5 W, because most excess energy is radiated away from the nozzle tip, which is sprayed with a high emissivity coating.

In addition to actively conditioning the power to the arcjet, the PCU contains electrical interfaces to the data acquisition and control subsystem, the power supply, and the arcjet thruster. Also, the PCU is programmed to refire automatically in the case of misfirings of the arc. Once the arc is established, the PCU maintains constant power output (rather than constant voltage or constant current) to the arcjet.

PROPELLANT SYSTEM

EPOP-1 will store and deliver gaseous hydrogen to the arcjet. A schematic of the proposed propellant system is shown in Fig. 2. Gaseous hydrogen, stored at a maximum pressure of 1900 psia, will be supplied to the system through a pyrotechnic valve that will be opened at the beginning of the experiment. A 10 micron filter will be used to insure the gas is devoid of particles, and a pressure regulator will be used to lower the pressure from tank pressure to 15 psia. This low pressure was chosen to simulate the pressure that would be present if a cryogenic storage system were used — the storage method an actual transfer vehicle would use for reduced storage tank mass and volume. A compressor will be used to increase the line

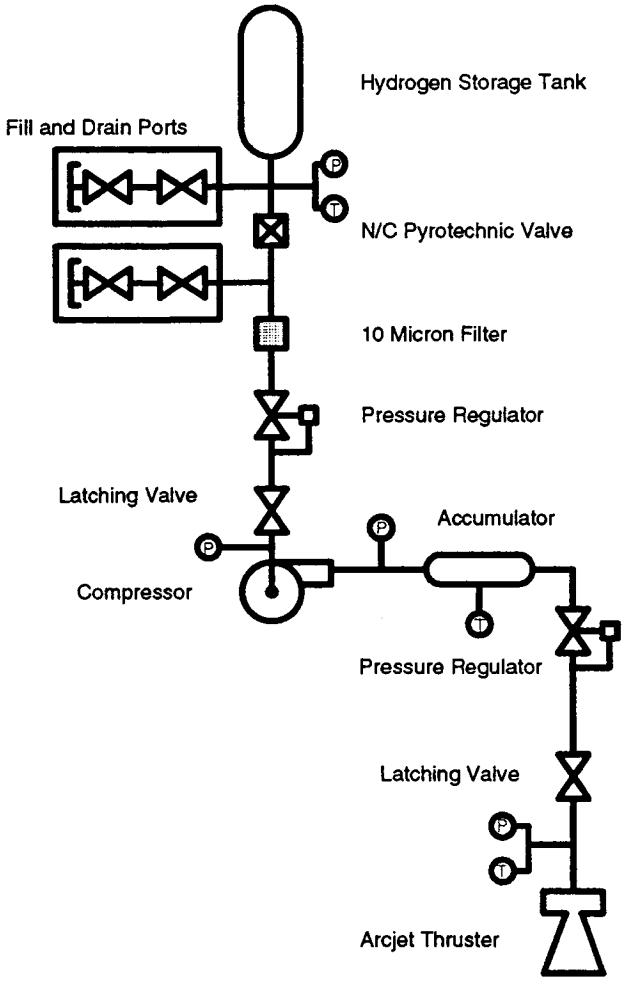

Fig. 2 Gaseous hydrogen storage and delivery system for EPOP-1.

pressure to ~100 psia, the pressure required by the arcjet, with the actual pressure being regulated by a pressure regulator near the arcjet. The operation of this flow control in a low-gravity environment is an important objective of demonstrating the operation of a complete hydrogen arcjet system. Temperature and pressure sensors are employed to help determine flowrates into the arcjet. Thus the actual flowrate will be calculated based on calibration measurements made before the flight.

EPOP-1 CARRIER

The Wake Shield Facility, being developed by the Space Vacuum Epitaxy Center (SVEC) at the University of Houston, has been baselined as the carrier for EPOP. The primary aim of the WSF program is to utilize the vacuum environment of low Earth orbit (LEO) for materials processing in an ultra-clean environment; specifically, for epitaxial film growth experiments.

As shown in Fig. 3, the WSF is a circular stainless steel disk, 3.7 m in diameter. It is released from the Shuttle by the remote manipulator system (RMS) such that the axis normal to the surface is orientated along its orbital flight path. The EPOP experiment will be mounted (see Fig. 3), along with WSF's avionics, batteries, grapple fixture, and attitude control system on the ram side. Telemetry and control of WSF will be through an S-band RF link with the Shuttle. This link also allows for transmission of compressed video data. An obvious advantage of using WSF as the carrier for EPOP is the availability of these data links.

The use of WSF imposes several constraints on the EPOP experiment, specifically with regard to experiment time, experiment mass, available power, and telemetry. The goals and mission schedule for WSF necessitate that any

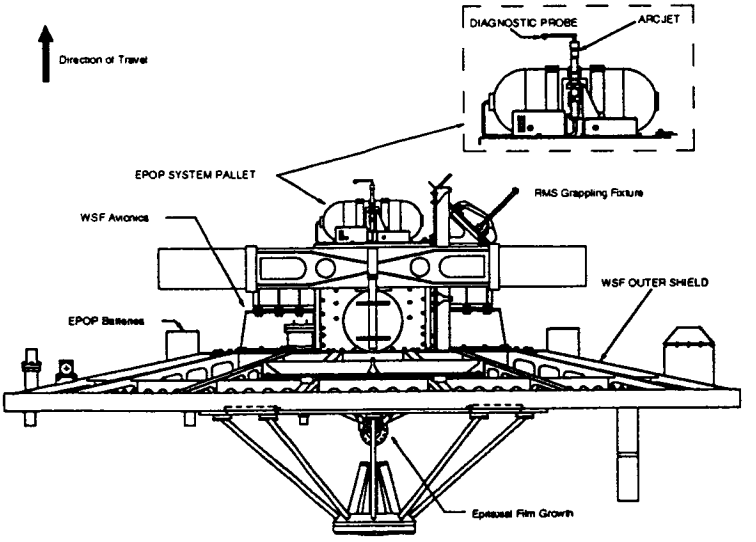

Fig. 3 Schematic of WSF with the EPOP pallet attached in a proposed configuration.

arcjet firings be conducted after completion of all crystal growth experiments, leaving a period of about 24 hours until retrieval of the WSF by the Shuttle.

Insufficient power levels are available from WSF for a 1.8 kW experiment, so that EPOP must carry its own batteries. Due to a total mass limitation of 350 kg, the maximum net firing time of the arcjet system becomes limited to about 150 minutes. While this time is long enough to benchmark general performance of the arcjet system, it is too short to perform contamination studies.

DIAGNOSTICS SYSTEMS

An integral part of EPOP-1 is to characterize the operation of the arcjet in space. This will allow for determination of the interaction of the arcjet system with the spacecraft (WSF-03) and allow for arcjet characteristics and operational data from a space-based demonstration to be compared with data from ground based test. Thus the instrumentation, voltages, currents, pressures, and temperatures will be made to determine the operational characteristics of the arcjet system and the propellant system. In addition, EPOP-1 will be equipped with a plume imaging device, Langmuir probe, and a communications monitoring system. The WSF will be equipped with accelerometers, another plasma measuring device, and additional video cameras that can be used to enhance the data from the EPOP-1 flight. For more detail on the EPOP-1 diagnostics please see the companion paper which is part of these proceedings (**Diagnostic Development for the Electric Propulsion Orbital Platform by Ruyten, Friedly, and Litchford**).

EXPERIMENT CONTROL and DATA ACQUISITION SYSTEM

EPOP-1 will have a seperate controller and data acquistion system from the WSF system. This independent controller will allow for more flexibility for EPOP and minimize the number of interfaces between EPOP and WSF. This controller will receive a command from the WSF controller which will allow the EPOP demonstration to begin or shutdown. The EPOP controller will send commands to all the EPOP systems, collect data from the instrumentation and diagnostics, store data, and send data to the WSF controller that will then be telemetered to the ground or the Shuttle.

The baseline hardware for the computer system for the EPOP controller is a single board computer with a 10 Mhz central processing unit, and on board memory and mass storage. This system will also be required to have sufficient input/output ports and data acquisition ports for communicating with EPOP and WSF. All inputs to this system will be high level.

SCHEDULE

EPOP-1 is scheduled to be launched in mid 1996 (see Fig. 4). To meet this schedule EPOP will have a Preliminary Design Review in January 1993 along with the corresponding safety reviews with NASA Johnson and Kennedy. A development test will occur in October/November of 1993 at the Rocket Research Company facility. This test will provide data required to design the arcjet power control unit and some of the diagnostics on EPOP-1. All hardware must be ready for integration and at McDonnell Douglas by February of 1995. SVEC will need the EPOP-1 system delivered to them by September 1995 to allow for time to integrate and test on WSF-03 prior to a June launch. This schedule will depend on project funding and Shuttle manifesting.

EPOP CONSORTIUM

A responsibility matrix for providing certain tasks for EPOP-1 is given in Table I. The table presents a general outline of responsibilities over the 5 year project. Although CSTAR is listed as having the lead in the EPOP program, technical and management decisions are made with complete consensus of the partners; BD&SG, MDA, and RRC. CSTAR has also taken the lead in developing and implementing the diagnostics to be used on EPOP.

McDonnell Douglas Aerospace will be the systems integrator for EPOP and will be the responsible partner for the areas that will support this role. They will also take the lead for the propellant and power supply subsystems, using their experience in this area. RRC will be responsible for

Table I: *Responsibility matrix for EPOP-1.*

	CSTAR	MDA	BD&SG	RRC	SVEC
Program Management	✓				
Diagnostics	✓				
System Engineering and Integration		✓			
Flight Operations		✓			
Power Supply		✓			
Propellant Subs.		✓			
Exp't Control & Data Acquisition			✓		
Arcjet and PCU				✓	
WSF Support and Modifications					✓

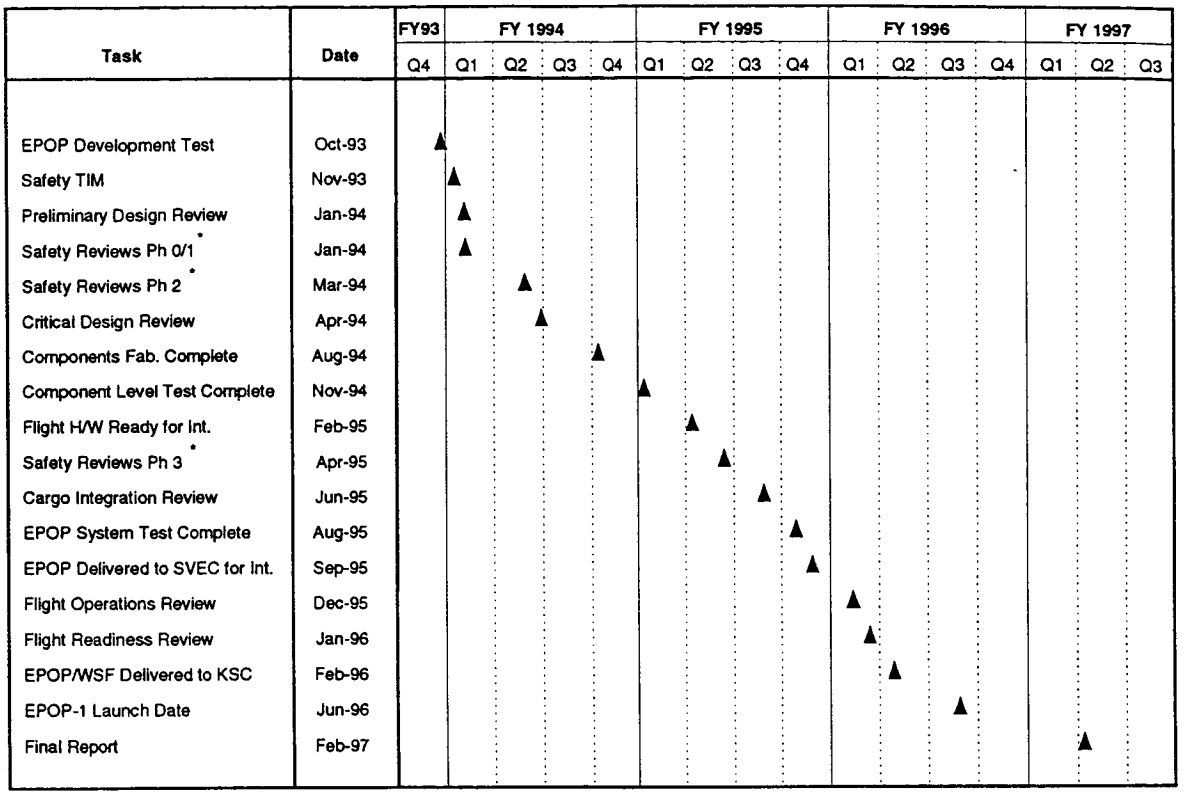

Fig. 4 EPOP-1 schedule to meet a June 1996 launch date.

production of the arcjet system. Boeing Defense & Space Group will be responsible for the experiment control and data acquisition subsystem.

ACCOMPLISHMENTS IN FISCAL YEAR 1993

- The EPOP program received a conditional approval from the Level I Payload Selection Board. This approval was based on that a contingency be developed for future EPOP flights if no augmentation from NASA is available.

- A flight ready arcjet has been identified for the arcjet to be used for EPOP-1 flight. This arcjet is from Rocket Research Company and will be used to do development test later this year. Hydrazine is the propellant originally intended for use with the arcjet. However, EPOP-1 will use hydrogen propellant. Required modifications are the removal of the gas generator, and a valve sized for hydrogen will need to be added.

- A baseline for the data acquisition and experiment control system was provided. The baseline instrumentation and control requirements list will be reviewed and revised as necessary, including the required sampling rates. It was recognized that how autonomous EPOP should be from the WSF data and control system requires technical trade studies that will be performed during the EPOP design.

- NASA Lewis Research Center is very interested in providing support for EPOP. This support will be in a development test of the EPOP diagnostics and a systems test in a vacuum chamber at Lewis.

- The EPOP consortium briefed Greg Reck, Acting Associate Administrator for the NASA Office of Advanced Concepts and Technology, on March 30, 1993. CSTAR presented the EPOP program overview.

  - Information on the benefits of a solar electric orbit transfer vehicle was presented. Data from the McDonnell Douglas study on SEOTVs showed that up to $100 million could be saved per launch when an SEOTV is used instead of the conventional chemical system. This savings is the result of using smaller launch vehicles to launch the same payload to orbit.

  - Reasons for a hydrogen EPOP were given during this briefing. EPOP is currently the only program

developing the technology for hydrogen arcjets. Hydrogen arcjets, with 1000 to 1200 s specific impulses, are superior to ammonia arcjets with < 820 s specific impulse. In addition, EPOP fills the technology gap from other arcjet flight programs (ESEX and ELITE) to the operational SEOTV. These programs address the power levels required by an SEOTV but do not address the issue of the hydrogen arcjet system. EPOP-1 begins to address the hydrogen issue.

- After the briefing, Mr. Reck stated that he supported the program. He felt that OACT should fund the program but stated that the Space Transportation Division would have to determine if the funds are available for the program. This has resulted in a requested briefing on the cost estimate and cost heritage to Mr. Earl VanLandingham, the Director of the Space Transportation Division. This briefing is scheduled to take place in June.

- A program review was conducted at NASA OACT, in which representatives from NASA OACT, CSTAR, Boeing, McDonnell Douglas, Rocket Research Company, SVEC, and other divisions of NASA were present. Following this meeting, Mr. Earl VanLandingham of NASA OACT indicated that NASA would support the EPOP-1 program as presented.

- A technical interchange meeting between EPOP consortium members was held in Monterey, CA, immediately following the Joint Propulsion Conference.

- Plume imaging development work started in preparation for tests of a 1.8 kW hydrogen arcjet thruster at Rocket Research Company (RRC) this fall. Various imaging techniques were evaluated this test, these involved a 35 mm wet photography, color digital red-green-blue (RGB) still photography, and color video. The results of this evaluation will be used to derive the final design for the EPOP imaging diagnostics package.

- Preliminary work was started at UTSI's Vacuum Research Facility using the 1 kW NASA LeRC arcjet operated on simulated ammonia propellant

- The necessary instrumentation for the plume imaging diagnostic package was shipped to the RRC facilities. Data on the flight model arcjet will be collected.

- EPOP-1 Project Plan was submitted to NASA Office of Advanced Concepts and Technology. This plan summarized the EPOP-1 benefits, cost, funding, and schedule.

- A development test for determining the arcjet operating potential and staring characteristics was initiated at Rocket Research Company at the end of the fiscal year. Initial tests using the CSTAR diagnostics were also done at this time to obtain data on the flight arcjet. The data from these tests were not available for publication here.

SUMMARY

We have explored the possibility of promoting the commercial use of electric propulsion systems in the U.S., namely by providing a flexible flight-testing capability for electric propulsion systems that would be funded jointly by NASA's Office of Commercial Programs and industry. In particular, we have performed a feasibility study for the flight of a 1.8 kW hydrogen arcjet experiment — EPOP-1 — aboard the Wake Shield Facility, a Shuttle-deployed free-flyer. At this point, it is envisioned that EPOP-1 will be manifested for a 1996 launch date.

Maximum cumulative thruster firing time for the experiment will be 2.5 hours. During this time, operating characteristics of the arcjet system will be monitored, including thrust, electrical efficiency, specific impulse, plasma properties of the plume, arcjet and plume temperatures, radio-frequency noise, and interference with spacecraft communications. Because of the small amount of hydrogen required, a simple gaseous storage system can be used. EPOP will draw supplemental power from the WSF bus, but primary power will be provided by a dedicated battery system. Thus, experiment time is limited by the maximum battery mass.

Responsibilities for the EPOP-1 experiment will be shared between CSTAR, which is a NASA-OACT- sponsored Center for the Commercial Development of Space, and industrial partners. At present, these partners are Boeing Defense & Space Group, Rocket Research Company, and McDonnell Douglas Aerospace. Also, as the responsible organization for the Wake Shield Facility, SVEC, another CCDS, will be involved.

ACKNOWLEDGMENTS

This work was funded by NASA Office of Commercial Programs under grant NAGW-1195 (EPOP supplement). We gratefully acknowledge inputs from other contributors and members of the EPOP consortium, present and past. These are: D. E. Hedges and J. S. Meserole at Boeing Defense & Space Group; K. Armbruster and R. J. Cassady at Olin Rocket Research Company; E. C. Cady, R. S. Bell, and T. Miller at McDonnell Douglas Aerospace; and A. Ignatiev, N. Combs, and M. Sterling at the Space Vacuum Epitaxy Center. We appreciate greatly the many contributions by Dr. F. A. Speer, former Director of CSTAR.

REFERENCES

1. ``Accessing Space: A Catalogue of Process, Equipment, and Resources for Commercial Users," NP-133, written for the Office of Commercial Programs, NASA Headquarters, Code CCL, December 1990.

2. Haag, T., and Curran, F., ``High Powered Hydrogen Arcjet Performance," AIAA 91-2227, 27th AIAA/ SAE/ASME/ASEE Joint Propulsion Conference, Sacremento, CA, June 1991.

3. Smith R. D., Roberts C. R., Davies K., and Vaz J., ``Development and Demonstration of a 1.8 kW Hydrazine Arcjet Thruster," AIAA paper 90-2547, Orlando, FL, July 1990.

4. Knowles S. C., Yano S. E., and Aadland R. S., ``Qualification and Life Testing of a Flight Design Hydrazine Arcjet System," AIAA paper 90-2576, Orlando, FL, July 1990.

Diagnostics Development for the Electric Propulsion Orbital Platform

W. M. Ruyten[†], V. J. Friedly,[*] and R. J. Litchford[*]
University of Tennessee-Calspan
Center for Space Transportation and Applied Research
Tullahoma, Tennessee 37388-8897

Abstract

We describe the development of the diagnostics systems for the first flight of the Electric Propulsion Orbital Platform (EPOP), which will center around the in-flight characterization of a 1.8 kW hydrogen arcjet system. In particular, we discuss a spacecraft communications experiment involving ground-to-spacecraft communications of the EPOP carrier; electrical probe measurements in the arcjet plume; and spectrally resolved plume imaging measurements of the same plume. The communications experiment is designed to measure small noise on the communications link which results from arcjet operation. The other two measurements primarily serve the purpose of characterization of the plume plasma. These measurements will be compared to similar measurements performed in a ground chamber to establish whether systematic differences exist between ground-based and in-flight performance of the arcjet system.

1. Introduction

Electric propulsion devices have undergone extensive testing in ground chambers. This is particularly true of arcjets, which will soon be operational on a series of satellites to provide orbit station keeping. Still there is a continuing need for flight demonstration of these devices. This is the motivation behind the Electric Propulsion Orbital Platform (EPOP), whose first flight is centered around a 1.8 kW hydrogen arcjet. Many of the specifics of the EPOP program are described in an accompanying paper (the preceding paper in these proceedings). Here we discuss in particular the diagnostics which are under development to support the EPOP arcjet flight.

Previous descriptions of the planned diagnostics may be found in Refs. [1-3]. Roughly speaking, they can be divided into two categories: those that are particular to the EPOP experiment and those that are available on the EPOP carrier: the Wake Shield Facility. Diagnostics which are strictly a part of the EPOP payload are the plume imaging system and the electrical (Langmuir) probe system (these are described, respectively, in Sections 3 and 4) and a number of sensors and ADC inputs to record temperatures, pressures, voltages, and currents at various points on the arcjet, power control unit, and propellant system.

Diagnostics which will be ``borrowed" from the Wake Shield Facility are accelerometer measurements and, possibly, electrical probe measurements performed by the CHAWS diagnostics package which is under development by Phillips Laboratory. The accelerometer measurements will be used to verify the thrust level of the arcjet system and, in combination with flow rate measurements, to calculate the specific impulse of the thruster. If available, the CHAWS package will provide information on any changes in the plasma environment around the spacecraft (away from the arcjet plume) as a result of arcjet operation. For example, it may provide insight into spacecraft charging and/or discharging phenomena.

Finally, one the experiments in preparation for EPOP is one which is really of a hybrid nature with

---

[†] Senior Research Engineer, CSTAR
[*] CSTAR Research Engineer

This work was supported by the Center for Space Transportation and Applied Research.

regard to the above classification. This is the spacecraft communications experiment which will use, almost entirely, hardware already present on the Wake Shield carrier. However, some modifications are needed in order to make it possible to use the Wake Shield communications link with a ground station as a means of measuring small noise levels which are introduced on the communications link due to operation of the arcjet system. This experiment is described in Section 2.

2. Spacecraft Communications Experiment

One of the primary concerns about the use of an electric thruster on a spacecraft is that of electromagnetic interference (EMI) on spacecraft communications. A communications experiment is planned for EPOP which will make use of one of the two communications links of the EPOP carrier, the Wake Shield Facility (WSF), to identify the presence and magnitude of such EMI effects.

To be sure, the effects of arcjet firings on the WSF communications links are expected to be very minimal. In fact, ground testing has shown that noise levels at S-band frequencies are extremely small (below MIL-STD-461C). Thus, a customizable experiment will be required to demonstrate, in a quantitative manner, that there is indeed an effect on the communications link (or, to demonstrate that, even with an extremely sensitive measurement, no effect on the communications link is detectable).

Like the first two flights of the WSF, the third flight (with EPOP as a payload) will rely on communications with the Shuttle for most of its operations. But also, a link with a ground station (COMPOCC) will be available. This WSF-to-ground link is the preferred communications link for a customized RF transmission experiment because it offers greater flexibility in customizing the link to the user than would the WSF-Shuttle link.

In short, the experiment will consist of the following principal steps (see Fig. 1):

(1) Uplink a tailored RF signal from COMPOCC to the WSF;

(2) Echo the received signal back to the COMPOCC ground station.

(3) Determine the integrity of the echoed signal.

(4) Repeat the above steps for ever-decreasing signal amplitudes until no usable signal can be detected.

The minimum signal amplitude at which a usable echoed signal can be detected will depend on the noise environment along the signal paths, including that induced by operation of the arcjet thruster. To distinguish between arcjet noise and other environmental noise, noise measurements will be performed both with arcjet-on and arcjet-off. The difference in minimum detectable signal amplitudes between arcjet-on and arcjet-off will be a measure of the noise level induced by the arcjet thruster. However, it is likely that the minimum detectable signal amplitude will also depend on other factors such as upper-atmospheric effects and day-night variations. Below, we describe the principal steps in some more detail.

2.1 Uplink a tailored RF signal

The choice of the uplink signal is governed by the requirement that the return signal lend itself to a quantitative determination of signal degradation. This can be accomplished by FM modulation of a sinusoidal wave onto the S-band carrier, allowing a SINAD noise measurement in Step 3.

Perhaps the measurement can be performed at several frequencies of the sinusoidal wave. Most importantly, it should be possible to vary the amplitude of the uplink signal over a sufficiently broad range to allow the signal amplitude to be decreased to the point that no usable return signal is received (Step 4).

Because the range from COMPOCC to WSF changes dramatically during each pass (from about 1600 nmi at the horizon to less than 300 nmi overhead and back to 1600 nmi at the opposite horizon) it will be necessary to vary the transmitted signal level in real-time so as to keep the strength of the received signal level roughly constant.

2.2 Echoing back the received signal

For obvious reasons, the number of modifications to the Wake Shield Facility should be kept to a minimum. In particular, it is desired that only minimum changes be made to the RF communications system. This is the primary motivation for echoing the COMPOCC signal back to COMPOCC: in this way, no data processing needs to be performed on the WSF.

Figure 2 shows a possible diagram of the approach: a relay switch could be added to WSF. When closed, the switch feeds the received signal back into the WSF transmitter. This switch would be operated by the Spacecraft Command Interface Unit. To resume normal operation, the switch would be opened. In this approach, no further processing of the signals is necessary by the WSF computers.

2.3 Determination of the integrity of the return signal

At COMPOCC, the return signal from the WSF is monitored in real-time. In particular, the imposed sinusoidal wave is recovered by demodulating the S-band signal, following which SINAD measurements will be performed to determine the signal-to-noise ratio of the recovered sinusoidal signal.

We anticipate that standard electronics instrumentation may be employed to perform these measurements. Thus hardware requirements for this step will be minimum.

2.4 Variation of the signal amplitudes

The objective of the experiment is to determine the minimum signal amplitude at which a usable signal can be recovered. Therefore it is necessary that the strength of the uplink signal be variable. Also, as explained in Sect. 2.1, it is important that the amplitude of the uplink signal be tailored so as to compensate for the dependence of the received signal strengths on the COMPOCC-WSF range.

Alternatively, the variation of received signal strengths with COMPOCC-WSF range may be exploited to achieve the desired variation in signal amplitudes. Details will have to be worked out at a later time, requiring further analysis and selection of options. In either case, we anticipate that the experiment will be performed interactively, allowing an operator at COMPOCC to control the experiment in real-time.

2.5 Hardware requirements and mission scenario:

The most important modification to WSF would be the installation of the relay switch from Fig. 2 which feeds the received signal back into the transmitter. This switch will have to be controlled by the Space Craft Interface Unit (SCIU). Furthermore, several pieces of equipment will be needed at COMPOCC for this test: a wave generator; a SINAD meter; and modulation and demodulation equipment. This is fairly standard electronics instrumentation which may already be available. Some further equipment may be required to tailor the strength of the received signal in such a way that the desired power levels are achieved. Also, it may be necessary to design and build a control circuit which will adjust the amplitude of the uplink signal in real-time to the instantaneous range from COMPOCC to WSF.

It is anticipated that, during the execution of the communications experiment, no other command and telemetry can be performed using the COMPOCC-WSF link. Thus it must be established how much experiment time is available for a dedicated test, or what fraction of the communications window for each pass can be made available for the measurements described.

Finally, although EPOP will be a payload on the third flight of WSF, plans are underway to perform a precursor experiment on WSF02. This precursor experiment would serve to establish and fine-tune the procedures for performing the actual EMI experiment on WSF03.

3. Electrical Probe Measurements

One of the objectives of the EPOP flight is to perform a comparison between ground-based and space-based diagnostic results. In particular, there exists an interest in identifying any differences in operation of the arcjet thruster as a result of the lower background pressure in space compared to that

which can be achieved in typical ground test chambers. Two plume diagnostics of this type are being developed for EPOP. Here we describe the first one: electrical probe measurements in the plume. The second one — optical plume measurements — is described in Sec. 4.

One of the most common of the various electrical probe measurements is that based on the use of a Langmuir probe [4-6]. This method consists of inserting a single, double, or triple probe (consisting of one or more insulated wires whose tips are exposed) into the plasma environment of interest and measuring the current on the probe as a function of the applied voltage on the probe. From the voltage-current characteristic thusly obtained it is possible to calculate the number density and temperature of the electrons, as well as the plasma potential, floating potential, and, in some cases, the density of ions in the plasma.

Initial probe measurements (using a single probe) were performed on the 1 kW class arcjet thruster which CSTAR has on loan from NASA Lewis Research Center. The thruster was operated on a flow rate of 38 mg/s (6 slm), a voltage of 108 V, a current of 10 A, and a steady-state background pressure of about 0.8 Torr. A 3:1 mixture of hydrogen and nitrogen was used as the propellant. Under these conditions, the most luminous part of the plume extends about 15 cm from the exit of the thruster. This is the region in which a series of measurements were performed.

Figure 3 shows schematics of the probes which were built after Ref. [4]. Although the probes were tested in the UTSI vacuum facility, they were designed specifically to be used in conjunction with an upcoming test on the actual EPOP arcjet at Rocket Research Company. Tungsten wire was used as the probe material. Alumina tubing was used as a shield around the tungsten wire, leaving only a few millimeters of tungsten exposed. In turn the alumina tubing was equipped with a gold connector which can be plugged into a stainless steel support tubing. Finally, the tubing was mounted to a metal fixture using a standard 1/4" tube fitting and electrical hookup was facilitated with a coaxial connector.

A simplified electrical circuit was used to perform the measurements. Previously, similar measurements were performed on an ion thruster plume using a waveform generator and step-up transformer as the voltage source, and using a digital oscilloscope to read out the voltage and current on the probe. Instead, we used the RTI-815 data acquisition board from a PC-based computer both as the voltage source (using the programmable DAC output channel) and as the current measurement device (using an ADC input channel). With this setup, Langmuir probe traces were easily performed directly from the computer, without a need for additional instrumentation.

Figure 4 shows a typical sweep of the Langmuir probe recorded with the NASA LeRC arcjet. For negative voltages on the probe the current is very small and is given essentially be the ion current on the probe. For positive voltages, a much larger electron current is collected, showing saturation currents (the points at which the slope of the positive-going part of the trace starts leveling off) in the range 0.1 to 0.5 mA. These currents correspond to number densities in the range 0.8 to 4×10^{10} cm^{-3}. Typical values of the electron temperature obtained from these data were in the range 0.35 to 0.40 eV.

Using the above method of acquiring the Langmuir probe data, the minimum sweep time for one trace was about 40 msec for 500 points on the curve. Faster sweep times were possible with fewer points on the curve. By averaging a number of sweeps (say, 100) it was possible to obtain excellent signal-to-noise ratios, despite significant RF noise generated by the power supply of the NASA LeRC arcjet. The effect of sweep rate was found to be very small: for example, both forward and backward traces were performed, giving essentially the same results. This shows that heating of the probe in the electron collection regime was small enough that the shape of the trace was not affected significantly.

We will present a more complete analysis of the data at a later time. Shortly, similar measurements will be performed on the actual EPOP arcjet, operating on hydrogen propellant. These measurements will be compared with the ones on the NASA LeRC arcjet operating on simulated ammonia propellant. Based on this comparison, it will be

possible to identify points in the NASA LeRC arcjet plume with the same conditions (especially, the same electron density) as in the EPOP arcjet. Using this knowledge it will be possible to perform further development of the flight Langmuir probe system, using the NASA LeRC arcjet as a benchmark thruster.

4. Plume Imaging

The goal of the plume imaging diagnostic is to acquire in-flight quantitative image data on plume shape, stability, and structure. By targeting the dominant atomic hydrogen emission spectra, core temperature measurements can be made. As such, we view the imaging diagnostic not as an extraneous visual aid but as a precise optical measurement. This measurement requires that image intensities be calibrated absolutely with respect to emission wavelength. Therefore, development of the imaging diagnostic is a challenging task demanding exacting pre-flight preparation in the laboratory.

Development of the plume imaging flight diagnostic was active in the recent year. Basic spectroscopic surveys were performed and various imaging techniques involving 35 mm wet still photography, digital still photography, and video were evaluated. The purpose of our early development work has been to quantify expected emission characteristics and establish performance levels and optimal instrument settings for the candidate imaging techniques.

Substantial work was carried out in the UTSI Vacuum Research Facility using the 1 kW NASA LeRC arcjet operated on simulated ammonia. Because spectral features in the plume are emissions from atomic hydrogen and NH rotational bands, relevant diagnostic development work could be performed. We acquired nonfiltered images and filtered images at the Balmer-alpha and Balmer-beta lines. These atomic hydrogen lines will be the strongest spectral features in the plume of the EPOP hydrogen arcjet.

The results of our 35 mm wet still photography survey produced high resolution quality images with large dynamic range, but this technique has certain disadvantages which make it an encumbering medium to utilize, particularly on a spacecraft. For instance, obtaining absolute calibration and analyzing individual images is a tedious undertaking. Furthermore, the total number of acquired in-flight images would be limited, and the risk of degrading or destroying the image data during post-flight operations would be considerable. Another drawback is the marked absence of real-time imaging during flight. This technique does not take advantage of modern digital electronics and data communication capabilities. Such considerations prompted us to de-emphasize, early in the development effort, wet photography in favor of digital electronic methods.

In considering digital instruments for the imaging diagnostic, digital video stands out as the natural candidate. The image data can be stored on a flight recorder or communicated over an existing video downlink, and slow image transients can be captured. Calibration of the system and analysis of the data are not exceedingly difficult or tedious. Unfortunately, the ability to vary the exposure time on a CCD array video camera is generally quite limited. At best, the longest exposure time will approach 1/30 sec for the normal interlaced video rate; however, with an electronic shutter, shorter image exposure times are possible. Long exposure times may be necessary to resolve weak emission regions in the plume. This raises the additional consideration of instrument dynamic range; a small dynamic range would result in saturation regions when using long exposure times. These are the issues which must be addressed when using digital electronic instruments.

An alternative to video is digital still photography. Fundamentally, the digital camera is a CCD camera directly connected to a video image digitizer with special software for acquiring still images. A digital camera has variable exposure time capability. Exposures lasting milliseconds or seconds are producible. The resulting images are captured, digitized, and stored in industry standard format. This instrument does not suffer from the exposure time limitations of video, but resolution of transient effects is more limited, and dynamic range remains an important issue.

Both video and digital still photography techniques have been investigated. Our results indicate that

either method would be suitable for the proposed diagnostic. Issues of continual concern are luminous sensitivity, dynamic range, and spaceflight compatibility. We have yet to identify and specify a flight camera having the optimal characteristics we desire. Indeed, we continue to evaluate variations on the proposed imaging diagnostic.

To separate the spectral components of interest, line filters have been used. That is, a separate image is acquired for each desired wavelength. However, if a color RGB (red-green-blue) camera is used, it is feasible to consider separating the important spectral components in an unfiltered digital image. Since the Balmer-alpha line is centered in the red portion of the spectrum and the Balmer-beta line is centered in the blue portion of the spectrum, it may be possible to relate the red component of the unfiltered image primarily to the alpha line and the blue component primarily to the beta line. By calibrating the spectral sensitivity for each component, the RGB camera assumes the function of a spectrometer. This idea has been investigated, and an example of a composite unfiltered RGB image, that of the plume from the NASA LeRC arcjet, and its RGB components is illustrated in Fig. 5.

This idea of digitally filtering an RGB image was pursued in the laboratory. But in doing so we discovered that continuum emission from the plume was not insignificant. Because the RGB components are wide-band signals, the integrated effect of low level continuum radiation can assume a significant portion of the total intensity level. As a check, the level of continuum emission was measured using a spectroscopic technique which assured no electronic offset bias. That is, zero emission corresponded directly with zero signal. A calibrated scan of the spectrum when the NASA LeRC arcjet plume is both on and off is shown in Fig. 6. Because a simulated ammonia propellant was used, the spectrum contains NH rotational bands in addition to the hydrogen Balmer lines. One should note that the window of the vacuum chamber does not transmit below roughly 3300 Å and that the structure beyond the alpha line is the second-order NH bands. Of more relevance is the clear indication of continuum emission across the entire visible spectrum. This continuum radiation complicates the interpretation of the filtered images but does not pose an insurmountable problem with the implementation of the technique.

It is possible that using pure hydrogen propellant will reduce or eliminate the continuum radiation. Some experience suggests otherwise: other researchers have found continuum emission from pure hydrogen arcjets having a similar power level [7]. These measurements, however, were made along the axis of the arcjet thruster, with direct optical access to the constrictor region of the arcjet nozzle. It remains to be seen whether the same will be observed when viewing the plume orthogonal to the thruster axis. We expect that the issue will be resolved with the upcoming test of the EPOP arcjet at Rocket Research Company.

Acknowledgments

This work was supported by CSTAR through NASA Grant NAGW-1195 and through an EPOP supplement. We gratefully acknowledge the assistance of Ms. Karen Harwell in performing background research for the EMI experiment and technical insights and suggestions by Mr. Joe Pineda of SII. We also acknowledge the assistance of Dr. L. Montgomery Smith with the plume imaging experiments. Finally, we acknowledge all the inputs from the other EPOP consortium members.

References

[1] W. M. Ruyten and V. J. Friedly, "EPOP diagnostics and data acquisition," Proceedings of the 3rd Annual Technical Symposium, Center for Space Transportation and Applied Research, Tullahoma, Tennessee, January 14-15, 1992, pp. 74-82.

[2] V. J. Friedly, G. W. Garrison, and W. M. Ruyten, "EPOP: toward the realization of an Electric Propulsion Orbital Platform," AIAA paper 92-3201, 28th AIAA Joint Propulsion Conference, Nashville, Tennessee, July 6-8, 1992.

[3] V. J. Friedly, G. W. Garrison, and W. M. Ruyten, ``Electric Propulsion Orbital Platform,'' Proceedings of the 4th Annual Technical Symposium, Center for Space Transportation and Applied Research, Tullahoma, Tennessee, November 11-12, 1992, pp. 15-21.

[4] J. M. Sankovic, ``Investigation of the arcjet plume near field using electrostatic probes,'' NASA TM 103638, 1990.

[5] L. M. Carney and T. G. Keith, ``Langmuir probe measurements of an arcjet exhaust,'' *J. Propulsion and Power*, Vol. 5, No. 3, May-June 1989, pp. 287-294.

[6] H. A. Habiger, M. Auweter-Kurtz, and H. Kurtz, ``Electrostatic probes for the investigation of arc-driven electric propulsion devices,'' Paper IEPC-93-124, 23rd International Electric Propulsion Conference, Seattle, Washington, September 13-16, 1993.

[7] P. V. Storm and M. A. Cappelli, ``Axial Emission Diagnostics of a Low Power Hydrogen Arcjet Thruster,'' Paper IEPC-93-219, 23rd International Electric Propulsion Conference, Seattle, Washington, September 13-16, 1993.

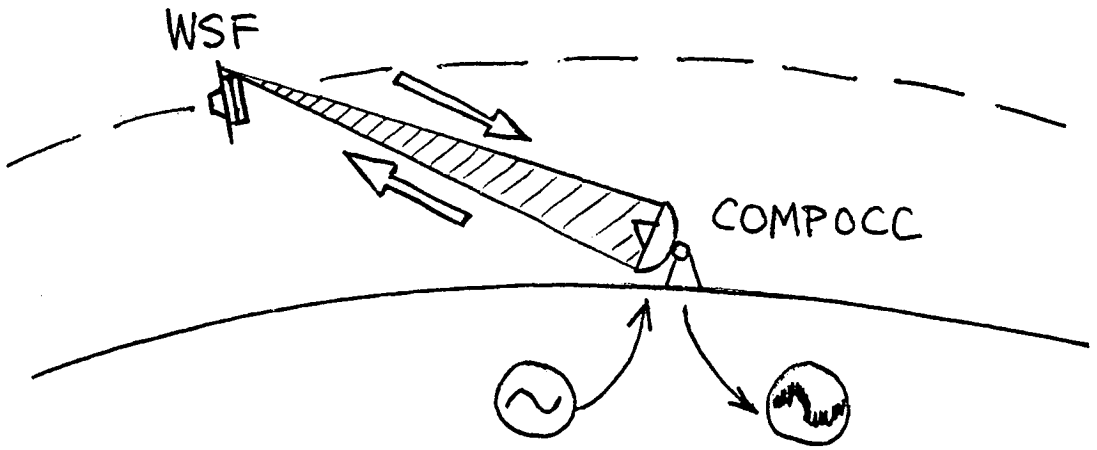

Figure 1: *Schematic diagram of the spacecraft communications experiment.*

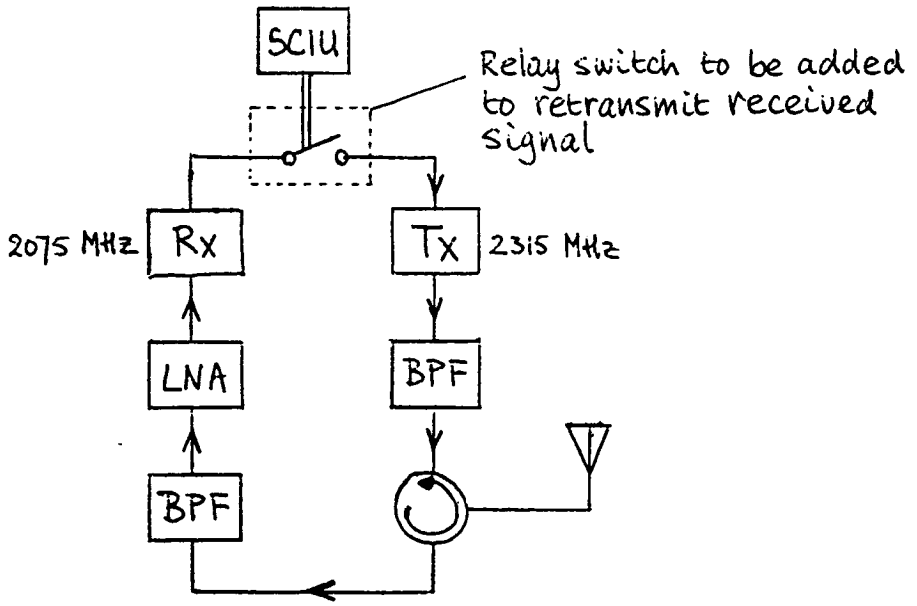

Figure 2: *Schematic of the proposed modification of the WSF RF system to accommodate the EPOP communications experiment.*

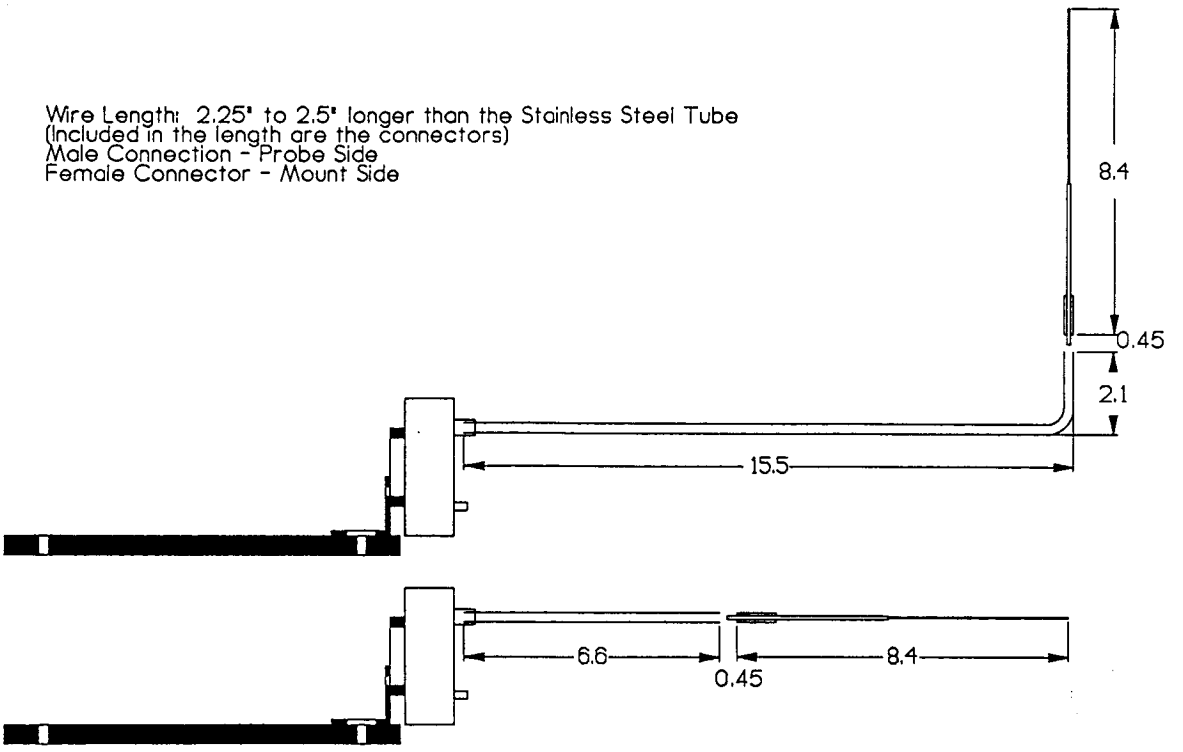

Figure 3: *Schematic of some of the Langmuir probes which have been constructed for initial electrical probe diagnostics on the NASA LeRC and the EPOP arcjets. All dimensions are in inches.*

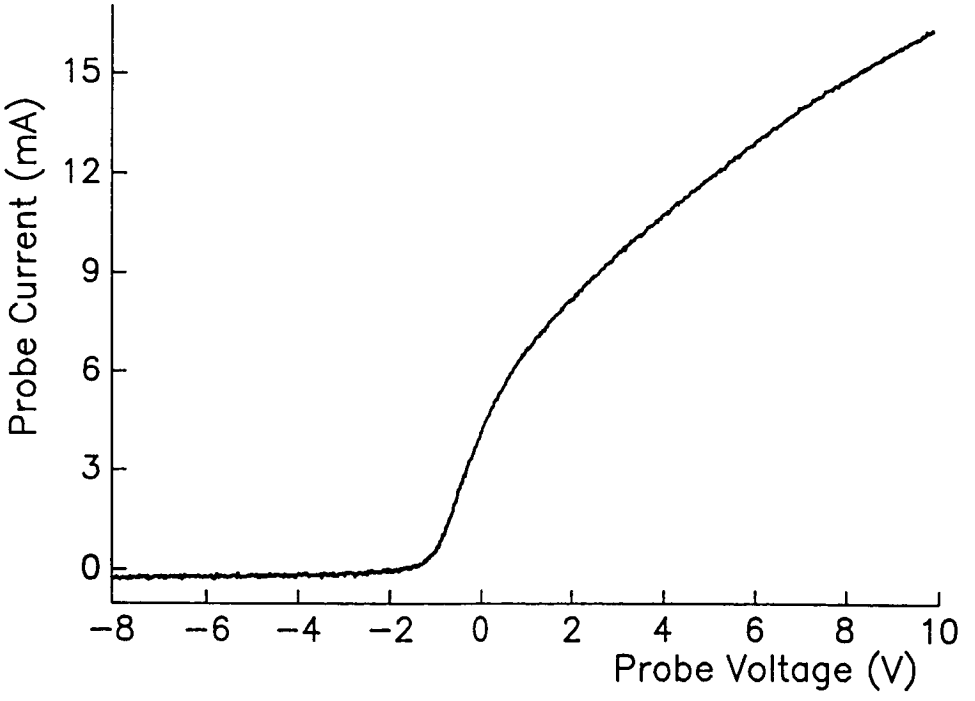

Figure 4: *Typical Langmuir probe trace collected in the NASA LeRC arcjet plume.*

Digital Color Camera

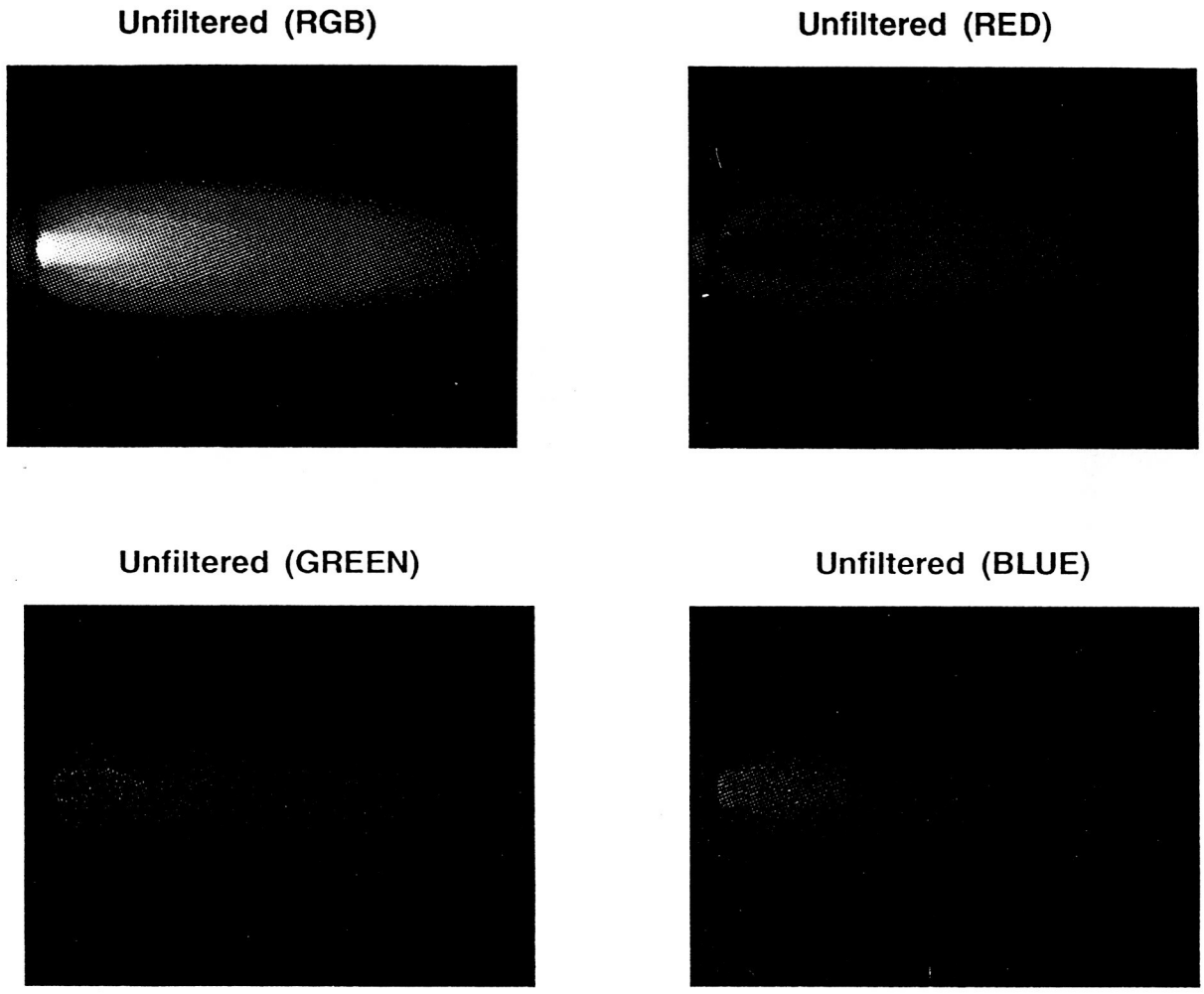

Figure 5: *Composite and RGB components of an unfiltered digital color image of the NASA LeRC arcjet operating on simulated ammonia propellant.*

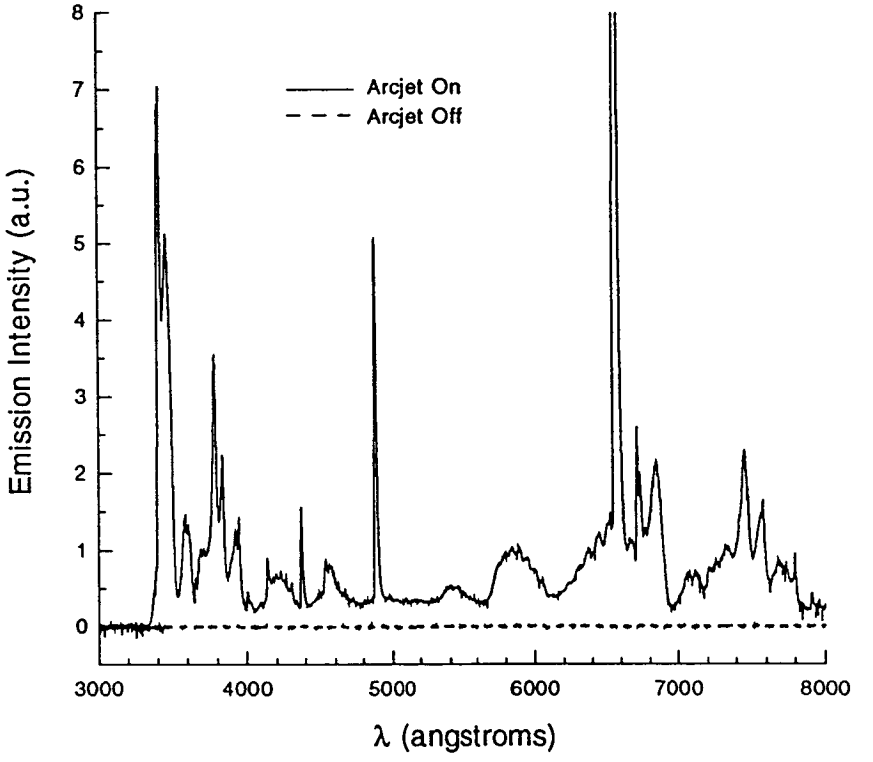

Figure 6: *Typical spectral emission scan taken on the NASA LeRC arcjet plume. The strongest signal (off scale) is that of the hydrogen Balmer alpha line at 6563 Å. Note however that significant continuum emission is present as well.*

Experimental and Analytical Ion Thruster Research

W. M. Ruyten†, V. J. Friedly,* and X. Peng*
University of Tennessee-Calspan
Center for Space Transportation and Applied Research
Tullahoma, Tennessee 37388-8897

and

D. Keefer**
Center for Laser Applications
University of Tennessee Space Institute
Tullahoma, Tennessee 37388-8897

Abstract

We report the results of further spectroscopic studies on the plume from a 3 cm ion source operated on argon propellant. In particular we show that it should be possible to use the spectroscopic technique to measure the plasma density of the ion plume close to the grids, where it is difficult to use electrical probe measurements. We outline how the technique, along with electrical probe measurements in the far downstream region of the plume, can be used to characterize the operation of a three-grid, 15 cm diameter thruster from NASA JPL. Pumping speed measurements on the Vacuum Research Facility have shown that this facility should be adequate for testing the JPL thruster at pressures in the low 10^{-5} Torr range. Finally, we describe a simple analytical model which can be used to calculate the grid impingement current which results from charge-exchange collisions in the ion plume.

1. Introduction

For a number of years, one of the key activities in CSTAR's electric propulsion program has been ion thruster research, comprising both numerical modeling and experimental work (see, for example, Refs. [1] and [2] from last year's symposium proceedings). One constant theme of this work has been to develop a better understanding of the mechanisms of grid erosion which remains to this day the principal complication in validating ion thrusters in ground testing. Another subject of interest has been the modeling and characterization of the ion optics of a given thruster system. For example, changes in grid optics lead directly to changes in plume divergence and thrust. Furthermore, because of their mutual dependence, minimization of grid erosion and optimization of grid optics cannot be performed separately, so a comprehensive approach is required. As noted, this approach has involved both numerical modeling and experimental research.

Efforts on the numerical side have been devoted largely to the development of a code which is able to predict the ion trajectories and grid erosion in a given thruster system [1]. Recent progress in this area is discussed elsewhere in these proceedings. During the course of the numerical work it has become increasing clear that, in order to make reliable predictions of ion thruster lifetime, it is of fundamental importance to know the properties of the downstream plasma region of the thruster. Thus a significant part of the experimental work has

† Senior Research Engineer, Principal Investigator
* CSTAR Research Engineer
** B. H. Goethert Professor of ES&M

This work was supported by the Center for Space Transportation and Applied Research, Boeing Defense & Space Group, and Engineering Research Consultants, Inc.

focused on the development of new optical diagnostic techniques to investigate the ion plume. Much of this work was presented in last year's proceedings [2] and in a paper at the 29th Joint Propulsion Conference [3]. An update and summary of these optical plume studies are given in Section 2.

The work described in Section 2 (and most of the associated numerical modeling) was performed on a two-grid ion source. A recent development in ion thruster research is a resurgence of interest in operation of three-grid sources [4-7]. The reason for this renewed interest is that the grid erosion of three-grid sources is expected to be significantly less, particularly in ground testing, than that of two-grid sources of the same power level. Thus, while three-grid thrusters may not out-perform two-grid thrusters during space operation, they may be the only thrusters which can be life-tested in ground facilities with limited pumping capabilities.

To accelerate the development of such three-grid ion thrusters, NASA JPL is utilizing the Small Business Innovative Research (SBIR) program. CSTAR has subcontracted with Engineering Research Consultants, Inc. (ERC) of Tullahoma to conduct an SBIR Phase-II program with the objective of developing an engineering design code for three-grid ion thrusters. CSTAR's specific contribution to this effort will be experimental testing of a prototype three-grid thruster, which will be provided by NASA JPL. In preparation for this testing, pumping speed measurements were performed in the Vacuum Research Facility of the University of Tennessee Space Institute. Results of these measurements are described in Section 3, which also discusses other aspects of operation of the JPL thruster.

In Section 4, we discuss the strategy which has been devised to allow a direct comparison between experimental and calculated results for the three-grid thruster. This comparison is not straightforward because the numerical code describes strictly only a single set of apertures, whereas the actual grid is comprised of thousands of such apertures. Also, some of the input parameters for the numerical code will have to be obtained from the experiment. At first sight, this would seem to lead to a circular argument (namely, by using the experimental results both as input to the code and as data to validate the code). However, we show in Section 4 how to resolve this situation, relying, in part, on the optical diagnostic techniques whose development is described in Section 2.

Finally, in Section 5, we discuss a simple analytical model which we have used to complement the numerical modeling efforts. Specifically, the model demonstrates that the impingement current on the last grid of the thruster during ground testing can be estimated reasonably well by a simple model in which the downstream plasma density does not have to be specified as an input parameter to the code, as is presently the case with the particle-in-cell model.

2. Optical diagnostics by emission spectroscopy

In Refs. [2] and [3] we have reported the results of a number of emission measurements which we performed on the plume from a two-grid, 3-cm ion source operated on argon propellant. Figure 1 shows a diagram of the experimental setup. All data were taken with a 1.25 m focal length spectrometer, capable of taking data with a spectral resolution of 0.1 Å. Light from the plume was collected with a Cassegrain telescope with an effective aperture of f/10. The signal from the photo-multiplier tube was amplified and measured by a computer-based data acquisition system.

Using this setup, a large number of spectral lines was identified in the range 4000 Å to 8000 Å. The lines were easily interpreted as being due to emissions from neutral (Ar I) and singly ionized argon (Ar II). Although the discharge voltage of the ion source was sufficiently high (40 to 50 V) that doubly charged ions could have been produced, no evidence for doubly charged ions was found in the emission spectra.

The magnitude of the emission signals depended clearly on the tank pressure. In fact, to produce sufficiently strong signals, the tank pressure was raised intentionally in some cases (to a maximum pressure of 3×10^{-4} Torr) so as to yield good signal-to-noise ratios on the detected signals. Figure 2 shows a typical photograph of the plume taken under such conditions. Figures 3 and 4 show the dependence of the measured strengths of the emission signals as a

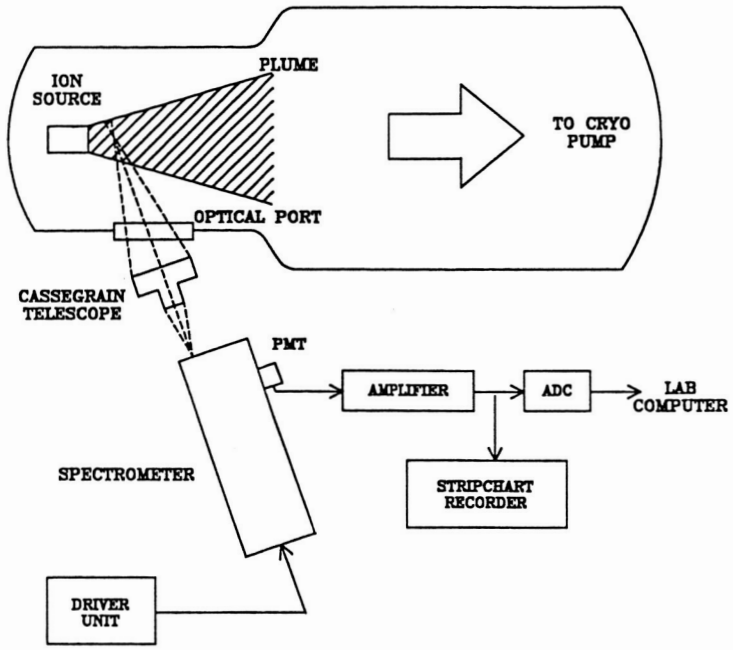

Figure 1: *Schematic of the experimental setup for the emission measurements on the 3 cm ion source. The spectrometer is positioned at an angle to the flow to allow a determination of the plume velocities by exploitation of the Doppler shift.*

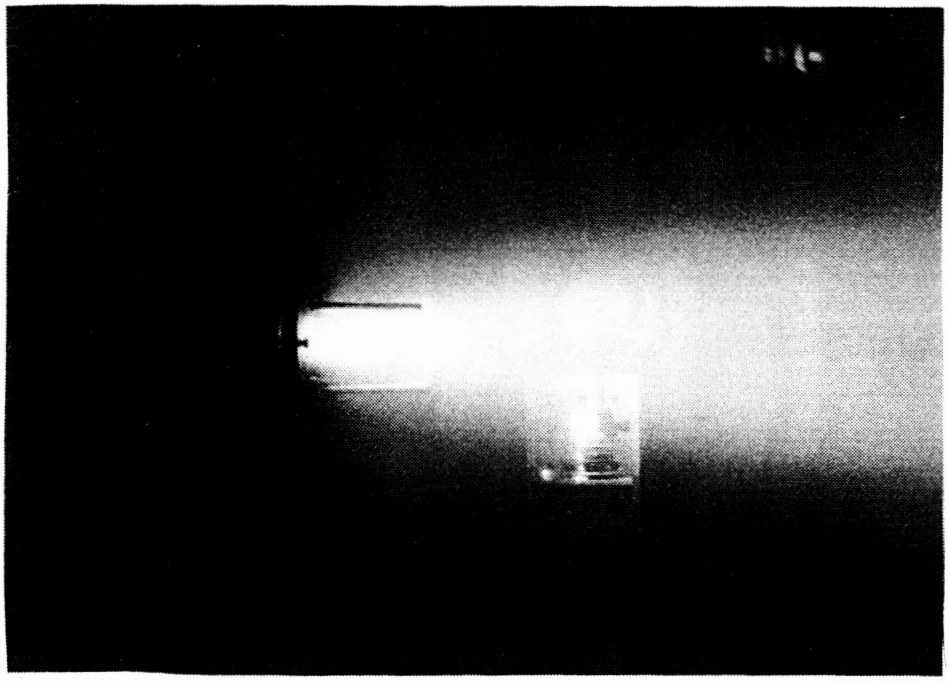

Figure 2: *Typical photograph of the plume from the 3 cm ion source.*

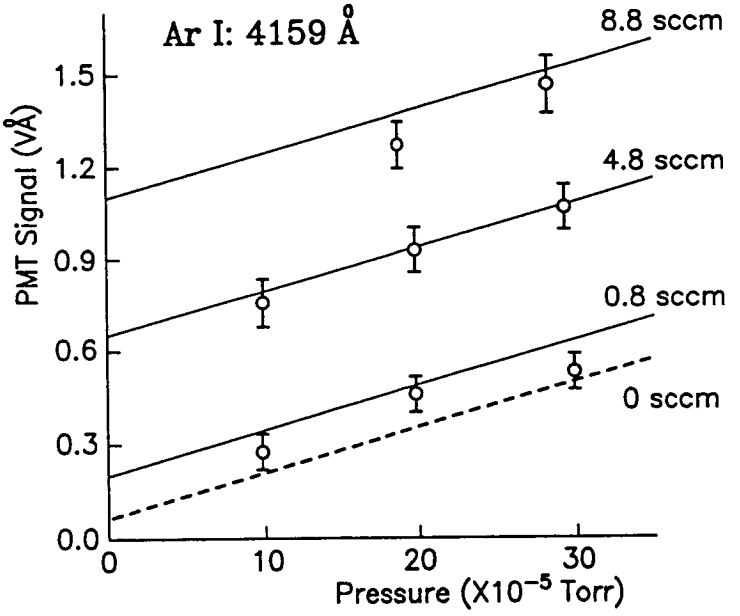

Figure 3: *Dependence of emission intensity on chamber pressure and net neutral flow rate for the argon neutral line at 4159 Å. Solid and dashed lines represent the results of a bilinear curve fit (for further details see Refs. [2] or [3]).*

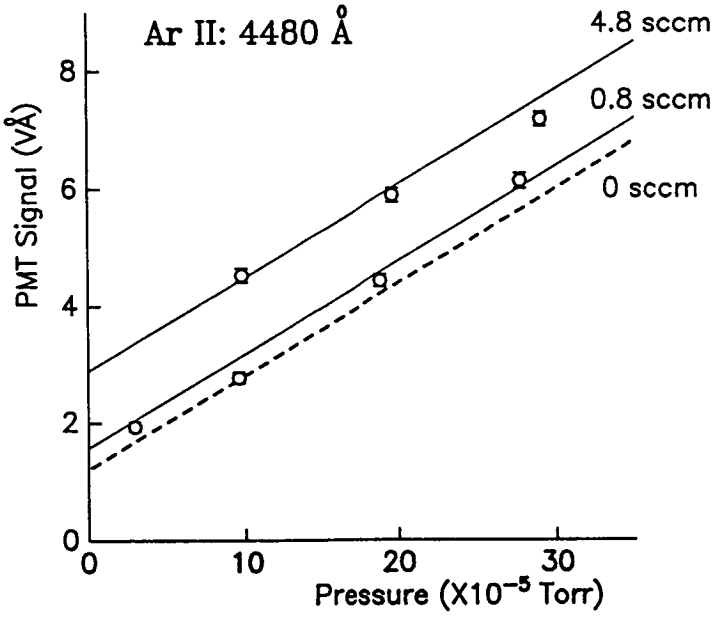

Figure 4: *Same as Fig. 3 for the argon ion line at 4480 Å.*

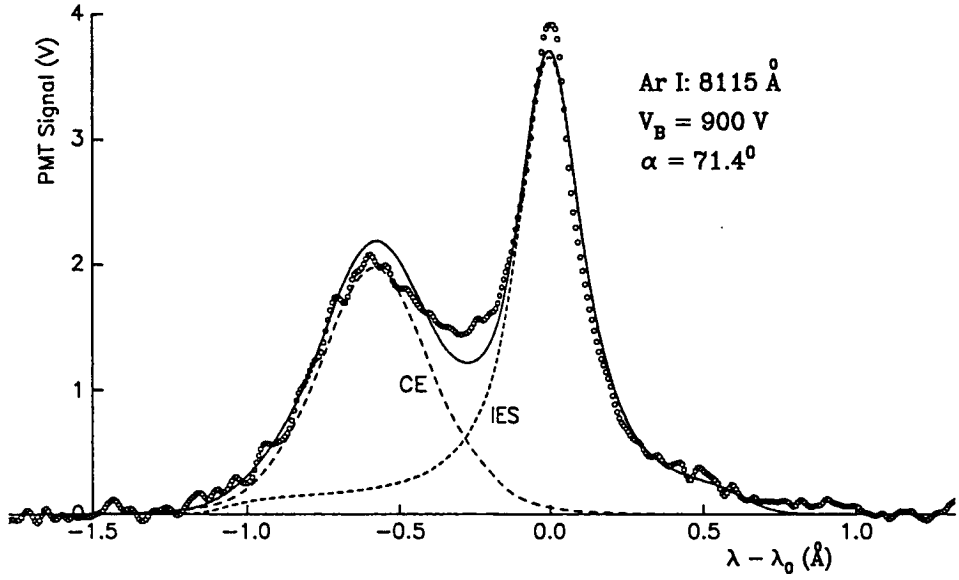

Figure 5: *Typical emission spectrum of an argon neutral line. The two peaks correspond to fast (left) and slow (right) neutral atoms. The beam energy was 900 V.*

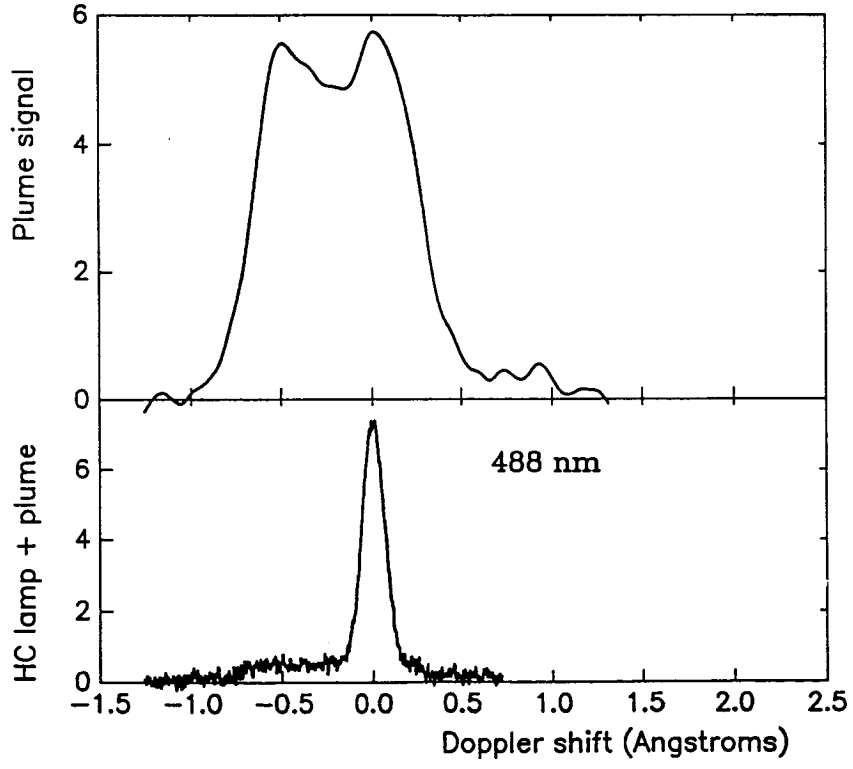

Figure 6: *Emission spectrum of an argon ion line (top) for the same conditions as in Fig. 5. At the bottom, a simultaneous scan of a hollow cathode lamp is displayed, which shows a thermal distribution only. The left peak in the ion signal is due to emissions from fast beam ions.*

function of tank pressure and propellant flow for constant electrical conditions of the source. Results are shown for a neutral line (Fig. 3) as well as an ion line (Fig. 4). The interpretation of these measurements is discussed in detail in Refs. [2] and [3]. Most importantly, the results show that (1) for constant operating conditions of the source, the signal varies linearly with chamber pressure and (2) unlike the signal at the neutral line, the signal at the ion line does not extrapolate to zero for zero neutral density, as is illustrated by the dashed lines in Figs. 3 and 4. These results confirm the predictions from a simple model for the scattering processes in the plume (see Section 4) and are relevant to the planned measurements on the three-grid thruster which are discussed in Section 4.

Another type of measurement was performed to study in detail the spectral shapes of the emission lines. In these measurements, high-resolution spectral scans were performed of a number of lines, with the spectrometer positioned at an angle of about 71 degrees to the plume axis. In this way, it was possible to separate, optically, emissions from fast and slow species in the flow, namely by exploitation of the Doppler shift. Figures 5 and 6 show typical results for a neutral line (Fig. 5) and an ion line (Fig. 6). In both cases, the spectral lines clearly consist of two peaks. Analysis of these data shows that the center of the right-most peaks in Figs. 5 and 6 corresponds to zero Doppler shift, and that the other peak is displaced by an amount which is precisely determined by the energy of the beam ions, the observation angle, and the wavelength of the unshifted transition.

A much more sophisticated analysis is required to describe the shapes of the spectral lines, as they depend on the beam divergence angles, the instrument broadening introduced by the optics, and, in the case of the fast component of the ion lines, the differential cross-section of the ion-neutral scattering process [2,3,8]. Initial results are presented in Refs. [2] and [3]. Possibly, such analysis will also prove to be of value for a comparison between experimental and numerical results on the three-grid ion thruster. However, this would require a significant effort and it may be possible to obtain the same kind of information from electrical probe measurements which can be performed and analyzed more easily.

Finally, during the course of the experimental work, several recent papers were found [9-11] in which similar optical measurements were reported for an ion source used in materials processing applications. To our knowledge, this is the only other such work which has been reported in the literature. By and large, the conclusions stated in Refs. [9-11] are the same as those which we had reached on the basis of our experiments. Also, some other insights were gleaned from this work which should be useful in further optical studies of ion thruster plumes.

3. Preparations for testing the JPL thruster

Recently, a 15 cm, three-grid ion thruster was developed at NASA JPL for use on small planetary space craft. The thruster is essentially a scaled-down version of the NASA Lewis light-weight, 30 cm thruster. A diagram of the 15 cm thruster is shown in Fig. 7, which was taken from Ref. [4]. Operating characteristics of the 15 cm thruster are reported in Ref. [4]. The thruster is designed for operation at power levels in the range 400 W to 1.25 kW, assuming xenon propellant. The maximum projected

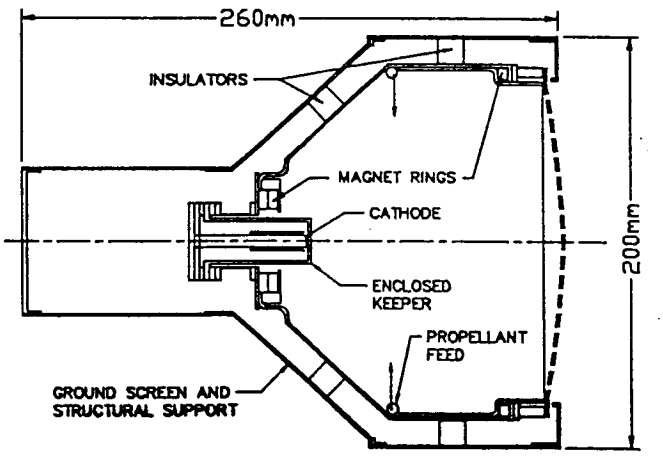

Figure 7: *Schematic of the 15 cm JPL thruster (from Ref. [4]).*

propellant flow rates are 1.5 mg/s (15 sccm) of xenon and 0.8 mg/s (30 sccm) for operation on argon propellant. These flow rates include the flow through the two hollow cathodes which ionize and neutralize the main propellant flow.

In preparation for testing of one of these JPL thrusters, pumping speed measurements were performed on the Vacuum Research Facility of the University of Tennessee Space Institute. Until now, it has been sufficient to use the small cryopump only. For example, all experiments on the 3 cm ion source reported in Section 2 were performed with this pump. The maximum chamber pressure during these tests was about 3×10^{-4} Torr for an argon flow rate of 12 sccm. By contrast, the target pressure for operation of the 15 cm JPL thruster has been set at 3×10^{-5} Torr. Clearly, this pressure cannot be maintained at the anticipated flow rates using the small cryopump only. Instead, the helium cryo system will have to be used.

A description of the helium cryo system may be found in Ref. [12]. In short, its principal elements are a liquid-helium-cooled cryo surface with an area of 23 m^2 and a nominal temperature of 20 K; a liquid nitrogen liner to shield the 20 K surface; and a helium compressor and refrigerator with a maximum capacity of 900 W. Previous tests on the cryo system have indicated that, due to poor insulation of the nitrogen liner and due to poor circulation of the liquid nitrogen through the cooling lines on the liner, the actual capacity of the helium system was less than the stated value by a factor of about three. By wrapping the nitrogen liner with milar, this capacity was improved to approximately 500 W.

Figure 8 shows the results of a pumping speed test performed with room-temperature argon gas. Shown is the steady state pressure as a function of flow rate. Even for the very large flow rate of 2000 sccm, a pressure of about 10^{-4} Torr could be maintained, implying a pumping speed of 250,000 l/s. At the lowest flow rate in the test (20 sccm), a pressure of 1.2×10^{-5} Torr was measured (the base pressure with no flow was in the 10^{-7} range). This pressure is sufficiently low that it should be possible to maintain the target pressure of 3×10^{-5} Torr (or lower) at all projected flow rates for the 15 cm thruster.

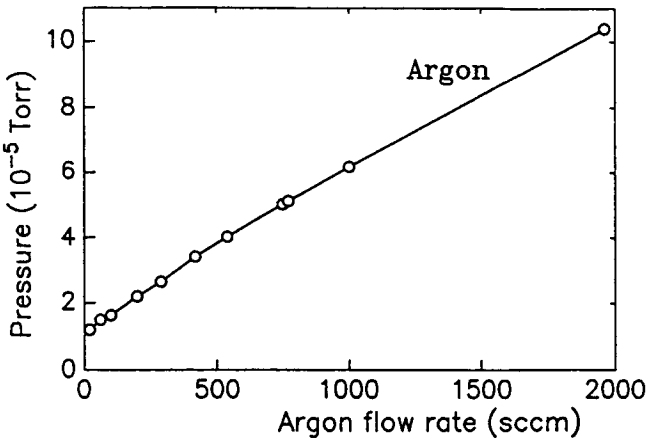

Figure 8: *Results of a pumping speed test on the helium cryo system of the Vacuum Research Facility using room-temperature argon propellant.*

Finally, to accommodate the JPL thruster, a number of modifications to the existing facilities and equipment will have to be made. These include adding electrical and propellant feedthroughs; design of a mounting bracket for the thruster; adding several power supplies; and design and installation of several electrical probes for plume studies. Most of these tasks have been initiated.

4. Planned diagnostics for JPL thruster

The principal goal of the experiments on the 15 cm thruster will be to perform measurements in support of the numerical code development for three-grid ion thrusters by ERC, Inc. of Tullahoma. A number of measurements will be obtained fairly easily. In particular, it should be straightforward to obtain measurements of impingement currents on the accelerator and decelerator grids for a series of operating conditions, including varying background pressures. These data should be particularly useful to verify that the grid impingement mechanisms in the code are modeled correctly.

To verify that the numerical code predicts the ion optics correctly, it will be desirable to perform beam profile measurements at different distances from the thruster. From these, it should be possible to calculate the beam divergence parameters. One complication in comparing experimental results to the model calculations is that the model results are

strictly valid for a single set of thruster grid apertures only. By comparison, the actual thruster grid is comprised of thousands of apertures. To remedy this situation, it will be necessary to integrate the numerical results over the extent of the thruster grid. This is illustrated schematically in Fig. 9. In order to perform this numerical integration, it is necessary, in turn, to know what the plasma density distribution is as a function of radial position. Typically, the density at the edges of the thruster is only 50 to 70 percent of that at the centerline. This information should be supplied as an input parameter to the code and must thus be obtained from experiment.

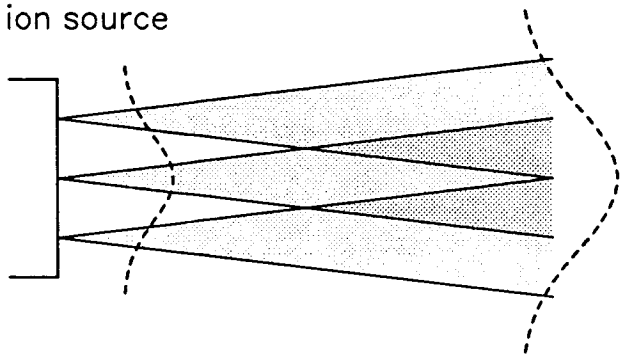

Figure 9: *Schematic diagram to indicate that the measured ion flux at some point downstream from the thruster is the sum of contributions from many apertures.*

In principle, this density could be estimated reasonably well from electrical probe measurements of the ion flux very close to the thruster grids (close to the grids, there is not yet any mixing of ion beamlets from adjacent apertures). Particularly close to the grids, however, such probe measurements could not be considered as nonintrusive. Not only might they disturb the ion flow enough to produce results which are no longer representative of the unperturbed flow, but they might also give rise to thruster contamination as a result of sputtering of the probe close to the thruster grids. Obviously, both of these problems would be avoided by nonintrusive optical measurements. Such an experiment has been devised and will be described briefly below.

The basic arrangement of the experiment would be similar to that shown in Fig. 1, with a spectrometer set up so as to be able to image the plume onto the entrance slit of the spectrometer. A perpendicular observation angle will be employed and the thruster will be positioned so that the observation region is as close to the thruster grids as possible. Also, using aperture stops, the collection optics will be designed so that only a small vertical region in the plume is imaged onto the grating. Thus, it will be possible to measure the emission intensity as a function of the distance from the thruster centerline. Of course, these emission data are still line-of-sight averages. However, because of the radial symmetry of the plume, the actual radial dependence of the emission intensity can be obtained by an Abel inversion of the measured data.

It now remains to show that the measured radial intensity distribution is proportional to the plasma density in the plume. To this effect, we express the (local) emission signals S_i of an ion line and S_0 of a neutral line in terms of the ion density n_i, the neutral density n_0, and the electron density n_e as:

$$S_i = k_1 n_i n_e + k_2 n_i n_0 \qquad (1)$$

and

$$S_0 = k_3 n_0 n_e + k_4 n_0 n_i, \qquad (2)$$

where the k's are proportionality constants. The two terms in Eq.(1) are due to excitation of an ion by electrons and neutrals, respectively. Similarly, the two terms in Eq.(2) are due to excitation of a neutral atom by electrons and ions, respectively. Next, it will be assumed that, even though the measurements are performed close to the grids, neutralization of the ion beam has already occurred. Thus we substitute $n_e = n_i$ in Eqs.(1) and (2) so that

$$S_i = k_1 (n_i)^2 + k_2 n_i n_0 \qquad (3)$$

and

$$S_0 = (k_3 + k_4) n_0 n_i. \qquad (4)$$

We now see that the intensity of a neutral line (but not that of an ion line!) is proportional to the ion density n_i, which is the quantity we wish to measure.

Also, the signal is proportional to the neutral density (see Section 2, Fig. 3 in particular). However, unlike the ion density, this neutral density should be fairly uniform across the exit of the thruster (the neutral efflux from the thruster is basically independent of the ionization processes inside the thruster). Thus, measurement of the spatial variation of the emission intensity at a neutral line should provide a measure of the local ion density, which is the quantity which we wish to obtain.

An important check on the technique would be to verify that the derived spatial dependence of the ion number density is the same for different emission lines. If so, one has a reasonable assurance that systematic errors in the experiment and in the analysis are small enough that they may be neglected.

Although the optical measurements are of particular importance close to the grids (where electrical probe measurements cannot be performed) they are not restricted to this region. Of course, the larger the distance from the thruster, the smaller are the relevant densities, and the smaller will be the emission signals. Also, far downstream, the chance of introducing systematic errors into the interpretation of the emission measurement increases. On the other hand, the far downstream region (at a distance of at least several thruster diameters from the grids) should lend itself ideally to electrical probe measurements. Through this combination of electrical probe measurements and emission spectroscopy, it should be possible to obtain high-quality data which can serve the purpose of validating the numerical code predictions with regard to ion optics and beam divergence.

5. Calculation of grid impingement currents

As is well known, the primary source of grid erosion in ion thrusters is the production of charge-exchange (CE) ions in the downstream region of the thruster. These ions are created with small (thermal) velocities and are easily accelerated back to the grids. An important parameter which governs how large the region is from which CE ions can be extracted is the charge-exchange length associated with the CE process. Typically, when equating this charge-exchange length with the distance between the grids and the neutralization plane in the plume, a smaller length is found than that required to explain the grid impingement currents which are observed in ground testing. In this work we have developed a simple model which results in an effective charge-exchange length which can be on the order of 0.4 times the thruster radius. This length is larger by about an order of magnitude than that associated with the location of the neutralization plane.

A detailed account of the analytical model is presented in Ref. [13]. Here we review briefly the outline and main results of the model. The basic premise is that at any point in the downstream region of an ion thruster the probability that a CE ion should return to the grid is determined by the solid angle subtended by the thruster, as seen from the point where the CE ion is produced. For example, close to the grid, this probability is 0.5, because the CE ion moves either toward the grid, or away from it. Figure 10 shows calculated equi-probability contours in the downstream region of the thruster. The larger the distance from the thruster, the smaller is the solid-angle probability.

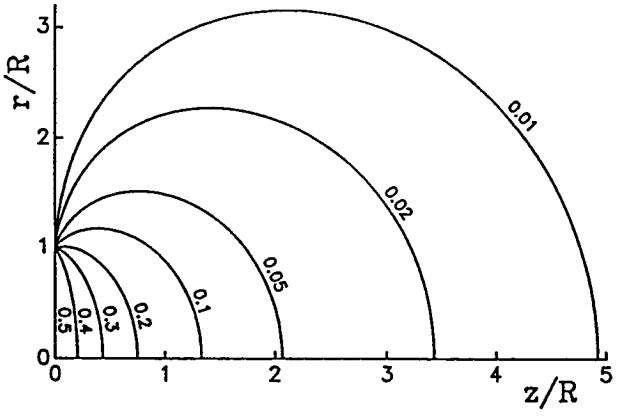

Figure 10: *Contours of equal solid-angle-probability $f_\Omega(z,r)$ in the downstream region of an ion thruster. The center of the thruster grid is located at the origin. The coordinates z and r represent axial and radial coordinates in the downstream region; they are normalized relative to the thruster radius R. Note that all contours coalesce at the thruster edge, located at position (0,1).*

Developing this concept further, it is shown in Ref. [13] that the ratio of accelerator-grid-impingement current to beam current can be expressed as

$$J_i / J_b = n_0 \sigma_{ce} \langle l_\Omega \rangle, \quad (5)$$

where n_0 is the neutral density in the chamber, σ_{ce} is the cross-section for charge-exchange, and $\langle l_\Omega \rangle$ is the effective charge-exchange length, which is given by

$$\langle l_\Omega \rangle = \int \int r \, dr \, dz \, f_\Omega(r,z) \, P_z(r), \quad (6)$$

where $f_\Omega(r,z)$ is the solid-angle-probability from Fig. 10, and $P_z(r)$ is the (normalized) transverse profile of the ion beam emanating from the thruster. The integration in Eq.(6) is over the entire downstream region of the thruster. In Ref. [13], the integral from Eq.(6) is calculated for a number of transverse beam profiles $P_z(r)$. Results are shown in Fig. 11, which shows the calculated value of the charge-exchange-length $\langle l_\Omega \rangle$ as a function of the beam divergence half-angle (denoted γ in Fig. 11), for three beam-shape parameters λ, which are chosen such that $\lambda = \infty$ corresponds to a top-hat profile, $\lambda = 1$ corresponds to a truncated cone, and the curve with $\lambda = 4$ corresponds roughly to a typical beam profile encountered for an actual thruster.

Figure 11 shows that typical values of the charge-exchange-length $\langle l_\Omega \rangle$ are in the range 0.35R to 0.45R, where R is the thruster radius. This charge-exchange length is significantly larger than the commonly used distance from the thruster grid to the neutralization plane, which is typically in the range 1 to 10 mm, even for a thruster with a radius as large as 150 mm. Physically, this means that the observed grid-impingement-current — and therefore the grid erosion — is much larger than would be estimated on the basis of the location of the neutralization plane alone.

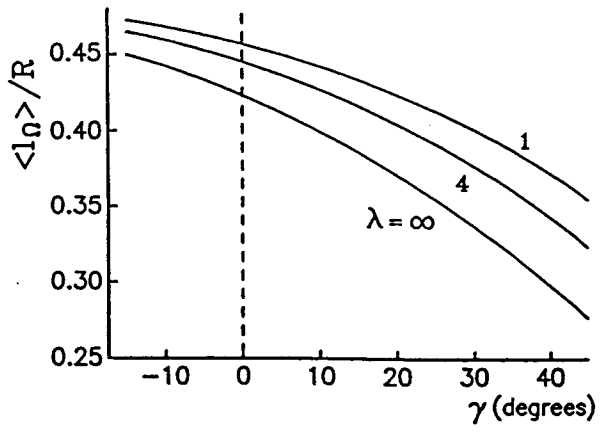

Figure 11: *Normalized charge-exchange-length $\langle l_\Omega \rangle / R$ as a function of the beam divergence half-angle γ and a beam-shape parameter λ (see text).*

In order to check the results of the model, the ratio $\langle l_\Omega \rangle / R$ was calculated from Eq.(5) for two widely different experiments: the first one corresponds to the test of a 30 cm thruster at NASA Lewis Research Center [14]; the second corresponds to experimental measurements on a 3 cm ion source performed at CSTAR [2]. Table I summarizes the results. The derived values for the ratio $\langle l_\Omega \rangle / R$ are 0.27 and 0.54 for the two cases, respectively. These values are in reasonable agreement with the values in Fig. 11, thereby proving the utility of the simple conceptual model.

Table I: *Verification of geometric model for two sets of experimental parameters, which are described in the text.*

Case	J_i/J_b (%)	n_0 (10^{17} m^{-3})	σ_{ce} (10^{-20} m^2)	$2R$ (cm)	$\langle l_\Omega \rangle / R$
1	0.55	4.5[1]	32.3[2]	28.2	0.27
2	0.55[4]	32[1]	21.2[3]	3.0	0.54

[1] Assuming a gas temperature of 300 K.
[2] For xenon at a beam energy of 1517 eV.
[3] For argon at a beam energy of 550 eV.
[4] Measured as a slope of 0.25 mA per 10^{-4} Torr at a constant beam current of 45 mA.

We should point out that the model is not intended to replace the much more complex particle simulation model which has been under development at CSTAR for several years. However, the model confirms that the properties of the downstream plasma in the particle simulation model can be estimated from first principles (presently, the downstream plasma density is chosen in such a way

as to yield the desired ratio of impingement-to-beam current). Also, the simple analytical model ceases to be valid for conditions approximating more closely those encountered during actual space operation of the thruster. This is because, in space, unlike in ground testing, the implicit assumption of an isotropic velocity distribution for the neutral gas is no longer valid, thereby invalidating the argument of a solid-angle-based probability of backstreaming of CE ions. The particle simulation model, on the other hand, can easily accommodate such non-isotropic velocity distributions.

Finally, one other advantage of the present model is that, unlike the particle simulation model (which models basically only a single set of grid apertures), the geometric model predicts that the erosion on a thruster grid should be nonuniform even for a uniform beam profile. This is illustrated in Fig. 12, which shows the normalized grid-impingement current as a function of the radial position s/R on the thruster grid for several beam-divergence half-angles γ, assuming a top-hat beam profile. The results from Fig. 12 support the experimental observation that the maximum grid erosion should occur at the center of the grid. The result may easily be understood by inspection of Fig. 10, which shows that close to the center of the grid, the solid-angle-probabilities f_Ω in the plume are larger, on average, than those close to the thruster edges. Thus, indeed, the impingement current and the grid erosion *should* be higher at the center of the grid.

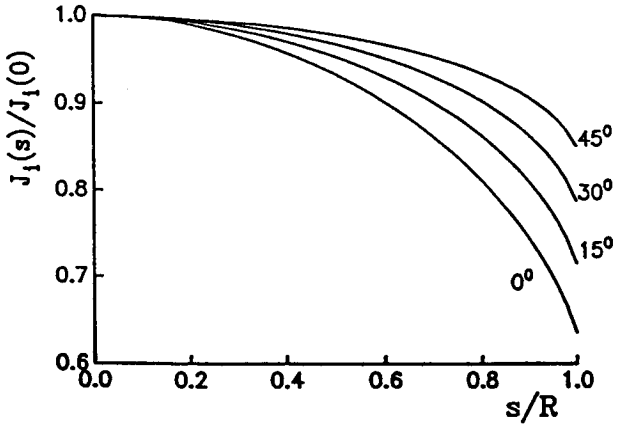

Figure 12: *Radial variation of the grid impingement current on the accelerator grid for a top-hat ion beam profile for different beam-divergence half-angles γ. The data are normalized to unity.*

Acknowledgment: Although the concept of a solid-angle-based calculation of the impingement current on a thruster grid is based in part on previous work by the authors [15], an important impetus for the present work was provided by a similar concept which has been proposed independently by Paul Wilbur and Jeff Monheiser of Colorado State University, who shared their work freely in the pre-publication stage.

6. Conclusions

It is likely that, like arcjets, ion thrusters may soon be employed as primary and/or auxiliary propulsion systems on a variety of satellites. Both two-grid and three-grid thrusters appear to be likely candidates for such applications. However, due to the grid erosion problems which two-grid thrusters are faced with in ground testing, it may be possible to space-qualify the three-grid version somewhat easier. On the other hand, the mechanisms of grid erosion are now sufficiently well understood that one may expect the erosion problems for two-grid as well as three-grid thrusters to be significantly less for operation in space than for operation in a ground facility.

CSTAR will remain active in the further development of ion space thrusters through both numerical and experimental efforts. In particular, CSTAR will be conducting tests on a NASA JPL three-grid thruster to enable the validation of an engineering design code for such thrusters. As part of this experimental effort, we plan to use the optical diagnostics which were developed during this program. These optical diagnostics should be particularly useful for obtaining plasma densities close to the thruster grids where electrical probes cannot be used due to their nonintrusive character.

Preparations for installation of the NASA JPL thruster are underway. In particular, pumping speed measurements have been performed on the helium cryo system of the Vacuum Research Facility. This test has indicated that it should be possible to maintain sufficiently low pressures (in the low 10^{-5} Torr range) during operation of the JPL thruster.

Finally, a simple analytical model was developed which can be used to calculate the grid impingement

current due to charge-exchange collisions in the downstream plasma plume of an ion thruster. The concept of the model (based on solid-angle-based extraction efficiency) might be incorporated into the numerical codes so that the downstream plasma density does not have to be supplied as an input parameter to the numerical code. This would enhance the predictive capabilities of the code.

Acknowledgments

This work was supported by CSTAR through NASA Grant NAGW-1195; by Boeing Defense & Space Group of Seattle, Washington (grant monitor Dr. J. S. Meserole); and by Engineering Research Consultants, Inc. of Tullahoma, Tennessee. We gratefully acknowledge the assistance of Julia Celenza, Fred Schwartz, and Newton Wright.

References

[1] X. Peng, W. M. Ruyten, and D. Keefer, ``Ion thruster numerical modeling," Proceedings of the CSTAR 4th Annual Symposium, Tullahoma, TN, November 11-12, 1992, pp. 22-25.

[2] W. M. Ruyten, V. J. Friedly, X. Peng, and J. A. Celenza, ``Ion thruster diagnostics," Proceedings of the CSTAR 4th Annual Symposium, Tullahoma, TN, November 11-12, 1992, pp. 26-39.

[3] W. M. Ruyten, V. J. Friedly, X. Peng, J. A. Celenza, and D. Keefer, ``Spectroscopic investigations of beam-plasma interactions in an ion plume," AIAA paper 93-1791, Monterey, CA, June 28-30, 1993.

[4] J. R. Brophy, L. C. Pless, J. Mueller, and J. R. Anderson, ``Operating characteristics of a 15-cm-diameter ion engine for small planetary spacecraft," IEPC paper 93-110, June 1993.

[5] S. Watson et al., ``500 Hour tests of the T5 ion thruster with dual and triple grid ion extraction systems," IEPC paper 93-170, June 1993.

[6] A. Martin, C. Banks, R. Eaton, and W. Moulford, ``Erosion measurements for two- and three-grid ion thruster extraction systems," IEPC paper 93-171, June 1993.

[7] Q. Zhang, X. Peng, and D. Keefer, ``Particle simulation of three-grid ion optics," IEPC paper 93-178, June 1993.

[8] F. J. Morgan, A. Marcuzzi, and C. H. Dugan, ``Shapes of optical emission lines from atoms excited by fast ion impact: I. calculated results," *Can. J. Phys.*, Vol. 52, 2525-2533, 1975.

[9] F. Heinrich, H.-P. Stoll, H.-C. Scheer, and P. Hoffman, ``Optical emission spectroscopy for analysis of broad ion beams, " *Vacuum*, Vol. 39, 1181-1184, 1989.

[10] F. Heinrich, H.-P. Stoll, H.-C. Scheer, and P. Hoffman, ``Energy analysis of neutral atoms in broad oxygen ion beams by Doppler-shift measurements," *J. Appl. Phys.*, Vol. 68, No. 11, 5428-5434, 1990.

[11] F. Heinrich, H.-P. Stoll, P. Hoffman, and H.-C. Scheer, ``Ion beam diagnostics by Doppler shifted light emissions," *Rev. Sci. Instrum.*, Vol. 63, No. 5, 3063-3067, 1992.

[12] W. M. Ruyten, V. J. Friedly, X. Peng, and D. Keefer, ``Experimental facilities for electric propulsion testing," Proceedings of the Second Annual Technical Symposium, Center for Space Transportation and Applied Research, November 1-2, 1993, pp. 64-72.

[13] W. M. Ruyten, ``Simple geometric model for estimating the impingement current on ion thruster grids in ground testing," submitted to *AIAA Journal of Propulsion and Power*, August 1993.

[14] M. J. Patterson and T. R. Verhey, ``5 kW Xenon ion thruster life test," AIAA paper 90-2543, July 1990.

[15] X. Peng, W. M. Ruyten, and D. Keefer, ``Plasma particle simulation of electrostatic ion thrusters," *AIAA Journal of Propulsion and Power*, Vol. 8, No. 2, March-April 1992, pp. 361-366; see, in particular, the last four paragraphs of Sec. II-B.

Emission Spectroscopy and Laser-Induced Fluorescence Measurements on the Plume from a 1-kW Arcjet Operated on Simulated Ammonia

W. M. Ruyten*
University of Tennessee-Calspan
Center for Space Transportation and Applied Research
Tullahoma, Tennessee 37388-8897

and

D. Burtner† and D. Keefer**
Center for Laser Applications
University of Tennessee Space Institute
Tullahoma, Tennessee 37388-8897

Abstract

Spectroscopic and laser-induced fluorescence measurements were performed on the exhaust plume from a 1 kW NASA Lewis arcjet, operated on simulated ammonia. In particular, emissions were analyzed from the Balmer lines of atomic hydrogen and from one of the rotational bands of the NH radical. The laser-induced fluorescence measurements were performed on the Balmer-alpha line of atomic hydrogen. We find that exit plane temperatures are in the range 1500 to 3500 K and that the electron density upstream of the exit plane is on the order of 1.5×10^{14} cm^{-3} as determined by the Stark width of the Balmer-alpha line. Both emission spectroscopy and laser-induced fluorescence were used to measure the plume velocities of atomic hydrogen. Using either technique, velocities on the order of 4 km/sec were found at the exit plane and significant acceleration of the flow was observed in the first 2 mm beyond the exit plane. This result indicates that the design of the arcjet nozzle may not be optimum.

1. Introduction

With the imminent deployment of hydrazine arcjets on Telstar 4, arcjets have reached the point of commercial viability. Still, a strong interest remains in improving their performance. To a significant extent, this effort is hampered by the limited understanding of the basic physical processes in the device. This accounts for the continuing interest in experimental diagnostics and numerical modeling.

Different techniques have been used to characterize arcjet plumes. These include Langmuir probes [1-2], emission spectroscopy [3-8], absorption [9-10], and laser induced fluorescence [8,11-15]. Emission spectroscopy has also been used to monitor the arc region itself [16]. At the same time there have been several modeling efforts [17-19]. The combined experimental and numerical work is providing greater insight into the mechanisms of arc physics, the generation of thrust, and the factors determining the electrical efficiency of the device.

The two techniques used in this work are emission spectroscopy and laser-induced fluorescence. Both were used to investigate the plume from a 1 kW benchmark thruster from NASA Lewis Research Center operated on simulated ammonia propellant. In particular, we report on line shape analysis of the hydrogen Balmer-alpha line (yielding values for

---

* Senior Research Engineer, Principal Investigator
† Graduate Research Assistant
** B. H. Goethert Professor of ES&M

This work was supported by the Center for Space Transportation and Applied Research, Rocket Research Company, the Air Force Office of Scientific Research, and NASA Lewis Research Center.

kinetic temperature and electron density); on determination of the intensity ratios of Balmer lines (yielding approximate values of electron temperature); and on the analysis of one of the rotational bands of the NH radical (yielding a value of the NH rotational temperature). Also, we report measurements of the exit velocities of atomic hydrogen as determined by the Doppler shift of the Balmer lines. These measurements indicate that the nozzle flow is underexpanded significantly, implying that the nozzle design may not be optimum.

The results of this work were presented previously as AIAA paper 93-1790 [20] and IEPC paper 93-127 [21]. Further measurements on the arcjet thruster are reported in a separate paper of these proceedings [22] in which the diagnostics are discussed which are being developed in support of the EPOP program.

2. Experimental

2.1 Arcjet and test facility

All work was performed in the Vacuum Research Facility of the University of Tennessee Space Institute. The vacuum tank consists of a cylindrical chamber, 6.0 m long by 2.7 m wide. The arcjet was mounted on a computer-controlled xyz stage in a bell-shaped section at one end of the chamber (see Fig. 1). Using two Stokes pumps with blowers, a steady-state pressure of 130 Pa (1.0 Torr) was maintained at a nominal flow rate of 6.0 slm (38 mg/sec) of simulated ammonia (three parts hydrogen to one part nitrogen by volume, premixed). The arcjet was on loan from NASA Lewis Research Center. A description of it may be found, for example, in Ref. [23]. The constrictor diameter was 0.50 mm. Typical power dissipation was 10 Amps at 108 Volts.

2.2 Emission spectroscopic measurements

Emission measurements were performed with a 1.25 meter SPEX spectrometer with an 1800 gr/mm grating. Typical slit widths were 25 μm with a corresponding resolution of 0.12 Å fwhm. Emissions from the plume were collected through a large optical access port in the chamber, and were focused onto the spectrometer entrance slit with a wide-aperture (f/10) Cassegrain telescope. The height of the entrance slit was always chosen large enough so as to image the entire cross-section of the plume onto the detector. No detailed measurements were performed to characterize the radial dependence of the emissions.

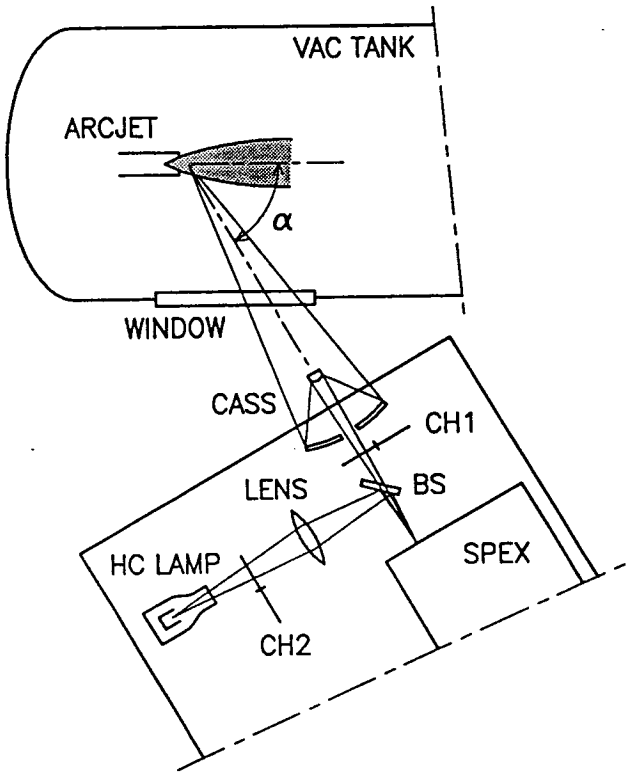

Figure 1: Experimental setup for the spectroscopic measurements. The optics can be positioned either perpendicular to the arcjet plume or at a nonorthogonal angle (as shown) to allow a determination of the Doppler shift of the flow.

A red-sensitized photo multiplier tube was used as the detector. The quantum efficiency of this tube falls off sharply above 8600 Å. Light below 3300 Å is not transmitted by the optical access port of the chamber. Using a standard filament source, the combined detection efficiency of the optical setup was calibrated over the whole detection range.

The dominant spectral features in the emission spectrum of the plume were those of atomic hydrogen (Sections 3 and 4) and the NH radical (Section 5). Also, weak emissions from the molecular

nitrogen ion (N_2^+) were present, with a bandhead at 3914 Å. No emissions from atomic nitrogen could be detected. As described in [22], some continuum emission from the plume was observed as well. To determine the Doppler shifts of atomic hydrogen in the plume, the signal from a hollow cathode lamp containing hydrogen gas was recorded along with the arcjet plume signal. This technique is explained in more detail in Section 6.

2.3 Laser-induced fluorescence measurements

Laser-induced fluorescence (LIF) measurements were performed using a setup which has been employed previously to measure velocities in an argon arcjet plume [13,14]. A schematic of the experimental setup is shown in Fig. 2. The beam from a frequency-stabilized dye laser is split and focused into the arcjet plume in such a way that one beam intersects the plume perpendicular to the plume axis and one beam is offset from the orthogonal direction by about 14 degrees. Previously, this was accomplished by focusing two parallel beams with a single lens. However, the resulting beam waists were small enough that saturation of the optical signal occurred at the maximum available laser power level. Thus, an alternative setup was chosen in which the beams were focussed with an extremely long-focal-length lens outside the vacuum chamber, and beam-steering of the 14-degree-off-perpendicular beam was achieved with a mirror inside the chamber. The resulting beam waists were much larger (on the order of 1 mm), thereby eliminating the saturation problem. However, a new complication of this approach was an increased level of scattered laser light on the detector.

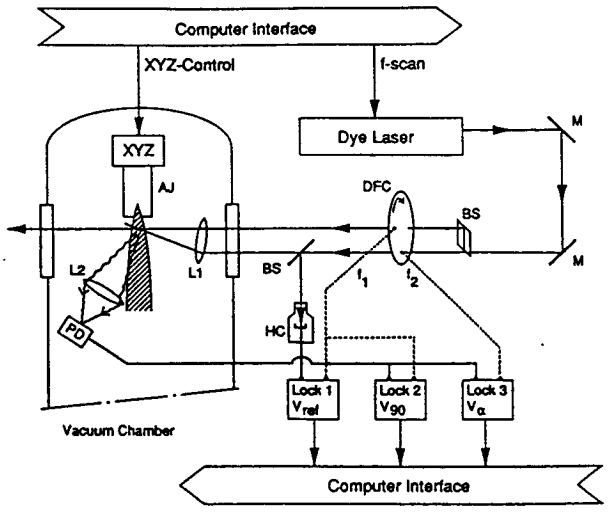

Figure 2: Experimental setup for the laser-induced fluorescence measurements.

As before, the detector was a photo-diode, mounted inside the vacuum chamber. Light from the plume was collected by a lens which was mounted perpendicular to the plane in which the two laser beams were crossed. A pinhole on the photo-diode was used to confine the observation region to a spot with a diameter equal to that of the laser beams, on the order of 1 mm. This setup proved quite adequate for the earlier measurements on the argon arcjet plume. However, a smaller signal-to-noise ratio resulted in the present measurements on the hydrogen Balmer-alpha line. Thus it would be desirable to repeat the measurements with a more sensitive detector (that is, a photo-multiplier tube), mounted outside of the chamber [12]. Such further measurements are planned for the near future.

3. Balmer-alpha line shape measurements

One of the strongest emission features in the plume was the hydrogen Balmer-alpha line at 6563 Å, which involves the states with principle quantum numbers n=3 and n=2. Figure 3 shows a typical scan of this line in which the fine structure of the line is indicated [12, 24, p. 233]. Due to this fine structure the measured line profile is slightly asymmetric and is broadened by about 0.14 Å. Further broadening of the lineshape is introduced by Doppler broadening, electron Stark broadening (especially noticeable in the wings), and instrument broadening due to the finite resolution of the spectrometer. For the Balmer-alpha line, the instrument profile was determined independently by a narrow band laser, tuned to the Balmer-alpha wavelength. This profile is shown in Fig. 3 also.

To analyze the Balmer-alpha lines, a fitting procedure was used which accounts for each of the broadening mechanisms explicitly. In it, a Voigt profile is convolved both with the fine structure and the measured instrument profile for each attempted set of fit parameters, consisting of the Gaussian and the Lorentzian widths of the Voigt profile, the center

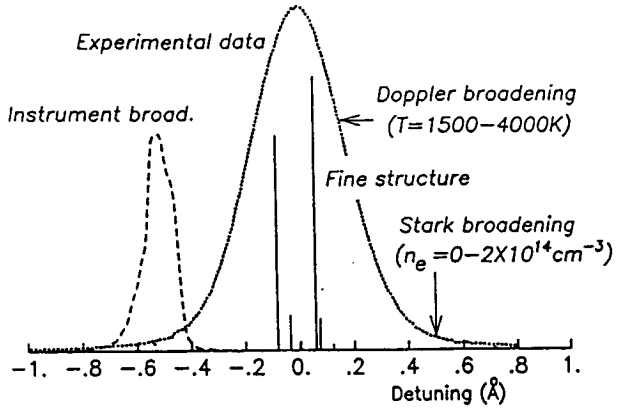

Figure 3: Typical emission lineshape of the hydrogen Balmer-alpha line. The fine structure components and the spectrometer instrument profile are indicated.

position of the profile, and the area under the profile. Baseline corrections were performed before carrying out the simplex fitting procedure so that a baseline offset did not have to be included as a fit parameter.

Values of the kinetic temperature T_{KIN} were calculated from the fwhm width Δ_D of the Gaussian component using the expression

$$8\ k\ T_{KIN}\ \ln 2 = m\ c^2\ (\Delta_D / \lambda)^2, \qquad (1)$$

where k is Boltzmann's constant, λ is the transition wavelength, and m is the mass of atomic hydrogen. Values of the electron density n_e (in cm^{-3}) were obtained from the fwhm width Δ_S (in Å) of the Lorentzian component using

$$\Delta_D = 2.507\times10^{-9}\ \alpha\ n_e^{2/3}, \qquad (2)$$

with α = 0.00969 [25].

Using this procedure, the cross-section-averaged value of the exit plane temperature was found to be T_{KIN} = 2300 ± 150 K and the similarly averaged value of the electron density was (0.4 ± 0.2)×10^{14} cm^{-3}. These values were obtained with the experimental setup shown in Fig. 1, except that the spectrometer was oriented perpendicularly to the arcjet plume. Additional measurements were performed at different axial positions using the nonorthogonal observation geometry from Fig.1 (see Section 6). Results of these measurements are shown in Figs. 4, 5, and 6 for two arcjet operating conditions (10 A @ 108 V and 8 A @ 114 V). The axial coordinates in these figures are to be interpreted on the basis of Fig. 7, which indicates that the ``average" location of the exit plane in Figs. 4-6 is located at the 2.5 mm position.

Figure 4 shows that, in the nonorthogonal observation geometry, the major contribution to the signal is due to emission *upstream* of the exit plane. (The reason for the drop in signal for negative values of the axial coordinate in Fig. 4 is merely the result of occlusion of the plasma region by the edge of the nozzle.) Therefore, values of the kinetic temperature and the electron density at the ``average" exit plane location (2.5 mm) are more representative of the plasma *upstream* from the exit plane. These values are considerably higher than those above, namely 3300 K (vs. 2300 K) and 1.6×10^{14} cm^{-3} (vs. 0.4×10^{14} cm^{-3}).

Two features in Figs. 4-6 stand out. Firstly, the intensity of the Balmer-alpha line depends very strongly on the arcjet power level, whereas values of the kinetic temperature and the electron density are only slightly lower for the 8 A case than they are for the 10 A case. Secondly, the electron density drops very sharply near the exit plane, whereas the decreases in intensity and kinetic temperature are more gradual. Of course, all values are line-of-sight averages, and are thus influenced by the distribution of emitters in the plume. By contrast, the LIF measurements are basically point measurements. As shown in Section 7, they lead to smaller values of the plume temperatures.

4. Ratios of hydrogen Balmer intensities

In addition to the hydrogen Balmer-alpha line, we also observed the beta (4→2), gamma (5→2), delta (6→2), and epsilon (7→2) members of the Balmer series. No conclusive fine structure analysis was performed on these lines. (The beta lines appear to yield smaller values of n_e than those obtained from the alpha lines; however, no accurate measurement of the instrument profile at the Balmer-beta wavelength was available.) However, the data were used to estimate the electron temperature T_e in the plume.

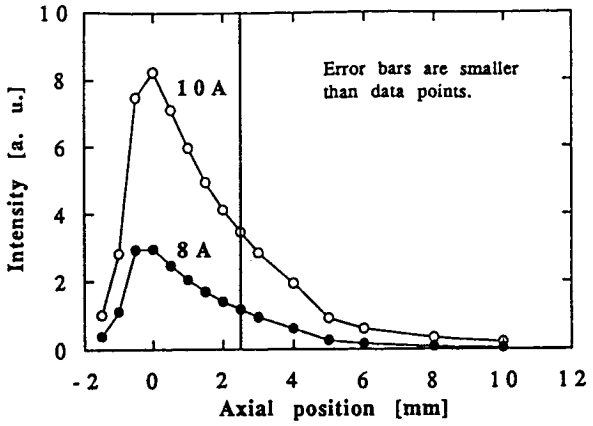

Figure 4: Intensities of the hydrogen Balmer-alpha line as a function of axial position (see Fig. 7) and arcjet current (8 or 10 Amps). The vertical line indicates the ``average'' location of the exit plane.

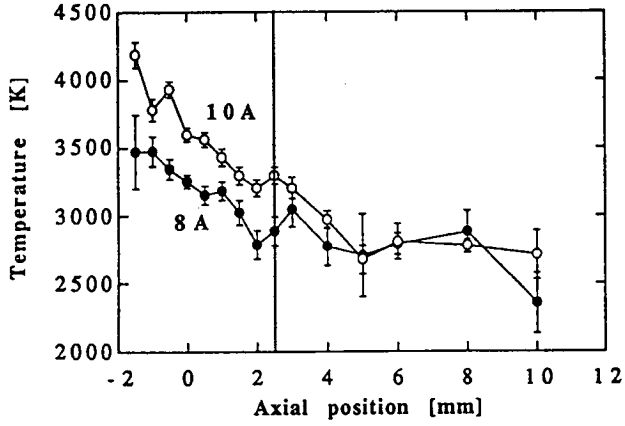

Figure 5: Kinetic temperature for the same data as those of Fig. 4, obtained from the Doppler widths of the Balmer-alpha lines.

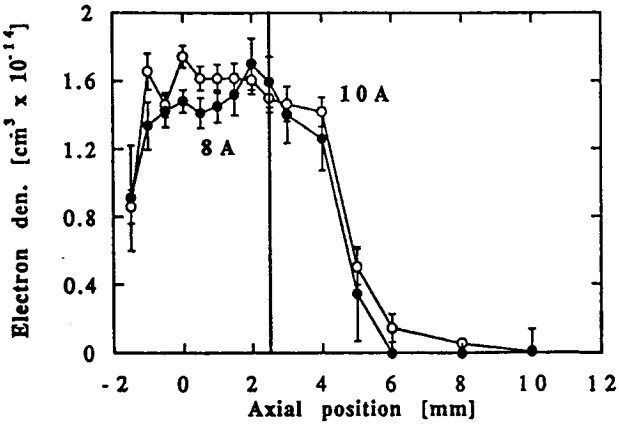

Figure 6: Electron densities for the same data as those in Figs. 4 and 5, obtained from the Stark widths of the Balmer-alpha lines.

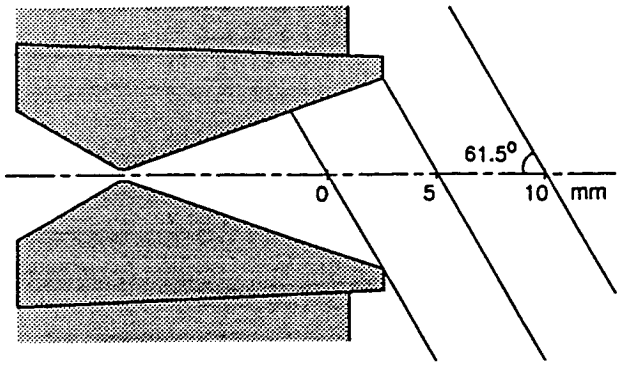

Figure 7: Nozzle- and observation-geometries employed in the measurements leading to the data in Figs. 4, 5, 6, 9, 14, and 15.

This is illustrated in the Boltzmann plot of Fig. 8, for data taken perpendicular to the plume a few mm downstream from the exit plane. In Fig. 8, the logarithm of the ratio S_i^*/S_i^∞ (with i=3-6) is plotted as a function of the upper state energy E_i of the transition, where S_i^∞ is a measure of the line intensity in the limit of infinite temperature [24, p.129] and $S_i^* = S_i/\eta_i$ is the measured line intensity S_i corrected for the detection efficiency η_i at the specified wavelength. From the expression

$$S_i^* \propto S_i^\infty \exp(-E_i / kT_e) \qquad (3)$$

it follows that the data should fall on a straight line. This is borne out quite well by the data in Fig. 8, which yield an electron temperature, T_e, of 0.261 eV, or 3030 K.

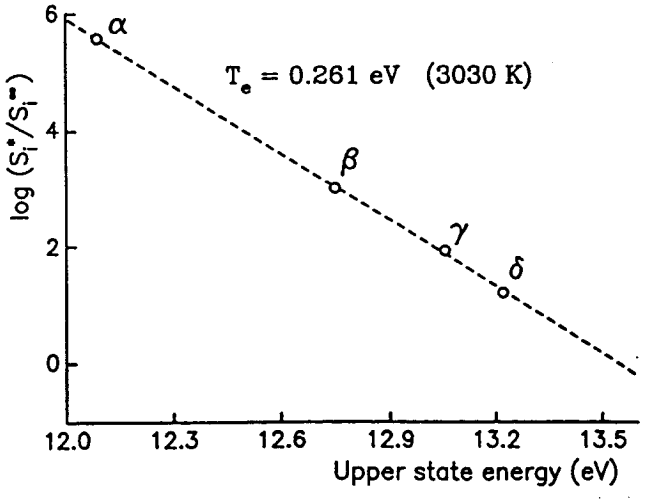

Figure 8: Boltzmann plot for the hydrogen Balmer lines. Data were recorded in the orthogonal observation geometry, a few mm downstream from the exit plane.

We have also measured the intensities of the Balmer-beta lines to complement the data leading to Figs. 4-6, using the same nonorthogonal observation geometry as that used for the Balmer-alpha measurements. From the ratio of alpha-to-beta intensities, electron temperatures were calculated using Eq.(3). The results are shown in Fig. 9, in which the axial coordinate is again to be interpreted as indicated in Fig. 7. Surprisingly, the so-derived value of the electron temperature *increases* with axial coordinate, in contrast to the kinetic temperature calculated from the Doppler widths (both the kinetic temperatures and the NH rotational temperature are shown in Fig. 9 for comparison).

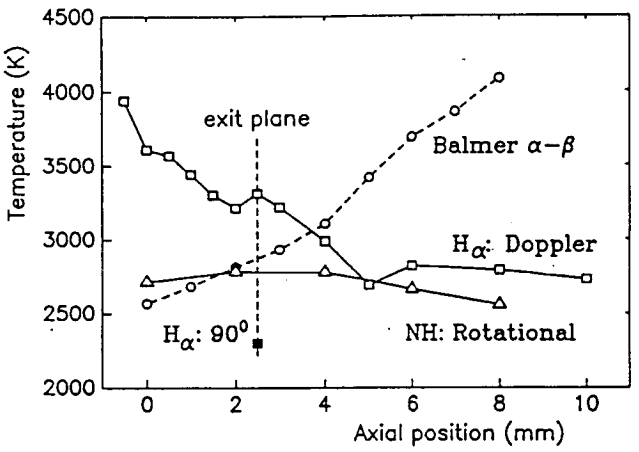

Figure 9: Results of different temperature determinations. All data were taken in the nonorthogonal observation geometry, with the exception of the single data point at the exit plane location.

We conclude that, on the one hand, a single value for the electron temperature is able to account accurately for the distribution of excited state densities of the hydrogen atoms but that, on the other hand, this distribution is not in equilibrium with the thermal motion of the gas.

5. Analysis of NH rotational bands

In addition to the lines of the hydrogen Balmer series, strong emissions from the NH radical were found. The most prominent of these are due to the $A^3\Pi \rightarrow X^3\Sigma^-$ band, which was studied in Refs. [4] and [8] for a 1 kW ammonia arcjet. A surprising finding of Ref. [8] was that the rotational temperatures measured in emission (around 4500 K) were significantly higher than those measured in excitation (about 2000 K). Also, the vibrational temperature, estimated from the ratio of 1-1 to 0-0 emissions, was significantly lower, namely 2500 K. However, as is stated in Ref. [8], these temperature determinations have a considerable uncertainty, due to an apparent violation of Boltzmann equilibrium among the rotational levels.

In this work we have focused primarily on emission from the (0-0) band of the $c^1\Pi \rightarrow b^1\Sigma^+$ system between 450 and 474 nm. (A comprehensive discussion of these and other NH band systems may be found in Ref. [26].) A typical scan, recorded a few mm downstream from the exit plane using an orthogonal observation geometry, is shown in Fig. 10. Because of the singlet structure, an analysis of the band is straightforward. In particular, we obtained the rotational temperature, T_{ROT}, from the expression

$$S^*(J') \propto S_{J'J''} \exp\left(-E(J') / kT_{ROT} \right), \qquad (4)$$

where $S^*(J')$ is the line intensity of the line with rotational quantum number J', corrected for the optical detection efficiency; $S_{J'J''}$ is the Hönl-London line strength factor; and E(J') is the energy of the upper rotational level. Expressions for the line strength factors were taken from Ref. [27]. They are given by $S_{J'J''} = \frac{1}{2}J'$ for the P-branch; $S_{J'J''} = J'+\frac{1}{2}$ for the Q-branch; and $S_{J'J''} = \frac{1}{2}(J'+1)$ for the R-branch transitions.

The resulting Boltzmann plot for the data from Fig. 10 is shown in Fig. 11. A linear fit to the data yields a rotational temperature of $T_{ROT} = 2680 \pm 60$ K, and is seen to approximate the data from all three branches (P, Q, and R) reasonably well. Based on this observation, we conclude that the assumption of Boltzmann equilibrium is justified for these data (the opposite conclusion was drawn in Ref. [8]).

We also performed line intensity measurements of selected lines within the band system for a number of different axial locations, using the nonorthogonal observation geometry from Fig. 7. Rotational temperatures calculated from these data are shown in Fig. 9, along with the kinetic temperatures calculated

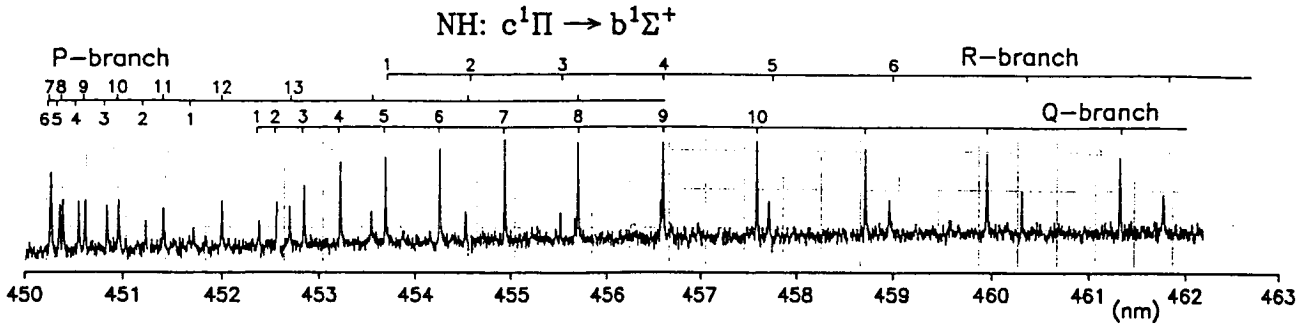

Figure 10: Typical scan of the NH $c^1\Pi \rightarrow b^1\Sigma^+$ band, performed about 2 mm downstream from the exit nozzle. Line designations are indicated.

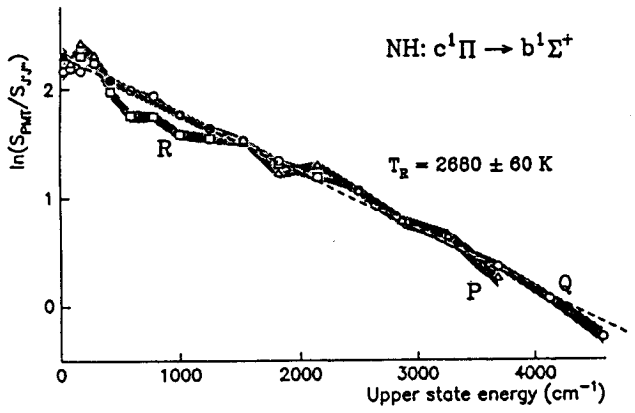

Figure 11: Boltzmann plot for the rotational lines of the NH $c^1\Pi \rightarrow b^1\Sigma^+$ band from Fig. 10. Triangular, round, and square data points represent P, Q, and R-branch transitions, respectively. The shaded bands indicate estimated uncertainties of the individual data points.

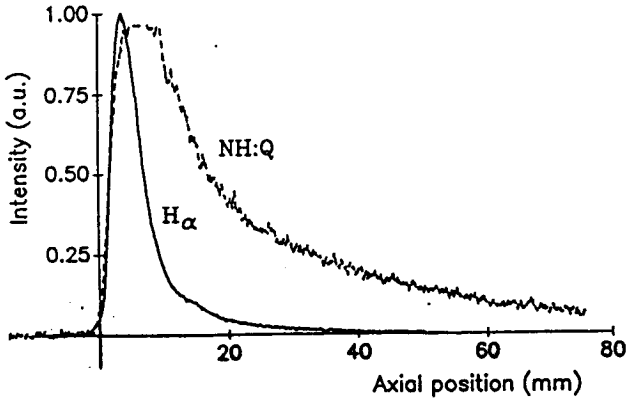

Figure 12: Axial variation of atomic hydrogen emission (Balmer-alpha) and NH emission (0-0 Q branch of the $A^3\Pi \rightarrow X^3\Sigma^-$ band), measured perpendicular to the plume. Both data sets are scaled to unit intensity at the peak.

from the Doppler widths of the hydrogen Balmer-alpha lines and the electron temperatures calculated from the hydrogen Balmer intensity ratios. Unlike the latter two, the NH rotational temperature depends only mildly on axial position. Its value is rather close to the other two temperatures, especially at the exit plane location (2.5 mm).

Finally, we note that, when moving downstream from the exit plane, emissions from the NH radical were found to persist long after the hydrogen Balmer emissions have subsided. This is illustrated in Fig. 12. This trend appears to be opposite of that calculated in Ref. [4; Fig. 3].

6. Spectroscopic velocity measurements

One new feature in this work was the use of emission spectroscopy to measure exit velocities of atomic hydrogen in the plume. More typically, laser-induced fluorescence is employed for this purpose, as described in Section 7. However, Doppler emission spectroscopy has been used previously, for example, to characterize the flow in MPD thrusters [28,29] and in plasma jets [30].

To perform the Doppler shift measurements, we positioned the spectrometer at a nonorthogonal observation angle to the plume (61.5 degrees to the plume centerline). Also, we recorded emissions from a hollow cathode lamp containing hydrogen gas simultaneously with emissions from the plume, using dual lock-in detection to separate the two signals. A typical set of measured line shapes is shown in Fig. 13. By curve-fitting the resulting line shapes, it was possible to measure Doppler shifts with a precision

of 0.001 Å, even in the presence of 0.12 Å spectrometer instrument broadening. However, it was necessary to calibrate the Doppler shift by performing independent measurements perpendicular to the plume. Details of the method will be presented elsewhere [31].

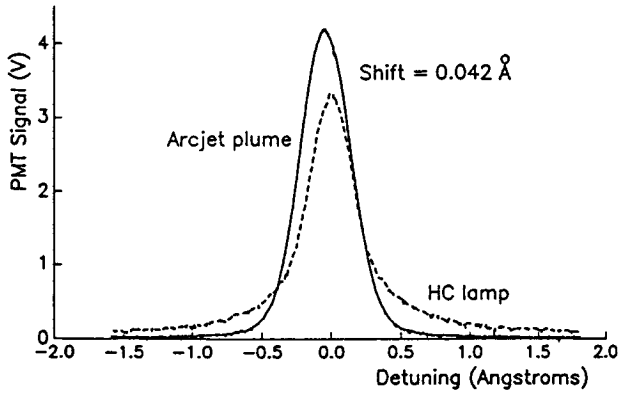

Figure 13: Example of a scan of the hydrogen Balmer-alpha line, in which the signals from both the plume and the hollow cathode lamp are shown.

From the Doppler shifts $\Delta\lambda_D$, the velocity component parallel to the plume centerline, v_l, was calculated using

$$v_l = (\Delta\lambda_D / \lambda) \times (c / \cos \alpha), \qquad (5)$$

where λ is the unshifted wavelength, c is the speed of light, and α is the observation angle. Of course, the calculated velocity is a line-of-sight averaged value. However, as is shown in Ref. [31], to first order, it is still a reasonable approximation for the velocity averaged across a plane perpendicular to the plume axis.

Results of velocity measurements based on the Doppler shifts of hydrogen Balmer emission lines are shown in Figs. 14 and 15. In both figures, the axial coordinate is again to be interpreted according to Fig. 7. Figure 14 shows results for the same two power levels as those in Figs. 4-6. Like the kinetic temperature (Fig. 5) and the electron density (Fig. 6), only slightly smaller values for the flow velocities are found in the 8 A case than in the 10 A case. Figure 15 indicates that there is excellent agreement between the velocities obtained from different spectral lines (Balmer-alpha, -beta, and -gamma).

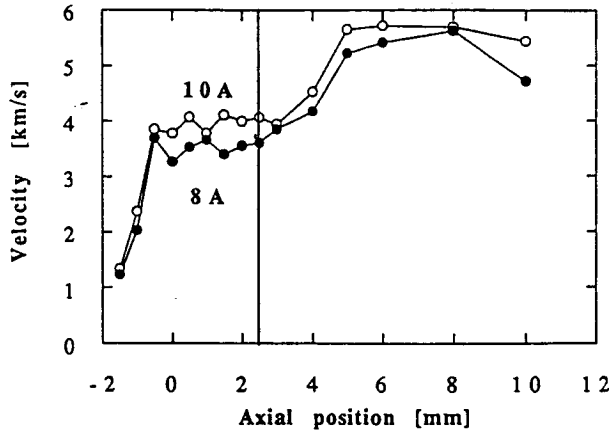

Figure 14: Values of parallel plume velocities calculated from the Doppler shifts of the hydrogen Balmer-alpha lines, for two arcjet currents. Axial coordinates are to be interpreted according to Fig. 7.

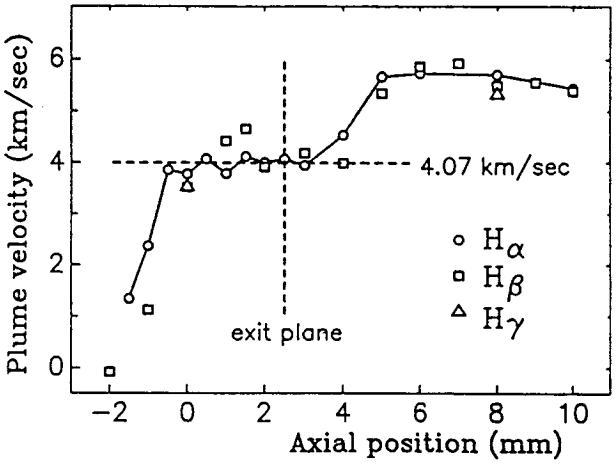

Figure 15: Like Fig. 14 for the 10 A case, but including data from the Balmer-beta and -gamma lines as well.

The most striking feature in Figs. 14 and 15 is the acceleration of the flow just downstream from the exit plane (namely, from 4.0 km/sec to 5.5 km/sec for the 10 A case). Clearly, the nozzle flow is underexpanded, despite the rather high facility background pressure of 1.0 Torr. This result is confirmed by the LIF measurements from Section 7, in which we report a centerline acceleration from about 3.5 km/sec at the exit plane to 8 km/sec a few mm downstream.

We also point out that the apparent drop in velocity upstream of the 0 mm position in Figs. 14 and 15 is merely the result of occlusion of the plasma region by the edge of the nozzle. Indeed,

when moving past the lower edge of the arcjet nozzle (see Fig. 7), only flow parallel to the opposite wall is observed (as determined by the f-number of the optical system). Because this wall is roughly perpendicular to the observation direction, it follows indeed that the calculated velocity should drop to zero, as it does in Figs. 14 and 15.

Finally, if we interpret the plateau values of the axial velocities in Fig. 14 as representative of the specific impulse of the thruster, we find values of 407±8 sec for the 10 A case and 365±7 sec for 8 A case. Corresponding values of the electrical efficiency are 28±1 % and 27±1 %. These values of specific impulse and electrical efficiency are roughly consistent with values stated in Ref. [32] for operation of a similar thruster on simulated ammonia propellant. However, for a more meaningful comparison, it will be necessary to perform thrust measurements on our thruster for the same operating conditions as those used in the optical studies. In this regard, it would also be of interest to measure the exit velocities of the heavy plume species by optical means, for example, by measuring the Doppler shifts of NH emissions using the same technique as employed here for the hydrogen Balmer lines.

It would be of particular interest to perform such measurements to resolve the question whether the different velocities of light and heavy species far downstream from the exit plane (for example, as determined by Welle et al. in a 1 kW arcjet operated on nitrogen-hydrogen mixtures using a time-of-flight sampling technique [33]) are the result of expansion of the plume *downstream* from the exit plane, or whether such flow separation has already taken place before the flow reaches the exit plane.

7. Results of the LIF measurements

Figure 16 shows a typical scan of the Balmer-alpha line, showing one of the two LIF signals and the reference signal, obtained from the hollow cathode lamp through the optogalvanic effect. Because of the much narrower instrument width of the laser (1 MHz) as compared to the emission measurements (0.12 Å or 8400 MHz), and because the lack of averaging over radial velocity gradients in the LIF measurements, the spectral width of the LIF signal is significantly less than that of the emission signal, thereby revealing the fine-structure of the Balmer-alpha line. On the other hand, the scan width of the laser system (30 GHz, or about 0.43 Å) was not sufficient to cover more much than just the central part of the line shape in a single scan.

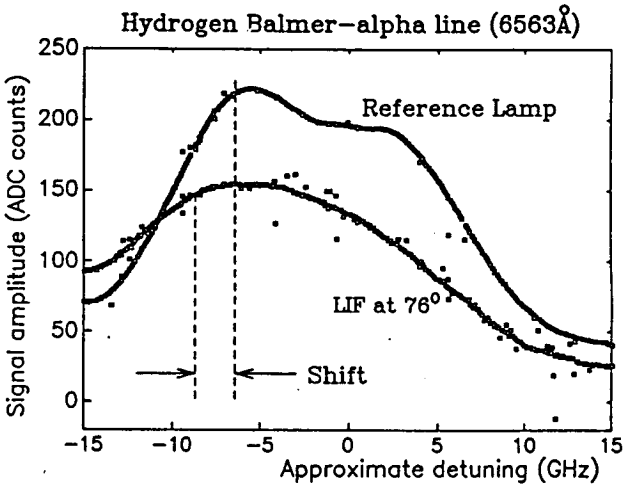

Figure 16: Typical LIF scan of the hydrogen Balmer-alpha line. The Doppler shift between the plume signal and the reference signal is indicated.

Using gaussian curve fits which accounted for the fine structure, line centers and line widths were extracted from each of the LIF measurements. Unlike for the emission measurements, no corrections to the line center determinations of the hollow-cathode data were necessary, and the Doppler shifts were calculated simply as the difference between the fitted line centers of the plume data and the data from the hollow cathode lamp. The resulting shifts were converted to radial and axial components of the plume flow velocities.

Results of these measurements are shown in Figs. 17 and 18. Figure 17 shows vector velocities measured at a number of positions in the plume, at axial positions of 1 mm, 2.5 mm, and 4 mm downstream from the exit plane and at several radial locations for each of these axial positions. Because of the reasons mentioned above (not enough sensitivity of the detector; a significant background signal due to laser scatter as a result of using 1 mm wide beams; limited range of the laser), the data are

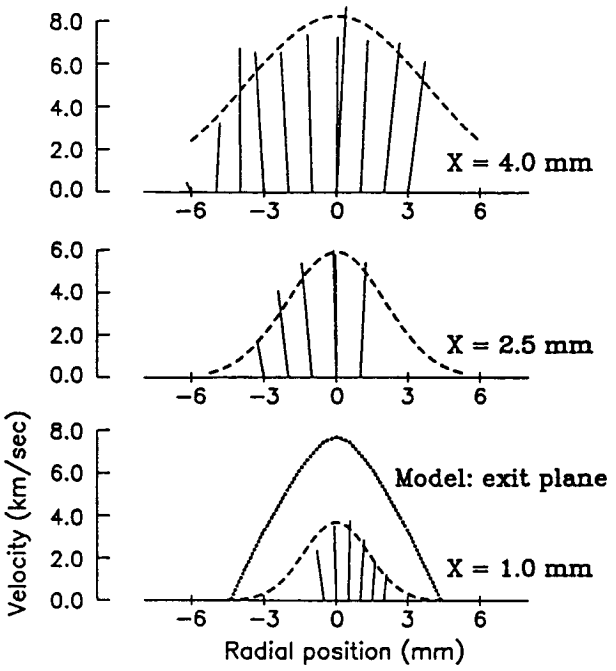

Figure 17: Vector velocities in the arcjet plume, obtained from the LIF measurements at different downstream positions in the plume. The dashed lines are added to emphasize the trend of the data. Also shown are the numerical results at the exit plane described in Ref. [21].

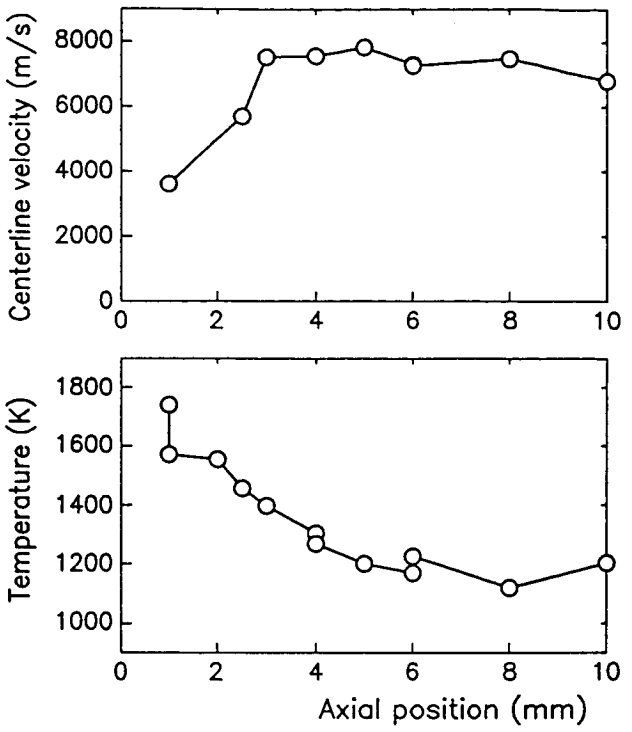

Figure 18: Axial velocities (a) and temperatures (b) measured on centerline by the LIF technique.

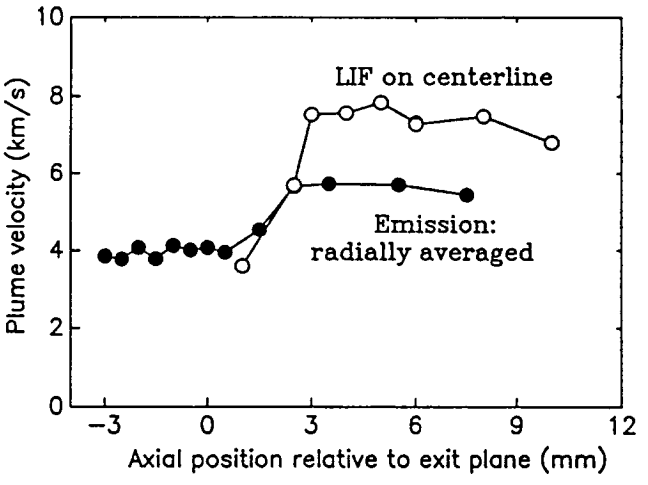

Figure 19: Comparison of axial velocity data obtained with LIF and emission spectroscopy.

not of the same quality as those obtained in our earlier work [13,14] or those obtained by Liebeskind et al. on the same spectral line in a hydrogen arcjet plume [12]. However, the trend of the data (which is emphasized by the dashed lines in Fig. 17) is quite clear: The plume velocity is largest on centerline, and increases dramatically from the 1 mm position (with a peak velocity of about 4 km/s) to the 4 mm position (with a peak velocity of 8 km/s—see also Fig. 18a). This is fundamentally the same result as that obtained in the emission measurements, namely that the flow accelerates upon exiting the thruster. Moreover, because the emission data are averaged over the radial extent of the plume, it seems quite reasonable that the velocities measured on centerline using LIF exceed those measured in the emission measurements. Figure 19 displays the LIF velocity data and the velocity data from the emission measurements in one figure to emphasize the qualitative agreement between the two sets of data (the axial coordinates of the emission data were adjusted so that the zero-position on the horizontal axis indicates the actual position of the nozzle exit plane for both sets of data).

The essential agreement between the line-of-sight-averaged emission spectroscopic measurements and the point-resolved laser-induced fluorescence measurements is especially significant in that it is a

demonstration of the ability to obtain plume velocity data using emission spectroscopy. Against the obvious shortcoming that the emission data are line-of-sight averages stands the advantage that the equipment to perform emission measurements is much less complex and costly, so that it is available to more researchers. Also, emission spectroscopy offers greater flexibility in measuring the plume velocities of multiple species in the plume (for example, in Section 6 we verified that the same plume velocities were obtained for the hydrogen Balmer-alpha, -beta, and -gamma lines).

We also calculated temperature data from the fitted widths of the LIF profiles. Because of the large background signals which resulted from laser scatter in the experiment, and because of the limited scan range of the laser, the fitted widths were only accurate to about ten percent. Results on centerline are shown in Fig. 18b. As expected, the temperature drops as the plume expands. These LIF-derived values are significantly lower than those obtained from the emission measurements (cf. Figs. 5 and 9). The values obtained from the LIF measurements should be more accurate because they do not involve averaging over the radial extent of the plume.

8. Conclusions

We have studied the plume from a 1 kW arcjet, operated on simulated ammonia, using emission spectroscopy and laser-induced fluorescence. Using the emission-spectroscopic results, three independent plume temperature determinations were performed, based on the Doppler width of the hydrogen Balmer-alpha line; the intensity ratios of the hydrogen Balmer-alpha and -beta lines; and the rotational line intensities of the (0-0) branch of the $c^1\Pi \rightarrow b^1\Sigma^+$ band of the NH radical. The respective temperatures at the exit plane are in fairly close agreement, although different spatial trends are found for each (namely, decreasing, increasing, and constant as a function of downstream position, respectively). The temperatures found using the LIF technique are lower than those from the emission measurement, presumably because they do not involve line-of-sight averaging.

Using a nonorthogonal observation geometry in the emission measurements, it was also possible to calculate the electron density upstream of the exit plane (yielding a value 1.6×10^{14} cm^{-3} based on the Stark width of the Balmer-alpha line). Based on the emission data, the average velocity of atomic hydrogen at the exit plane was determined to be 4.0 km/sec at a power level of 1080 W. This result is supported by the LIF measurements, which yielded roughly similar values for the exit velocities. Both techniques indicated that the plume is underexpanded, as witnessed by the acceleration of the atomic hydrogen just downstream from the nozzle exit plane. This results indicates that the design of the nozzle may not be optimum, at least for the operating conditions which were studied in this work.

Finally, it was established in this work that emission spectroscopy can be used as a valuable technique for the measurement of velocities in an electric thruster plume. This technique should be of particular interest in cases where the much more complex equipment needed to perform laser-induced fluorescence measurements is not available, or where it is desired to measure exit velocities of multiple species, something which may be impractical or impossible given the limited tuning capabilities of a laser system.

Acknowledgments

This work was supported by grants from Rocket Research Company of Redmond, Washington; the Air Force Office of Scientific Research under grant AFOSR-91-0200; and by the Center for Space Transportation and Applied Research under NASA grant NAGW-1195. We gratefully acknowledge the loan of the arcjet system from NASA Lewis Research Center. Finally, we thank N. Wright for his expert technical assistance.

References

[1] Sankovic, J. M., "Investigation of the arcjet near field using electrostatic probes," NASA TM 103638, Washington, D.C., 1990.

[2] Carney, L. C., and Keith, T. G., "Langmuir probe measurements of an arcjet exhaust," *J. Propulsion*

and Power, Vol. 5, No. 3, pp. 287-294, May-June 1989.

[3] Hoskins, W. A., Kull, A. E., and Butler, G. W., "Measurement of population and temperature profiles in an arcjet plume," AIAA paper 92-3240, Nashville, TN, July 1992.

[4] Janson, S. W., Welle, R. P., Schulthess, D. R., and Cohen, R. B., "Arcjet plume characterization part II: optical diagnostics results," AIAA paper 90-2643, Orlando, FL, July 1990.

[5] Manzella, D. H., Curran, F. M., Myers, R. M., and Zube, D. M., "Preliminary plume characteristics of an arcjet thruster," AIAA paper 90-2645, Orlando, FL, 1990.

[6] Tosti, E., Deininger, W. D., Mazzacurati, V., and Ruocco, G. C., "Arcjet plume analysis using emissions spectroscopy," paper 91-092, 22nd IEPC, Viareggio, Italy, October 1991.

[7] Cernogora G., et al., "Rotational temperature measurements of N_2^+ in an arcjet at low pressure," AIAA 92-2967, Nashville, TN, July 1992.

[8] Crofton, M. W., Welle, R. P., Janson, S. W., and Cohen, R. B., "Temperature, velocity, and density studies in the 1 kW ammonia arcjet plume by LIF," AIAA paper 92-3241, Nashville, TN, July 1992.

[9] Pollard, J. E., "Arcjet diagnostics by XUV absorption spectroscopy," AIAA paper 92-2966, Nashville, TN, July 1992.

[10] Manzella, D. H., and Cappelli, M. A., "Vacuum ultraviolet absorption in a hydrogen arcjet," AIAA paper 92-3564, Nashville, TN, July 1992.

[11] Erwin, D. A., Pham-Van-Diep, G. C., and Deininger, W. D., "Laser induced fluorescence measurements of flow velocities in high-power arcjet thruster plumes," *AIAA Journal*, Vol. 29, No. 8., 1991, pp. 1298-1303.

[12] Liebeskind, J. G., Hanson, R. K., and Cappelli, M. A., "Flow diagnostics of an arcjet using laser induced fluorescence," AIAA paper 92-3243, Nashville, TN, July 1992; see also AIAA paper 93-2530, Monterey, CA, June 1993.

[13] Ruyten, W. M., and Keefer, D., "Characterization of electric thruster plumes using laser induced fluorescence measurements," AIAA paper 92-2965, Nashville, TN, July 1992.

[14] Ruyten, W. M., and Keefer, D., "Laser fluorescence velocimetry of an arcjet exhaust plume," paper 91-093, 22nd IEPC, Viareggio, Italy, October 1991.

[15] Ruyten, W. M., Friedly, V. J., and Keefer, D., "Electric propulsion: experimental research," Proceedings of the 3rd Annual Technical Symposium, Center for Space Transportation and Applied Research, Tullahoma, Tennessee, January 14-15, 1992, pp. 83-90.

[16] Zube, D. M., and Myers, R. M., "Techniques for spectroscopic measurements in an arcjet nozzle," *J. Propulsion and Power*, Vol. 8, No. 1, pp. 254-256, Jan.-Feb. 1992.

[17] Moeller, T., Rhodes, R., Keefer, D., Sedghi-Nasab, A., and Ruyten, W., "Comparison of experimental and numerical results for an argon arcjet," AIAA paper 92-3105.

[18] Rhodes, R. P., and Keefer, D., "Modeling of a hydrogen arcjet thruster," AIAA paper 91-1994, Sacramento, CA, June 1991.

[19] Tanaka, K., Tschiya, K., Kaita, K., and Nishida, M., "Computational simulation of arcjet thruster flow fields," paper A90-25826, 3rd International Symposium on Computational Fluid Dynamics, Nagoya, Japan, August 1989.

[20] Ruyten, W. M., Burtner, D., and Keefer, D., "Spectroscopic investigation of a low-power arcjet plume," AIAA paper 93-1790, presented at the 29th Joint Propulsion Conference, Monterey, CA, June 28-30, 1993.

[21] Ruyten, W. M., Burtner, D., and Keefer, D., "Laser-induced fluorescence measurements on the plume from a 1 kW arcjet operated on simulated ammonia," IEPC paper 93-127, presented at the 23rd International Electric Propulsion Conference, Seattle, WA, September 13-16, 1993.

[22] Ruyten, W. M., Friedly, V. J., and Litchford, R. J., "Diagnostic development for the electric propulsion orbital platform," 5th Annual Technical Symposium, Center for Space Transportation and Applied Research, Tullahoma, Tennessee, November 10, 1993, pp. F-9-F-19.

[23] Curran, F. M., and Sarmiento, C. J., ``Low power arcjet performance characterization,'' AIAA paper 90-2578, Orlando, FL, July 1990.

[24] Kuhn, H. G., ``Atomic Spectra,'' 2nd Ed., Academic Press, New York, 1969.

[25] Griem, H. R., *Spectral Line Broadening by Plasmas* (Academic Press, New York, 1974); as quoted by Blau, P., Smilanski, I., and Rosenwaks, S., ``Simultaneous time-averaged measurements of gas temperature and electron density in a copper-vapor laser using hydrogen emission spectroscopy,'' *J. Appl. Phys.*, Vol. 72, 1992, pp. 849-854.

[26] Lents, J. M., ``An evaluation of molecular constants and transition probabilities for the NH free radical,'' *J. Quant. Spectrosc. Radiat. Transfer*, Vol. 13, 1973, pp. 297-310.

[27] Kovacs, I., ``Rotational structure in the spectra of diatomic molecules,'' American Elsevier, New York, 1969, p. 123.

[28] Kogelschatz, U., ``Doppler-shift mesurements of axial and rotational velocities in an MPD arc,'' *AIAA J.*, Vol. 8, 1970, pp. 150-154.

[29] Nakayama, T., Toki, K., Kuriki, K., and Yoshida, T., ``Optical measurement of velocity distributions in MPD arcjet,'' paper 91-048, 22nd IEPC, Viareggio, Italy, October 1991.

[30] Bohn, W. L., Beth, M.-U., Nedder, G., ``On spectroscopic measurements of velocity profiles and non-equilibrium radial temperatures in an argon plasma jet,'' *J. Quant. Spectrosc. Radiat. Transfer*, Vol. 7, 1967, pp. 661-676.

[31] Ruyten, W. M., ``Velocity measurements in an electric thruster plume by emission spectroscopy,'' submitted to *Applied Optics*, August 1993.

[32] Curran, F. M., and Nakanishi, S., ``Low power dc arcjet operation with hydrogen/nitrogen propellant mixtures,'' NASA TM 87279, prepared for the 22nd Joint Propulsion Conference, Huntsville, AL, June 1986.

[33] Welle, R. P., Pollard, J. E., Janson, S. W., Crofton, M. W., and Cohen, R. B., ``One kilowatt hydrogen and helium arcjet performance,'' Aerospace Report No. ATR-91 (8343)-2, The Aerospace Corporation, El Segundo, CA, 15 April 1993 (also presented at the 27th Joint Propulsion Conference in Sacramento, CA, June 1991).

Charge-Exchange Erosion Studies of Accelerator Grids in Ion Thrusters

Xiaohang Peng*, Wilhelmus M. Ruyten†, and Dennis Keefer‡

The University of Tennessee-Calspan
Center for Space Transportation and Applied Research
UTSI Research Park
Tullahoma, TN 37388-8897

The University of Tennessee Space Institute
Center for Laser Applications
Tullahoma, TN 37388-8897

Abstract

A particle simulation model is developed to study the charge-exchange grid erosion in ion thrusters for both ground-based and space-based operations. Because the neutral gas downstream from the accelerator grid is different for space and ground operation conditions, the charge-exchange erosion processes are also different. Based on an assumption of no electric potential hill downstream from the ion thruster, the calculations show that the accelerator grid erosion rate for space-based operating condition should be significantly less than experimentally observed erosion rates from the ground-based tests conducted at NASA Lewis Research Center (LeRC) and NASA Jet Propulsion Laboratory (JPL). To resolve this erosion issue completely, we believe that it is necessary to accurately measure the entire electric potential field downstream from the thruster.

1. Introduction

Accelerator grid charge-exchange ion erosion for two-grid ion thrusters is still an issue for applications of two-grid ion thrusters. The reason is that serious accelerator grid erosion has been observed in several ground tests [1-3]. However, whether or not such serious accelerator grid erosion will occur in space is the question. In other words, what role the residual gas inside the vacuum chamber plays in terms of the observed accelerator grid erosion needs to be understood before trying to interpolate the ground test results and predict the engine life in space operations.

The nature of accelerator grid charge-exchange ion erosion was found to be complex, due to the large range of operating parameters and the influence of the facility background pressure [1]. This leads to different interpolations in terms of the erosion rate observed in the ground tests and different perspectives of explanation of this charge-exchange ion erosion process. Actually, the main reason for different interpolations of serious accelerator grid erosion observed in the ground tests is the lack of the electric potential measurements downstream from the ion thrusters.

To address this issue and to help interpolate the ground test results for space operations, CSTAR has developed both 2-D and 3-D particle simulation models over the last four years. In this paper, we will offer our perspective in terms of charge-exchange ion erosion process for both ground-based and space-based operations. However, to resolve this issue, it is necessary to accurately measure the entire electric potential field downstream from the thruster.

2. Charge-Exchange Ion Erosion

It is well known that the accelerator grid erosion is caused by charge-exchange ions. Charge-exchange collisions occur between beam ions and neutral atoms. Since an ion source cannot be perfect, there will always be some neutral efflux from the thruster. Thus charge-exchange collisions between beam ions and

---

* Research Engineer, CSTAR; Principal Investigator
† Senior Research Engineer, CSTAR
‡ Professor of ES&M, UTSI

This work was supported by the Center for Space Transportation and Applied Research under NASA Grant NAGW-1195.

neutral propellant atoms are inevitable. In the case of ground testing, charge-exchange collisions can also occur between beam ions and residual neutral atoms inside the test facility. Thus the prediction of ion engine lifetime for space applications based on ground test results requires a thorough understanding of the grid erosion process and of the effects of chamber background pressure in particular.

Space-based operation

For a typical space-based operating condition, charge-exchange collisions only occur between beam ions and neutral particles escaping from the discharge chamber. Since the typical Knudsen number of the neutral flow from an ion thruster is greater than 100, the neutral flow actually is a free molecular flow. In the downstream region of the accelerator grid, most of the neutral atoms move away from the thruster. Fig. 1 shows an example of such a flow for a single aperture. Therefore, the downstream charge-exchange plasma created between beam ions and these neutral atoms will also move away from the thruster. Thus those charge-exchange ions created beyond the neutralization plane have little chance to return to the grid. Only those charge-exchange ions created inside the potential well, as shown in Fig. 2, can be accelerated to the accelerator grid and may cause grid erosion.

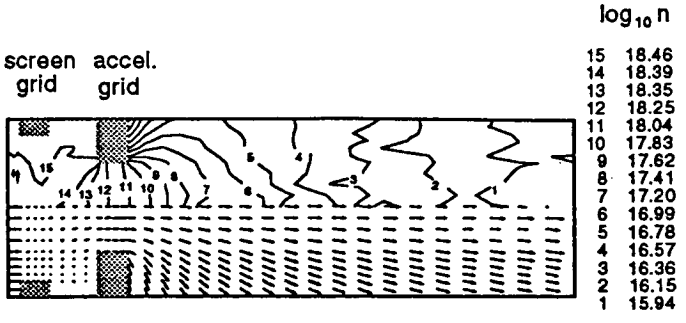

Figure 1: Calculated neutral flow.

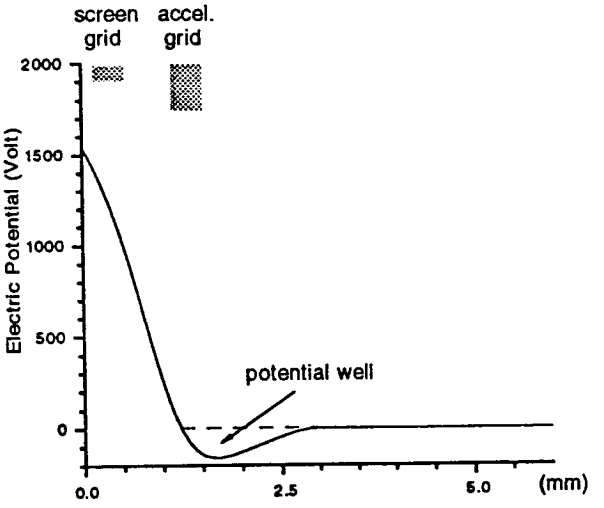

Figure 2: Centerline potential profile.

Ground-based operation

The residual neutral gas inside the vacuum chamber enhances the grid erosion rate in two ways. First, more charge-exchange ions will be created inside the potential well. The grid erosion rate, however, will not increase significantly, if the background neutral density is low enough in this region compared to the neutral density which results from the neutral loss from the discharge chamber. Second, unlike the space-based operation, charge-exchange ions created beyond the neutralization plane still have a chance to cause grid erosion. The reason is that, for ground-based operations, the residual neutral atoms inside the vacuum chamber move isotropically as do the neutral particles escaped from the discharge chamber after reflection by the vacuum chamber walls. Thus, at relatively high background pressure, the downstream charge-exchange plasma created between beam ions and residual neutral atoms is a stationary plasma. So, not only those charge-exchange ions created inside the potential well, as shown in Fig. 2, can be accelerated to the grid but also those charge-exchange ions created beyond the neutralization plane in the downstream plasma region. Therefore, the question is what percentage of the accelerator grid erosion is the result of the charge-exchange ions created between beam ions and residual neutral atoms inside the vacuum chamber. Based on our simulation, the majority of the accelerator grid erosion observed in tests operated on inert gases is caused by charge-exchange ions created between beam ions and residual neutral atoms inside the

vacuum chamber, particularly those created beyond the neutralization plane.

So, basically the charge-exchange collision process --- and thus the charge-exchange ion grid erosion process--- are different between space-based and ground-based operations. This can also be addressed using the simple one-dimensional model used by Kerslake [7]. In this one-dimensional model, the charge-exchange ion production rate is given by

$$dN = n_0 \sigma_{CE} n_b v_b A_b dz \qquad (1)$$

where N is the charge-exchange ion production rate, n_0 is the neutral number density, σ_{CE} is the charge-exchange collision cross-section, n_b is the number density of the beam ions, v_b is the beam ion velocity, and A_b is the diameter of the ion beam. By integrating Eq. (1), it is possible to obtain an expression for the accelerator grid impingement current:

$$J_a = \int_0^{l_{CE}} n_0 \sigma_{CE} n_b V_b A_b dz \,, \qquad (2)$$

where l_{CE} is the charge-exchange length. For the space operation condition, the charge-exchange length is about the distance between the accelerator grid and the neutralization plane. Charge-exchange ions created beyond the neutralization plane have little chance to return to the grid. However, for the ion thrusters operated inside ground-based vacuum chambers, charge-exchange ions created beyond the neutralization plane still have a chance to move back to the grid because the motion of the residual neutral gas is isotropic. Therefore, the charge-exchange length is really some characteristic length describing the charge-exchange volume, including both the potential well region and the downstream plasma region, in which charge-exchange ions being created could impact the accelerator grid. In other words, this characteristic length determines how much current can be extracted from the downstream plasma to the accelerator grid at a certain background pressure.

In conclusion, because the neutral flow field for space operation is different from the neutral flow field inside the ground vacuum chamber, the accelerator grid charge-exchange erosion process is also different for these two operations. More charge-exchange ions will strike the accelerator grid in ground-based operations than in space-based operations if the background pressure inside the ground vacuum chamber is not low enough. Hence, the grid erosion rate for space-based operating condition should be much less than that found in a ground test with a stationary downstream charge-exchange plasma at a relatively high background pressure (as in the case in Refs. [1-3]). Thus the observed accelerator grid erosion rate in ground tests [1,2] should not be used to estimate the accelerator grid lifetime for space operations.

3. Downstream Electric Potential Field

The above conclusion is based on the assumption that there is no electric potential hill downstream from the accelerator grid.

However, it has generally been thought that an electric potential hill exists within one centimeter downstream of the accelerator grid, and that only the charge-exchange ions formed upstream of this electric potential hill flow back toward the grid. Thus, those charge-exchange ions created beyond this potential hill will be accelerated away from the thruster and will not cause grid erosion. This theory has been used to explain the experimental results of mercury ion thruster ground tests and used by Kaufman [8] to predict space operations of ion thrusters.

However, an experiment conducted by Hughs Research Laboratory [9] has shown that the location of the electric potential maximum is at least several centimeters downstream of the accelerator grid and an experiment conducted by Colorado State University [10] has observed no electric potential hill at all.

In conclusion, some pertinent questions are whether there is such an electric potential hill existing downstream from the thruster; how big the potential hill is; and if it is a potential hill or potential island which the charge-exchange ions created far downstream from the thruster still can be accelerated around to get back to the grid.

4. Particle Simulation of Charge-Exchange Ion Grid Erosion

Three-dimensional particle simulations for studying charge-exchange ion grid erosion were performed for both ground-based operating conditions and space-based operating conditions. Two sets of the simulation parameters were chosen, corresponding to the experiments conducted at NASA LeRC [1] and NASA JPL [2]. Then, by assuming zero background pressure, the corresponding charge- exchange ion grid erosion rates under space-based conditions were obtained.

The ion optics used in both LeRC and JPL tests are of a two-grid, small hole accel. grid geometry with a

nominal grid diameter of 30 cm (effective beam diameter of 28.2 cm). Screen and accelerator grid aperture diameters are 1.9 mm and 1.1 mm, respectively. The separation of the two grids is 0.76 mm and the thickness of the grids is 0.36 mm. The holes for both grids are arranged in a hexagonal array with an open-fraction of 0.67 for the screen grid and 0.24 for the accelerator grid. In the model, the mean extracted ion velocity is determined using the Bohm criterion with assumed electron temperature of 1.5 eV. It is assumed that a neutral plasma exists at the upstream boundary of the computational domain. The plasma density is determined by the given beam current of 3.2 A for the LeRC test and 2.8 A for the JPL test. The screen grids are at 1517 Volt and 1800 Volt for the LeRC and JPL tests, respectively. The accelerator grids are at -331 Volt and -500 Volt, respectively. The LeRC test used xenon gas as propellant, for which the discharge voltage is assumed to be 28 Volt. The JPL test used krypton as propellant, for which the discharge voltage is assumed to be 40 Volt.

The Direct Simulation Monte Carlo (DSMC) model [11] is used to calculate the distribution of the neutral density resulting from the neutral atoms escaping from the discharge chamber. The propellant utilization efficiency is assumed to be 90% for the LeRC test and 81% for the JPL test. For simulations of space-based operating conditions, only this calculated neutral density is used to calculate the charge-exchange collisions. For the ground test cases, the total local neutral number density equals the local neutral density resulting from the neutral atoms escaped from the discharge chamber plus a constant neutral number density based on the background pressure inside the vacuum chamber.

For the ground test case, the charge-exchange ions striking the accelerator grid consist of charge-exchange ions created in the potential well and also those charge-exchange ions created beyond the neutralization plane. Actually, there is a stationary charge-exchange plasma formed beyond the neutralization plane. Thus, charge-exchange ions created beyond the neutralization plane (far downstream from the accelerator grid) still have a certain chance of being extracted from the downstream plasma to cause grid erosion. To include those charge-exchange ions created beyond the neutralization plane (far beyond the computational domain), a neutral plasma is assumed downstream from the accelerator grid. The calculation of grid erosion was made by choosing the number density of this downstream plasma in such a way as to yield the same impingement-to-beam current for the accelerator grid as observed in the ground test.

LeRC 890 hours test case

Figure 3 shows the calculated erosion contours for the downstream surface of the accelerator grid for the LeRC 890 hours test case (to aid in the visual interpretation, several cross-sections are shown together). The concentration of sputtering between grid apertures is clearly visible. Both the shape (roughly triangular) and orientation of these erosion contours are as observed in the experiment [1].

In previous papers [5], we have shown that such grid erosion pattern is a direct effect of the transverse electric fields downstream from the accelerator grid. There is a potential gradient in the transverse direction because of the presence of positive ion beamlets. Thus, slow charge-exchange ions are accelerated and focused into the geometric centers between apertures. This accounts for the pitting between apertures which was observed in the experiments.

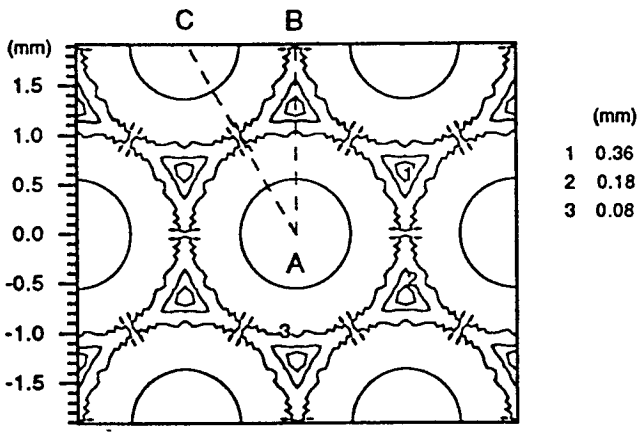

Figure 3. Calculated grid erosion contours on the downstream surface of the accelerator grid. Note the concentration of sputtering between apertures. The indicated length scale is in mm. (LeRC 890 hours test case.)

Figure 4 shows calculated erosion rates on the downstream surface of the accelerator grid for two cuts through the cross-section from Fig. 3. The erosion rate was obtained by converting the numbers of atoms sputtered during steady state conditions to a sputtering depth per 1000 hours of operation. Again, the tendency toward pitting between apertures is clearly evident, as witnessed by the much higher peak erosion rate along the cut A-B in Fig. 3 as compared with that along the cut A-C.

To reproduce the 0.55% ratio accelerator grid impingement current to beam current found in Ref. [1], it is required to have a downstream plasma density of 0.877×10^{15} m^{-3} with electron temperature of 1.5 eV. Using these values, the calculated cumulative mass loss from the downstream surface of the accelerator grid corresponding to an 890 hour test [1] is 23.2 grams. By comparison, the experimental value for the total accelerator grid mass loss from Ref. [1] is about 17.8 grams with an estimated 17.2 gm due to charge-exchange erosion on the downstream surface of the grid.

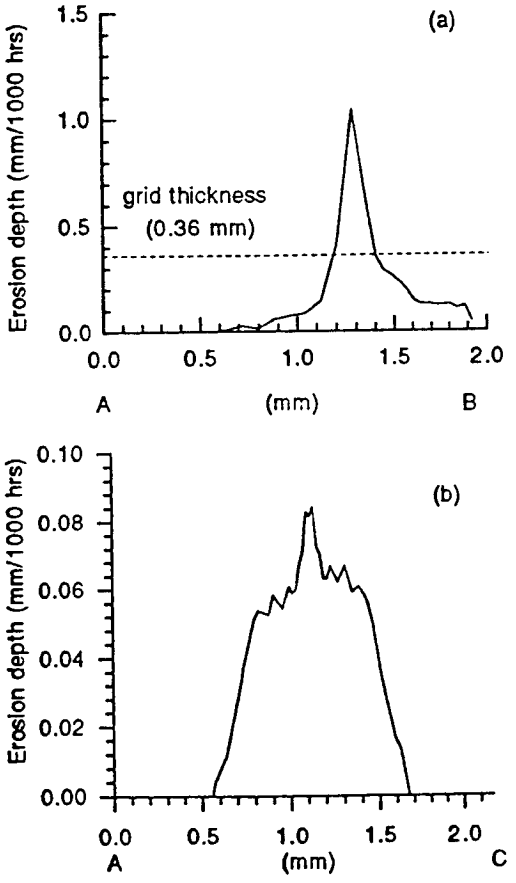

Figure 4. Calculated sputtering depths per 1000 hours of operation along the cuts A-B (a) and A-C (b) in Fig. 3.

For space-based operation, however, only those charge-exchange ions created in the potential well will be accelerated to the accelerator grid. The calculated ratio of accelerator grid impingement current to beam current is about 0.156% (4.99 mA). The calculated cumulative mass loss from the downstream surface of the accelerator grid for an 890 hours period is about 3.728 gm. That is, the expected mass loss for the space-based condition is almost an order of magnitude lower than for ground-based operation.

JPL 663 hours test case

Calculated erosion contours of the downstream surface of the accelerator grid for the JPL 663 hours test case is shown in Fig. 5 (again, to aid in the visual interpretation, several cross-sections are shown together). Because of a higher background pressure, 3×10^{-5} torr, more serious accelerator grid erosion was observed in the JPL test [2]. The calculated erosion depths on the downstream surface of the accelerator grid for two cuts through the cross-section from Fig. 5 are shown in Fig. 6. The erosion depth was obtained by converting the numbers of atoms sputtered during steady state conditions for 663 hours of operation.

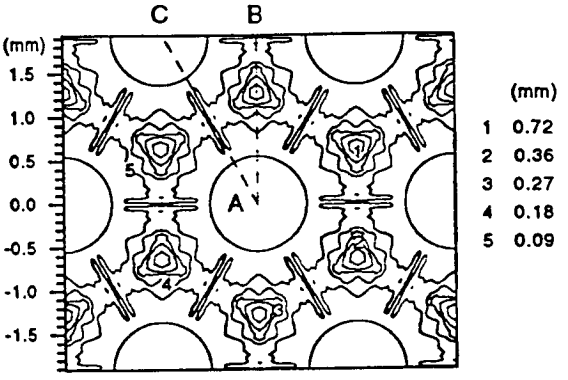

Figure 5. Calculated grid erosion contours on the downstream surface of the accelerator grid. Note again the concentration of sputtering between apertures. The indicated length scale is in mm. (JPL 663 hours test case.)

To reproduce the 1.23% ratio accelerator grid impingement current to beam current found in Ref. [2], it is required to have a downstream plasma density of 1.344×10^{15} m^{-3} for an assumed electron temperature of 1.5 eV. Using these values, the calculated cumulative mass loss from the downstream surface of the accelerator grid corresponding to a 663 hour test is 55 grams. By comparison, the experimental value for the total accelerator grid mass loss was about 45 grams.

For space-based operation, the calculated ratio of accelerator grid impingement current to beam current is about 0.168% (4.69 mA), compared to the LeRC case of 0.156%. The calculated cumulative mass loss from the downstream surface of the accelerator grid for a 663 hour period is about 3.35 gm (or 4.50 gm for 890 hours), compared to the LeRC case of 3.73 gm. This indicates that it would be desirable to operate the

accelerator grid close to ground potential if possible. Thus, the charge-exchange ions created inside the potential well would have less energy when they strike the grid. The comparison between the LeRC case and the JPL case also indicates that the propellant utilization efficiency becomes important in terms of the accelerator grid lifetime for space operations. Because the accelerator grid erosion is caused primarily by those charge-exchange ions created inside the potential well, an increased propellant utilization efficiency will decrease the neutral number density and therefore decrease the production rate of the charge-exchange ions inside the potential well. This effect is especially important for ion thrusters operated on krypton or argon as propellant for long duration operations, because the propellant utilization efficiency for operating on krypton and argon is usually less than for xenon.

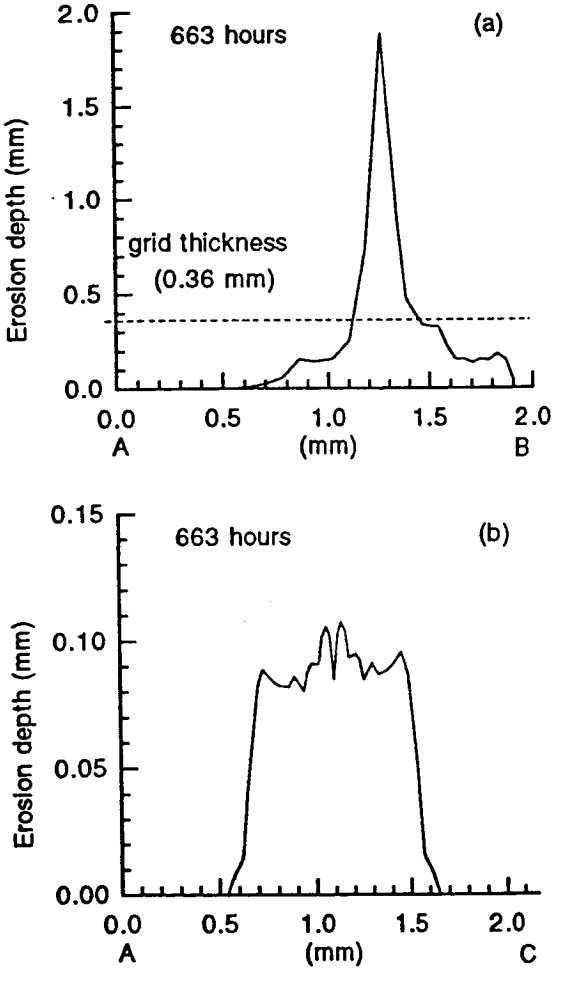

Figure 6. Calculated sputtering depths per 663 hours of operation along the cuts A-B (a) and A-C (b) in Fig. 5.

Finally, sputtering yields for xenon and krypton ions impinging on a molybdenum surface were taken from Ref. [12]. The sputtering yield measured in Ref. [12] is for the incidence of ions normal to the target surface. It is assumed, in our calculations, that the sputtering yield is independent of the angle of incidence of the impacting ions. This makes the calculated erosion rate doubtful if the incident ions strike the surface with large incident angle. This probably will not change the calculated erosion rate for the downstream surface of the accelerator grid for thrusters operated inside the vacuum chamber with relatively high background pressure, because most erosion is caused by those charge-exchange ions with full accelerator potential. But, since most ions strike the interior surface of the accelerator grid with large incident angles, the calculated erosion rate based on the sputtering yield data from Ref. [12] is probably too large. Charge-exchange ions created in the potential well usually have larger incident angles than those created far downstream from the accelerator grid when striking the downstream surface the accelerator grid. Therefore, the calculations based on Ref. [12] might overestimate the actual erosion rate for space-based operations. Furthermore it is assumed that no geometry changes result from the sputtering process. However, according to Ref. 9, increased surface roughness decreases the sputtering yield because more sputtered atoms become trapped and cannot escape from the target. This effect is more pronounced at lower ion energy because the material then tends to be ejected more obliquely to the target surface. Thus, strictly speaking, the calculations are valid only for small erosion depths, and comparisons between our calculated results and experiments in which full penetration of the grids occurs must be undertaken with some caution. This may also be used to explain why our model always overestimates the mass loss rate of the grid erosion compared to the experiments.

5. Discussion and Summary

Based on our PIC simulation model, the serious accelerator grid erosion observed inside the ground test chamber [1-2] is largely caused by charge-exchange ions created between beam ions and residual neutral atoms. In other words, the facility effect dominates the charge-exchange erosion process with background pressure in the 10^{-5} Torr range. The major difference between space-based operation and ground-based operation in terms of the charge-exchange erosion process is that the downstream neutral flow field is different and therefore the downstream charge-exchange plasma is different. For a space-based operating condition, the

neutral atoms move away from the thruster. Therefore, only those charge-exchange ions created inside the potential well can be accelerated to the grid. Most charge-exchange ions created beyond the neutralization plane will move away from the thruster. For ground-based operation, however, the motion of the downstream neutral gas is isotropic. Thus, not only those charge-exchange ions created inside the potential well can be accelerated to the grid but also those charge-exchange ions created beyond the neutralization plane. Hence, the grid erosion rate for space-based operating condition should be much less than that in a ground test with relatively high background pressure.

Calculations were performed to simulate both a NASA LeRC 890 hours test case and a NASA JPL 663 hours test case. The erosion rates under space condition were also calculated for these two cases. For NASA LeRC 890 hours test case, the calculated mass loss from the downstream surface of the accelerator grid is 23.3 gm, compared to the experimental value of about 17.8 gm. The calculated mass loss under space condition is about 3.7 gm. For the NASA JPL 663 hours test case, the calculated mass loss from the downstream surface of the accelerator grid is about 55.16 gm compared to the experimental value of about 44.75 gm. The calculated mass loss under space condition is only about 3.35 gm.

Comparing the NASA LeRC case and the NASA JPL case, it appears that the propellant utilization efficiency plays an important role in terms of the accelerator grid erosion for space operation. Because the accelerator grid erosion is caused primarily by those charge-exchange ions created inside the potential well, an increased propellant utilization efficiency will decrease the neutral number density and therefore decrease the production rate of the charge-exchange ions inside the potential well. This effect is especially important for ion thrusters operated on krypton or argon as propellant for long duration operations.

(An earlier version of this paper was presented at the 23rd International Electric Propulsion Conference [13].

Acknowledgements

This work was jointly supported by Boeing Defense & Space Group in Seattle, Washington (grant monitor Dr. J. S. Meserole) and the University of Tennessee--Calspan Center for Space transportation and Applied Research under NASA grant NAGW-1195. We thank Dr. J. Brophy for making the results from Ref. 2 available in advance of the 23rd International Electric Propulsion Conference.

References

[1] Patterson, M. J., and Verhey, T. R., ``5 kW Xenon Ion Thruster Lifetest," AIAA Paper 90-2543, Orlando, FL, July 1990.

[2] Brophy, J., and Pless, L., ``Test-to-Failure of a Two-Grid, 30-cm-dia. Ion Accelerator System," IEPC Paper 93-172, Seattle, WA, September 1993.

[3] Rawlin, V. K., ``Internal Erosion Rates of a 10-kW Xenon Ion Thruster," AIAA Paper 88-2912, Boston, MA, July 1988.

[4] Peng, X., Keefer, D., and Ruyten, W. M., ``Plasma Particle Simulation of Electrostatic Ion Thruster," *J. of Propulsion and Power,* Vol. 8, No. 2, pp. 361-366, March-April 1992.

[5] Peng, X., Ruyten, W. M., and Keefer, D., ``Three-Dimensional Particle Simulation of Grid Erosion in Ion Thrusters," IEPC Paper 91-119, Viareggio, Italy, October 1991.

[6] Peng, X., Ruyten, W. M., and Keefer, D., ``Further Study of the Downstream Plasma Condition on Accelerator Grid Erosion in an Ion Thruster," AIAA Paper 92-3829, Nashville, TN, July, 1992.

[7] Kerslake, W. R., ``Charge-Exchange Effects on The Accelerator Impingement of an Electro-Bombardment Ion Rocket," NASA TN D-1657, NASA Lewis Research Center, May 1963.

[8] Kaufman, H. R., "Accelerator-System Solutions for Broad-Beam Ion Sources," AIAA Journal, Vol. 15, No. 7, July 1977, pp. 1025-1034.

[9] Beattie, J. R. and Matossian, J. N., "High Power Ion Thruster Technology, " NASA Contract Report CR-187161, February 1992.

[10] Monheiser, J. and Wilbur, P., "Effects of Design and Operating Conditions on Accelerator-Grid Impingement Current," IEPC Paper 93-174, 23rd International Electric Propulsion Conference, Seattle, WA, September 13-16, 1993.

[11] Zhang, Q., Peng, X., and Keefer, D., ``Particle Simulation of Grid Erosion for a Three-Grid Ion Thruster," ERC-R-92-080, ERC, Inc., October 1992.

[12] Rosenberg, D., and Wehner, G. K., ``Sputtering Yields for Low Energy He^+-, Kr^+-, and Xe^+-Ion Bombardment," *J. of Applied Physics*, Vol. 33, No. 5, pp. 1842-1845, May 1962.

[13] Peng, X., Ruyten, W. M., and Keefer, D., "Charge-Exchange Grid Erosion Study for Ground-Based and Space-Based Operations of the Ion Thrusters," IEPC Paper 93-173, 23rd International Electric Propulsion Conference, Seattle, WA, September 13-16, 1993.

Electric Propulsion Technology Applications

R. Chapman[**], V. J. Friedly[*], X. Peng[*], W. M. Ruyten[‡], and G. W. Garrison[†]

University of Tennessee—Calspan
Center for Space Transportation and Applied Research
UTSI Research Park, Tullahoma, Tennessee 37388-8897

ABSTRACT

CSTAR has recently initiated an activity in the commercial development of electric propulsion technologies. This effort will utilize the expertise at CSTAR in various technologies developed for electric propulsion to adapt and apply those technologies for use in industrial applications. The purpose of this paper is to describe the approach that is being developed for technology transfer and to discuss opportunities that have been presently identified.

INTRODUCTION

One of the objectives of the NASA Centers for Commercial Development of Space (CCDS) is to support the commercial development of space-based technologies. As the CCDS with a major research area in electric propulsion, CSTAR is pursuing the transfer of technologies developed for electric propulsion for use in industrial applications.

TECHNOLOGY TRANSFER APPROACH

The approach that has been initally developed to effect transfer of electric propulsion technologies consists of the following phases. In addition, the approach will draw from the experience of other successfull efforts at CSTAR such as the Laser Industrial Partnership Program (LIPP).

1. Complete a literature review to assess the electric propulsion related devices and techniques that are currently available and utilized by industry. This review will include a determination of the requirements imposed on these devices by the various application processes and also an identification of additional commercial applications that may benefit from the use of electric propulsion related technologies.

2. Perform market surveys and compile a list of potential industries to be contacted. These surveys can be obtained through the following sources:

   - Peat Marwick Management Consultants - Commercial
   - Industry Contacts - Industrial
   - Tennessee Valley Aerospace Region (TVAR) - Government
   - Center for Industrial Surveys (CIS) - Academia

3. Attend various conferences and symposia to establish initial contacts with industry and to follow up on the assessment in phase 1 and the surveys in phase 2.

4. Identify potential opportunities for technology transfer and categorize by perceived risk/payoff.

5. Establish contacts with individual companies that have an interest in the opportunities identified in phase 4.

6. Develop technology transfer projects with companies contacted in phase 5.

[**] Principal Research Engineer, CSTAR/Calspan
[*] Research Engineer, CSTAR/UTSI
[‡] Senior Research Engineer, CSTAR/Calspan
[†] CSTAR Executive Director and Professor of Mechanical Engineering

TECHNOLOGY TRANSFER PROJECTS

Although the literature review and market surveys in phases 1 and 2 of the technology transfer approach are still in progress, two promising technology transfer opportunities have already been identified.

One opportunity is in the development of ion sources for materials processing (i.e., ion etching, deposition, and/or implantation). A requirement has been identified for a broad-beam (45-60 cm) ion source with a flat (<4% max-min/max+min) beam profile. Modifications to a PIC code, which was originally developed to model the ion dynamics through a single aperature of an ion thruster, are currently underway to enable the numerical simulation of multiple-aperature, broad-beam, accelerator grids. Preliminary calculations will be made to determine the predominate parameters (e.g., discharge chamber plasma density profiles, grid geometry, aperature alignment, etc.) that control the ion beam profile. Based on the results of the preliminary calculations, a parameteric study will be performed to determine the set of parameters that result in the desired beam profile. A small scale experiment will then be designed in order to achieve the desired beam profile and to verify the theoretical model.

The other opportunity is in the commercial development of a gas leak detection system based on Raman scattering. A technique using laser induced spontaneous Raman scattering of gases to accurately measure temperature and species concentrations in low thrust chemical rocket engines has been developed at the NASA-Lewis Research Center. With some modifications, this technique can be easily adapted to commercial applications for gas leak detection. The major advantage of this particular detection method is that the measurement itself is accomplished with a compact, lightweight optical head attached to flexible optical fibers. This allows the measurements to be made over a large area quickly in hostile and inaccessible environments with the data processing occuring in a safe and convenient location. Other advantages are that several gases can be detected at very low concentrations simultaneously, gases without an infrared spectrum (e.g., many diatomic gases) can be detected, in-situ, real-time measurements are possible, and gas temperatures over a wide range can be determined.

SUMMARY

An approach to effect the transfer of electric propulsion technologies for use in industrial applications has been developed. A literature review to identify potential technology transfer opportunites has been initiated. Two possible opportunities, the development of an ion source for materials processing and the commercial development of a gas leak detection system, have been identified and are currently being pursured. Future work will involve completing the literature review and performing market surveys, establishing contacts with industry, and developing several technology transfer projects with individual companies.

ACKNOWLEDGMENTS

This work is supported by the NASA-Lewis Research Center under Grant NAG3-1506.